Design and Optimization of the Recovery and Recycling of Fluorinated Working Fluids Using a Multiscale Simulation Approach

Daniel Jovell Hidalgo

UNIVERSITAT RAMON LLULL

DOCTORAL THESIS

Title	Design and Optimization of the Recovery and Recycling of Fluorinated Working Fluids Using a Multiscale Simulation Approach
Presented by	Daniel Jovell Hidalgo
Centre	IQS School of Engineering
Department	Chemical Engineering and Material Science
Directed by	Dr. Fèlix Llovell Ferret Dr. Rafael González Olmos

"If I waited for perfection, I would never write a word."

Margaret Atwood.

This thesis has been funded with support from the Project KET4F-Gas, SOE2/P1/P0823, which is cofinanced by the European Regional Develompent Fund whithin the framework of the Interreg SUDOE Program.

Acknowledgements

No és casualitat que la primera pàgina d'aquesta tesi doctoral siguin els agraïments. Aquesta és, sense cap mena de dubte, la pàgina més especial de tota la tesi doctoral perquè tota la feina que hi ha a les pàgines posteriors no hagués estat possible sense tota la gent que aquí hi apareix. És per això que tinc la necessitat d'agrair-los-hi i de fer-los saber que aquesta tesi és, també, una miqueta seva.

En primer lloc, agrair als meus dos directors, el Fèlix i el Rafa, per l'esforç, la paciència i la dedicació durant aquests quatre anys. Ells han sabut adaptar-se a qualsevol situació per molt complicada que fos i m'han ensenyat a ser una persona més crítica, analítica, humil i a la vegada valenta. A través de cada consell, cada revisió i cada trucada han esdevingut els meus pares científics i és gràcies a ells que aquesta tesi està avui acabada. Si el Dani d'ara és en algun aspecte millor que el de fa quatre anys, és segurament cosa seva i això no ho puc representar en un gràfic, en una taula de resultats ni fins i tot en aquestes línies. De tot cor: gràcies.

Cal incloure també en aquesta llista al Gerard i al Pablo, de la Universitat de Barcelona, per tota la seva immesurable ajuda en la realització de les simulacions moleculars. En especial al Gerard, que ha demostrat tenir una paciència infinita amb mi. Gràcies per l'oportunitat.

A l'Ari i l'Albert, sense els quals aquesta tesi doctoral no hauria tirat endavant. Gràcies per haver fet del doctorat una experiència de vida; gràcies per tots els esmorzars, les sortides, les calçotades i les sessions de cures i gràcies haver-me deixat aprendre de vosaltres aquesta habilitat que teniu de fer tot allò que us proposeu. No oblideu mai tot el potencial que teniu (i si arribés el cas, aquí queda escrit per recordar-vos-ho). Tant de bo allà on em porti la vida, tingui al meu costat a una Ari i/o a un Albert.

També vull agrair a la resta de companys del GCQV perquè totes heu aportat el vostre gra de sorra: els cafès eterns amb l'Héctor, els dinars, també eterns del Ferran, el cuc de sortir a córrer del Josep, els debats amb el Guillermo i o l'obsessió del Ricard pels gestors de contrasenyes. No m'oblido del Jan ni de la Laia. Si no hem arreglat el món a hores d'ara és perquè no s'ha deixat arreglar, però espero tenir-vos al meu costat durant molts més anys per continuar intentant-ho.

A la resta de la bona gent d'IQS: a l'Oriol Pou, al Damià, a la Vane, a la resta del grup GESPA i a tots els TFMs i TFGs que han passat per la planta pilot, amb menció especial pel Santi i la Clara. Gràcies per fer una miqueta més amena l'estada a la planta pilot i a IQS.

A en Gallardo, la Mercè, en Quim, la Mariona, l'Alba, el Martí, la Laura, la Glòria i la Lara que, a banda d'haver escoltat la problemàtica dels *fosforitos* més de quinze vegades, fan una

feina incansable per lluitar contra la ingerència que té el capital sobre el sistema universitari i de recerca. Gràcies i no defalliu.

A la Lidia, que malgrat els anys que fa que ens coneixem, tota una vida ja, encara em sorprèn la seva habilitat per conèixer-me a mi millor que jo mateix i saber què necessito en tot moment. Psicòloga, consellera, i una referent a qui agraeixes tenir al costat en els moments bons i els dolents. Al món hi hauria d'haver més Lidies.

A la Mire, que potser sense ser-ne ella del tot conscient, ha sigut des del primer dia que la vaig conèixer, un model a seguir. Si bé no arribaré mai a tenir la seva empenta ni la seva capacitat de resolució, el fet d'haver-la tingut al costat m'ha ajudat a convertir les meves mancances en virtuts. Gràcies pels consells i per deixar-me créixer al teu costat.

Al Ramon, perquè amb ell, tot. Per la seva capacitat d'escoltar, de fer seus els meus problemes i de tenir tota la tendresa que jo no tindré ni en dues vides. Gràcies per deixar-me recolzar en tu.

No em descuido ni de la resta d'*objectiu* (l'Ainhoa, l'Oriol, l'Ale, i l'Andreu) ni dels amics de la UAB (l'Elena, la Laia, la Júlia, l'Estela, el Roger i el Sergi). Sou sempre una alegria, una via d'escapament i una (o a vegades més d'una) birra quan hom la necessita.

A totes les persones que segur que em descuido i que hauríeu de ser-hi...

A la meva família, pel vostre suport i amor incondicional, per fer-me millor persona i per continuar aprenent de vosaltres.

I per últim a tu, lector/a, que si has arribat fins aquí, és per l'interès que et genera aquesta tesi o per l'estima que em tens. En qualsevol dels casos, gràcies i gaudeix-la.

Abstract

Climate change is a real phenomenon, undoubtedly caused by human activities and, most notably, by the emissions of CO_2 and other greenhouse gases from the combustion of fossil fuels. While CO_2 emissions account for at least two-thirds of global greenhouse gas emissions, other compounds, like fluorinated gases (F-gases), also contribute to the increase of those emissions. The specific case of F-gases is particularly alarming since they have a global warming potential up to 12,400 times that of CO_2, meaning that even relatively low atmospheric concentrations can disproportionately influence global climate change. Hydrofluorocarbons (HFCs) account for the majority of these F-gas emissions and were, in 2020, about 5,700 times higher than in 1990 in Europe. Apart from the obvious environmental concern, the underlying problem related to these gases is the nonexistence of a standardized technology for their treatment. Therefore, they are sent for incineration with the corresponding environmental cost when their life cycle is over. The overall purpose of this Ph.D. thesis is to design recovery and recycling ecotechnological methods for HFCs in order to provide a sustainable solution to the current environmental challenge. The recovery and reuse of F-gases is a promising strategy that extends their lifespan while reducing the amount of new F-gases brought to the market and their eventual release into the atmosphere, thereby pushing the market toward a circular economy. To that end, the feasibility of recovering HFCs using absorption techniques and advanced solvents, like different families of ionic liquids and deep eutectic solvents, is addressed by means of a combination of multiscale modeling tools to provide different levels of resolution and complexity to study these systems, which range from quantum-based calculations to commercial process simulators and life cycle assessment. First, molecular models were built employing relatively simple coarse-grained models for several F-gases and advanced solvents to perform a conductive study modeling the solubility and the recovery capacity in these solvents. The results obtained guided two process simulation studies performed to estimate the approximate energy and environmental costs of the separation and recovery process from commercial HFC blends. The final step of this work comprises the study of sustainable alternatives to currently used HFCs, including promising fluorinated families like hydrofluoroolefins and hydrofluoroethers in a wide range of applications. Once again, different computational tools are combined to gain insight into their thermophysical behavior through the use of molecular simulations or to address its capacity to substitute current HFCs in specific applications from a complete thermodynamic and energy analysis done using SAFT equations of state. The final purpose of this thesis is to offer a variety of solutions to tackle the necessary change of a model from a linear economy to a circular economy, as well as to provide basic knowledge of future alternatives according to the coming restrictive legislation via a multiscale approach of techniques, contributing to the planet's sustainability.

Resum

El canvi climàtic és un fenomen real, indubtablement causat per l'activitat humana i, més notòriament, per les emissions de CO_2 i altres gasos d'efecte hivernacle procedents de la crema de combustibles fòssils. Tot i que les emissions de CO_2 representen almenys dos terços de les emissions mundials de gasos d'efecte d'hivernacle, altres compostos, com els gasos fluorats (gasos-F), també contribueixen a l'augment d'aquestes emissions. El cas concret dels gasos-F és especialment alarmant, ja que tenen un potencial d'escalfament global fins a 12.400 vegades superior al del CO_2, fet que suposa que fins i tot concentracions atmosfèriques relativament baixes poden influir de manera desproporcionada en el canvi climàtic global. Els hidrofluorocarbonis (HFCs) representen la major part d'aquestes emissions de gasos-F i, el 2020, eren unes 5.700 vegades superiors al valor de 1990 a Europa. A banda de l'evident preocupació ambiental, el problema subjacent relacionat amb aquests gasos és la inexistència d'una tecnologia estandarditzada per al seu tractament. Per tant, s'envien a incinerar amb el corresponent cost ambiental quan acaba el seu cicle de vida. L'objectiu general d'aquesta tesi doctoral és dissenyar mètodes ecotecnològics de recuperació i reciclatge dels HFCs per a donar una solució sostenible a l'actual repte ambiental. La recuperació i reutilització dels gasos-F és una estratègia prometedora que prolonga la seva vida útil, a la vegada que redueix la quantitat de nous gasos-F introduïts al mercat i el seu eventual alliberament a l'atmosfera, impulsant així el mercat cap a una economia circular. Amb aquest propòsit, s'estudia la viabilitat de la recuperació dels HFC mitjançant tècniques d'absorció i dissolvents avançats, com diferents famílies de líquids iònics i dissolvents eutèctics profunds, mitjançant una combinació d'eines de modelatge multiescala que proporcionen diferents nivells de resolució i complexitat per a estudiar aquests sistemes, que van des de càlculs químico-quàntics fins als simuladors de processos comercials i l'anàlisi del cicle de vida. En primer lloc, es van construir models moleculars emprant models *coarse-grained* relativament senzills per a diversos gasos-F i dissolvents avançats per a realitzar un estudi amb la finalitat de modelar la solubilitat i capacitat de recuperació en aquests dissolvents. Els resultats van guiar dos estudis de simulació de processos amb l'objectiu d'estimar els costos energètics i ambientals aproximats del procés de separació i recuperació de les mescles comercials de HFCs. L'últim pas d'aquest treball comprèn l'estudi d'alternatives als HFC emprats actualment, incloent-hi famílies fluorades prometedores com les hidrofluoroolefines i els hidrofluoroèters en una àmplia gamma d'aplicacions. Una vegada més, es combinen diferents eines computacionals per a conèixer el seu comportament termofísic, mitjançant l'ús de simulacions moleculars, o per adreçar la seva capacitat de substituir als actuals HFC en aplicacions específiques a partir d'una completa anàlisi termodinàmica i energètica mitjançant equacions d'estat SAFT. El propòsit final d'aquesta tesi és oferir una varietat de solucions per a abordar el necessari canvi de model d'una economia lineal a una de circular, així com proporcionar un coneixement bàsic de les alternatives d'acord amb la nova legislació a través d'un enfocament multiescala, contribuint a la sostenibilitat del planeta.

Resumen

El cambio climático es un fenómeno real, indudablemente causado por la actividad humana y, más notoriamente, por las emisiones de CO_2 y otros gases de efecto invernadero procedentes de la quema de combustibles fósiles. Aunque las emisiones de CO_2 representan al menos dos tercios de las emisiones mundiales de gases de efecto invernadero, otros compuestos, como los gases fluorados (gases-F), también contribuyen al aumento de esas emisiones. El caso concreto de los gases-F es especialmente alarmante, ya que tienen un potencial de calentamiento global hasta 12.400 veces superiores al del CO_2, lo que significa que incluso concentraciones atmosféricas relativamente bajas pueden influir de forma desproporcionada en el cambio climático global. Los hidrofluorocarbonos (HFCs) representan la mayor parte de estas emisiones de gases-F y, en 2020, eran unas 5.700 veces superiores al valor de 1990 en Europa. Aparte de la evidente preocupación ambiental, el problema subyacente relacionado con estos gases es la inexistencia de una tecnología estandarizada para su tratamiento, enviándose a incinerar con el correspondiente coste ambiental cuando termina su ciclo de vida. El objetivo general de esta tesis doctoral es diseñar métodos ecotecnológicos de recuperación y reciclaje de los HFCs para dar una solución sostenible al actual reto ambiental. La recuperación y reutilización de los gases-F es una estrategia prometedora que prolonga su vida útil, al tiempo que reduce la cantidad de nuevos gases-F introducidos en el mercado y su eventual liberación a la atmósfera, impulsando así el mercado hacia una economía circular. Para ello, se aborda la viabilidad de la recuperación de los HFC mediante técnicas de absorción y disolventes avanzados, como diferentes familias de líquidos iónicos y disolventes eutécticos profundos, mediante una combinación de herramientas de modelado multiescala que proporcionan diferentes niveles de resolución y complejidad para estudiar estos sistemas, que van desde cálculos químico-cuánticos hasta los simuladores de procesos comerciales y la evaluación del ciclo de vida. En primer lugar, se construyeron modelos moleculares empleando modelos *coarse-grained* relativamente sencillos para varios gases-F y disolventes avanzados para realizar un estudio con el fin de modelar la solubilidad y capacidad de recuperación en estos disolventes. Los resultados guiaron dos estudios de simulación de procesos con el objetivo de estimar los costes energéticos y ambientales aproximados del proceso de separación y recuperación de las mezclas comerciales de HFCs. El último paso de este trabajo comprende el estudio de alternativas a los HFC utilizados actualmente, incluyendo familias fluoradas prometedoras como las hidrofluoroolefinas y los hidrofluoroéteres en una amplia gama de aplicaciones. Una vez más, se combinan diferentes herramientas computacionales para conocer su comportamiento termofísico, mediante el uso de simulaciones moleculares, o para abordar su capacidad de sustituir a los actuales HFC en aplicaciones específicas a partir de un completo análisis termodinámico y energético mediante ecuaciones de estado SAFT. El propósito final de esta tesis es ofrecer una variedad de soluciones para abordar el necesario cambio de modelo de una economía lineal a una circular, así como proporcionar un conocimiento básico de las alternativas de acuerdo con la nueva legislación a través de un enfoque multiescala de técnicas, contribuyendo a la sostenibilidad del planeta.

Contents

List of Figures

List of Tables

List of Abbreviations

AAD	**A**bsolute **A**verage **D**eviation
AARD	**A**bsolute **A**verage **R**elative **D**eviation
ADF	**A**biotic **D**epletion **F**actor
ADP	**A**biotic **D**epletion **P**otential
AP	**A**cidification **P**otential
API	**A**merical **P**etroleum **I**nstitute
ASHRAE	**A**merican **S**ociety of **H**eating, **R**efrigerating and **A**ir-Conditioning **E**ngineers
ASTM	**A**merican **S**ociety for **T**esting and **M**aterials
CFC	**C**hloro**f**luoro**c**arbon
COSMO-RS	**CO**nductor-like **S**creening **M**odel for **R**eal **S**olvents
COP	**C**oefficient **O**f **P**erformance
DES	**D**eep **E**utectic **S**olvent
DGT	**D**ensity **G**radient **T**heory
EoL	**E**nd **O**f **L**ife
EoS	**E**quation **O**f **S**tate
ER	**E**xpansion **R**atio
EU	**E**uropean **U**nion
EP	**E**utrophication **P**otential
FAETP	**F**reshwater **A**quatic **E**co**t**oxicity **P**otential
F-gases	**F**luorinated **gases**
FIL	**F**luorinated **I**onic **L**iquid
FVT	**F**ree **V**olume **T**theory
GHG	**G**reen**h**ouse **G**ases
GWP	**G**lobal **W**arming **P**otential
HBA	**H**ydrogen **B**ond **A**ceptor
HBD	**H**ydrogen **B**ond **D**onor
HCFC	**H**ydro**c**hloro**f**luoro**c**arbon
HFC	**H**ydro**f**luoro**c**arbon
HFE	**H**ydro**f**luoro**e**thers
HFO	**H**ydro**f**luoro**o**lefins
HTF	**H**eat **T**ransfer **F**luid
HTP	**H**uman **T**oxicity **P**otential
HVAR	**H**eating, **V**entilating and **A**ir **C**onditioning
IL	**I**onic **L**iquid
IPCC	**I**ntergovernamental **P**anel on **C**limate **C**hange
KET	**K**ey **E**nabling **T**echnologies
KP	**K**ioto **P**rotocol
LAR	**L**east **A**bsolute **R**esiduals
LCA	**L**ife **C**ycle **A**ssessment
LCI	**L**ife **C**ycle **I**inventory
LCIA	**L**ife **C**ycle **I**mpact **A**ssessment
LFL	**L**ower **F**lammabiliry **L**imit
LJ	**L**ennard **J**ones
LULUCF	**L**and-**U**se, **L**and-**U**se **C**hange and **F**orestry

LHV	**L**ower **H**eating **V**alue
MAC	**M**obile **A**ir-**C**onditioning **S**ystem
MAE	**M**ean **A**bsolute **E**rror
MAETP	**M**arine **A**quatic **Eco**t**o**xicity **P**otential
MFA	**M**aterial **F**low **A**nalysis
NA	**N**ot **A**pplicable
NBP	**N**ormal **B**oiling **P**oint
NE	**N**ot **E**stimated
NIST	**N**ational **I**nstitute of **S**tandards and **T**echnology
NO	**N**ot **O**curring
NRTL	**N**on-**R**andom-**T**wo-textbfLiquids
OEM	**O**riginal **E**quipment **M**anufacturer
ODP	**O**zone **D**epletion **P**otential
ORC	**O**rganic **R**ankine **C**ycle
PEL	**P**ermissible **E**xposure **L**imit
PFC	**P**er**f**luoro**c**arbon
POCP	**P**hotochemical **O**zone **C**reation **P**otential
PS	**P**rocess **S**imulation
RACHP	**R**efrigeration **A**ir **C**onditioning and **H**eat **P**ump
RAINS	**R**egional **A**ir Polution **IN**formation and **S**imulation
RF	**R**eference **F**luid
SAFT	**S**tatistical **A**ssociation **F**luid **T**heory
SNAP	**S**ignificant **N**ew **A**lternatives **P**rogram
ST	**S**urface **T**ension
TETP	**T**errestrial **Eco**t**o**xicity **P**otential
UNIFAC	**UNI**versal **F**unctional **A**ctivity **C**oefficient
UNIQUAC	**UNI**versal **QU**asichemical **A**ctivity **C**oefficient
UNECE	**U**nited **N**ations **E**conomic **C**omission for **E**urope
USES	**U**niform **S**ystem for the **E**valuation of **S**ubstances
VLE	**V**apor-**L**iquid **E**quilibria
VLLE	**V**apor-**L**iquid-**L**iquid **E**quilibria
WMO	**W**orld **M**eteorological **O**rganization
WRI	**W**orld **R**esource **I**nstitute

Physical Constants

Avogadro constant	$N_{\mathrm{A}} = 6.022\,140 \times 10^{23}\,\mathrm{mol}^{-1}$
Boltzmann constant	$k_{\mathrm{B}} = 1.380\,649 \times 10^{-23}\,\mathrm{J\,K}^{-1}$
Molar gas constant	$R = 8.314\,472\,\mathrm{J\,mol}^{-1}\,\mathrm{K}^{-1}$
Planck's constant	$h = 6.626\,070 \times 10^{-34}\,\mathrm{J\,Hz}^{-1}$
Vacuum permittivity	$\epsilon_0 = 8.854\,187 \times 10^{-12}\,\mathrm{F\,m}^{-1}$

List of Symbols

Latin symbols

a	Perturbation term	(-)
a_{eff}	Effective contact area	Å^2
$\vec{a}$	Acceleration vector	$\text{m}\,\text{s}^{-2}$
A	Helmholtz free energy	J
A_i	Molecular surface of component i	Å^2
$\mathcal{A}$	Thermodynamic property	(-)
$\vec{b}$	Third derivative coordinate vector	$\text{m}\,\text{s}^{-3}$
B	Free-volume overlap	(-)
c	Influence parameter of the DGT	$\text{Jmol}^5\text{mol}^{-2}$
c_{HB}	Hydrogen bond strength	$\text{kJ}\,\text{mol}^{-1}\,\text{Å}^{-2}\text{e}^{-2}$
C_{x}	Constant parameter	(-)
C_p	Isobaric heat capacity	$\text{J}\,\text{mol}^{-1}\,\text{K}^{-1}$
C_v	Isochoric heat capacity	$\text{J}\,\text{mol}^{-1}\,\text{K}^{-1}$
E	Total energy	J
E	Internal energy	J
f	Fugacity	MPa
F_c	Correction factor	(-)
$\vec{F}$	Force vector	N
g	Radial distribution function	(-)
g_R	Pair correlation function of the RF	(-)
G	Gibbs free energy	J
H	Enthalpy	$\text{J}\,\text{mol}^{-1}$
$\vec{J}$	Flux (mass, heat, current)	(-)
$\vec{k}$	Reciprocal space vector (Ewald sum)	(-)
k_{H}	Henry's coefficient	MPa
k_{bend}	Force constant for angle bending	$\text{kJ}\,\text{mol}^{-1}\,\text{rad}^{-2}$
k_{bond}	Force constant for bond stretching	$\text{kJ}\,\text{mol}^{-1}\,\text{Å}^{-2}$
k_{tors}	Force constant for torsion	$\text{kJ}\,\text{mol}^{-1}$
K	Kinetic energy	J
K	Volume of association	Å^3
L	Length (simulation box)	Å
L_{ij}	Phenomenological (or Onsager) coefficients	(-)
L_v	Length parameter of the FVT	Å
m	Mass	g
m	Chain lenght (SAFT parameter)	(-)
M_i	Number of association sites of i	(-)
M_w	Molecular weight	$\text{g}\,\text{mol}^{-1}$
n	Number of moles	mol
$\vec{n}$	Cell vector	(-)
N	Number of particles, atoms,...	(-)
$\mathcal{O}(\delta t^N)$	Order of truncation error	(-)

$\vec{p}$	Momentum vector	$\mathrm{N\,s}$
P	Pressure	Pa
Q	Partition function	(-)
q_i	Partial charge	C
$\wp$	Probability distribution	(-)
$\vec{r}$	Position vector	$\mathrm{Å}$
r_{ij}	Interatomic distance	$\mathrm{Å}$
r_c	Cutoff radius	$\mathrm{Å}$
$\vec{r}$	Position vector	$\mathrm{Å}$
S	Entropy	$\mathrm{J\,K^{-1}}$
t	Time	s
T	Thermodynamic temperature	K
U	Potential (configurational) energy	$\mathrm{J\,mol^{-1}}$
$\vec{v}$	Velocity vector	$\mathrm{m\,s^{-1}}$
V	Volume	$\mathrm{m^3}$
w	Speed of sound	$\mathrm{m\,s^{-1}}$
x	Mole fraction	$\mathrm{mol\,mol^{-1}}$
X_x	Fraction of molecules not bonded to the site x	$\mathrm{mol\,mol^{-1}}$
z	Feed concentration	$\mathrm{mol\,L^{-1}}$

Greek symbols

α	Proportionality parameter of the FVT	$\mathrm{J\,m^3\,mol^{-1}\,kg^{-1}}$
α	Ideal selectivity	(-)
α	Width of the Gaussian distribution	(-)
α'	Misfit energy parameter	$\mathrm{kJ\,mol^{-1}\,Å^{-2}e^{-2}}$
γ	Activity coefficient	(-)
γ	Surface tension	$\mathrm{N\,m^{-1}}$
Γ	Phase space	(-)
δ	Phase of a dihedral angle	rad
Δ	Increment	(-)
Δt	Stepsize	s
ϵ_{ij}	Lennard-Jones parameter: dispersion energy	J
ε^{HB}	Association energy	J
η	Shear viscosity	$\mathrm{mPa\,s}$
η_{ij}	Lorentz-Berthelot size binary parameter	(-)
λ	Thermal conductivity	$\mathrm{W\,m^{-1}\,K^{-1}}$
Λ	Thermal de Broglie wavelength	m
μ	Chemical potential	$\mathrm{J\,mol^{-1}}$
μ	Dipole moment	$\mathrm{C\,m}$
ξ_{ij}	Lorentz-Berthelot energy binary parameter	(-)
ρ_{ij}	Density	$\mathrm{mol\,L^{-1}}$
σ_{HB}	Threshold value for hydrogen bonding	$\mathrm{e\,Å^{-2}}$
σ_{ij}	Lennard-Jones parameter: size of the particle	$\mathrm{Å}$
τ	Element-specific COSMO-RS parameter	$\mathrm{kJ\,mol^{-1}\,Å^{-2}}$
ϕ	Dihedral angle	rad
φ	Fugacity coefficient	(-)
Ψ	Thermodynamic potential of the ensemble	(-)
ω	Acentric factor	(-)

Ω	Collision integral	(-)

Superscripts

α, β	Referring to atoms within molecules
assoc	Association
D	dipole-dipole interactions
HB	Hydrogen bond
id (ID)	Ideal
L	Liquid phase related
Q	quadupolar-quadrupolar interactions
ref	Reference
res	Residual
SG	Staverman-Guggenheim combinatorial model
V	Vapor phase related
0	Reference state
*	Reduced property

Subscripts

c	Critical
d-r	Dispersive-repulsive interactions
dis	Dissolution
eff	Effective
el	Electrostatic (coulombic) interactions
eq	Equilibrium condition
ext	External (intermolecular) terms or contributions
HB	Hydrogen bond
id (ID)	Ideal
i,j,k	Index (molecules)
IL	Ionic liquid
int	Intramolecular terms or contributions
μVT	μVT ensemble
max	Maximum
min	Minimum
NpT	NpT ensemble
NVE	NVE ensemble
NVT	NVT ensemble
P	At constant pressure
r	Reduced
str	Bond stretching energy
S	Isentropic
tors	Torsion energy
tot	Total
T	At constant temperature
vap	Vapor
vdW	Van der Waals
V	At constant volume
0	Reference value

1

Introduction

In this chapter, a general introduction to the subject of this doctoral thesis is given. The motivation behind this work is addressed, and the document's main objectives and structure are presented.

1.1 Motivation

2,279 jurisdictions in 39 nations have declared Climate Emergency[1] (Aidt, 2020), conceived as one of the most serious scientific issues confronting civilization in the 21st century. While a previous generation's primary goal was to accelerate scientific and technical growth, today's reality is to rescue a world that has been imperiled precisely because of that self-centered belief that we could exploit our planet's natural resources regardless of the consequences.

In a nutshell, climate change is a real phenomenon unquestionably caused by human activity, most notably, the emission of hazardous gases from the combustion of fossil fuels such as gas, coal, and oil, as the IPCC reported in 2013. Global warming caused by humans is already underway, is irreversible in the time span of currently living people, and will accelerate in the following decades. At the time of writing this thesis, global temperature has risen 1.01 °C since 1880, polar ice sheets are losing 428 billion metric tons of ice per year, and sea level is rising at a rate of 3.4 millimeters per year (NASA, 2022).

The explanation for this alteration of the earth's climate is the large amounts of carbon dioxide, and other greenhouse gases (GHG) emitted due to human activities. It should be noted that natural activities such as volcanic eruptions or the sun's energy also contribute to this alteration, but they do not explain the long-term trend observed over the last century (*Climate Change: Evidence and Causes: Update 2020*, 2020).

While CO_2 emissions from the energy sector account for at least two-thirds of global GHG emissions (IEA, 2021), other substances such as methane, nitrous oxide, or fluorinated gases (F-gases) also contribute to the increase of those emissions. The last ones have extremely high global warming potentials (GWP) of up to 12,400 times CO_2 values, implying that even relatively low atmospheric concentrations can have a disproportionately big influence on global temperatures because of their long atmospheric lifetimes, reaching up to thousands of years for some compounds. They are mainly used as refrigerants and have become a key element in relevant sectors such as food, chemical, electronic, cosmetics, pharmaceutical, automotive industries, or energy production.

Apart from the obvious environmental concern, the underlying problem related to these gases is the nonexistence of a standardized technology for their treatment. For this reason, once their life cycle is over, they are sent for incineration, with the corresponding environmental cost. Only in particular cases are they treated for total or partial recovery with energy-demanding processes such as cryogenic distillation, reactive absorption, or pressure swing adsorption. International regulations are pushing the scientific community to find Key Enabling Technologies (KET) to ensure proper treatment and recyclability and shift towards a more circular economy, as the F-gases from waste refrigeration equipment could be reused.

[1] Data updated by October 23th, 2022

These are new frontiers being explored only in the last few years. Alternative technologies have been encouraged by the European Union (EU) and other government agencies, and the use of advanced solvents like Deep Eutectic Solvents (DESs) or Ionic Liquids (ILs) for capture and subsequent recovery may be a good option to consider.

Even yet, the number of conceivable absorbents is enormous and impractical to handle experimentally due to the high expense in terms of money and time. The use of computer simulation tools enables the rapid and reliable examination of all these combinations, as well as the discovery of new formulations and blends that may be used to replace fluorinated gases in the near or medium term. This encompasses a broad range of techniques ranging from the atomic level, such as *ab initio* quantum chemistry methods, to the molecular level, like molecular simulations or advanced equations of state, to the use of commercial process simulators for the design of fluorinated gas recovery procedures.

Solving climate change will be complicated. Paradoxically, what was intended to improve societies' well-being is endangering them. We must rely on novel, rapid, and inventive solutions, such as computer simulations, to identify not just alternate working fluids and refrigerants but also to develop standardized technology for the treatment of F-gases. This will not happen overnight, but it needs to change as quickly as possible. And it is still very much possible.

1.2 Environmental concern

F-gases are a class of synthetic gases used in several industrial processes. They consist of the hydrofluorocarbon (HFC) and perfluorocarbon (PFC) families, as well as the sulfur hexafluoride (SF_6) molecule. They are mainly employed as refrigerants (see Figure 1.1 (A)), playing a crucial role in a wide variety of industries, including the food and agroindustrial, automotive, and chemical, as well as the electronics (insulating gas), cosmetics, and pharmaceutical industries.

As stated above, although having 0% ozone depletion potential (ODP), HFCs are GHGs, with GWP values of up to 12,400 kg CO_2 eq. The implementation of HFCs since 1989 in various sectors of the refrigeration and air conditioning and heat pump (RACHP) sector to replace chlorofluorocarbons (CFCs), hydrochlorofluorocarbons (HCFCs), and halons that damaged the ozone layer, led to a consequent increase in their emissions to the atmosphere. F-gas emissions account for 2.6% of total European Union-Kioto Protocol (EU-KP) GHG emissions (without land-use, land-use change, and forestry, LULUCF) in 2020 (European Environment Agency, 2022) (see Figure 1.1 (B)).

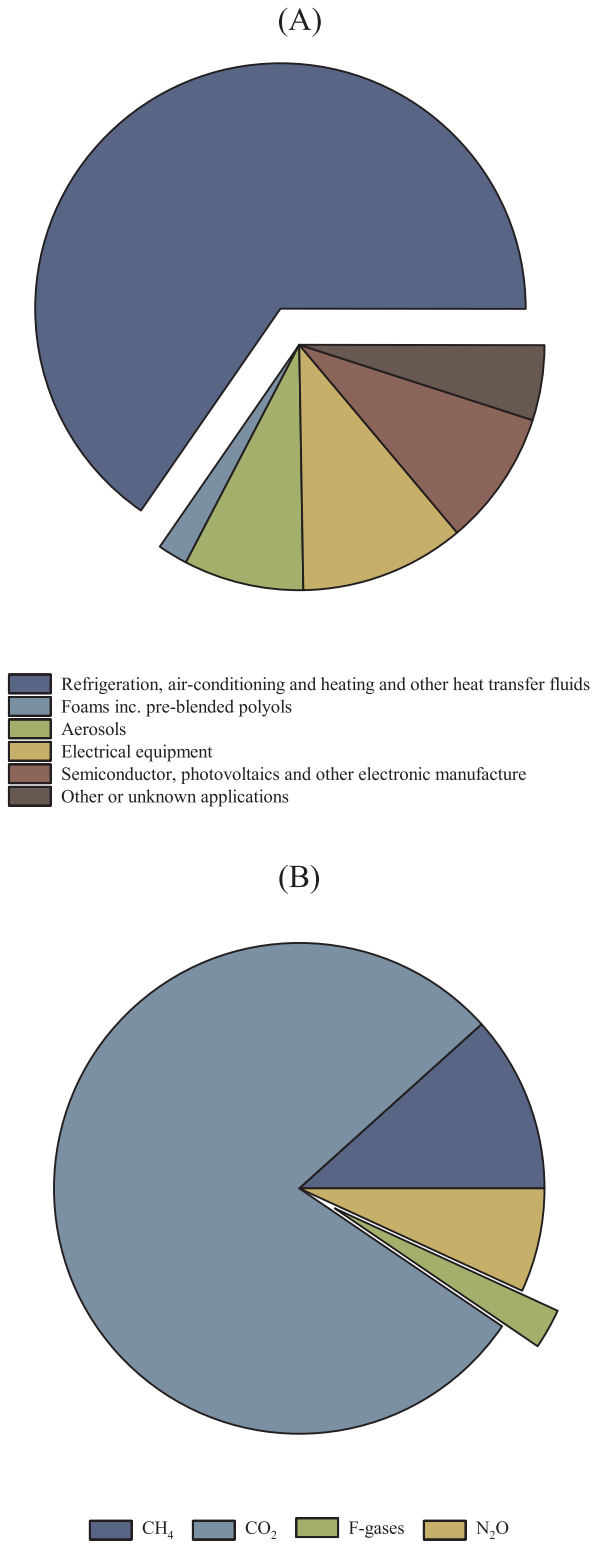

Figure 1.1: Intended applications of EU total supply of fluorinated gases (A) and gas shares (B) in EU-27.

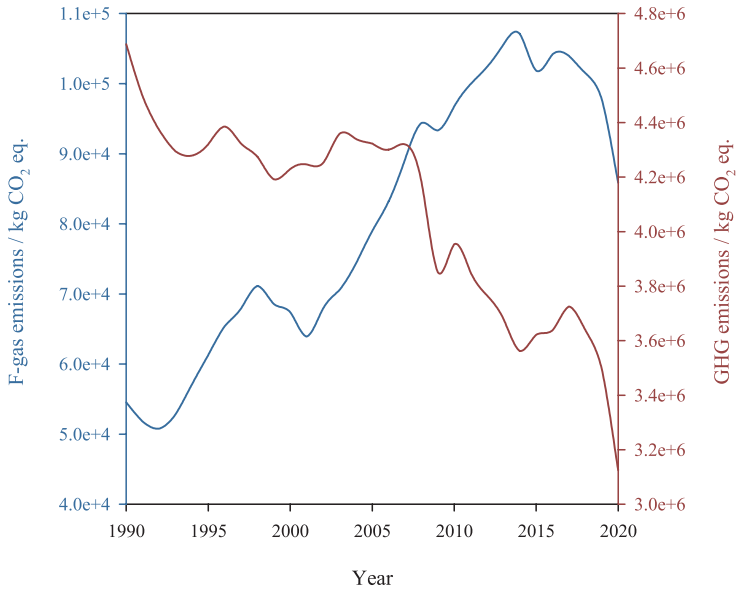

Figure 1.2: GHG and F-gas emissions in EU-27. Data from European Environment Agency (2022).

HFC emissions account for most of these F-gas emissions (98%) and were in 2020 about 5,700 times higher than in 1990. In fact, while the average emissions of all other GHGs decreased up to a 33.34% in 2020 compared to 1990 values, F-gases were the only group whose emissions increased, up to 57.44%, as Figure 1.2 shows.

1.2.1 Regulatory framework

The international consensus on the harmful contribution of HFCs to climate change resulted in the adoption of the Kigali Amendment to the Montreal Protocol in 2016. The new regulation includes specific targets and timetables (85% of the 2011–2013 average by the late 2040s) to replace HFCs with more planet-friendly alternatives, provisions to prohibit or restrict countries that have ratified the protocol or its amendments from trading in controlled substances with states that are yet to ratify it, and an agreement by rich countries to help finance the transition of developing countries to alternative safer products (United Nations, 2016).

In line with this, the EU F-gas Regulation (Regulation (EU) No 517/2014, 2014), began phasing down HFCs across the EU in 2015. It aims to cut EU emissions of HFCs by two-thirds by 2030 compared with 2014 levels. It also establishes other provisions such as bans on new equipment, new requirements for containment and certification of professionals, and new reporting obligations. The prohibitions on HFCs market placing in the European Union are included in Figure 1.3. Note that this figure is just a representation for the reader to get the whole vision of the prohibitions, and exceptions to what is included in this figure may apply. Similarly, the USA has implemented incentive credits for using low-GWP refrigerants

according to the US Environmental Protection Agency's Significant New Alternatives Policy (SNAP), which reviews substitutes within a comparative risk framework in several industrial sectors. To arrive at determinations on the acceptability of substitutes, the Agency performs a cross-media analysis of risks to human health and the environment from the use of various substitutes in different industrial and consumer uses that have historically used ozone-depleting substances (ODS): ODP, GWP, toxicity, flammability, occupational and consumer health/safety, local air quality, and ecosystem effects.

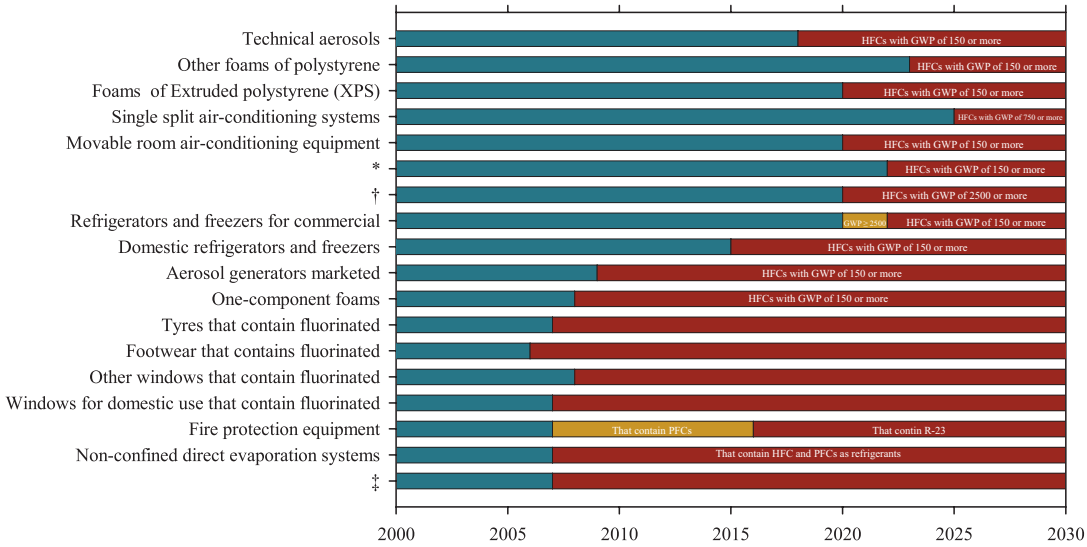

*Multipack centralised refrigeration systems for commercial use with a rated capacity of 40 kW
†Stationary refrigeration equipment, except equipment intended for application designed to cool products to temperatures below -50 °C
‡Non-refillable containers for fluorinated greenhouse gases used to service, maintain or fill refrigeration, air-conditioning or heat-pump equipment, fire protection systems or switchgear, or for use as solvents

Figure 1.3: Placing on the market prohibitions established by Regulation (EU) No 517/2014. The green color means no limits are applicable. Red and orange indicate restrictions apply, with the limitations indicating if applicable.

Other countries have also implemented new policies to fully comply with international legislation requirements. In Spain, Ley 16/2013, 2013 introduces in the Spanish legislation a tax on fluorinated greenhouse gases, including HFCs, PFCs and SF_6 listed in Annex I of Regulation (EC) No. 842/2006, 2006 of the European Parliament. Tax rates are set on a weight basis (per kg of gas) so that they are proportional to the GWP of each gas between 150 and 4300 kg CO_2 eq. For F-gases with a GWP above 4300, a constant tax rate of 100€ per kg is applied (see Table 1.1). This approach implies that the emissions of the most harmful gases are proportionally cheaper.

In the short term, new low-GWP refrigerants are being adopted to replace the high-GWP HFC blends due to these restrictions on using HFCs (Mota-Babiloni et al., 2016). In addition to ODP, flammability, stability, energy efficiency, and system complexity, it is evident that low GWP is a new environmental restriction that must be considered in the formulation of this new generation of working fluids (McLinden et al., 2017; McLinden & Huber, 2020; McLinden et al., 2020).

Table 1.1: Rates of the tax on fluorinated greenhouse gases in Spain as in Ley 16/2013.

Type of gas	GWP ($kg\ CO_2$ eq.)	Rate (€ kg^{-1})
Sulphur hexafluoride	22,200	100
HFC - 23	12,000	100
HFC - 32	550	11
HFC - 41	97	n.A
HFC - 43-10mee	1,500	30
HFC - 125	3,400	68
HFC - 134	1,100	22
HFC - 134a	1,300	26
HFC - 152a	120	n.A
HFC - 143	330	6.6
HFC - 143a	4,300	86
HFC - 227ea	3,500	70
HFC - 236cb	1,300	26
HFC - 236ea	1,200	24
HFC - 236fa	9,400	100
HFC - 245ca	640	12.8
HFC - 245fa	950	19
HFC - 365mfc	890	17.8
Perfluoromethane	5,700	100
Perfluoroethane	11,900	100
Perfluropropane	8,600	100
Perfluorobutane	8,600	100
Perfluoropentane	8,900	100
Perfluorohexane	9,000	100
Perfluoro Cyclobutane	10,000	100

1.3 General objectives and working hypothesis

This Ph.D. thesis' overall purpose is to design recovery and recycling ecotechnological methods to recover fluorinated working fluids from commercial mixtures in order to provide a sustainable solution to the current challenge of reducing high GWP working fluids. In this respect, the main objective is the development of novel circular economy-based initiatives through a multiscale simulation approach to facilitate the phase-out of these F-gases affected by the new legislation resulting from the Kigali Amendment. This thesis departs from the statement that there are available solvents and revalorization techniques to recover and convert high GWP refrigerants into added-value products. From this assumption, here is a list of working hypotheses for this work:

- Alternative solvents can lower the energy penalty and/or environmental impact of F-gas separation.
- F-gas absorption could use task-specific ILs. DESs have also shown similar results having cheaper production costs and lesser toxicity, according to preliminary studies.

- It is possible to find the right ILs and DESs based on the type of refrigerant that will be recovered to reach the goal, which improves the life cycle of the process from an environmental, economic, or energy point of view.
- It is possible to find an alternative to incineration of high-GWP refrigerants by combining these molecules with other low-GWP refrigerants, increasing their lifetime while minimizing the amount of new HFCs introduced into the market, promoting the concept of a circular economy.

Based on the overall goal of developing adequate and environmentally efficient strategies to mitigate the effect of high GWP fluorinated working fluids, this thesis will cover the following sub-objectives:

- Development of accurate transferable molecular models for each F-Gas and solvent molecule involved, intended to perform reliable molecular simulation calculations using different computational tools.
- Describe the solubility and selectivity of F-Gases in new cheap and non-toxic solvents with the obtained thermodynamic models.
- Design and simulation of a process for the recovery and valorization of phased-out commercial refrigerant blends.
- Evaluate the environmental improvement of designing these recovery processes compared to their current linear production and destruction after use.
- Formulation of new alternative working fluids, with the possibility of including other compounds with a lower GWP and similar coefficient of performance

1.4 Thesis outline

Following this general introduction chapter, which presents the motivation behind this work and establishes the basis of this Ph.D. thesis, *Chapter 2* guides the reader through the historical evolution of fluorinated working fluids and emphasizes the importance of recovering those compounds. On that note, state-of-the-art separation techniques are discussed, highlighting the challenges behind these operations. This doctoral thesis has focused on recovery through absorption processes; therefore, this chapter also presents the advanced solvents for this purpose and the successful cases in which they have been applied. This chapter also mentions the main alternatives to the use of HFCs: hydrofluoroethers (HFE) and hydrofluoroolefins (HFO), as well as the research lines that they have motivated.

Chapter 3 is devoted to theory. Here, a general description of the many approaches used throughout this thesis, ranging from quantum-chemical *ab-initio* calculations to process scale

simulations, is given. First, a general overview of the COSMO-RS theoretical background is given, together with the practical implementation used in this thesis. Next, molecular simulations at the atomistic scale are explained, including a brief introduction to statistical mechanics and molecular dynamics simulations. Next, simulations at a coarse-grained scale are explained, including the physical background for the SAFT equation of state (EoS), Wertheim's theory of association, and the EoS used in this thesis, the soft-SAFT EoS, a variant from the original SAFT. The final section is devoted to computational tools to design separation processes. These tools include commercial process simulator software like Aspen Plus for process flowsheeting and SimaPro for Life Cycle Assessment (LCA). The main aspects of the methodology regarding these two tools are highlighted in this section.

Chapter 4 is the first chapter of the results, where the feasibility of F-gas recovery using absorption techniques and advanced solvents, such as ionic liquids (ILs) and Deep Eutectic Solvents (DESs), is analyzed. In order to assess their absorption potential, the ILs, and DESs that would be examined, as well as the F-gases, were first modeled using soft-SAFT. The results have been used to guide the design of recovery processes of two commercial HFC blends at a macroscopic scale, using process simulation tools such as Aspen Plus. Finally, for one of the proposed separation schemes, the environmental impacts have been analyzed using a life-cycle approach (LCA) methodology with a direct comparison with conventional F-gas production.

The second chapter of the results, *Chapter 5*, investigates alternatives to using F-gases as working fluids. Here, using molecular dynamics simulations, the application of HFOs as refrigerants is investigated, either as individual components or as binary and ternary blends with HFCs. In addition, the utilization of HFEs in low-grade waste heat recovery Organic Rankine cycles (ORCs) to generate energy from exhaust steam in industrial processes is examined in depth. The components were modeled using soft-SAFT EoS, and the process conditions of up to nine distinct HFEs were optimized using Aspen Plus in a simple ORC.

A concluding chapter reviews the most significant conclusions presented in the preceding chapters and discusses potential future possibilities for this work.

2

State of the art

The aim of this chapter is to guide the reader through the recent investigations on separation processes for mixtures of fluorinated gases. First, the evolution of refrigerants from the early days of mechanical refrigeration to the present is traced, and after, a brief introduction to ASHRAE's nomenclature for the classification of refrigerants is provided. The main block of this chapter includes the most recent investigations for the absorption of fluorinated gases with Ionic Liquids and Deep Eutectic Solvents. In the final part, the focus is placed on the recent developments regarding two promising low-GWP alternatives to F-gases: hydrofluoroolefins and hydrofluoroethers.

2.1 Fluorinated refrigerants

2.1.1 Historical background: evolution of refrigerants

Refrigeration has been recently named one of the 20th century's top twenty engineering achievements, placing it alongside computer technology, space exploration, and the internet (Constable & Somerville, 2003). Refrigeration and air conditioning demand account for over 20% of the world's total energy consumption (Kitanovski et al., 2015).

Over time, refrigerants have evolved, adjusting to the evolution of the constraints on the characteristics required, including safety and environmental factors, which have largely driven the need to develop new systems. Following the approach of Calm (Calm, 2008), four refrigerant generations have been defined and examined throughout the chapter as depicted in Figure 2.1.

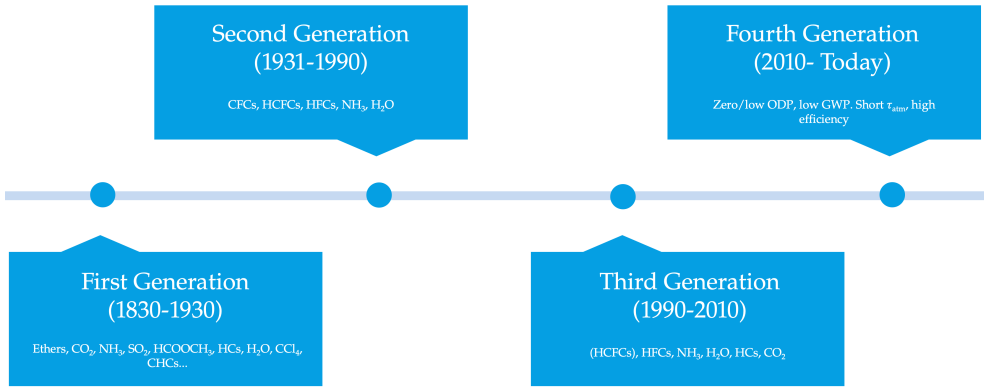

Figure 2.1: Refrigerant progression defined by Calm (2008).

Calm described the *first generation* of refrigerants as *whatever worked*. Refrigeration was primarily employed to create ice at industrial sites during this time period, which coincided with the introduction of the first residential refrigerators in 1927 developed by General Electric (McLinden & Huber, 2020). In this period, the primary constraints on a refrigerant were availability and suitability. Nonetheless, early refrigerants identified in these years comprised both excellent refrigerants (e.g., ammonia, propane, CO_2) and hazardous refrigerants (e.g., sulfur dioxide). As an example, dichloroethylene (i.e., *trans*-1,2-dichloroethylene) was stated as a suitable refrigerant for use in centrifugal compressors given its thermodynamic efficiency, and stability (Calm, 2008; Carrier & Waterfill, 1924). This organochloride, yet quite flammable, is part of the azeotropic blend named R-514A with *cis*-1,1,1,4,4,4-Hexafluoro-2-butene, which is sold as a replacement for R-123 (phased out under the Montreal Protocol).

The *second generation* of refrigerants was distinguished by a shift towards halogenated refrigerants for *safety and durability reasons* (Calm, 2008; McLinden & Huber, 2020). In the

words of Charles Kettering, head of research at General Motors, *the refrigerant industry needs a new refrigerant if it wants to get anywhere*, as the continuous leaks of toxic refrigerants used in the equipment of the time blurred the vision of the company in which domestic refrigerators could replace the ice boxes.

Thomas Midgley, Jr. and his associates set out to find a new non-toxic, non-flammable refrigerant with a boiling point between 0 and -40 °C. They went through the periodic table of the elements and discarded those elements with insufficient volatility and those resulting in unstable or toxic components, as well as noble gases, due to their low boiling point. Carbon, nitrogen, oxygen, sulfur, hydrogen, fluorine, chlorine, and bromine were the only eight elements that remained. Midgley and his colleagues immediately made observations on these chemicals' flammability. Additionally, they determined that the majority of refrigerants, with the exception of fluorine, were made of seven of these atoms. They demonstrated how the degree of halogenation of refrigerants had an effect on their boiling point, flammability, and toxicity in their first article in 1930 (Midgley & Henne, 1930) (see Figure 2.2). Dichlorofluoromethane (R-21) was identified as a viable candidate. Following further research into additional chlorofluorocarbons, commercial production of dichlorodifluoromethane (R-12) began in 1931, followed by trichlorofluoromethane (R-11) in 1932 (Calm, 2008), collectively called *Freons*.

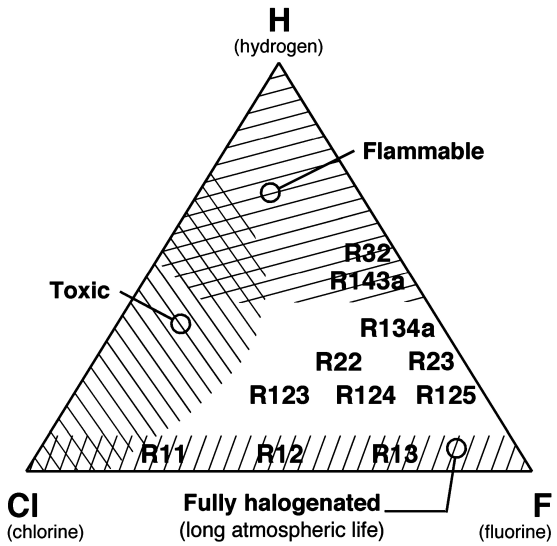

Figure 2.2: Summary of refrigerant characteristics as published from McLinden and Didion (1987) and later re-adapted by McLinden and Huber (2020).

Additional CFCs and HCFCs (hydrochlorofluorocarbons) were produced and commercialized during the 1930s, 1940s, and 1950s. Among them all, it's worth noting R-22, chlorodifluoromethane, an HCFC that was widely used in air conditioning systems throughout the late 1950s (Bhatti, 1999). Simultaneously, blends of CFCs and HCFCs began to be used to boost

volumetric refrigeration capacity, reduce compression ratios, or enhance any other thermodynamic property for a particular application (Pearson, 2020). These were azeotropic mixtures that could be treated similarly to single-component fluids.

Until 1990, CFCs and HCFCs dominated the majority of refrigeration and air conditioning applications (Calm, 2008). Ammonia was the only primary relic of the early refrigerants at industrial-scale refrigeration.

It's worth noting that by the late 1980s, CFCs were being employed as foam blowing agents, cleaning solvents, and aerosol propellants for personal care items (Midgley & Henne, 1930). Lovelock et al. (1973) stated in 1973 that nearly all of the R-11 and R12 produced remained in the atmosphere. Molina and Rowland (1974) theorized the following year that the sink for CFCs was in the stratosphere, where they would be dissociated by ultraviolet light, releasing atomic chlorine and destroying ozone:

$$
\begin{aligned}
h\nu + O_2 &\longrightarrow 2\,O^- \\
2\,Cl + 2\,O_3 &\longrightarrow 2\,ClO + 2\,O_2 \\
2\,ClO + 2\,O^- &\longrightarrow 2\,Cl + 2\,O_2
\end{aligned}
$$

Not long after, in 1978, and based on several studies completed to date, the United States outlawed the use of CFCs as aerosol propellants. By 1982, numerous additional studies had been conducted, and a report by the United States National Academy of Sciences (Environmental Studies Board & National Research Council, 1982) indicated that maintaining R-11 and R-12 production at 1977 levels would result in a 5 to 7% reduction in worldwide ozone. The subject of ozone depletion disappeared from public consciousness, yet the study and usage of CFCs as refrigerants persisted.

In 1985, the Vienna Convention for the Protection of the Ozone Layer was adopted; this convention established a framework for exchanging ozone research and controlling the manufacture of ozone-depleting compounds. Shortly thereafter, Farman et al. (1985) discovered the Antarctic's *ozone hole*. The stratosphere has relatively high concentrations of ozone; the *ozone hole* is not so much a hole devoid of ozone as it is an area of diminished ozone concentration in the stratosphere above the southern polar region. In 1986, using balloon-sonde data from the Antarctic spring, Solomon et al. (1986) revealed the ozone hole was created by chlorine chemistry on the surfaces of polar stratospheric clouds, and that the ClO employed in these reactions was coming from CFCs.

These new findings made it even more important to cut back on the use of CFCs. This led to the adoption of the Montreal Protocol on Substances that Deplete the Ozone Layer in 1987. The original Montreal Protocol specified a 50% reduction in the production of five of the most prevalent CFCs (R-11, R-12, R-113, R-114, R-115) and three halons used as fire-extinguishing agents (R-12B1, R-13B1, and R-114B2). However, following Montreal Protocol amendments

compelled the entire phase-out of CFCs and many HCFCs. This was the starting point of the *third generation* of refrigerants, named as *ozone protection* by Calm (Calm, 2008).

The manufacturers that commercialized the first alternative refrigerants in late 1989 were suddenly faced with the problem of replacing the widely-used CFC-based ozone-depleting refrigerants. 1,1,1,2-tetrafluoroethane, R-134a, and 2,2-dichloro-1,1,1-trifluoroethane, R-123, emerged as possible alternatives, although those refrigerants were, indeed, known before that: R-134a was already mentioned in the literature in 1936 (Henne & Renoll, 1936) and proposed as a possible refrigerant in a patent in 1959 (Ruh et al., 1959). In 1987, McLinden and Didion (1987) conducted a study that concluded that R-134 could replace R-12 in vehicle air-conditioning, and R-123 could replace R-11 in systems with low-pressure centrifugal compressors. Also, a binary mixture of flammable R-32 (difluoromethane) with R-125 (pentafluoroethane), known as R-410A, demonstrated good thermodynamic properties and has supplanted R-22 nowadays in small air-conditioning and heat-pump systems (Booten et al., 2020).

Despite McLinden and Didion's belief that trade-offs were unavoidable, totally suitable substitute refrigerants (based on HFCs) were developed and implemented without any concessions in terms of toxicity or flammability. Several studies were conducted to test the adequacy of these new refrigerants in terms of material compatibility and thermophysical behavior and concluded that these new third-generation refrigerants were, in fact, more energy efficient than their predecessors (McLinden & Huber, 2020).

The extremely successful response to ozone depletion contrasts sharply with the deteriorating situation with climate change, as shown in Figure 2.3. New discoveries and political debates over global warming have become regular occurrences, particularly in recent years. Indeed, the IPCC's Fourth Assessment report stated that *warming of the climate system is unequivocal, as is now evident from observations of increases in global average air and ocean temperatures, widespread melting of snow and ice, and rising global average sea level*. Even though most of the HFCs have a substantially lower Global Warming Potential (GWP)[1] than CFCs, these values still remain very high. However, the GWP issue was not a priority at that moment, as the urgent need was to replace the ozone-depleting substances. Despite this, it is important to underline the good impact that the adoption of the Montreal Protocol has had on global warming: when R-12 was replaced with R-134a in automotive systems, the GWP_{100} was reduced from 10200 to 1300 $kg\ CO_2$ eq., almost 8 times. Some authors estimate that the adoption of the Montreal protocol delayed climate change by 7-12 years (Velders et al., 2007).

However, the use of HFCs continued to increase, and new regulations had to be adopted to control their use. In this sense, the F-gas regulation adopted by the European Union was the first to regulate the usage of HFCs (Regulation (EU) No 517/2014, 2014). Similarly, the

[1] GWP is a measure of how much energy the emissions of 1 ton of a gas will absorb over a given period of time, relative to the emissions of 1 ton of CO_2. The time period usually used for GWPs is 100 years.

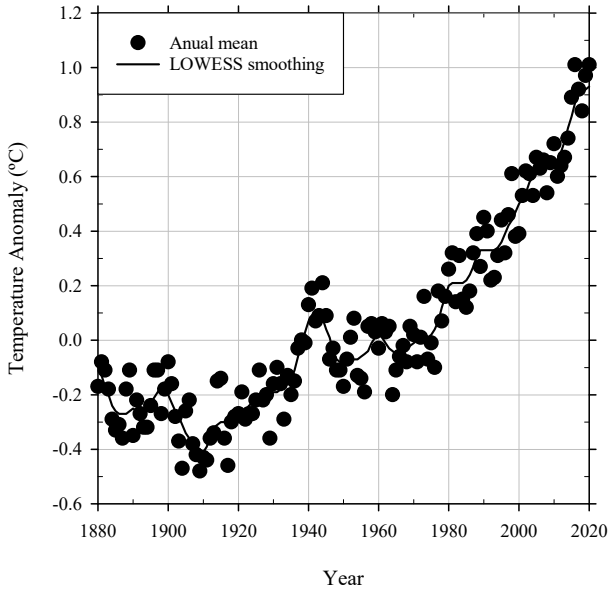

Figure 2.3: Change in global surface temperature relative to 1951-1980 average temperatures. Source NASA (2022).

SNAP program (United States Environmental Protection Agency, 2022) (Significant New Alternatives Program) adopted by the Environmental Protection Agency, EPA, of the United States was designed to identify and evaluate substitutes in end-uses that have historically used ozone-depleting and high-GWP substances.

In a *business as usual* scenario, Velders et al. (2015) estimated that HFCs would add between 0.28 and 0.52 K to warming at the earth's surface by the end of the century. Such a consequence prompted a global accord to restrict HFC emissions. In 2016, the Kigali Amendment to the Protocol (United Nations, 2016) called for a decrease of HFCs by 85% over time. It entered into force on January 1, 2019. The quest for replacements was (and is) ongoing, within the so-called *fourth generation* of refrigerants, which Calm (Calm, 2008) defines as *global warming*. Kujak and Schultz (2016) presented an enhanced list of environmental, safety, and sustainability goals for each new refrigerant. These include product sustainability factors such as longer operating life, recyclable materials, and minimal material consumption. It is also interesting to note that they list *low flammability* and *de minimis ODP* as essential constraints rather than *non-flammable* and *zero ODP*.

As in the 1980s and 1990s, when CFCs were phased out, manufacturers of refrigerants drew from their inventory of known compounds and proposed potential alternatives to the refrigeration sector. Primarily, they suggested hydrofluoroolefins (HFOs) compounds having a carbon-carbon double bond, which drastically lowered their atmospheric lifetime and, thus,

their GWP. SAE International (previously known as the Society of Automotive Engineers) supported two successive Cooperative Research Programs to study refrigerants that would achieve the F-gas target of $GWP_{100} < 150$ in response to the first wave of European Union F-gas regulations. These programs sparked the early interest in 2,3,3,3-tetrafluoropropene, R-1234yf, hydrofluoroolefin. However, and as in previous refrigerant generations, R-1234yf was discovered well before this time: the synthesis of R-1234yf was initially published in 1946 by Henne and Waalkes (1946) for the aim of researching interatomic distances, and it was listed as a polymer precursor in a 1961 patent by Lo (1961). By 2008, HFO refrigerants were a popular seminar topic at scientific conferences. In particular, R-1234yf was tested in a range of equipment, in addition to the automotive systems for which it was initially designed.

2.1.2 ASHRAE nomenclature and safety designations

Refrigerant fluids are mostly designated according to the American Society of Heating, Refrigerating, and Air-Conditioning Engineers (ASHRAE). This taxonomy is a non-proprietary shorthand to eliminate uncertainty about refrigerant product composition, regardless of the manufacturer. Refrigerants are represented by the letter R (as in Refrigerants) followed by a (up to) four-digit number and, in some cases, one or two letters. In some marketing brochures, major OEMs (Original Equipment Manufacturer), substitute a brand name for the R- abbreviation to differentiate their products from those of competitors. The most notorious example is the rebranding of Du Pont's CFC-12, renamed as *Freon 12*. The marketing was so successful that the term *Freon* is often used by laymen as a synonym for any refrigerant gas.

The designation is determined by the chemical composition of the molecule, as described in Figure 2.4. The first digit (d) corresponds to the number of unsaturated bonds (double bonds), the second number (c) is the number of carbons minus one, the third number (h) is the number of hydrogen atoms plus one, and the last one (f) is the number of fluorine atoms. If any number ends up being zero, it is deleted, unless it follows a nonzero number. Chlorine atoms, if any, are calculated from the available carbons after subtracting the number of hydrogen and fluorine (digits 3 and 4) atoms present in the molecule. For example, R-32 is a molecule containing 1 carbon, 2 hydrogen, and 2 fluorine atoms, therefore:

$$\text{R-}(0)(1-1=0)(2+1=3)(2) = \text{R-0032} \rightarrow \text{omit left-sided zeros} \rightarrow \text{R-32}$$

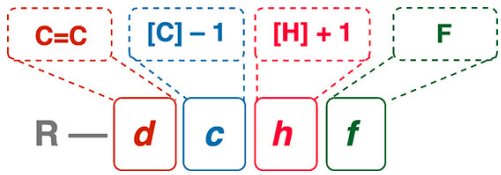

Figure 2.4: ASHRAE refrigerant code system. Retrieved from Sicard and Baker (2020).

If the molecule has atoms of other elements, like bromine, the element and the number of atoms are placed at the end (Deiters, 1997) as in $CHBrF_2$ which is named as R-22B1. The same rule applies to iodine-containing molecules.

Isomers are identified with a lowercase letter after the number. For two-carbon refrigerants, the letters *a*, *b* or *c* are added at the end of the R-numbering. The choice of the letter is based on the symmetry of the molecule, moving from the most (a) to the least (c) symmetrical; the most symmetrical isomer is not accompanied by any letter (Sicard & Baker, 2020). As an example, tetrafluoroethane has two isomers; the most symmetrical one, $CHF_2{-}CHF_2$, is designated as R-134, while the (more common) unsymmetrical isomer $CHF_3{-}CH_2F$ is R-134a. Higher haloalkanes (C_3 and beyond) are more complex and possess far too many constitutional isomers for their nomenclature using the rudimentary symmetry arguments. Those fragments are designated according to Table 2.1. Additionally, the cis/trans isomerism is denoted at the end of the R-number with the Z/E letters appended (in brackets) to denote cis and trans, respectively.

Table 2.1: ASHRAE designation for isomer differentiation.

Fragment	Designation
CCl_2	a
CClF	b
CF_2	c
CHCl	d
CHF	e
CH_2	f
CCl_3	j
CCl_2F	k
$CClF_2$	l
CF_3	m
$CHCl_2$	n
CH_2Cl	o
CHF_2	p
CHClF	r
CH_3	s
C	t
CCl	x
CF	y
CH	z

ASHRAE has also developed a Standard that describes a shorthand way of naming refrigerants and assigns safety classifications based on toxicity and flammability data. The flammability classification is determined by the rate of flame propagation and the lower flammability limit (LFL) as determined by ASTM E681-04 (*Standard Test Method for Concentration Limits of Flammability of Chemicals (Vapors and Gases)*, 2010) and the toxicity classification, by the permissible exposure limit (PEL) (Sicard & Baker, 2020): class A denotes refrigerants of lower toxicity

(below 400 ppm), and class B denotes refrigerants of higher toxicity (above 400 ppm). F-gases are non-toxic and are classified as A (Asensio-Delgado et al., 2021). For flammability classification, there are three groups and one subclass. The three main flammability classifications are class 1, for refrigerants that do not propagate a flame when tested as per the standard; class 2, for refrigerants of lower flammability, delimited by an LFL of 0.10 $\mathrm{kg\,m^{-3}}$ (Sicard & Baker, 2020); and class 3, for highly flammable refrigerants, such as the hydrocarbons. A more recent fourth group has been included as a sub-group of class 2 (class 2L) to account for refrigerants having intermediate flammability, yet having a burning velocity of less than 10 $\mathrm{cm\,s^{-1}}$ (i.e., burn very slow).

Most of the F-gases used nowadays in refrigeration systems are mixtures, which are classified under the 400 series and the 500 series by the ASHRAE, depending if the mixture is non-azeotropic (zeotropic) or azeotropic, respectively. The designation is also followed by an uppercase letter to distinguish between the blends with the same components but different compositions. For example, R-410A is a mixture of 50 wt % of R-32, difluoromethane, and 50 wt % of R-125, pentafluoroethane.

However, for separation purposes, it should be noted that a mixture of compounds belonging to the 400-series may also present azeotropic behavior at specific compositions (Asensio-Delgado et al., 2021). Precisely in R-410A, an azeotropic point is found at a 92 mol % composition of R-32. More details on this are given in the following section (2.2).

2.2 Separation of refrigerants

Azeotropic mixtures (500-series) or near-azeotropic mixtures (such as R-410A) are attractive as refrigerants because they behave very nearly as pure compounds (G. Morrison & McLinden, 1993). Azeotropic mixtures are preferred over zeotropic mixtures (400-series) because the latter can undergo compositional changes, in case of leaks, that may decrease the efficiency of the cycle (Asensio-Delgado et al., 2021; Bolaji, 2011; Maalem et al., 2020; Y. Zhao et al., 2019) and exhibit a higher temperature glide [1]. All this results in systems with worse volumetric refrigeration capacity (VRC), coefficient of performance (COP), discharge temperature, and pressure ratio (Y. Zhao et al., 2016; Y. Zhao et al., 2019).

Disposal of HFCs at end-of-life has become an issue, as no standardized procedures are available, and many are illegally vented into the atmosphere. The alternative is incineration, which is energy-intensive and generates harmful pollutants. Separating high-GWP refrigerants from low to moderate-GWP refrigerants, such as difluoroethane (HFC-32, GWP = 771), in commercial HFC blends would be more environmentally beneficial as the recovered compounds could be reused in new HFO/HFC blends.

[1] Glide is the difference between the boiling point of the most volatile component compared to the least volatile component within the refrigerant blend

However, as aforementioned, these mixtures are mostly azeotropic or near-azeotropic mixtures, making their separation from difficult to impossible using conventional distillation methods. In a nutshell, what is best for refrigeration air conditioning and heat pump (RACHP) equipment is worst for the recycling and recovery of the individual F-gases of such mixtures.

In an effort to characterize the general behavior of the different commercial mixtures containing F-gases, Asensio-Delgado et al. (2021) identified 5 cases, classified according to the difficulty of performing the separation of the individual components. To facilitate the reader the identification of these cases, they are all represented in Figure 2.5 (A) and (B).

1. Zeotropic mixtures with high-temperature glide: This is the case of the systems R-32 + R-134a or R-134a + R-125. These mixtures are easy to separate using conventional distillation methods as a result of the phase transition, which increases the proportion in which one component is found with respect to the other.

2. Zeotropic mixtures with very low-temperature glide: This is the case of the system R-134a + R-143a. While theoretically, these mixtures can be separated using conventional VLE technologies, it comes at the cost of an excessive number of stages.

3. Zeotropic mixtures showing the "pinch effect": This is the case of R-32 + R-143a. The bubble and dew lines tend to overlap when approaching pure composition.

4. Azeotropic mixtures at a certain composition: This is the case of R-32 + R-125. The mixture presents an azeotrope at a certain composition, although the vapor and liquid compositions are very narrow throughout the entire range of compositions.

5. Azeotropic mixtures over the entire range of compositions: This is the case of R-125 + R-143a system. This behavior is common in mixtures with very similar vapor pressures.

Therefore, the recovery, reclamation, and reuse of refrigerants from end-of-life RACHP equipment demands, in the majority of scenarios (types 3-5), the implementation of advanced separation technologies to break the azeotropic behavior or facilitate the separation of near-azeotropic mixtures.

Solvents are widely used for that purpose in extractive distillation or absorption columns and membrane separation technologies. Here, *solvent* refers to a separating agent used to enhance the separation of azeotropic or near-azeotropic mixtures (Deorukhkar et al., 2016). Good miscibility with the feed, selective absorption between components, and low volatility are the distinguishing basic qualities of a solvent. Also, the solvent and feed components should not produce any azeotropes. Most of the time, the solvent is much less volatile than the feed components so it can be easily recovered. Finally, low miscibility between the solvent and components can result in the formation of two liquid phases, which must be avoided. Lei et al. (2003) listed a total of four types of solvents: solid salts, liquid solvents, combinations of

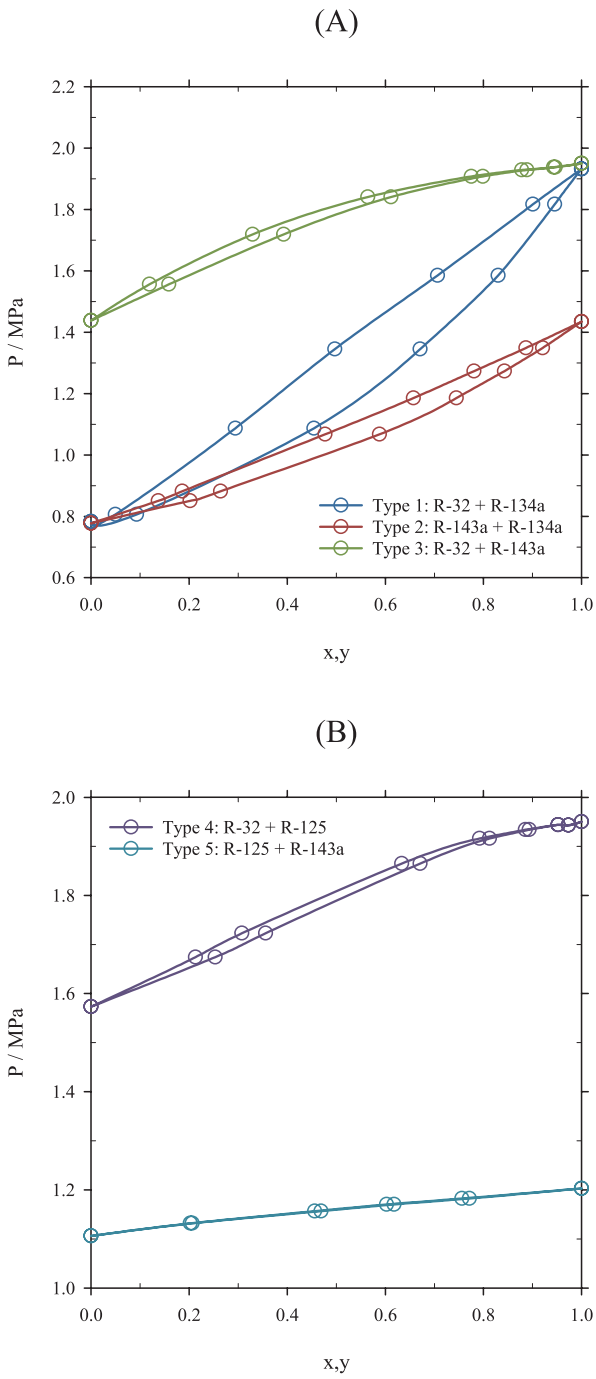

Figure 2.5: Behaviors of commercial HFC blends. Isotherms are measured at 303.15 K, except for R-125 + R-143a, which was measured at 293.16 K. Experimental data obtained from Higashi (1999), B. G. Lee et al. (1999), and Lim et al. (2002).

liquid solvents and solid salts, and ionic liquids (ILs). Organic liquid solvents have traditionally been used as solvents, although ILs have demonstrated greater selectivity in numerous applications. (Lei et al., 2014; Meindersma et al., 2016). Also, Deep Eutectic Solvents (DESs) have been recently studied for the same purpose (Castro et al., 2020; Neubauer et al., 2022) with a significant reduction in energy demand for the extractive distillation process.

ILs and DESs are interesting solvents that present promising properties enabling the successful separations of F-gases, allowing the design of new reclamation technologies and processes. To illustrate this, the following sections contain the most important scientific contributions regarding the separation of F-gases with DES and ILs.

2.2.1 Absorption of fluorinated gases in ionic liquids

ILs are a promising alternative absorbent for enhancing the current status of gas separation technology. Widespread interest in ILs stems from a need for environmentally friendly new green solvents to replace conventional organic ones (Earle & Seddon, 2000; H. Zhao et al., 2005), which present various concerns, including intrinsic toxicity and excessive volatility. The remarkable interest over the past decade in ILs (Plechkova & Seddon, 2008) comes both from the industry and academia due to the physicochemical properties of ILs (Aparicio et al., 2010), which can be modified through suitable anion and cation combinations (Niedermeyer et al., 2013). This opens the possibility of developing task-specific ILs for a variety of applications (Albà et al., 2020b; Ramdin et al., 2012; Sosa et al., 2019; C. Wang et al., 2013), including refrigerant separation. Many of the physicochemical properties of ILs, such as almost minimal vapor pressure (Ahrenberg et al., 2016), good thermal stability (Y. Chen & Mu, 2019; Xu & Cheng, 2021), and low flammability (Amde et al., 2015; Fox et al., 2008), are ideally suited for F-gas absorption and can be tuned by selecting the participating ions.

Despite all of these potential benefits, the literature has also addressed the difficulties and limitations of ILs. Indeed, a remarkable number investigations have highlighted ILs' toxicity (Thuy Pham et al., 2010; D. Zhao et al., 2007), poor biodegradability (Jordan & Gathergood, 2015), combustibility (Smiglak et al., 2006), unfavorable transport properties such as high viscosity (Philippi et al., 2022; Ribeiro, 2012; Yuan et al., 2018), and expensive manufacture (L. Chen et al., 2014). Many of these disadvantages of ILs can be addressed through appropriate selection or design (Petkovic et al., 2011) and, as a result, the literature also contains references for non-toxic (Ventura et al., 2014), highly biodegradable (Gathergood et al., 2004), low-viscosity (Tao et al., 2014), and inexpensive (L. Chen et al., 2014) ILs.

Vapor-liquid equilibria measurements

Several references can be found in the literature regarding the binary equilibrium of ILs with F-gases, where the IL acts as the solvent of the F-gas. On top of that, a few references address the VLLE (Vapor-Liquid-Liquid Equilibria) that is achieved when the IL reaches the maximum absorption capacity and the refrigerant gas condensates in a different liquid phase.

The vast majority of the works examine the absorption capacity of imidazolium-based ILs because the imidazolium cation has been widely studied, and there is plenty of experimental information (Fredlake et al., 2004; J. K. Singh et al., 2018; H. Yang et al., 2017). In a lesser extent, other studies have addressed the thermophysical properties and applications of pyridinium (Bittner et al., 2012), phosphonium (Khazalpour et al., 2020) or ammonium-based (Bhattacharjee et al., 2014) ILs. The most common anions and cations of the ILs frequently found in the literature are listed in Figures 2.6 and 2.7.

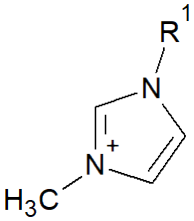

(a) 1-Alkyl-3-methylimidazolium

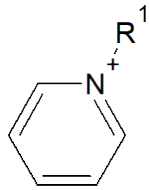

(b) 1-Alkylpyridinium

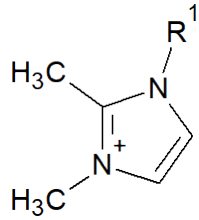

(c) 1-Alkyl-2,3-dimethylimidazolium

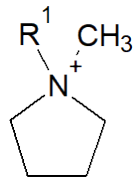

(d) 1-Alkyl-1-methylpyrrolidinium

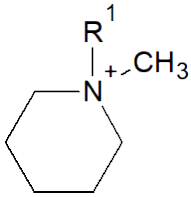

(e) 1-Alkyl-1-methylpiperidinium

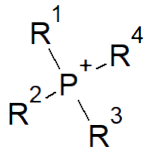

(f) Tetraalkylphosphonium

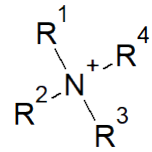

(g) Tetraethylammonium

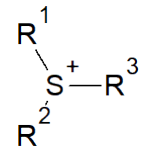

(h) Triethylsulfonium

Figure 2.6: Typical cations in ILs.

At this point, it is important to highlight the review of Asensio-Delgado et al. (2021), where the authors provided an extensive literature review containing experimental information on the absorption pairs formed by HFCs and ILs. All the information has been gathered in the UC-RAIL database, where the reader is referred to get a more comprehensive view and further details regarding the experimental method or the range of experimental conditions, as only the most important contributions are highlighted in this section. The information from this study is listed in Table 2.2 for 52 different ILs and indicates whether the information comprises many different temperatures and pressures and if it is limited to a set of conditions.

Table 2.2: VLE pairs studied. Blue color stands for systems studied in a wide set of pressure and temperature conditions, grey color marks absorption pairs studied at a single temperature, and orange color indicates systems studied at a single pressure. Table retrieved from Asensio-Delgado et al. (2021).

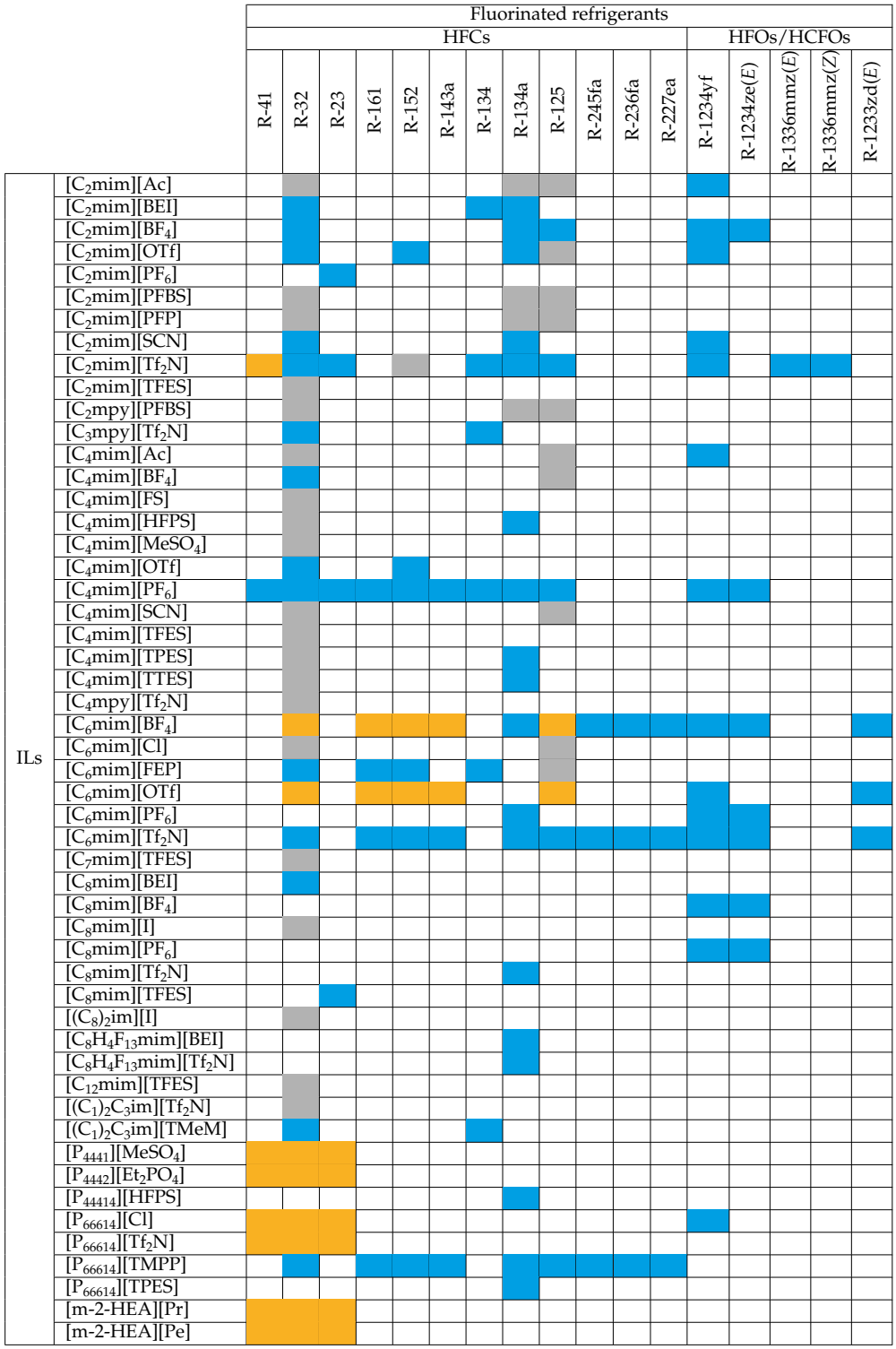

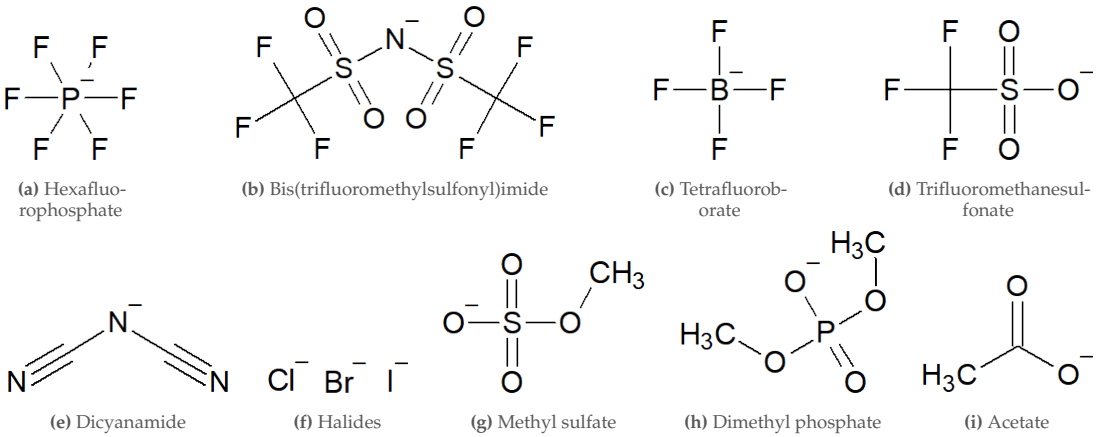

(a) Hexafluorophosphate **(b)** Bis(trifluoromethylsulfonyl)imide **(c)** Tetrafluoroborate **(d)** Trifluoromethanesulfonate

(e) Dicyanamide **(f)** Halides **(g)** Methyl sulfate **(h)** Dimethyl phosphate **(i)** Acetate

Figure 2.7: Typical anions in ILs.

As it can be observed from Table 2.2, the pioneering work of Shiflett's group has made the imidazolium-based [C_2mim][Tf_2N] and [C_6mim][PF_6] (Minnick & Shiflett, 2019; Morais et al., 2020; Ren et al., 2009; Shiflett et al., 2013; Shiflett et al., 2006; Shiflett & Yokozeki, 2006a; 2006c; 2008) ILs the most well studied, followed by [C_6mim][Tf_2N] and [P_{66614}][TMPP] thanks to the work of Liu and coworkers (X. Liu, He, et al., 2015a; 2015b; X. Liu et al., 2016; X. Liu et al., 2018; X. Liu, Qi, et al., 2015).

Understanding the factors that influence the solubility of F-gases in ILs is crucial for selecting the appropriate IL for a particular application. Nonetheless, there are several factors influencing the solubility of F-gases, and there is no rule of thumb to describe the solubility of all gases in the vast amount of available ILs; both enthalpic and entropic effects are present in the solvation process, and research has shown that the predominance of either of them depends on the type of absorbed gas.

Enthalpic effects are related to gas-liquid interactions, such as hydrogen bonding or ion-dipole interactions. Although one may think that the dipole moment of the solute may be a possible driver for F-gas solubility, there is no clear evidence of this, because other interactions may also affect the solubility to a greater extent (Camper et al., 2006; X. Liu et al., 2016). In addition, HFCs can form clusters that enhance their effective dipole moment, making it more difficult to examine the dipole effect on solubility (Asensio-Delgado et al., 2021; Costa Cabral et al., 2001; Sadeqzadeh et al., 2016) and there is evidence that the hydrogen bonding interactions may increase the solubility in fluorinated anions compared to those that are in non-fluorinated (X. Liu, Nguyen, et al., 2019; Sosa et al., 2019). These ILs are named fluorinated ionic liquids (FILs) and are a class of ILs in which variable-length fluorine chains with at least four carbon atoms, are employed in the cation or anion (Vieira et al., 2015). Pereiro, Pastoriza-Gallego, et al. (2013) demonstrated that the inclusion of these fluorinated alkyl chains creates three nanosegregated domains (polar, nonpolar, and fluorinated) which exhibit completely different behaviors and a unique ability to interact with three completely different groups at

the same time. This nanosegregation expands the number of possible conformations for these absorbents, enhancing interactions with a variety of solutes and boosting their solubility and tunability (Ferreira et al., 2017; Pereiro, Tomé, et al., 2013).

Entropic effects correspond to the degree of order achieved in the solvation process and the free volume available in the IL. The general trend observed is that a lower solvation entropy favors the solubility of F-gases (Asensio-Delgado et al., 2020a; 2020b), which explains why the solubility increases when increasing IL molar volumes (Shannon et al., 2012). This is also favorable for FILs, which exhibit higher free volumes because of the greater rigidity of the fluorinated chains (Lepre et al., 2019).

Modeling gas solubility

The main limitation when it comes to the implementation of ILs in industrial processes is the lack of fundamental understanding of their performance in relation to their compositional structure (Vega et al., 2010). Given this lack of information, the use of thermodynamic models for the description of the phase behavior is fundamental to advance in the design of novel separation processes involving advanced solvents like ILs. In this sense, the literature contains several publications intending to describe the thermodynamic behavior of the F-gas + ILs systems with different approaches, including activity coefficient models, cubic EoS, SAFT EoS, quantum-chemical calculations, and neural networks.

The VLE is normally described using activity coefficient models based on excess Gibbs free energy, where the NRTL models have been the most widely applied: Asensio-Delgado et al. (2021) reported that a total of 91 F-gas + ILs systems have been modeled using NRTL with accurate results. Other models include the UNIFAC group contribution method, for which Dong et al. (2012) used experimental VLE data from 18 HFC + ILs mixtures to fit 16 new group interaction parameters to describe the behavior of such mixtures. Finally, a new version of the NRTL model, named e-NRTL has been used by Bai et al. (2019) to take into account the different sizes of the particles by introducing volume elements into the new model.

Cubic EoSs consider the IL to be a whole molecule with a certain volume and cohesive energy, but no specification about its structure nor its association effects are explicitly considered (Vega et al., 2010). They have been widely used to model VLE and predict VLLE of F-gases and ILs. However, cubic EoS make use of critical parameters to model the phase behavior, which is immeasurable in ILs, so in many cases, pseudocritical properties have to be used instead, applying different methods, as in the works of Valderrama and coworkers (Valderrama & Robles, 2007; Valderrama & Rojas, 2009). Still, Morais et al. (2020) found that the van der Waals Eos was insensitive to the choice of critical parameters ($600 < P_c < 1400$ K and $0.5 < P_c < 5.0$ MPa), a hypothesis to be worked in other cubic EoSs.

The Redlich-Kwong Eos and the van der Waals Eos with the modifications of Yokozeki (Yokozeki, 2001) were used to model the solubility of 46 HFC + ILs mixtures (Asensio-Delgado et al., 2021). Also, the Soave-Redlich-Kwong and the Peng-Robinson EoS with typical van der Waals-two parameter mixing rules are other cubic EoSs used for modeling systems of HFCs and ILs (Freitas et al., 2013; Ren & Scurto, 2009b). The Peng-Robinson EoS, has also been applied with both, the Wong-Sandler (Parvaneh et al., 2019) and the Adachi and Sugie mixing rules (Shariati & Peters, 2003). Finally, the modified Peng-Robinson equation of state proposed by Kwak and Mansoori (Faúndez et al., 2013) and the so-called VPT EoS (a generalization of the Patel-Teja model) also with the mixing rules of Kwak and Mansoori (Faúndez, Valderrama, et al., 2020; Valderrama et al., 2019) are also employed for the same purpose.

SAFT EoSs are also employed in the literature in a wide range of applications, but to a lesser extent than previous methods. From all the SAFT variants, the soft-SAFT EoS has been the most widely applied and has shown accurate descriptions of the VLE and VLLE of systems containing IL and F-gases (Albà et al., 2020b; Vega et al., 2010). Other SAFT types include PC-SAFT, employed to calculate absorption refrigeration cycles (Sujatha & Venkatarathnam, 2018), the truncated PC-SAFT, named tPC-SAFT (Karakatsani et al., 2007), and the critical-point-based modified PC-SAFT (CP-PC-SAFT) (Polishuk, 2017).

COSMO-RS method has been used to predict the VLE of F-gas-IL mixtures comprising R-134a, R-125, and R-1234ze(E) in 900 ILs (Moreno et al., 2018). In a more recent contribution, the same authors analyze the solute-solvent interactions and determine Henry's constants of R-32 and R-134a in more than 600 ILs (Sosa et al., 2022). The results obtained are fairly accurate, considering that this methodology is a fully predictive approach.

Finally, artificial neural networks have also been applied to calculate the solubility of R-32 in 17 ILs (Faúndez, Campusano, et al., 2020). This research was later extended, covering the solubility of 10 F-gases in 8 ILs for a total of 22 systems (Fierro et al., 2021). More recently, Alkhatib et al. (2022) have also presented a novel integrated approach employing machine learning algorithms for predicting thermophysical properties of fluids. The procedure is used for modeling 18 refrigerants including hydrofluorocarbons, hydrofluoroolefins, and hydrochlorofluoroolefins. Similarly, Asensio-Delgado et al. (2022) have published a contribution in which their UC-RAIL database (Asensio-Delgado et al., 2021) containing solubility data for 24 F-gases in 52 ILs, was used to train an artificial neural network (ANN) for the prescreening of ionic liquids for the absorption of F-gases using the Neural Network Toolbox of MATLAB. The spreadsheet resulting from this study is capable of predicting the feed dataset with an average absolute relative deviation (AARD) and mean absolute error (MAE) of 10.93 and 0.014%, respectively. The authors also demonstrate its predictive capabilities showing the very accurate prediction of a system, including R-1243zf, that was not present in the training set. In light of the positive results obtained, these networks could serve as a preliminary screening method for the selection of suitable IL absorbents.

Process design for separating fluorinated refrigerants

In addition to describing the phase equilibria of refrigerant gases and ILs and modeling their solubility following different methodologies, several works have investigated the potential use of ILs as entrainers, revealing that they are promising absorbents for separating complex mixtures (Lei et al., 2014; Pereiro et al., 2012).

The separation of R-410A into R-32 and R-125 has been addressed by Shiflett's group using the NRTL model (Shiflett & Yokozeki, 2006b) and equilibrium column models. The authors concluded that high-purity R-32 could be achieved using [C_4mim][PF_6] as an entrainer. Further aspects related to the scale-up and the influence of feed composition were evaluated in a patent by Shiflett and Yokozeki (Shiflett & Yokozeki, 2014).

Shiflett's group recently published a new contribution (Finberg & Shiflett, 2021) where they fitted VLE data for R-32, R-22, R-125, R-143a, and R-134a in ILs [C_2mim][Tf_2N], and [C_4mim][PF_6] with the Peng-Robinson equation of state to simulate the separation of four azeotropic commercial refrigerant mixtures, including R-404A, R-407C, R-410A, and R-410A + R-22, and to develop rate based and equilibrium models in Aspen Plus.

Regarding the capture of either R-134a and R-32, Palomar's group has recently published an article (Sosa et al., 2020) in which a COSMO-based/Aspen Plus methodology was used to evaluate the performance of 12 different FILs as R-32 and R-134a absorbents in a commercial packing column at process scale. First, the authors simulated an absorption column in equilibrium mode, which revealed that the performance of the different FILs was similar under the same conditions. Rate-based calculations were then performed in a packing column, and demonstrated a kinetic control with highly viscous FILs, revealing higher performance differences (up to 40% lower) depending on the solvent employed, the difference being attributed to mass transfer limitations. In this contribution, the viscosity of the different FILs was fitted from experimental data using an Arrhenius-like expression, although other authors suggest that the mixture viscosity does not follow ideal behavior, and therefore, the rate-based models should also consider the non-ideal mixture behavior to obtain more accurate simulation results (Asensio-Delgado et al., 2021). Operating conditions of the absorption column for each F-gas-FIL pair were optimized with a column of height 10 m and a diameter ranging from 1.1 to 1.2 m at 10 bar total pressure, reaching 90% F gas recovery with an L/G range of 6–10.

Indeed, performing simulations using rate-based models is a step closer to accounting for the decreased separation efficiency caused by the high viscosity of IL (Quijada-Maldonado et al., 2013; Weiss & Arlt, 1987), since mass transfer has been demonstrated to play a crucial role in absorption and extractive distillation processes, where rate-based models accurately reproduce pilot plant studies (Quijada-Maldonado et al., 2016). To be more accurate, however, these models may need more information, such as the viscosities and surface tensions of the mixtures, which are often not available. In the absence of mass transfer data, equilibrium

model simulations are the most appropriate method for evaluating the performance of extractive distillation columns, given that ILs with high viscosity may have limited applicability (Asensio-Delgado et al., 2021).

For the design of F-gases separation, the predominant strategy so far has been the selection of a suitable IL entrainer with a high absorption capacity and selectivity. The choice of a proper IL should be complemented by optimizing the operation conditions while maximizing the purity of the end product and recovery of the value-added refrigerant gases, as well as performing a cost analysis. It is important to highlight that a highly consistent thermodynamic model should support this research, complemented, if available, with experimental work and case studies to reinforce the model's validity.

2.2.2 Absorption of fluorinated gases in deep eutectic solvents

Various ways are being explored to take advantage of ILs features while minimizing their unfavorable aspects. As pointed out before, many reports have brought out their toxicity (Biczak et al., 2014), poor biodegradability (Peric et al., 2013; Thuy Pham et al., 2010) or high viscosity (Paduszyński & Domańska, 2014) apart from its high production cost (L. Chen et al., 2014).

In this sense, DESs are emerging as an alternative to ILs, that may provide similar features. Precisely because of these similarities, numerous studies have focused on their use in organic synthesis, catalysis, biodiesel transformation, electrochemistry, nanotechnology, and separation technologies (Tang & Row, 2013).

DESs are defined as a mixture of two or more compounds with a lower melting point than either of its individual constituents (Abbott et al., 2003; Q. Zhang et al., 2012). Being DES systems of two or more compounds, they are represented by a solid-liquid phase diagram, just as the one in Figure 2.8, which shows the melting point as a function of the fraction of one compound. Martins et al. (2019) stated that in order to be called *deep*, the melting point of the eutectic composition has to be significantly lower than those of the individual compounds and also lower than the value of the ideal liquid mixture. They also claimed that a DESs must be liquid at operating temperature, even if this entails working with a composition different than the eutectic one. Precisely because of this, having a phase diagram and knowing the eutectic composition of the DES is of paramount importance.

DESs can be generally described by the formula:

$$\mathrm{Cat}^{+}\mathrm{X}^{-}zY$$

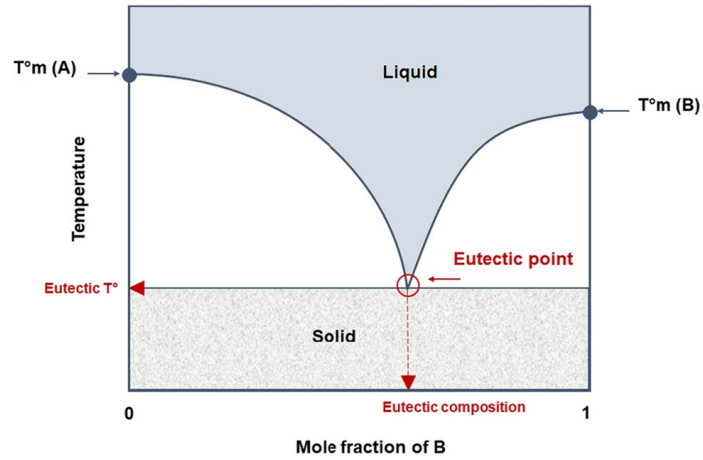

Figure 2.8: Schematic representation of a eutectic point on a two-component phase diagram. Figure retrieved from El Achkar et al. (2021).

where Cat^+ is any cation, and X is a Lewis base, generally a halide anion. The complex anionic species are formed between X^- and either a Lewis or Brønsted acid Y (z refers to the number of Y molecules that interact with the anion). DESs are classified depending on the nature of the complexing agent used, as in Table 2.3:

Table 2.3: Classification and general formula for DESs. Table retrieved from E. L. Smith et al. (2014).

Type	general formula	Terms
Type I	$Cat^+X^-zMCl_x$	M = Zn, Sn, Fe, Al, Ga, In
Type II	$Cat^+X^-zMCl_x \cdot yH_2O$	M = Cr, Co, Cu, Ni, Fe
Type III	Cat^+X^-zRZ	Z = $CONH_2$, COOH, OH
Type IV	$MCl_x + RZ = MCl^+_{x-1} \cdot RZ + MCl^-_{x+1}$	M = Al, Zn and Z = $CONH_2$, OH

From these four groups, the most studied correspond to Type III DESs, as their nature allows them to act as solvents.

Although DESs are (mostly) formed of ions, they are not ILs since they are not totally composed of ions; These are typically, but not always, synthesized by combining quaternary ammonium halide salts, which act as a hydrogen-bond donor (HBD), with hydrogen-bond acceptor (HBA) molecules, which should form a complex with the halide with a significantly lower freezing point (G. García et al., 2015).

The first DES was based on a mixture of the salt choline chloride and urea in a 1:2 molar ratio (Abbott et al., 2003). Since then, a vast amount of combinations of HBAs and HBDs have been explored. Still, choline chloride-based DESs are the most studied in the literature (G. García et al., 2015) because of the low cost and toxicity (H. G. Morrison et al., 2009), biodegradability and biocompatibility (B. S. Singh et al., 2012) of the salt. Other studied salts (HBA) comprise imidazolium (Ghareh Bagh et al., 2013; Hou et al., 2008), ammonium (Ghareh Bagh

et al., 2013; Shahbaz et al., 2012), and phosphonium-based (Ghareh Bagh et al., 2013; Hayyan, Ali Hashim, et al., 2013) ones. DESs based on FILs and perfluorinated acids with a 4-carbon chain are also under study (Castro et al., 2020). Figure 2.9 summarizes some hydrogen bond acceptor and hydrogen bond donor counterparts described in the literature.

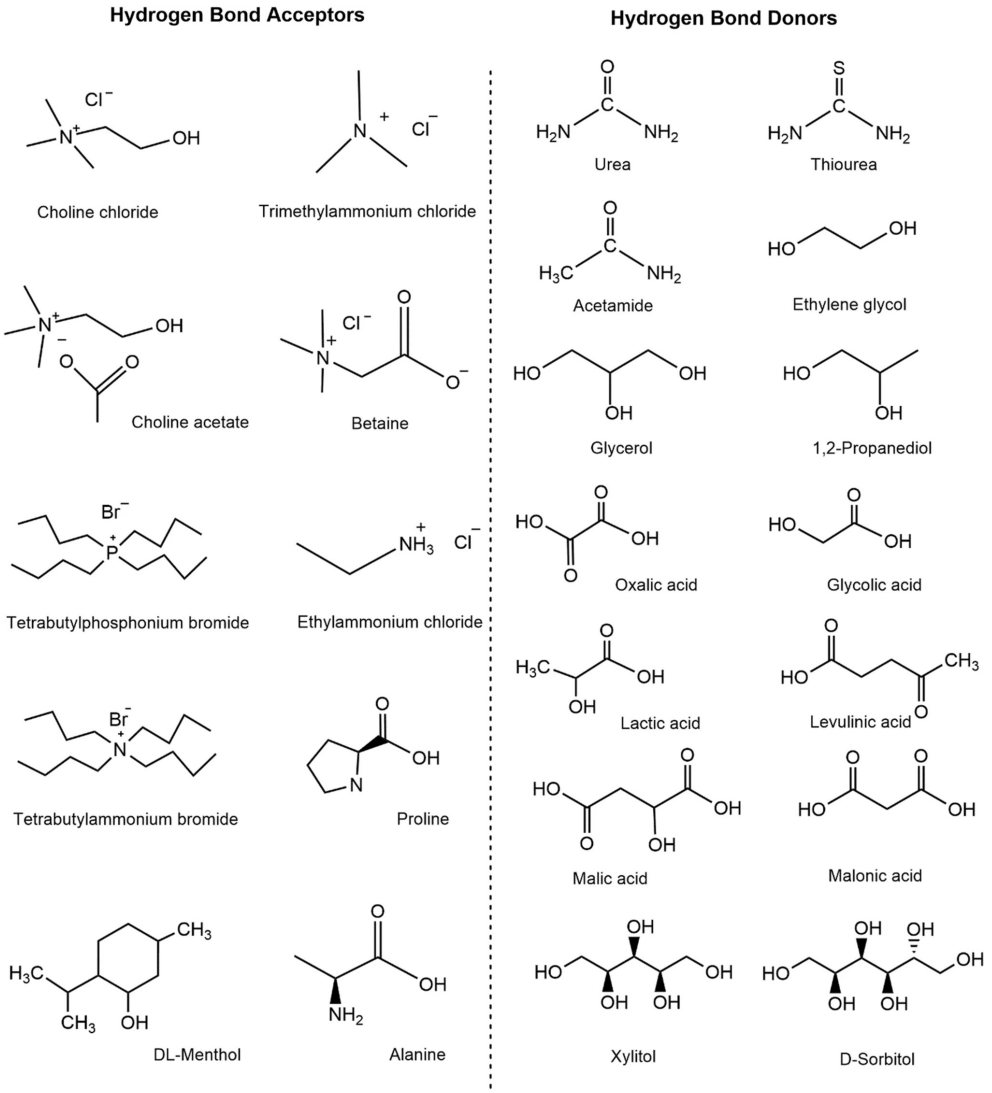

Figure 2.9: Most common structures of hydrogen-bond donors and halide salts as hydrogen-bond acceptors for the preparation of DESs. Figure taken from (G. García et al., 2015).

This section covers the physicochemical properties of DESs, such as phase behavior, density, viscosity, ionic conductivity, surface tension, and polarity, which are also detailed. Also, the main advances in gas separation applications involving DES are exposed.

Physicochemical properties

Apart from the exceptional properties of DES, similar to those of ILs (low volatility, low flammability, low vapor pressure…) DESs are chemically tunable, just as ILs are. This means that they can be designed for specific applications given the wide variety of possible combinations of HBD and HBA.

Below, the main physicochemical properties of DES, namely their phase behavior, vapor pressure, density, viscosity, and surface tension, are discussed.

Up to date, very little has been reported about the thermodynamic behavior of DESs. The freezing points of most DESs are comprised between -69 and 149 °C and several factors like the selection of the HBD (Abbott, Boothby, et al., 2004; Abbott, Capper, Davies, & Rasheed, 2004), the nature of the organic salt and its ion (Abbott et al., 2003), the molar ratio (Shahbaz et al., 2011), and the method of preparation (Abbott et al., 2006) can influence on it. Moreover, there is no correlation between the freezing point of a DES and the melting points of the individual components (Abbott, Boothby, et al., 2004; Abbott, Capper, Davies, & Rasheed, 2004; Q. Zhang et al., 2012). There is evidence, however, that the freezing point depression seems to be affected by the HBD's molecular weight (Abbott, Boothby, et al., 2004; Abbott, Capper, Davies, & Rasheed, 2004; E. L. Smith et al., 2014).

One of the most appreciated properties of ILs is their negligible vapor pressure. As DESs are formed by mixing a nonvolatile compound (the IL) plus a volatile compound, one can conclude that they should have larger values than ILs. Given this fact, the question arises as to whether the vapor pressure will be low enough to compete with ILs.

An analysis of the available literature leads to only two studies of vapor pressure: the work of Boisset et al. (2013) showed experimentally that the DES formed by lithium bis[(trifluoromethyl)sulfonyl]imide and N-methylacetamide had a vapor pressure of 0.2 mbar at 323.15 K, several orders of magnitude lower than other organic substances. S.-H. Wu et al. (2012) also reported vapor pressure measurements for choline chloride-based DESs with ethaline, glyceline, maline, and reline at 30-70 °C. As in the work of Boisset et al., the results showed a remarkable decrease in vapor pressure (from 14.2 $\mathrm{mm\,Hg}$ for reline up to 225.5 $\mathrm{mm\,Hg}$ for maline) in comparison with pure water as the DESs concentration increased. S.-H. Wu et al. (2012) also stated that the lower the melting point was, the lower the vapor pressure.

Regarding density, most of the DESs present higher densities than water, with values between 1.0 and 1.3 $\mathrm{g\,cm^{-3}}$ (El Achkar et al., 2021). DESs' density is inversely proportional to temperature (Cui et al., 2017; Ibrahim et al., 2019), and it is dependent on the choice of HBD (Florindo et al., 2014; G. García et al., 2015) and the molar ratio (Abbott et al., 2011).

Viscosity has been extensively studied because of its importance for industrial purposes. Most of the DESs exhibit high viscosity ($\eta > 100$ mPa at room temperature, which can be attributable to the expensive number of hydrogen bonds between DES' components (El Achkar et al., 2021). Although they are mostly viscous solvents, they also have a wide scope of viscosities, from very low viscosity (37 mPa s for choline chloride:ethylene glycol (1:2) at 25 °C), to extremely high values for metal salts-based DES (85,000 mPa s for 1:2 choline chloride:zinc chloride (1:2) also at 25 °C) (Q. Zhang et al., 2012). As it happens with other properties, the viscosity is clearly affected by the nature of its components (Abbott et al., 2007), the molar ratio (Abbott et al., 2011), the temperature (Abbott, Boothby, et al., 2004; Abbott, Capper, Davies, & Rasheed, 2004), and the water content (D'Agostino et al., 2015; Dai et al., 2015).

Finally, the studies related to surface tension (ST) are quite limited in comparison with density or viscosity. As expected, highly viscous DESs present high surface tensions (El Achkar et al., 2021). Values reported range from 35 to 75 mN m^{-1} at 25 °C (G. García et al., 2015). Again, those DESs exhibiting large hydrogen-bond networks have remarkably high values, like choline chloride:D-glucose/D-fructose (Hayyan et al., 2012; Hayyan, Mjalli, AlNashef, Al-Wahaibi, et al., 2013). The surface tension has proven to be affected by the salt mole fraction and the cation type and is inversely proportional to temperature (G. García et al., 2015; Lapeña et al., 2019; Nunes et al., 2019).

Separation and gas capture

The interest in the application of DESs for gas separation/capture technologies has been growing during the last decade. The use of DESs as absorbents for the capture of CO_2, as well as other pollutant gases such as carbon monoxide, nitrogen oxides, and sulfur dioxide, among others, is by far the most studied area. This interest is motivated by the possibility that DESs may be an alternative to amine-based technologies that have been in use for more than 70 years (G. García et al., 2015), and based on the similar properties they share with ILs, which have shown to have enormous potential for CO_2 (Yokozeki & Shiflett, 2009), SO_2 (Anderson et al., 2006) and H_2S (Jalili et al., 2009) capture.

As for the capture of CO_2, C. Wang et al. (2010) investigated the use of imidazolium-based ILs and superbase mixtures to develop DESs for CO_2 absorption. This study focused on the effect of the superbase, which would remove the weakly acidic proton from the imidazolium cation to enhance the CO_2 affinity, which would, in turn, increase CO_2 capture. Li et al. (2008) also studied the solubility of CO_2 in DES systems, but this time, formed with choline chloride and urea at different molar ratios at various pressures and temperatures. It was shown that the choline chloride:urea molar ratio had a significant effect on x_{CO_2}. Francisco et al. (2013) also employed choline chloride-based DES but coupled with an organic acid (lactic acid) in a 1:2 ratio. In contrast to imidazolium-based DES systems, the solubility of CO_2 in DESs made

from the combination of choline chloride with urea and/or ethylene glycol has shown good results and exhibits excellent thermophysical properties.

Based on the consulted bibliography, the DES composed of choline chloride and urea has demonstrated the highest performance to date, with a measured CO_2 uptake of 3.559 $\mathrm{mol\,kg^{-1}}$ at 303.15 K and 60 bar (G. García et al., 2015). This value is significantly lower than the 4.52 mol of CO_2 $\mathrm{kg^{-1}}$ that sulfonate ILs at 307 K and 80 bar are able to retain (S. Zhang et al., 2005). However, at normal temperature and atmospheric pressure, triethylene glycol:DBU in a molar ratio of 1:1 has a CO_2 uptake of 1.04 $\mathrm{mol\,mol^{-1}}$ at 298 K and 1 bar (Z.-Z. Yang et al., 2011), which is comparable to the 0.28 $\mathrm{mol\,mol^{-1}}$ absorbed by monoethanolamine-modified ILs at 303 K and 10 bar (Galán Sánchez et al., 2007), which corroborates that DESs are able to compete in terms of CO_2 absorption with ILs.

Less has been investigated for the capture and recycling of fluorinated compounds using DES. Up to date, the only experimental work performed is the one of Pereiro and Araújo's research group (Castro et al., 2020), where they employ DESs based on FILs and perfluorinated acids, so-called fluorinated DES to study the absorption of domestic F-gases like R-32, R-125, and R-134a at several temperatures and pressures up to 1 MPa. The obtained data was later correlated with an NRTL model. The results showed that R-134a had the greatest solubility in all tested DES combinations. Where the results obtained for R-134a and R-125 with fluorinated DES showed similar results than those obtained with FILs, the results obtained for R-32 using $[N_{4444}][C_4F_9SO_3]/C_4F_9CO_2H$ (1:1), $[N_{4444}][C_4F_9SO_3]/C_4F_9CO_2H$ (2:1), and $[C_2mim][C_8F_{17}SO_3]/C_4F_9CO_2H$ (2:1) present higher solubilities.

Absorption of F-gases employing computational models has also been under study. Abedin et al. (2017) employed computational tools to evaluate three working fluids mixtures composed of R-134a with choline chloride-based DES; first, COSMO-RS calculations were employed to perform a thermodynamic evaluation of the mixtures, and then, classical molecular dynamics (MD) simulations were made to gain deeper insight on these systems at the molecular level. The largest efficiencies were obtained when R-134a was combined with choline chloride + ethylene glycol, followed by glycerol and urea as HBDs. The study was lately expanded to R-245fa and the hydrofluoroolefins R-1234ze(*E*) and R-1336mzz(*E*) (Abedin et al., 2020) using ethylene glycol or levulinic acid as HBDs.

All of these works reflect an improvement in the study of DESs for the selective separation of commercial F-gas mixtures, which is essential for the development and scalability of unique gas separation technologies.

2.3 Fluorinated fluids with low global warming potential

Despite natural refrigerants have always been considered in refrigeration and air conditioning systems (Riffat et al., 1997), including CO_2, water, ammonia, hydrocarbons, or even air, the use of synthetic refrigerants has eventually prevailed for a variety of reasons (cost of the equipment, safety, etc.). Although some authors (Ma et al., 2013; Pearson, 2008) have continued to focus on the use of natural refrigerants, researchers and manufacturers are considering alternative synthetic refrigerants with a low GWP that are more reliable and industry-appropriate (Mota-Babiloni, Makhnatch, & Khodabandeh, 2017).

In their pioneering article, McLinden et al. (2014) examined a set of about 1,200 candidate fluids by applying screening criteria to estimates for GWP, flammability, stability, toxicity, and critical temperature. From the initial set, only 62 low-GWP halogenated olefins were usable in RACHP equipment. From this selection, McLinden and coworkers' conclusions were that no fluid was ideal in all regards, and all have one or more negative attributes. In a more recent contribution (McLinden & Huber, 2020), McLinden and coworkers performed a screening of 184,000 molecules to be considered as possible replacements, from which only 29 molecules were considered after applying filters in terms of toxicity, GWP and performance in a vapor-compression cycle. The list comprises four hydrocarbons and the closely related dimethyl ether; five fluorinated alkanes (i.e., HFCs); 10 fluorinated alkenes and an alkyne; two fluorinated oxygen-containing molecules; three fluorinated nitrogen or sulfur compounds; CF_3I; and two inorganic molecules (NH_3 and CO_2).

While the search for a low-GWP alternative refrigerant to HFCs is still ongoing, this section focuses on the most recent investigations about two potential alternatives: HFOs and HFEs.

2.3.1 Hydrofluoroolefins

HFOs were developed at the beginning of the 2000s to replace HFCs in a similar way that HFCs were developed to replace HCFCs (Mota-Babiloni, 2016). HFOs are unsaturated compounds composed by hydrogen, fluorine, and in some cases (named hydrochlorofluoroolefins, HCFO), chlorine atoms. The usage of HFOs and their mixtures is still at an early stage of development, although several investigations point out that HFOs are regarded as the most promising alternative refrigerant for HFCs because of their better environmental performance (Devecioğlu & Oruç, 2015; X. Liu, Wang, et al., 2019).

Some of the most studied HFO refrigerants are R-1234yf, R-1234ze(*E*), R-1234ze(*Z*), R-1233zd(*E*). Many fewer references are available for R-1123, R1243zf, R-1225ye(*Z*), R-1336mzz(*E*), R-1336mzz(*Z*), R-1354mzy(*E*), and R-1354myf(*E*) (Bobbo et al., 2018). Among the aforementioned refrigerants, R-1234yf and R-1234ze(*E*) are the two HFO-alternatives

highlighted as alternatives in heating, ventilating and air-conditioning (HVACR) systems, R-1234yf being the one which has attracted the most attention from the scientific community because of its similar properties to R-134a. In fact, some researchers consider R-1234yf to be a direct drop-in replacement for R-134a (Mota-Babiloni, Makhnatch, & Khodabandeh, 2017; Righetti et al., 2015).

In the following sections, the research performed in the last few years regarding its thermophysical properties and their performance in actual refrigeration systems, both as pure compounds or as mixtures with HFCs, is discussed.

Thermophysical properties

As previously exposed, an adequate thermophysical characterization is necessary for the prediction and evaluation of the performance of any working fluid. Despite being relatively new compounds, many studies have been conducted to study PVT behavior, critical properties, thermal conductivity, viscosity, density, and heat capacity of the HFO refrigerants.

Brown et al. (2010) employed group contribution methods to predict the critical properties, acentric factors, and ideal gas specific heats at constant pressure for eight fluorinated olefins, namely: R-1225ye(*E*), R-1225ye(*Z*), R-1225zc, R-1234ye(*E*), R-1234yf, R-1234ze(*E*), R-1234ze(*Z*), and R-1243zf. The authors also employed, for the same eight refrigerants, the Peng–Robinson EoS to predict thermodynamic properties (pressure-enthalpy and temperature-entropy state diagrams) and compared the results with the EoS implemented in NIST Reference Fluid Thermodynamic and Transport Properties Database (REFPROP) 8.0. Indeed, many researchers use the properties obtained from REFPROP database (Lemmon et al., 2018) as a standard to compare the accuracy of both prediction and new experimental data for refrigerants. REFPROP predicts the thermodynamic properties on the basis of a specific equation of state. In its 10th version includes the HFOs R-1123, R-1224yd(*Z*), R-1233zd(*E*), R-1234yf, R-1234ze(*E*), R-1234ze(*Z*), R-1243zf, and R-1336mzz(*Z*).

A considerable amount of experimental measurements of HFOs' thermophysical properties are available in the literature. Some of the most significant contributions in this area are the works of Higashi, Tanaka and coworkers for R-1234yf (Tanaka & Higashi, 2010b; Tanaka, Higashi, & Akasaka, 2010) and R-1234ze(*E*) (Higashi et al., 2010; Tanaka & Higashi, 2010a; Tanaka, Takahashi, et al., 2010a; 2010b) including heat capacity, one-phase densities, $P\rho T$, vapor pressures, and critical parameters. The same researchers also carried out measurements for the *cis* isomer of R-1234ze, R-1234ze(*Z*) (Higashi et al., 2015) and R-1336ze(*E/Z*) isomers (Tanaka et al., 2016; Tanaka et al., 2017). In the same line, Meng et al. (2013) reported viscosity measurements and saturated pressures up to 30 MPa for both R-1234yf and R-1234ze(*E*), and Di Nicola et al. (2012) reported triple point measurements for four HFOs: R-1234yf, R-1234ze(*E*), R-1243zf, and R-1225ye(*Z*).

In 2018, Bobbo et al. (2018) conducted a review of a large number of HFOs compounds described in the available literature. Table 2.4 contains the number of references reporting each HFO property, retrieved from the work of Bobbo and coworkers. The aim of the work was to identify possible HFO substitutes in RACHP equipment and Organic Rankine Cycles (ORC). The reader is referred to the original text for further insight into all the literature, up to 2017, published regarding the experimental measurement of HFO's thermophysical properties.

Table 2.4: Number of references reporting experimental data/estimations for several HFO and HCFO refrigerants. Table retrieved from Bobbo et al. (2018).

ASHRAE designation	Thermodynamic properties					Transport properties		
	Critical point	P_{vap}	PVT	C_p	w	λ	μ/ν	σ
R-1123	2	2	2					
R-1141								
R-1132(E)								
R-1234yf	2	11	10	5	4	1	7	2
R-1243zf	1	2	1					1
R-1234ye(E)								
R-1234ze(E)	2	13	14	6	4	2	4	3
R-1225ye(Z)		1	1					
R-1132(Z)								
R-1225ye(E)								
R-1234ze(Z)	1	8	7		1	1	2	1
R-1233zd(E)	1	4	5	1	2		1	2
R-1336mzz(E)	1	1	1					
R-1336mzz(Z)	1	4	1		1			
R-1354mzy(E)	1	1	3					
R-1354myf(E)			1					

Regarding estimations with computational methods, several studies are devoted to predict thermodynamic derived properties such as thermal conductivity or specific heat capacity as well as transport properties such as viscosity. Fouad and Vega (2018b) used a SAFT-based excess entropy scaling approach to predict transport properties of several refrigerants, including R-1234ze(E) and R-1234yf. The same authors also presented a PCP-SAFT model coupled with the Density Gradient Theory (DGT) to predict the vapor-liquid equilibrium, isobaric heat capacity, speed of sound, and surface tension of several HFC and HFO-based commercial azeotropic blends (Fouad & Vega, 2018a). In the same line, Lai (2014) used the BACKONE and PC-SAFT EoS to describe the thermodynamic properties of R-1234ze(E). Other versions of SAFT, like the soft-SAFT EoS were used by Albà and coworkers to model R-1234yf, R-1234ze(E), R-1234ze(Z), R-1233zd(E), R-1243zf and blends among them (Albà et al., 2020a).

Molecular simulation studies have also been performed to model the thermophysical behavior of HFOs and their blends. It is worth highlighting the work of Raabe and coworkers

to describe the thermophysical properties of selected HFOs and mixtures by molecular simulation, including vapor-liquid equilibria and thermophysical properties of selected HFOs (Raabe, 2015; 2020; Raabe & Maginn, 2010a) and mixtures (Raabe, 2013a; 2013b; 2014; 2016). The authors presented a transferable force field that allows accurate predictions for thermophysical and transport properties (Raabe, 2012; Raabe & Maginn, 2010b). Similarly T. Wang et al. (2020) investigated the density and heat capacity of R-1233zd(*E*) using molecular dynamics simulations. The results were in good agreement with the REFPROP 10.0 correlations.

Performance of hydrofluoroolefins in actual systems

The majority of the studies regarding the performance of HFO in actual systems are based on its direct performance comparison to that of HFCs (primarily, R-134a and R-410A).

Aprea et al. conducted a drop-in[1] test with R-1234yf (Aprea et al., 2016) and R-1234ze(*E*) (Aprea et al., 2018) in a domestic refrigerator. R-1234ze(*E*) was found to be a better replacement than R-1234yf, with a degree of subcooling of 8.3 K (compared to 0.3 K for R-134a) and a 24h energy consumption of the system reduced as much as 9%. Conversely, Sánchez et al. (2017) claimed that the use of R-1234yf and R-1234ze(*E*) in vapor-compression refrigeration systems led to a reduction in the cooling capacity as much as 8.6 and 17.8% respectively, and concluded that R-1234ze(*E*) cannot be considered a direct drop-in replacement of R-134a in such systems.

Mota-Babiloni et al. (2014) also studied the performance of R-1234yf and R-1234ze(*E*) as replacements in vapor-compression refrigeration systems and found that volumetric efficiency lowered by 3% to 5% for R-1234yf, and by 5% to 6% for R-1234ze(*E*), compared to R-134a. Also, the coefficient of performance (COP) difference obtained using R-1234yf was found to be between 3% and 11% lower than those obtained with R-134a, more in line of the results of Sánchez et al.

Furthermore, the performance of HFO refrigerants in mobile air conditioning systems (MAC) and automotive air conditioning has been widely studied in the past years, showing lower cooling capacity and COP for R-1234yf. Y. Lee and Jung (2012) found a 2.7% and 4% reduction in the cooling capacity and COP for R-1234yf, respectively, when compared to R-134a. Similar results were obtained by Rajendran et al. (2021) (2-11% lower COP). The same authors also observed that the power consumption and refrigerant mass flow rate increased up to a 14% and 24%, respectively, compared to R-134a.

To sum up, although it has been proved that R-1234yf and R-1234ze(*E*) are potential alternatives to R-134a and R-410A, and can indeed be used in the same refrigeration systems, they

[1]Drop-in denotes direct replacement wherein the existing refrigerant is replaced by a new one without making any significant modification to the existing refrigeration system (Nair, 2021).

present some limitations. These disadvantages can be partially solved by mixing them with some HFCs at the expense of a higher GWP (Mota-Babiloni, 2016).

Finally, HFOs and HCFO have also been investigated in the literature as potential replacements for R-245fa in current ORC systems, and R-1233zd(E) has been stated as a suitable drop-in replacement for R-245fa (Eyerer et al., 2019; Eyerer et al., 2016; Piña-Martinez et al., 2021; J. Yang et al., 2018a; 2018b; J. Yang et al., 2019). In particular, Eyerer and coworkers conducted an experimental study in an ORC test rig and concluded that R-1233zd(E) HCFO can effectively replace R-245fa and may even result in higher thermal efficiencies, although particular care on the lubricant choice and the material compatibility of all the components in contact with the refrigerant (especially in sealing materials), should be considered (Eyerer et al., 2016). Other working fluids studied include R-1234ze(Z) (Petr & Raabe, 2015), R-1336mzz(E) (J. Yang et al., 2019), and R-1224yd (Eyerer et al., 2019). While R-1234ze(*Z*) has proven to be a suitable drop-in replacement for R-245fa in ORC applications, further studies are required to evaluate whether the others may fulfill the requirements for such applications.

Studies on hydrofluorocarbons/hydrofluoroolefins mixtures performance

From McLinden's review (McLinden et al., 2017), it is clear that refrigerant blends between HFCs and HFOs can offer a trade-off between flammability (higher in HFOs) and GWP (higher in HFCs) as the final blend achieves intermediate properties. In the same article, the authors point out that R134a can be considered as one candidate for preparing blends with HFO due to its non-flammability and despite its high GWP.

More authors have investigated the performance analysis of HFO/HFC mixtures by adding R-134a in R-1234yf. Indeed, the addition of R-134a reduces the flammability of the resulting blend to such an extent that the composition 90/10 wt % is no longer flammable. Aprea et al. (2017a) conducted a comparative experimental analysis between R-134a, R-1234yf and a refrigerant mixture of R-134a/R-1234yf (10/90 wt %) in a domestic refrigerator. When it came to temperatures and pressures, the mixture exhibited the closest behavior to that of R-134a. Also, when the optimal charge of the mixture was used, the cycle saved 16 and 14% of energy compared to R-134a and R-1234yf, respectively. In another study (Aprea et al., 2017b) they performed the same comparison, this time with pure R-1234ze(*E*), and a binary mixture R-134a/R-1234ze(*E*) at the same composition 10/90 wt %. The authors concluded that both pure R-1234ze(*E*) and the binary mixture can be considered as a drop in of R-134a in domestic refrigeration: both working fluids achieved the same temperature levels as pure R-134a. Moreover, after 24 hours of working, 14 and 5.6 % energy savings were obtained with the mixture and with pure HFO, respectively.

Similarly, Mota-Babiloni et al. (2020) suggested that the A2 class hydrofluoroolefin R-1132a can be a blend component in advanced ultra-low temperature refrigeration configurations

(below 223K), but additional experimental research is needed to characterize their behavior and reliability as a substitute. Another work from Mota-Babiloni's group (Heredia-Aricapa et al., 2020) reviewed several HFO-based ultra-low GWP mixtures and found that the mixture R-515A, an azeotropic mixture consisting of 88 wt % R-1234ze(*E*) and 12 wt % R-227ea (a fire suppressant), had a similar COP compared to that of R-134a.

2.3.2 Hydrofluoroethers

Hydrofluoroethers (HFEs) have also been stated as alternative working fluids to HFCs (Husband & Beyene, 2008; Muñoz Rujas, 2018; Qiu, 2012; H. Wang et al., 2017). HFEs exhibit similar physicochemical properties compared to HFCs, including high volatility, low thermal conductivity, surface tension, toxicity and flammability, and zero ODP (Muñoz-Rujas et al., 2018; Tsai, 2005). Moreover, the addition of the ether group in its chemical structure lowers the atmospheric lifespan, decreasing their GWPs. Common potential alternatives include HFE-7500, HFE-7200, HFE-7100, HFE-7000, HFE-356mec, HFC-356mmz, HFE-143a, HFE-134, HFE-245mc or HFE-227me (Tsai, 2005).

HFEs began to be synthesized in the 1990s decade while searching for new fluids suitable to replace the widely used CFCs, HCFCs, HFCs, and PFCs. There is a broad variety of HFEs, whose performance and applications can vary widely as their thermophysical properties differ from one to another. The challenge in finding a replacement for the working fluids now in use stems not only from the need to identify an alternative compound with similar thermophysical properties, but also to evaluate the environmental effects, flammability, toxicity, and material compatibility of the new fluid. In this sense, the contribution of Tsai (2005) explores the commercial and industrial uses of such compounds as refrigerants, cleaning solvents, foaming agents, or dry etching agents.

HFEs such as HFE-125, HFE-134, HFE-143a, HFE-227me, HFE-245mf, and HFE-245mc can be used as potential refrigerants based on their excellent aforementioned properties such as thermal stability, cycle performance, flammability, and toxicity (Bivens & Minor, 1998; Sekiya & Misaki, 1996; 2000). Du Pont Company presented in 1996 a patent describing their use as refrigerants (Bivens et al., 1996). However, scarce evidence is found on this topic, and further investigation is necessary.

HFEs could also be a replacement for HFCs as cleaning solvents in some precision processes or equipment. Precision cleaning is performed on some electronic parts, aerospace military, medical, and analytical equipment or instruments to ensure the extreme level of cleanliness and product integrity required (Tsai, 2005). To that end, HFE-7000, HFE-7100, and HFE-7200 (from 3M's Novec family) are used in the industry because of their similar properties to HFC-43-10mme (1,1,1,2,3,4,4,5,5,5-decafluoropentane).

Due to their thermal conductivity, HFE-245mf, HFE-245mc, HFE-254pc, and HFE-356me are potential replacements for classic blowing agents (Matsuo et al., 1998; Takada et al., 1999; Takada et al., 1998). Finally, HFE-227me has also been proposed to use as clean etching agent for semiconductor manufacture, replacing C_3F_8 and c-C_4F_8 (Takahashi et al., 2002).

Precisely because of their good heat conductivity and their excellent dielectric properties, the field in which hydrofluoroethers have been most widely considered is as heat transfer fluids (HTF) (Costello et al., 2004; Tuma, 2001; 2006). Their use as HTF is investigated in numerous electronic devices where PFCs were originally employed, including ion implanters, steppers, etchers, plasma-aided tools, and automated testers (Tuma & Tousignant, 2000). Indeed, its heat transfer performance is shown to be superior to that of perfluorinated fluids of similar boiling points. 3M also has several patents describing their use as HTF for HFE-7500 (Tousignant & Tuma, 2000) and others (Flynn et al., 2011; Tuma, 2000). More recently Zakhidov et al. (2012) tested HFE-7100, HFE-7200, HFE-7300, HFE-7500, and HFE-7600 as HTFs for OLED devices.

Based on high molecular weight HFEs, HFE-649, HFE-7000, and even HFE-7100 in some cases, are particularly suitable to be used in ORCs (Muñoz Rujas, 2018), requiring low or medium boiling temperatures, good thermal stability, nonflammability, and high molecular weight, which contributes to reducing the engine speed of the turbine. Indeed, the thermodynamic, environmental, and safety analysis based on the spinal point method carried out by Qiu (2012) for eight different working fluids recommends HFE-7000 and HFE-7100 as preferred over other HFC, HCFC, and PFC alternatives. In this regard, both the US Environmental Protection and the European Environmental Agencies have suggested replacing HFCs with HFEs (Vinš et al., 2021).

ORCs are presented as an effective way to minimize fossil fuel usage and GHG, as they can recover the heat discharged in power plants from flue gas, drained water, and exhaust steam to generate electricity. In ORCs, organic fluids, including fluorinated refrigerants, are typically used as working fluids for low-temperature waste-heat recovery (J. Yang et al., 2018b). HFCs stand out as the dominant working fluids among the different refrigerants, R-245fa being the most suitable one used in the industry (Eyerer et al., 2019; Petr & Raabe, 2015; J. Yang et al., 2018a; J. Yang et al., 2019).

Only two papers have addressed the feasibility of HFEs as alternative working fluids in ORCs (Jang & Lee, 2018; H. Wang et al., 2017). In particular, it is worthy of highlighting the work of Jang and Lee (2018). In this contribution, the authors built four different micro-combined heat and power (CHP) thermodynamic models and determined the best-operating conditions for three different working fluid groups, including two HFEs (HFE-7000 and HFE-7100). The results suggested that these two HFEs might be used as alternative working fluids, albeit the ORC configuration strongly impacts the fluid's choice.

An accurate analysis of the use of HFEs as efficient substitutes for phased-out HFCs requires a detailed thermophysical characterization to fully understand the behavior of these fluids in the ORC's operating conditions. While some properties, such as liquid density and vapor pressure, have been reported for most fluids (Q. Chen et al., 2020; Goodwin et al., 1998; Kayukawa et al., 2003; Murata et al., 2002; Ohta et al., 2001; Rausch et al., 2015; Ripple & Matar, 1993; Yasumoto et al., 2003), this information is limited to specific temperature and pressure ranges. In addition, there is a lack of standardized information on other key data, such as enthalpies and entropies.

The absence of a comprehensive experimental characterization can be addressed using computational strategies with the capacity to quickly identify suitable HFCs' substitutes while meeting environmental and technological constraints in an efficient, cost-saving and reliable way. Few approaches have been made to address this issue using molecular-based EoS, including those derived from SAFT. In particular, Vijande et al. (2004) described the PVT behavior of several HFEs based on available experimental data and proposed a group contribution scheme from the perturbed-chain PC-SAFT EoS variant to extrapolate the parameters for other molecules of the same family. Similarly, Vinš et al. (2021) developed a PCP-SAFT model, including polar effects, for the aforementioned HFEs, where DGT was coupled to estimate the surface tension. More recently, Doubek and Vacek (2022), fitted experimental data from several perfluoroalkyl methyl ethers and one C6-fluoroketone to 3 different SAFT-based Eos: sPC-SAFT, Soft-SAFT, and SAFT-BACK. Other approaches combining the SAFT-VR version with a group contribution approach have also been used to model the main thermodynamic properties of HFEs (Haley & McCabe, 2017).

Certainly, the use of molecular modeling tools allows a complete description of the thermophysical properties of HFEs and may provide handy information regarding their intermolecular interactions. This would expand the analysis of alternative working fluids for potential drop-in candidates both from a process and economic point of view.

3

Theoretical background

This chapter will outline the many approaches employed throughout this thesis. The multiscalar approach presented in this work consists of quantum-based methods (such as COSMO-RS), which excel at treating systems with a few atoms, molecular simulations, which can handle the evolution of thousands of interconnected molecules, and thermodynamic equilibrium theories (such as SAFT EoS). Together, this information can be used as input information to guide process simulation modeling using commercial simulation software to design recovery processes in a wide range of operating conditions.

The prodigious evolution of computers in the past few decades has drastically changed how we live and perceive the world around us. Science, the driving factor of this new historical paradigm, is reaping the benefits from it as well: data analysis is now more tractable, certain experimental signals can be easily transformed into intelligible information, and complex mathematical equations are now easier to solve. The rapid spread of computers has also given rise to a new branch of scientific research: computer simulations.

Multiscale modeling is a class of computer simulations in which multiple models at different scales (see Figure 3.1) are used simultaneously to describe a system (E & Lu, 2011). In the multiscale approach, one uses a variety of models at different levels of resolution and complexity to study one system; the different models are linked together either analytically or numerically.

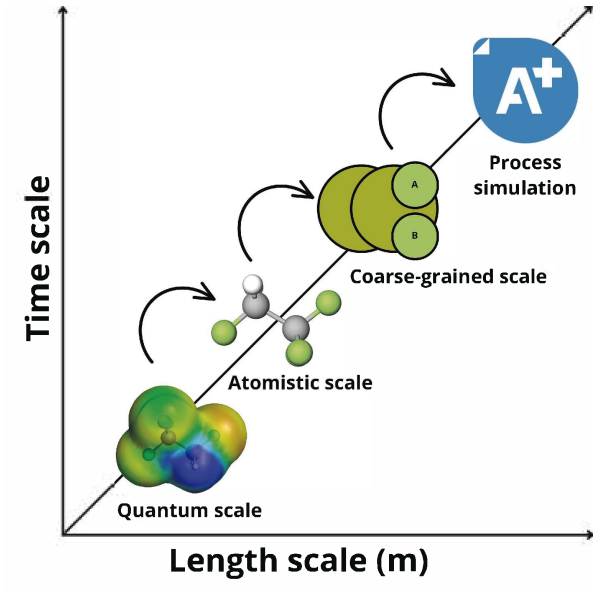

Figure 3.1: Schematic diagram of multiscale simulation.

The idea behind this is that by using such a multiscale (and multi-physics) approach, one might be able to strike a balance between accuracy (which favors using more detailed and microscopic models) and feasibility (which favors using less detailed, more macroscopic models). The necessity for such modeling typically stems from the inaccuracy of available macroscale models and the inefficiency and/or excess of information provided by microscale models. Combining these perspectives aims to find a good balance between precision and efficiency.

3.1 Quantum-based methods: COSMO-RS

COSMO-RS (short for COnductor-like Screening MOdel for Real Solvents) is an equilibrium thermodynamics approach based on quantum chemistry and designed to predict chemical potentials, μ, in the liquid phase (Klamt, 1995; 2005; Klamt et al., 2010) and has become a frequently used alternative to force field–based molecular simulation methods on one side and group contribution methods on the other (Klamt et al., 2010).

In a first step, a quantum-chemical COSMO (Klamt & Schüürmann, 1993) calculation is performed over the whole molecule. In a COSMO calculation, the solute is placed inside a cavity shaped like a molecule, while the surrounding solvent is represented as a continuum. The solute electron density and shape are converged into their energetically ideal condition in a conductor, which serves as the reference state for further COSMO-RS calculations. The resulting COSMO files contain the geometries, energies, and surface screening charge densities. COSMO-RS has some adjustable parameters in its equations which reflect in a general way how the molecules interact. They are not related to the nature of the system but to the nature of the interactions. In practice, these parameters are integrated into the software distributions available for sale (Klamt et al., 1998; Pye et al., 2009), so COSMO-RS calculations do not require fitting any specific parameters prior to the calculation. COSMO-RS considers the solvent to be a set of pair-wise interacting surface segments. The interaction energy of surface pairs is defined by the screening charge densities σ and σ' of respective surface segments. For COSMO-RS statistical thermodynamics, the histograms of the screened charge density, the so-called σ-profiles $p^x(\sigma)$, i.e., the amount of surface with polarity σ for a molecule x. (Diedenhofen & Klamt, 2010). Two energetic contributions of the most relevant molecular interaction modes, i.e., electrostatics (E_{misfit}) and hydrogen bonding (E_{HB}), are described as functions of the screening charges of two interacting surface segments σ and σ' (σ_{aceptor} or σ_{donor} if the interacting segments are located on an HB donor or acceptor atom) as illustrated in Figure 3.2. Also, the van der Waals (E_{vdW}) interactions are taken into account but in a more approximate way (see equations 3.1-3.3).

With this, the screening charges can be used to calculate the chemical potential of the molecules in a liquid solvent or mixture through equation 3.4. Many other thermodynamic equilibrium parameters, including activity coefficients, solubility, partition coefficients, vapor pressure, and free energy of solvation, are derived from the calculation of chemical potential using classical thermodynamics.

$$E_{\text{misfit}}(\sigma, \sigma') = a_{\text{eff}} \frac{\alpha}{2} (\sigma + \sigma')^2 \tag{3.1}$$

$$E_{\text{HB}} = a_{\text{eff}} c_{HB} \min(0; \min(0; \sigma' + \sigma_{\text{HB}}) \max(0; \sigma - \sigma_{\text{HB}}) \tag{3.2}$$

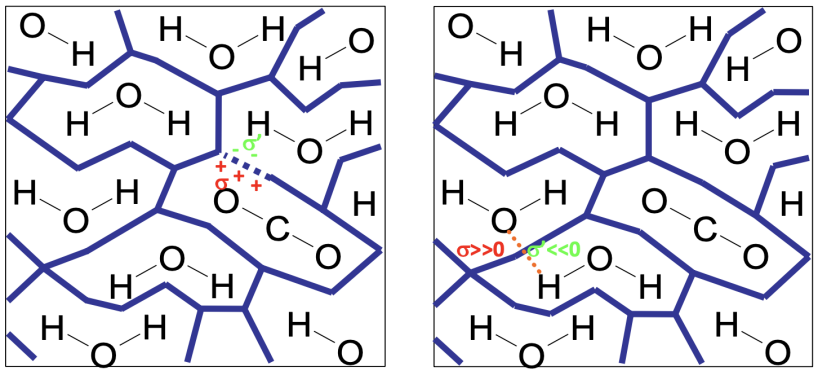

Figure 3.2: Electrostatic energy arising from the misfit of screening charge densities σ and σ'. Figure retrieved from (Dassault Systèmes, 2020).

$$E_{\text{vdW}} = a_{\text{eff}}(\tau_{\text{vdW}} + \tau'_{\text{vdW}}) \tag{3.3}$$

$$\mu_S(\sigma) = -\frac{RT}{a_{\text{eff}}} \ln \times \left[\int p_S(\sigma') \exp\left(\frac{1}{RT} \left(a_{\text{eff}} \mu_S(\sigma') - E_{\text{misfit}}(\sigma, \sigma') - E_{\text{HB}}(\sigma, \sigma') \right) \right) \mathrm{d}\sigma' \right] \tag{3.4}$$

As aforementioned, the adjustable parameters present in COSMO-RS model are α', which is an interaction parameter, a_{eff} is the effective contact area, c_{HB} is the hydrogen bond strength, σ_{HB} is the threshold value for hydrogen bonding, and τ_{vdW} is the element-specific interaction parameter.

$\mu_s(\sigma)$ is called σ-potential, and it can be defined as the affinity of the solvent S for a surface of polarity σ. Finally, the pseudo-chemical potential (Ben-Naim, 1987) of compound x_i in the system S can be calculated by integration of $\mu_s(\sigma)$ over the surface of the compound (equation 3.5). To take into account the size and shape differences of the molecules in the system, an additional combinatorial term, $\mu^X_{C,S}$, which depends on the area and volume of all compounds in the mixture, and three adjustable parameters, is added.

$$\mu^X_s = \mu^X_{C,S} + \int p^X(\sigma) \mu_S(\sigma) \mathrm{d}\sigma \tag{3.5}$$

Regarding how COSMO-RS calculates the VLE equilibrium of a mixture, one should consider that it is a model based on the condensed phase and assumes the ideality of gases. Hence, the fugacity of gases is discarded, and the equilibrium condition is described as in equation 3.6. COSMO iteratively solves equation 3.6 that satisfies the resulting pressure as P_{tot}.

$$P_{\text{tot}} = \sum_i \left(P_i^0 x_i \gamma_i\right) \tag{3.6}$$

3.2 Atomistic scale: molecular simulations

Molecular simulations consider small-size systems at a typical scale of a few nanometers and determine their behavior from a careful computation of the interactions between their components (Ungerer et al., 2007). In a nutshell, molecular simulation is the technique of replicating chemical and physical processes in a computer. This can be accomplished by designing a computer program that defines the properties of the system to be emulated through force fields, which are a set of potential functions and parameters that define the interactions in a molecular system. Depending on the system and its complexity, this simulation can take much more computational time than classical thermodynamic models: from a few hours to several weeks of computing time.

Molecular simulations are getting attention in chemical engineering, not only for their capacity to predict thermophysical properties of poorly known systems but for the information they return regarding the molecular interpretation of the properties (i.e., information on preferred interactions, etc.).

3.2.1 Introduction to statistical mechanics

Molecular simulations are capable of predicting all thermophysical properties in a single theoretical framework, which is statistical thermodynamics (Allen & Tildesley, 2017; McQuarrie, 1976). The idea behind this is that any property of a macroscopic system, $\mathcal{A}$, can be studied by determining the properties of the microstate (i.e., the detailed configuration of the system at a molecular level).

An ensemble is a collection of microstates with the same constrained properties as the macroscopic system of interest. Take, for example, a macroscopic system with a fixed number of particles (N), constant volume (V), and energy E. Although the macroscopic properties remain the same after a certain period of time, one can observe a permanent rearrangement of the configuration on the microscopic level as particles move, collide and exchange energy, rotate, etc. Ensembles are characterized by the choice of constraint properties. The different types of ensembles are shortly introduced in the following section. Typically, the constrained properties are the same as in experimental studies, so the results obtained from molecular simulations are comparable with the experimental values.

In essence, molecular simulations generate a large number of microstates corresponding to the macroscopic system of interest. Those can be generated through molecular dynamic (MD) simulations or Monte Carlo (MC) simulations.

In MD, the time evolution of a macrostate is followed by numerically integrating Newton's equation of motion of its particles with time (Allen & Tildesley, 2017; Haile, 1992). Therefore, the statistical average of a property of interest is determined from the values of $\mathcal{A}_i(t)$ of the property at different timesteps Δt. That is:

$$\mathcal{A}_{\text{macro}} = \frac{1}{N_{\Delta t}} \sum_{i=1}^{N_{\Delta t}} \mathcal{A}_i(t) \tag{3.7}$$

In MC simulations, different microstates are generated randomly by a statistical method to respect the probability distribution of the desired statistical ensemble (Ungerer et al., 2007). The statistical averages are calculated as:

$$\mathcal{A}_{\text{macro}} = \int_{\Gamma} \mathcal{A}(\Gamma)\wp(\Gamma)\mathrm{d}\Gamma \approx \sum^{N_{\text{microstate}}} \mathcal{A}(\Gamma)\wp(\Gamma)\mathrm{d}\Gamma \tag{3.8}$$

Where Γ is the phase space of possible states and $\wp$ is the probability distribution. At this point is important to note that a basic postulate of statistical mechanics, and therefore of molecular simulations, is the so-called *Ergodic Hipothesis*, which states that if a system is at equilibrium, at any point in time, the thermodynamic properties remain constant. In short, both methodologies yield the same results of equilibrium properties within the given statistical uncertainties (Haile, 1992).

For the calculation of an ensemble average of a property of interest, the value of this property is weighted by the probability that this state occurs, which, in turn, depends on the constraints imposed on the system. Thus, each kind of ensemble is characterized by its probability distribution, also known as the probability density, $\wp$ (Raabe, 2017). Another property of interest of an ensemble is its partition function, Q, which is the sum of all available states under the given constraints of the ensemble. If the partition function is known, all ensemble thermodynamic properties can be obtained from derivatives or by algebraic operations. The connection of the partition function to thermodynamics is established through the bridge equation (Raabe, 2017):

$$\Psi_{\text{ensemble}} = -\ln Q_{\text{ensemble}} \tag{3.9}$$

Being Ψ the thermodynamic potential of the ensemble (the property whose minimum defines the equilibrium condition).

Table 3.1: Comparison of the classical ensemble types. Table retrieved from (Raabe, 2017).

Ensemble	Imposed variables (constraints)	Fluctuating Properties	Corresponding thermodynamic system	Ψ Ensamble
Microcanonical	N, V, E	Energy (quantum state) of each particle ε_i	Isolated	$\Psi_{NVE} = -\frac{S}{k_B}$
Canonical	N, V, T	Internal energy E_j	Closed	$\Psi_{NVT} = \frac{A}{k_B T}$
Grand Canonical	μ, V, T	Number of particles N_i Internal energy E_j	Open	$\Psi_{\mu_i VT} = -\frac{PV}{k_B T}$
Isothermal-isobaric ensemble	N, P, T	Volume V_i Internal energy E_j	-	$\Psi_{NPT} = \frac{G}{k_B T}$

A brief introduction to the classical ensemble types and their application in molecular simulation studies is provided next. Table 3.1 compares the classical ensemble types used in statistical mechanics. For a more detailed description, the reader is referred to the textbooks of Allen and Tildesley (2017), Carey (1999), Gasser and Richards (1995), Raabe (2017), and Sears et al. (1975)

The microcanonical ensemble comprises all the microstates with the same constant volume V, internal energy E, and the number of particles N. It relates to an isolated thermodynamic system with solid, adiabatic, and impermeable walls that prevent energy and mass transfer with the surrounding environment. As the imposed variables do not correspond to those of actual experimental setups, the microcanonical ensemble is of little value for molecular simulation analyses on thermophysical properties.

The imposed variables in the canonical ensemble are the volume V, the temperature T, and the number of particles N. Consequently, each microstate can be viewed as a closed system with impermeable walls. Nevertheless, the walls are now diathermic to facilitate energy transfer with an isothermal heat bath to maintain a constant temperature. This ensemble is implemented in simulation studies for fluids with known density in order to predict parameters such as pressure, chemical potential, internal energy, and transport properties.

The grand canonical ensemble is comprised of a large number of microstates with constant volume V and temperature T. In addition, the chemical potential μ is fixed, although the number of particles in the system is variable. The grand canonical ensemble is analogous to an open system with solid yet diathermic and permeable walls that allow both mass and energy exchange with the surrounding environment. This is the only ensemble in which the number of particles is not imposed. Hence, it is helpful in adsorption or chemical reaction simulation research.

The isothermal-isobaric ensemble's imposed variables are pressure P, temperature T, and the number of particles N. Although it does not correspond to a classical thermodynamic system, the NPT ensemble is frequently employed in molecular simulation research since its limitations are consistent with typical experimental settings. Because of this, simulations in

the NPT ensemble can be used to predict thermophysical properties as a function of temperature and pressure based on experimental results.

Thermodynamic properties of the ensemble

As described above, the partition function in statistical thermodynamics is of similar importance to the fundamental state equation in macroscopic thermodynamics. All thermodynamic properties of an ensemble are derived from its partition function.

Taking for example the canonical ensemble and its partition function (equation 3.10), the thermodynamic properties S, P, μ, and E can be derived from the bridge equation (equation 3.9).

$$Q_{NVT} = \frac{1}{N!}\frac{1}{h^{3N}} \int\int \exp\left(\frac{-E_i}{k_\mathrm{B}T}\right) dr^{3N} dp^{3N} \tag{3.10}$$

$$A = -k_\mathrm{B}T \ln Q_{NVT} \tag{3.11}$$

which yields:

$$S = -\left(\frac{\partial A}{\partial T}\right)_{V,N} = k_\mathrm{B}\left(\ln Q_{NVT} + T\left(\frac{\partial \ln Q_{NVT}}{\partial T}\right)_{V,N}\right) \tag{3.12}$$

$$P = -\left(\frac{\partial A}{\partial V}\right)_{T,N} = k_\mathrm{B}T\left(\frac{\partial \ln Q_{NVT}}{\partial V}\right)_{T,N} \tag{3.13}$$

$$\mu = -\left(\frac{\partial A}{\partial N}\right)_{T,V} = -k_\mathrm{B}T\left(\frac{\partial \ln Q_{NVT}}{\partial N}\right)_{T,V} \tag{3.14}$$

$$E = A + TS = k_\mathrm{B}T^2\left(\frac{\partial \ln Q_{NVT}}{\partial T}\right)_{V,N} \tag{3.15}$$

3.2.2 Energy of molecular systems (force fields)

As has already been stated, energy is a central concept in statistical mechanics. The correct description of the fluid intended to model is primarily influenced by the thermodynamic and kinetic properties, which, in turn, are determined by the nature of the external and internal energy. The total energy of the system is determined as the sum of the potential, U, and kinetic energy, K, as defined in equation 3.16. Despite this, only the potential energy needs to be

provided as an explicit function of molecular coordinates through a suitable intermolecular energy potential model (Ungerer et al., 2007); in MD simulations, it is enough to compute the forces acting between particles, and as a result of this simulations, kinetic energy is obtained. Something similar happens when performing MC simulations, where an analytical integration accounts for the influence of kinetic energy.

$$E = U + K \tag{3.16}$$

Both MD and MC techniques use interaction potentials for the calculation of the total energy. The parameterization used to compute this energy is called the force field. Force fields usually derive from experimental data and/or quantum chemical calculations and are simplified analytical potential energy functions that relate the chemical structure of the system to its conformational energy. There are many different force fields available in the literature, and they differ in the functional forms used to describe the interaction and the parameters used to describe the functional forms.

The particular expression of the force field depends on the atomic model used to represent the atoms in the system. A classical representation used in molecular simulations is to treat all atoms as charged spheres interconnected by wires to simulate bonds. This representation is known as atomistic molecular simulation or All-Atom (AA) approach.

The potential energy is decomposed as a sum of the intermolecular (external) and intramolecular (internal) interactions of the system:

$$U = U_{\text{ext}} + U_{\text{int}} \tag{3.17}$$

Intramolecular interactions result from the interaction belonging to the same molecule and are expressed as:

$$U_{\text{int}} = U_{\text{str}} + U_{\text{bend}} + U_{\text{tors}} \tag{3.18}$$

Where U_{str} is the stretching energy, associated with the variations of bond length (i.e., 1-2 interactions), U_{bend} is the bending energy, arising from the variations of angles formed by two atoms (i.e., 1-3 interactions) and U_{tors} is the torsion energy caused by the variations of the dihedral angles formed by four successive atoms (1-4 interactions) in a chain. There are several forms to represent each term depending on the force-field type. The ones used in this doctoral thesis are described through equations 3.19 to 3.21.

$$U_{\text{str}} = \frac{1}{2} k_{\text{bond}} (r - r_0)^2 \tag{3.19}$$

$$U_{\text{bend}} = \frac{1}{2} k_{\text{bend}} (\theta - \theta_0)^2 \tag{3.20}$$

$$U_{\text{tors}} = \frac{1}{2} K_1 \left[1 + \cos(\phi)\right] + \frac{1}{2} K_2 \left[1 - \cos(2\phi)\right] + \frac{1}{2} K_3 \left[1 + \cos(3\phi)\right] + \frac{1}{2} K_4 \left[1 - \cos(4\phi)\right] \tag{3.21}$$

Intermolecular energy arises from the interaction between different molecules. The non-intermolecular terms generally comprise van der Waals, dispersive-repulsive interactions as well as electrostatic (or coulombic) interactions: $U_{\text{ext}} = U_{\text{d-r}} + U_{\text{el}}$.

The dispersion-repulsion energy is often the leading term among attractive energies (Ungerer et al., 2005) and is obtained by a summation over all the pairs of force centers. Although the Buckingham exp-6 model has shown to be more accurate on several important systems (Errington & Panagiotopoulos, 1998; 1999a; 1999b) the most popular model is still the Lennard-Jones (LJ) 6–12:

$$U_{\text{d-r}} = \sum_{ij} 4\epsilon_{ij} \left[\left(\frac{\sigma_{ij}}{r_{ij}} \right)^{12} - \left(\frac{\sigma_{ij}}{r_{ij}} \right)^{6} \right] \quad \text{being} \quad i < j \tag{3.22}$$

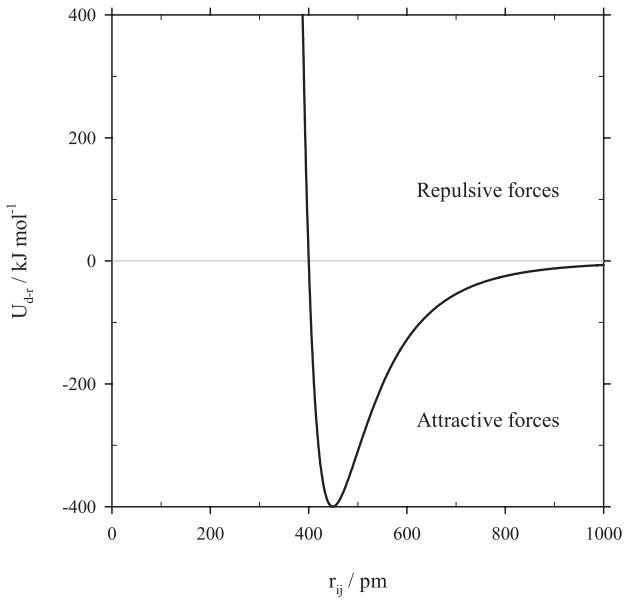

Figure 3.3: LJ potential as a function of r_{ij}.

Where r_{ij} is the separation distance between force centers. The LJ parameters are typically obtained not for single atoms but rather for atom types that are defined by their element type and their chemical environment, i.e., hybridization, aromaticity, etc. (Hinchliffe, 2005; J.

Wang et al., 2004). Like in the soft-SAFT framework, the heteroatomic interactions between two unlike atom types, are determined by the Lorentz-Berthelot combining rules (in this case, without binary adjustable parameter) as in equations 3.51 and 3.52.

As these forces decrease with the separation distance between two molecules, it is logical to establish a threshold value from which the potential energy associated with this distance is no longer considered, reducing significantly time-consuming computations. This value is known as *cutoff radius* (r_c).

$$U(r) = \begin{cases} 4\epsilon \left(\left(\frac{\sigma_{ij}}{r_{ij}} \right)^{12} - \left(\frac{\sigma_{ij}}{r_{ij}} \right)^{6} \right) & ; r < r_c \\ \\ 0 & ; r \geq r_c \end{cases} \tag{3.23}$$

As a rule of thumb, a typical cutoff radius of the LJ potential is chosen as $r_c \leq 2.5\sigma$.

In classical analytical force fields, electrostatic interactions are modeled by locating static point charges, q_i, at their atomic nuclei. The interaction between two point-particles is described by the Coulomb law:

$$U_{\text{el}} = \sum_{ij} \frac{1}{4\pi\varepsilon_0} \frac{q_i q_j}{r_{ij}} \tag{3.24}$$

Where the sum includes all possible pairs of partial charges q_i and q_j; r_{ij} is the separation distance and $\epsilon_0 = 8.85419 \times 10^{-12}\ \mathrm{C\,N^{-1}\,m^{-2}}$. The total electrostatic interactions due to all pairs of charges are given by:

$$U_{el} = \frac{1}{2} {\sum_{n}}' \sum_{i=1}^{N} \sum_{j=1}^{N} \frac{q_i q_j}{4\pi\epsilon_0 (\vec{r}_{ij} + \vec{n}L)}, \quad \vec{n} = \begin{pmatrix} n_x \\ n_y \\ n_z \end{pmatrix} \; n_{x,y,z} = 0, 1, \ldots \tag{3.25}$$

For the central simulation box (n=0), the interaction between q_i and q_j for $i = j$ has to be omitted, which is indicated by the prime symbol in the previous equation.

Equation 3.25 is a *conditionally converging sum*, meaning that it does not converge absolutely, but the results depend on the order of the summation (Ungerer et al., 2005).

Compared to the LJ potential, the range of the electrostatic interaction is much larger. Electrostatic interactions are, by definition, long-range interactions, and the solution applied in the LJ potential (truncation at r_c), cannot be used in this case (Allen & Tildesley, 2017; Frenkel & Smit, 2001; Raabe, 2017). Moreover, electrostatic interactions are a *conditionally converging sum*, thus, the coulombic interactions are usually calculated using the Ewald sum method.

This methodology was first introduced in 1921; in short, the idea is to transform the conditionally convergent sum over all pairs of charges in equation 3.25 into a rapidly and absolutely converging summation. For further details, the reader is referred to the textbooks of Allen and Tildesley (2017) and Raabe (2017) as only the final expression is shown here (equation 3.26).

Here, α is the width of the Gaussian distribution, and erf(x) is the error function. The sum over $\vec{k}$ extends over linear combinations of the reciprocal vectors of the simulation box. The accuracy of the Ewald sum to reproduce the exact coulombic energy and its convergence behavior depends on the parameter α, the real space cutoff r_c and the largest reciprocal space vector $\vec{k}_{max}$ that determines the number of cells included in the reciprocal sum.

$$\begin{aligned} U_{el} = & \frac{q_i q_j}{r_{ij}} erf\left(\sqrt{\alpha} r_{ij}\right) \\ & + \frac{1}{2} \sum_{k \neq 0} \sum_{i=1}^{N} \sum_{j=1}^{N} \frac{4\pi}{\epsilon_0 V k^2} q_i q_j \exp\left(-i\vec{k} \cdot (\vec{r}_i - \vec{r}_j)\right) \exp\left(-k^2/4\alpha\right) \\ & + \sqrt{\frac{\alpha}{\pi}} \sum_{i=1}^{N} q_i^2 \\ & + \frac{1}{2} \sum_{i=1}^{N} \sum_{a=1}^{N_{i,atoms}} \sum_{b=1}^{N_{i,atoms}} \frac{q_{i,a} q_{i,b}\, erf(\alpha\, r_{i,ab})}{r_{i,ab}} \end{aligned} \tag{3.26}$$

3.2.3 Molecular dynamics

Molecular Dynamics samples the phase space (i.e., vector space spanned by combinations of the velocity and position coordinates of a system) by numerically integrating Newton's equations of motions (equation 3.27) for a relatively small set of N particles. (Allen & Tildesley, 2017; Haile, 1992). In contrast with MC simulations, dynamic properties can only be obtained with MD, either at equilibrium or far from it (Ungerer et al., 2007).

$$\vec{F}_i = m_i \frac{d^2 \vec{r}_i}{dt^2} \tag{3.27}$$

In MD simulations, the force between two particles varies simultaneously as the potential energy does. However, as each particle interacts simultaneously with all other particles in the system, the motions of all particles are coupled. Taking this into account, the integration of the second-order differential equation 3.27, is impossible (Raabe, 2017). A classical solution for this is to use the fine-difference methods in which the integration over time t is broken into a series of short time steps, δt. Finite-difference methods generally make use of truncated Taylor expansions for the position, $\vec{r}(t)$, and its derivatives (equation 3.28). In this expression,

the first derivative of the particle position is the velocity (i.e., $\dot{\vec{r}}_i = \vec{v}_i$), the second derivative is the acceleration ($\ddot{\vec{r}}_i = \vec{a}_i$) and $\vec{b}_i$ represents the third derivative of the coordinate vector.

$$\vec{r}_i(t+\delta t) = \vec{r}_i(t) + \vec{v}_i(t)\delta t + \frac{1}{2}\vec{a}_i(t)\delta t^2 + \frac{1}{6}\vec{b}_i(t)\delta t^3 + \dots \tag{3.28}$$

The truncation of this expansion at low-order derivatives introduces a numerical error in long-time evolution that makes the simulation non-time reversible, so it would not resemble real system dynamics. There are several finite-difference methods, and several aspects need to be considered, such as computational expense, accuracy, stability, and energy conservation (Raabe, 2017).

The Velocity Verlet algorithm by Swope et al. (1982) is one of the most widely-used finite-difference algorithms and is the one used in this doctoral thesis; it offers simplicity, numerical stability, and adequate handling of velocities (Allen & Tildesley, 2017). In the Velocity Verlet algorithm, positions are derived from a Taylor expansion accurate to $\mathcal{O}(\delta t^3)$ (equation 3.29), and the velocity only involves a Taylor expression accurate to $\mathcal{O}(\delta t^2)$, although the velocities are transmitted in two stages that, again, involve an intermediate step.

As illustrated in Figure 3.4, the positions at $t+\delta t$ are obtained from the positions, velocities, and accelerations at current time t. The current values of $\vec{v}_i(t)$ and $\vec{a}_i(t)$ also yield the velocities at a mid-step $\frac{1}{2}\delta t$ (equation 3.30). For the new positions $\vec{r}_i(t+\delta t)$ obtained, the forces at timestep $t+\delta t$ (i.e., accelerations $\vec{a}_i(t+\delta t)$) are evaluated. The previously calculated velocity at the intermediate timestep together with the evaluated accelerations at $t+\delta t$ are used to calculate the velocity $\vec{v}_i(t+\delta t)$ (equation 3.31).

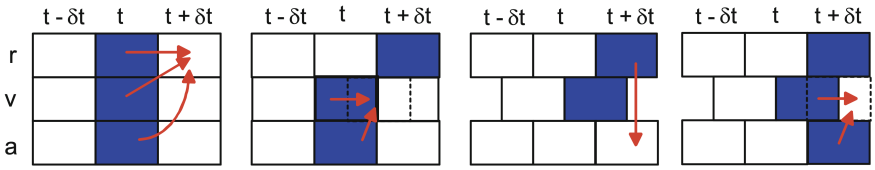

Figure 3.4: Scheme of the Velocity Verlet algorithm. Figure retrieved from Raabe (2017).

$$\vec{r}_i(t+\delta t) = \vec{r}_i(t) + \vec{v}_i(t)\delta t + \frac{1}{2}\vec{a}_i(t)\delta t^2 + \mathcal{O}(\delta t^3) \tag{3.29}$$

$$\vec{v}_i\left(t+\frac{1}{2}\delta t\right) = \vec{v}_i(t) + \frac{1}{2}\vec{a}_i(t)\delta t + \mathcal{O}(\delta t^3) \tag{3.30}$$

$$\vec{v}_i(t+\delta t) = \vec{v}_i\left(t+\frac{1}{2}\delta t\right) + \frac{1}{2}\vec{a}_i(t+\delta t)\delta t + \mathcal{O}(\delta t^2) \tag{3.31}$$

3.2.4 Heat capacity calculation from equilibrium molecular dynamics simulations

In a nutshell, there are two different ways to calculate the heat capacities of a system (C_v or C_p) with MD . In the first one, one can employ the thermodynamic C_v or C_p definition shown in equations 3.32 and 3.33. This first method assumes that the heat capacity grows linearly in small temperature variations, so one needs to build at least three simulations with the same number of molecules, N, but different temperatures (e.g., $\Delta T \approx 3.5$ K between each simulation), while keeping V (for C_p) or P (for C_v) constant. Then, from the slope obtained in plotting E vs T or H vs T, the C_v or C_p values can be extracted. It is recommended to try at least 5 points to ensure that the heat capacity grows linearly with temperature. A visual summary of the process required to calculate the heat capacity is summarized in Figure 3.5.

$$C_v = \left(\frac{\partial E}{\partial T}\right)_{NV} \tag{3.32}$$

$$C_p = \left(\frac{\partial H}{\partial T}\right)_{NP} = \left(\frac{\partial E}{\partial T}\right)_{NP} + P\left(\frac{\partial V}{\partial T}\right) \tag{3.33}$$

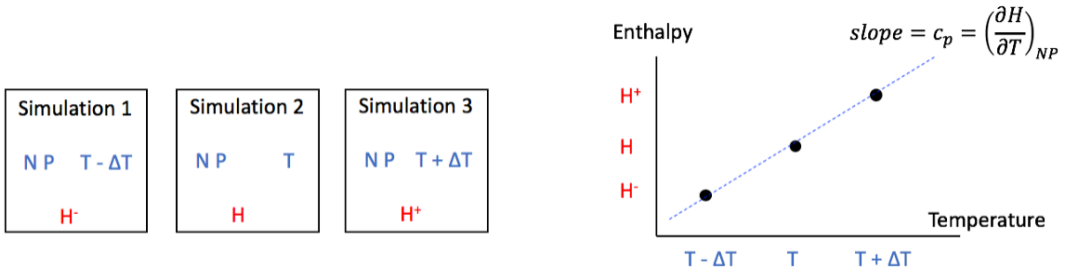

Figure 3.5: Visual scheme on how to calculate the C_p via equation 3.33. Blue magnitudes are simulation inputs, while red magnitudes are simulation outputs.

The second method obtains the C_v and C_p through energy fluctuations in the NPT or the NVT ensamble, as shown in equations 3.34 and 3.35. First, one has to equilibrate the system to the desired temperature, pressure, and density conditions and then extract the average values $\langle E^2 \rangle$ and $\langle E \rangle$ for C_v and $\langle E^2 \rangle$, $\langle E \rangle$, $\langle V \rangle$, $\langle EV \rangle$, and $\langle V^2 \rangle$ for C_p.

$$C_v = \frac{1}{k_B T^2}\left[\left(\langle E^2 \rangle - \langle E \rangle^2\right)\right]_{NVT} \tag{3.34}$$

$$C_p = \frac{1}{k_B T^2}\left[\left(\langle E^2 \rangle - \langle E \rangle^2\right) + 2P\left(\langle EV \rangle - \langle E \rangle \langle V \rangle\right) + P^2\left(\langle V^2 \rangle - \langle V \rangle^2\right)\right]_{NPT} \tag{3.35}$$

In their work, W. R. Smith et al. (2017) explained the differences between using each of the two calculation methods with both rigid and flexible molecules. The first conclusion they drew is that the second method gives higher deviations than the first method when obtaining heat capacities, so it is recommended to stick to the first method whenever possible. Then, they also explained that equations 3.32-3.35 are formally wrong and should only work with rigid or monoatomic fluids, but not for a general polyatomic flexible fluid. The reason can be seen when developing these equations from the partition functions of the system.

The complete expressions that should be used to calculate the heat capacities of a general, flexible polyatomic fluid are:

$$\begin{aligned} C_v &= \left(\frac{\partial E_{\text{tot}}}{\partial T}\right)_{NV} = \left(\frac{\partial E_{\text{ID}}}{\partial T}\right)_{NV} + \left(\frac{\partial U_{\text{ext}}}{\partial T}\right)_{NV} + \left(\frac{\partial U_{\text{int}}}{\partial T}\right)_{NV} - \left(\frac{\partial U_{\text{int,ID}}}{\partial T}\right)_{NV} \\ &= C_v^{\text{ID}} + C_v^{\text{res}} - C_v^{\text{bond,ID}} \end{aligned} \tag{3.36}$$

$$\begin{aligned} C_p &= \left(\frac{\partial H_{\text{tot}}}{\partial T}\right)_{NP} = \left(\frac{\partial U_{\text{ID}}}{\partial T}\right)_{NP} + \left(\frac{\partial U_{\text{ext}}}{\partial T}\right)_{NP} + \left(\frac{\partial U_{\text{int}}}{\partial T}\right)_{NP} - \left(\frac{\partial U_{\text{int,ID}}}{\partial T}\right)_{NV} \\ &- R + P\left(\frac{\partial V}{\partial T}\right) = \left(C_v^{\text{ID}} + R\right) + C_p^{\text{res}} - C_p^{\text{int,res}} - \left(C_v^{\text{int,ID}} + R\right) \end{aligned} \tag{3.37}$$

Where U_{ext} and U_{int} are the intermolecular and intramolecular potential energies (not to be confused with the (total) internal energy of the molecule, E_{tot}).

However, equations 3.36 and 3.37 imply to get somehow the ideal heat capacity, then running a set of MD simulations (3-5) to get the appropriate $\left(\frac{\partial E}{\partial T}\right)$ contributions and calculate the $U_{\text{int,ID}}$ term in another simulation. Since this is generally a complex process, one can assume that the vibrational contribution from an ideal gas will not be very different from the residual vibrational contribution (giving $C_p^{\text{int,res}} = C_v^{\text{int,ID}}$). With this handy approximation, equations 3.36 and 3.37 become the much simpler equations 3.38 and 3.39:

$$C_v = \left(\frac{\partial E_{\text{tot}}}{\partial T}\right)_{NV} \approx \left(\frac{\partial E_{\text{ID}}}{\partial T}\right)_{NV} + \left(\frac{\partial U_{\text{ext}}}{\partial T}\right)_{NV} = C_v^{\text{ID}} + C_v^{\text{res}} \tag{3.38}$$

$$C_v = \left(\frac{\partial H_{\text{tot}}}{\partial T}\right)_{NP} \approx \left(\frac{\partial E_{\text{ID}}}{\partial T}\right)_{NP} + \left(\frac{\partial U_{\text{ext}}}{\partial T}\right)_{NP} + P\left(\frac{\partial V}{\partial T}\right) = C_v^{\text{ID}} + C_p^{\text{res}} \tag{3.39}$$

This means that a relatively simple way to calculate the heat capacity of a fluid is to calculate the intermolecular $\left(\frac{\partial U_{\text{ext}}}{\partial T}\right)$ derivative at NVT or NPT to obtain the residual heat capacity and add that to the ideal heat capacity term.

3.2.5 Viscosity calculation from equilibrium molecular dynamics simulations

There are several methods to compute transport properties in MD simulations. In a practical approach, due to its simplicity, the Green-Kubo (GK) relations (Kubo, 1957) based on equilibrium molecular dynamics (MD) simulations is perhaps the most widely used method (Allen & Tildesley, 2017). In short, the GK approach relates the equilibrium fluctuations of the fluxes to the corresponding phenomenological coefficients, L_{ij} (Ungerer et al., 2007):

$$L_{ij} = \frac{V}{3k_B}\int_0^\infty \langle J_i(t)J_j(0)\rangle_{\text{eq}}\mathrm{d}t \tag{3.40}$$

Within the framework of irreversible processes, the L_{ij} can be related with transport coefficients (de Groot & Mazur, 1984). The shear viscosity is calculated from the integral over time of the pressure tensor autocorrelation function:

$$\eta = \frac{V}{k_B T}\int_0^\infty \langle P_{\alpha\beta}(t)P_{\alpha\beta}(0)\rangle \mathrm{d}t \tag{3.41}$$

Where $P_{\alpha\beta}$ denotes the off-diagonal element $\alpha\beta$ of the pressure tensor, and the angle bracket indicates the ensemble average.

In the long time limit, the pressure tensor autocorrelation function decays to zero, and the integral in equation 3.41 eventually reaches a constant value corresponding to the predicted shear viscosity. In practice, however, due to the accumulation of noise at long times, (Hess, 2001; Rey-Castro & Vega, 2006) the integral does not necessarily converge to a constant value, but it instead fluctuates at long times.

In 2015, Y. Zhang et al. (2015) introduced a time decomposition method for the calculation of shear viscosity that provides an objective way of computing shear viscosity from MD trajectories (the shear viscosity is estimated from a finite time plateau region of the integral, but the plateau region can be difficult to identify). Additionally, the proposed implementation reduces the uncertainty caused by the long-term noise of the pressure tensor autocorrelation function. This methodology has been used in this work to compute the shear viscosity from Equilibrium MD simulations. The reader is referred to the entire contribution for additional details as only the main steps are explained below:

1. Generate N independent NVT trajectories at a given temperature;

2. Calculate the shear viscosity trough equation 3.41;

3. Calculate the average of the running integrals over N trajectories $\langle\eta(t)\rangle$ and the standard deviation, which is a function of time:

$$\sigma(t) = \sqrt{\frac{1}{N-1}\sum_{i=1}^{N}\left(\eta(t)_i - \langle\eta(t)\rangle\right)^2} \tag{3.42}$$

4. Fit the standard deviation to a power law function

$$\sigma(t) = At^b \tag{3.43}$$

5. Fit the averaged running integral by the double-exponential function (equation 3.44) for the time period up to t_{cut} with the weight $1/t^b$, where b is the fitting result from step 4 and t_{cut} can be decided from the relation between η and $\sigma(t)$. The authors found that the time when $\sigma(t)$ is about 40% of $\langle\eta(t)\rangle$ is a good choice. Take the long time limit of the fitted double-exponential function as the calculated viscosity;

$$\sigma(t) = A\alpha\tau_1(1-\exp(-t/\tau_1)) + A(1-\alpha)\tau_2(1-\exp(-t/\tau_2) \tag{3.44}$$

   where A, α, τ_1, and τ_2 are fitting parameters. To reduce the noise at long times, Rey-Castro and Vega (2006) applied a weighting factor of $1/t^2$ in the fitting.

6. Increase N and repeat steps 1-5 until the change in the calculated viscosity in step 5 is smaller than a tolerance. This doctoral thesis uses $N = 30$ for pure compounds and $N = 60$ for binary and ternary blends.

3.3 Mesoscopic (coarse-grained) scale: SAFT equation of state

An Equation of State (EoS) is a thermodynamic equation that relates state variables such as pressure (P), volume (V), temperature (T), and internal energy (E) for a pure homogeneous fluid in equilibrium states. This is expressed analytically by means of $f(P, V, T, E) = 0$. As an example, the simplest EoS is the ideal gas law:

$$PV = nRT \tag{3.45}$$

Where n is the number of gas moles, and R is the ideal gas constant. The ideal gas law can also be rewritten in terms of the Helmholtz free energy:

$$A^{\text{id}} = Nk_BT\left[\ln\left(\frac{N\Lambda^3}{V}\right) - 1\right] \tag{3.46}$$

Note that the latter expression is written in terms of the number of molecules N, the Boltzmann constant, k_B, and the De Broglie wavelength, $\Lambda = h/\sqrt{2\pi m k_B T}$.

Even so, and despite many real gases behave qualitatively like an ideal gas under various temperature and pressure conditions, with the gas molecules (or atoms in the case of monoatomic gases) acting as the ideal particles when intermolecular interactions and molecular size become significant at lower temperatures or greater pressures, the model frequently fails. Also, it deviates for most heavy gases, including many refrigerants (Çengel, 2018) and gases with strong intermolecular forces.

Despite being very accurate and valuable tools, EoSs still depict molecules as spheres moving through an attractive mean field, which leads to some drawbacks when describing the behavior of more complex fluids, especially those with strong directional interactions or very large chains.

In the cubic EoS framework, this is usually overcome by fitting additional parameters to make more flexible the equation, such as temperature-dependent parameters (e.g., acentric factor in the Soave-Redlich-Kwong equation); however, these parameters are not related to an explicit intermolecular potential and limit the transferability and predictability of the equation, and are sometimes inaccurate to calculate liquid molecular volumes.

The Statistical Association Fluid Theory (SAFT) is a family of molecular-based equations of state built under Wertheim's 1st order thermodynamic perturbation theory (TPT1) that considers strong directional interactions and formations of chains as perturbations of the system (W. G. Chapman et al., 1989; W. G. Chapman et al., 1990). SAFT equations rely on a solid statistical mechanics basis, allowing a physical interpretation of the system. Indeed, the effects of molecular shape and interactions on the thermodynamic properties can be separated and quantified.

3.3.1 Wertheim's theory of association

In a nutshell, association in fluids implies the existence of strong and highly directive molecular interactions, such as hydrogen bonding and charge transfer, which lead to the formation of molecular clusters. This phenomenon has an important weight in the computation of thermodynamic properties and is responsible for significant deviations from ideality.

Several attempts to understand the behavior of associating fluids have evolved from chemical theory (Dolezalek, 1908) and statistical mechanics (Abrams & Prausnitz, 1975; Guggenheim, 1952; Wilson, 1964). One of the first statistical mechanical theories was developed by Andersen (Andersen, 1973; 1974), who was one of the first to introduce the geometry of the interaction in an early stage of the theory for the description of highly directional hydrogen bonds. Andersen developed the ideas of physical clusters and proposed a cluster expansion

in terms of two densities: the overall density and a density weighted by the strength of the hydrogen bond. The nature of the attractive sites of this model restricts the system to single bonds at each site, so many diagrams in the cluster expansion were negligible. Still, graph cancellation due to steric effects is unwieldy and inefficient. Although thermodynamic properties could not be calculated from this method, his work inspired later theories for associating fluids (Chandler & Pratt, 1976; HØye & Olaussen, 1980), including the work of Wertheim, which is the basis of the SAFT.

In Wertheim's theory (Wertheim, 1984a; 1984b), molecules are treated as different species according to the number of associated sites. He postulated that graph cancellation due to steric effects is more straightforward and more effective using the fugacity expansion in terms of two densities: the equilibrium monomer density and the overall number density. He also assumed that steric effects due to the repulsive core of each molecule restrict the formation of a single bond at each attractive site. The key final result of Wertheim's work is a final expression written as a first-order thermodynamic perturbation theory (TPT1) that establishes a relation between the change in residual Helmholtz free energy due to association and the monomer density.

Wertheim extended his theory, initially developed for hard-core molecules with one attractive site, to systems with multiple bonding sites per molecule Wertheim (1986a), 1986b. Later, W. G. Chapman et al. (1986) and Joslin et al. (1987) extended Wertheim's theory to binary mixtures of components A and B where only AB dimers could be formed.

Wertheim's theory considers that the intermolecular potential has a short-range highly directional component that causes the formation of associated species but does not specify any particular intermolecular potential, being necessary to specify one at the time of implementing the theory. The most straightforward approach is to employ the hard-sphere model as a reference fluid because its EoS and pair distribution functions are known and have accurate analytical expressions. W. G. Chapman et al. (1988) employed the hard-sphere model as a reference fluid and obtained an EoS by imposing the condition of total bonding (i.e., zero nonbonded segments) and establishing the correct stoichiometry of segments with bonding sites (i.e., to form a chain from m segments of the same diameter, a stoichiometric ratio of m segments with either one or two association sites is required). This work can be considered the birth of the SAFT.

The derivation of Wertheim's TPT1 involves some approximations which must be taken into account when using the theory:

- The theory assumes a tree-like cluster structure with no closed loops.
- Only one single bond is allowed at each associating site. It implies that (see Figure 3.6):
  - The repulsive cores of two bonded molecules prevent a third molecule from coming close enough to bond to any of the occupied sites.

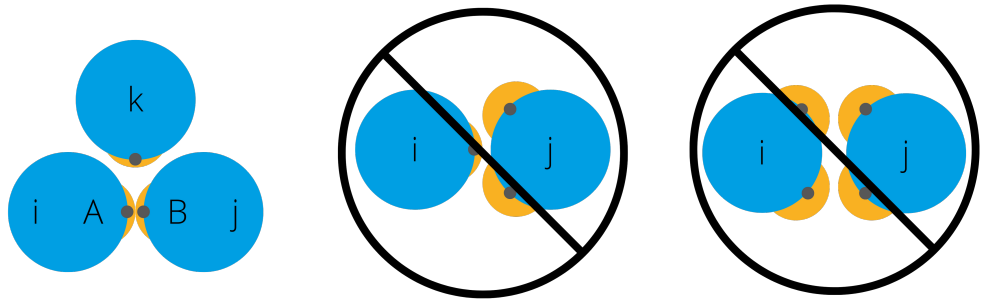

Figure 3.6: Model approximations representing types of steric incompatibility: The repulsive cores of the molecules prevent more than two molecules from bonding at a single site (left). No site on one molecule can bond simultaneously with two sites on another molecule (center). Double bonding between molecules is not allowed (right). Figure adapted from W. G. Chapman et al. (1990).

  - No site on a molecule can bond simultaneously to two sites on another molecule.
  - No double bonds are allowed.

- The activity of a site is independent of bonding at other sites in the same molecule (i.e., sites on a molecule are independent from each other). Therefore, terms involving the repulsion between two molecules trying to join at two sites on a third one are neglected.
- Angles between bonding sites are not defined, only the distance from the center of the repulsive core and the short-range interaction potential of the bonding site.

3.3.2 Soft-SAFT equation of state

As described in the previous section, Wertheim provided a relationship between the residual Helmholtz free energy in a series of integrals of molecular distribution functions and the association potential. SAFT EoS is usually written in terms of the residual Helmholtz free energy as a sum of different microscopic contributions to the total free energy of the fluid (Figure 3.7):

$$A = A^{\text{id}} + A^{\text{res}} = A^{\text{id}} + A^{\text{ref}} + A^{\text{chain}} + A^{\text{assoc}} \tag{3.47}$$

Where A^{res} and A^{id} are the residual and ideal Helmholtz free energy of the system, the latter one already presented in equation 3.46. The rest of the terms of equation 3.47 are explained below. The different contributions depend on several molecular parameters to define the molecular model for each compound. In the original SAFT equation, a total of five molecular parameters are needed. Those are the number of spherical segments forming each molecule, m, the diameter of the segments, σ, and their disperse energy, ε. The association contribution, A^{assoc}, adds the volume, $k_{ij}^{\alpha\beta}$, and energy, $\varepsilon_{ij}^{\alpha\beta}$ of association between a site α on specie i and a site β on j.

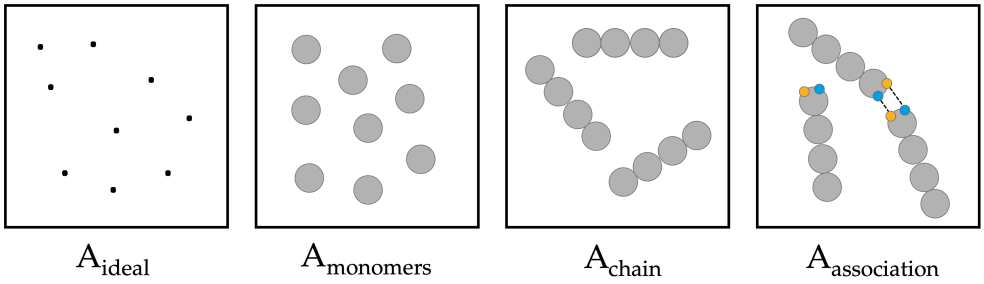

Figure 3.7: Representation of the energy terms in SAFT-based EoS. The grey beads denote molecular segments, the dotted lines represent intermolecular interactions, and the orange and blue dots model two different associative sites in the SAFT framework.

In this thesis, the soft-SAFT version of the original SAFT EoS is used as a modeling tool. Soft-SAFT is based on a reference LJ intermolecular potential and was presented in 1997 by Blas and Vega (1997). Using a soft potential as opposed to a hard (repulsive) potential as a reference simplifies the overall approach since both repulsive and discursive contributions are taken into account simultaneously. The main differences between the original SAFT contribution and the soft-SAFT version are explained below.

A^{ref} refers to the residual Helmholtz free energy of nonassociated spherical segments, which is not specified within SAFT. The original SAFT of Chapman et al. (W. G. Chapman et al., 1990; W. G. Chapman et al., 1988) uses a perturbation expansion using a hard-sphere as a reference term and a dispersion term as a perturbation, while as mentioned above, soft-SAFT uses a LJ intermolecular potential to describe the interactions among the molecules in the reference term. At this point is important to note that each term contribution to the total residual Helmholtz free energy must be expressed in terms of composition for mixture studies. Unlike the rest of the contributions, the reference term is written for a pure compound. In order to deal with multicomponent mixtures, each compound having a different number of segments with different sizes or dispersive energies, "averaged" values should be taken into account to create a pseudo-binary with the same thermodynamic values of the mixtures. This is done by means of mixing rules, being the van der Waals' fluid theory the most used one. The corresponding expressions for the size and energy parameters of the conformal fluid are:

$$m = \sum_{i=1}^{n} x_i m_i \tag{3.48}$$

$$\sigma^3 = \frac{\sum_i \sum_j x_i x_j m_i m_j \sigma_{ij}^3}{\left(\sum_i x_i m_i\right)^2} \tag{3.49}$$

$$\varepsilon\sigma^3 = \frac{\sum_i \sum_j x_i x_j m_i m_j \varepsilon_{ij} \sigma_{ij}^3}{\left(\sum_i x_i m_i\right)^2} \tag{3.50}$$

Where x_i is the mole fraction and m_i is the chain length of each of the components of the mixture, denoted by the indexes i and j. σ_{ij} and ε_{ij} are the crossed interaction parameters and are calculated using the Lorentz-Berthelot combination rules:

$$\sigma ij = \eta_{ij} \frac{\sigma_{ii} + \sigma jj}{2} \tag{3.51}$$

$$\varepsilon_{ij} = \xi_{ij} \sqrt{\varepsilon_{ii}, \varepsilon_{jj}} \tag{3.52}$$

Where η_{ij} and ξ_{ij} are the adjustable binary parameters that modify the arithmetic and geometric averages, respectively.

A^{chain} is the Helmholtz free energy due to the formation of chains from m_i spherical monomers:

$$A^{\text{chain}} = RT \sum_i x_i (1 - m_i) \ln g_R(\sigma) \tag{3.53}$$

Where g_R is the pair correlation function of the reference fluid for the interaction of two segments in a mixture of segments, evaluated at the segment contact σ. Again, the original SAFT uses the radial distribution function (or pair correlation function) of hard spheres, while soft-SAFt uses a radial distribution function of a LJ fluid.

The association term, A^{assoc} depends on the number of association sites of each component, M_i, and the fraction of molecules not bonded to the site α, X_α. A molecule can have one or more associating sites, but even if the theory allows an infinite number of sites, more than four seem, in practice, quite unrealistic for a molecule.

$$A^{\text{assoc}} = RT \sum_i x_i \sum_\alpha \left(\ln X_{\alpha_i} - \frac{X_{\alpha_i}}{2} + \frac{M_i}{2} \right) \tag{3.54}$$

To calculate X_{α_i}, one needs to adjust two parameters for each hydrogen bonding: the site-site bonding volume of association $K^{HB}_{\alpha\beta_{ii}}$, and the site-site association energy $\varepsilon^{HB}_{\alpha\beta_{jj}}$, which are related to X_{α_i} through a mass action balance (equations 3.55 and 3.56)

$$X_i^\alpha = \frac{1}{1 + N_a \rho \sum_j x_j \sum_\beta x_j^\beta \Delta^{\alpha_i \beta_j}} \tag{3.55}$$

Where $\Delta^{\alpha_i \beta_j}$ is the association strenght between site α on molecule i and site β on molecule j, and is defined as:

$$\Delta^{\alpha_i\beta_j} = K^{HB}_{\alpha\beta_{ij}} \left[\exp\left(\varepsilon^{HB}_{\alpha\beta_{ij}}/k_BT\right) - 1\right] g_{ij} \tag{3.56}$$

The cross-association interaction for the site-site bonding volume and association energy can be obtained by means of equivalent Lorenth-Berthelot combining rules without the addition of binary parameters:

$$K^{HB}_{\alpha\beta_{ij}} = \left(\frac{\sqrt[3]{K^{HB}_{\alpha\beta_{ii}}} + \sqrt[3]{K^{HB}_{\alpha\beta_{jj}}}}{2}\right)^3 \tag{3.57}$$

$$\varepsilon^{HB}_{\alpha\beta_{ij}} = \sqrt{\varepsilon^{HB}_{\alpha\beta_{ii}} \cdot \varepsilon^{HB}_{\alpha\beta_{jj}}} \tag{3.58}$$

Soft-SAFT considers an additional A^{polar} term to equation 3.47 for the explicit consideration and accurate modeling of polar forces such as dipolar forces. The polar contribution to the residual Helmholtz energy is based on the multipolar expression of Twu and Gubbins (Gubbins & Twu, 1978; Twu & Gubbins, 1978) for spherical molecules written as the Padé approximation of Stell et al. (1972):

$$A^{\text{polar}} \approx \frac{a_2}{1 - \frac{a_3}{a_2}} \tag{3.59}$$

Where a_2 and a_3 are the second and third-order terms in the perturbation expansion terms, respectively, and are related to two and three-body interactions.

$$a_2^{\text{polar}} = a_2^{\text{D}} + 2a_2^{\text{cross}} + a_2^{\text{Q}} \tag{3.60}$$

$$a_3^{\text{polar}} = a_{3\text{A}}^{\text{polar}} + a_{3\text{B}}^{\text{polar}} \tag{3.61}$$

$$a_{3\text{A}}^{\text{polar}} = 3a_{3\text{A}}^{\text{cross}_1} + 6a_{3\text{A}}^{\text{cross}_2} + 6a_{3\text{A}}^{\text{cross}_3} + 3a_{3\text{A}}^{\text{Q}} \tag{3.62}$$

$$a_{3\text{B}}^{\text{polar}} = 3a_{3\text{B}}^{\text{D}} + 3a_{3\text{B}}^{\text{cross}_2} + 3a_{3\text{B}}^{\text{cross}_3} + a_{3\text{B}}^{\text{Q}} \tag{3.63}$$

Where a_2^{D} and $a_{3\text{B}}^{\text{D}}$ refer to the second and third-order perturbation terms for dipole-dipole interactions, a_2^{Q} and $a_{3\text{A}}^{\text{Q}}$ and $a_{3\text{B}}^{\text{Q}}$ refer to the perturbation terms for quadrupolar–quadrupolar interactions, while the rest of the terms are those for all possible cross-polar interactions such as dipolar–quadrupolar interactions (Alkhatib et al., 2020). The reader is referred to the original contribution for further details about the expressions. In this work, a_2 and a_3 are taken from the interpolation equations over pair- and triplet-correlation functions of a LJ fluid proposed by Luckas et al. (1986). The application of the polar term to chain molecules is made

using the segment approach of Jog et al. (2001), which assumes that polar moments are located on certain segments of the chain molecules and oriented perpendicular to the moment axis. In turn, each polar moment is associated with two additional molecular parameters: the fraction of polar segments x_p and the dipole moment μ.

3.3.3 Density gradient theory

Although accurate techniques are available for determining phase equilibria, interfacial estimates are rare. To some extent, this is attributable to the inhomogeneous nature of the liquid-vapor interfacial system. Taking apart direct molecular simulations, which are capable of predicting the interfacial behavior of a system (at a high computational cost), most theoretical approaches can be categorized under the term of density functional theories (DFTs) (Henderson, 1992).

One of the most versatile approaches from this group is the density gradient theory (DGT) obtained from the work of Cahn and Hilliard (Cahn & Hilliard, 1958), originating from the theory of van der Waals for inhomogeneous fluids (van der Waals, 1894). In this theory, the free energy of a homogeneous theory is evaluated for every local density value and extended by means of a term with a squared gradient of the density profile. The total free energy is the integral of the sum of the two contributions and has to be minimized with respect to all possible density distributions (Duque et al., 2004).

The expression for the Helmholtz free energy is expanded in a Taylor series around $a_0(\rho)$, the free energy density term of the homogeneous fluid at the local density, and truncated after the second order term. This series may not converge, but because of the short range of the intermolecular potential, it is assumed to have at least an asymptotic validity (Bongiorno & Davis, 1975):

$$A = \int \left[a_0(\rho) + \sum_i \sum_j \frac{1}{2} c_{ij} \nabla_{\rho_i} \nabla_{\rho_j} \right] \mathrm{d}^3 r \tag{3.64}$$

where ∇_{ρ_x} is the local gradient in the density of a component $x = i, j$. An influence parameter c_{ij} is defined, which is treated phenomenologically as a parameter fitted to experimental surface tension data.

For a planar interface, and assuming that the density dependence of the influence parameter can be neglected, functional minimization of equation 3.64 for phase coexistence conditions leads to the following expression for the surface tension:

$$\gamma = \sum_i \sum_j \int_{-\infty}^{\infty} c_{ij} \frac{\mathrm{d}\rho_i}{\mathrm{d}z} \frac{\mathrm{d}\rho_j}{\mathrm{d}z} = 2 \int_{-\infty}^{\infty} \left[a_0(\rho) - \sum_i \rho_i \mu_{0i} - P_0 \right] \mathrm{d}z \tag{3.65}$$

where μ_{0i} and P_0 are the equilibrium chemical potential and pressure, respectively, and z is the direction perpendicular to the interface. For additional details on the implementation of the theory, the reader is referred to the works of Duque et al. (2004), Mejía and Segura (2004), and Vilaseca et al. (2010).

3.3.4 Viscosity calculation with soft-SAFT: free-volume theory

There are a variety of methods in the literature for describing the viscosity of fluids, ranging from purely empirical methods, which are only applicable to the specific range of the experimental data, to theoretical models (Monnery et al., 1995; Reid et al., 1987; Viswanath et al., 2007). The free-volume theory (FVT) (Allal, Boned, et al., 2001; Allal, Moha-ouchane, et al., 2001) is one of these theoretical models that have been widely employed in the literature, obtaining good agreement with experimental data (Allal, Boned, et al., 2001; Comuñas et al., 2004; Reghem et al., 2005; Zéberg-Mikkelsen et al., 2003). As it will be seen later in this subsection, the FVT requires the density of the fluid as input data, so the coupling of sophisticated equations of state with the FVT is a good approach (Llovell et al., 2013a; 2013b) and it has been the methodology followed in this thesis to calculate viscosity with soft-SAFT EoS.

The original theory was developed by Allal, Boned, et al. (2001) and later extended (Allal, Moha-ouchane, et al., 2001) to low-density fluids as the former work was only applicable to dense fluids.

In essence, the FVT relates the viscosity to the molecular structure of the fluids and divides the contribution to the viscosity into a diluted gas (ideal) term, η_0, and a dense liquid term $(\Delta\eta)$.

$$\eta = \eta_0 + \Delta\eta \tag{3.66}$$

The dilute term describes the viscosity of a fluid in a gaseous state (or with very low density). The modified equation of Chung et al. (1988) to the original kinetic theory of S. Chapman and Cowling (1990) is used here and reads:

$$\eta_0 = 40.785 \times 10^{-2} \frac{\sqrt{M_w T}}{V_c^{3/2} \Omega^*(T^*)} F_c \tag{3.67}$$

where the dimensionless temperature, $T^* = 1.2593 \times T_r$, being T_r the reduced temperature with respect to the critical temperature of the compound. F_c is the corrected factor

introduced by Chung et al. (1988) (equation 3.68) to encompass the effects of chain bonding, hydrogen bonding, and polarity to the original kinetic theory of Chapman-Eskong, and Ω^* is the reduced collision integral which depends on the intermolecular potential chosen and is a complex function of the temperature. Neufeld et al. (1972) determined the collision integral for the LJ potential, used in the soft-SAFT framework, and came up with an empirical correlated expression (equation 3.69).

$$F_C = 1 - 0.2756\omega - 0.059035 \tag{3.68}$$

$$\begin{aligned}\Omega(2;2) = &\frac{1.16145}{T^{*0.14874}} + \frac{0.52487}{\exp\left(0.77320 \cdot T^*\right)} + \frac{2.16178}{\exp\left(2.43787 \cdot T^*\right)} \\ &- 6.435 \times 10^{-4} \cdot T^{*0.14874} \times \sin\left(18.0323 \cdot T^{*-0.76830} - 7.27371\right)\end{aligned} \tag{3.69}$$

The dense-state term comes from linking two different ideas: from one side, the viscosity is believed to be connected to the microstructure of the fluid, considering its density and friction due to fluid mobility. Conversely, the viscosity is assumed to be related to the empty space (or free volume) between molecules through an exponential relation according to the behavior observed experimentally (Cohen & Turnbull, 1959; Hogenboom et al., 1967). From the combination of both ideas, the dense term reads:

$$\Delta\eta = L_v\left(0.1P + 10^{-4}\alpha\rho^2 M_w\right)\sqrt{\frac{10^{-3}M_w}{3RT}}\exp\left[B\left(\frac{10^3 P + \alpha\rho^2 M_W}{\rho RT}\right)^{3/2}\right] \tag{3.70}$$

where the adjustable parameters are L_v, a length parameter related to the structure of the molecules, α, the proportionality between the energy barrier and the density, and B, which corresponds to the free-volume overlap. Note that the final expression (equation 3.70) links the molecular structure to a representation of the free-volume fraction, and this fraction to the intermolecular energy that controls the potential field in which molecular diffusion occurs (Allal, Moha-ouchane, et al., 2001).

3.4 Computational tools to design separation processes

3.4.1 Process simulators: Aspen Plus

Process simulators can be used not only to develop new processes based on ILs but also to reduce experimental tests by selecting the IL based on its performance in the process. In this

way, process simulation can be used to evaluate the actual feasibility of a process, the unit operations design, the entire process costs, and further optimization of the process.

Among commercial process simulators, Aspen Plus, Aspen HYSYS, SuperPro Designer, or DWSIM are broadly used. In this Ph.D. thesis, Aspen Plus has been used to that end. Aspen[1] Plus allows predicting the behavior of a process using basic engineering relationships. A physical process can be described with a set of linearly independent algebraic or differential equations. The number of equations written must be equal to the number of variables, or unknown quantities, and the physical process is said to be specified or described by an equivalent mathematical model. In general, these equations come from (Al-Malah, 2017):

- Balance equations of extensive thermodynamic properties, such as mass, mole, and energy.
- Thermodynamic relationships for reacting and non-reacting medium, such as phase and chemical equilibrium.
- Rate correlations for momentum, heat, and mass transfer.
- Reaction stoichiometry and kinetic data.
- Physical constraints imposed on the process.

The stages required to convert a process into an Aspen Plus process simulation model are as follows:

1. Specify the chemical components in the process. These can be fetched from Aspen plus databanks or manually introduced.
2. Specify the thermodynamic model to calculate the physicochemical properties of the previously introduced compounds.
3. Define the process flowsheet, including:
    - Unit operations
    - Process streams
    - Models to describe each unit operation
4. Specify the component flow rates and process conditions (temperature, pressure, and composition) of all feed streams.
5. Specify the operating conditions for the unit operation models.

[1] Aspen is an acronym of **A**dvanced **S**ystem for **P**rocess **EN**gineering

One of the key and most important decisions is the selection of the property method. A property method calculates thermodynamic, kinetic, and transport properties. The thermodynamic method, a subset of the property method, can be roughly classified as i) an activity coefficient base method or ii) an equation of state method.

The activity coefficient method is mainly described for subcritical and non-ideal liquid systems at pressures below $10\ \mathrm{bar}$ and has been the one implemented for process simulations in this doctoral thesis. The parameters within the model are temperature-dependent, so the model is problematic in regions near the critical point.

In a practical implementation, the non-ideal liquid mixture is described through the concept of fugacity of species i in a mixture:

$$f_i^L = x_i \cdot \gamma_i \cdot f_i^0 \tag{3.71}$$

Being f_i the fugacity of species i in a mixture at a given pressure, temperature, and composition, x_i the mole fraction of species i in a mixture, γ_i the activity coefficient of species i in a solution at a given pressure, temperature, and composition, and f_i^0 the fugacity of pure liquid species i at a given pressure temperature and composition.

Equation 3.71 can be simplified for an ideal liquid mixture: the activity coefficient is reduced to unity, and the fugacity of the pure compound is taken as the vapor pressure of substance i:

$$f_i^L = x_i \cdot P_{\text{sat},i}(T) \tag{3.72}$$

Similarly, the gas-phase fugacity is defined as in equation 3.73, and for low pressures, the fugacity coefficient of species i, φ_i, reduces to one.

$$f_i^V = \varphi_i \cdot \gamma_i \cdot P \tag{3.73}$$

There are several widely-used activity coefficient-based methods, like NRTL (Non-Random Two-Liquid), UNIFAC (UNIversal Functional Activity Coefficient), or UNIQUAC (UNIversal QUasichemical Activity Coefficient).

Due to the non-complexity of the species that make up the study mixtures of this thesis and the scarce number of experimental data that would be used to fit a model like the ones beforementioned, in this work, an activity-coefficient model based on COSMO-RS calculations has been chosen to model the absorption of fluorinated gases in ILs.

Due to the negligible vapor pressure that ILs present, the binary VLE equilibrium can be simplified as in equation 3.74 taking into account the vapor pressure of the pure solute (P^0_{sat}) and the activity coefficient of the solute (γ_i) in the mixture at composition x_i.

$$P_{\text{tot}} = P^0_{\text{sat}} \cdot x_S \cdot \gamma_S \tag{3.74}$$

The vapor pressure of the pure solute (i.e., HFC) is known and usually implemented by means of an extended Antoine's equation adjusted to experimental data in the property definition environment of Aspen Plus (named PLXANT, equation 3.80).

In Aspen Plus, COSMO is implemented in Lin and Sandler's variation of the original COSMO-RS published by Klamt in 1995 (Klamt, 1995), named COSMO-SAC (where SAC denotes segment activity coefficient) (S.-T. Lin & Sandler, 2002) as a liquid activity coefficient model. Two other different versions are available using the option codes in the Aspen Plus interface: the COSMO-RS model by Klamt and Eckert and the modification in the exchange energy of the original Lin and Sandler model (S. T. Lin et al., 2002). In this work, the original COSMO-RS model has been used in this thesis as other authors recommend (Sosa et al., 2020) since it presents the lowest deviations from experimental data.

As previously noted, individual atoms, rather than functional groups, are used as building blocks in this activity-coefficient model, increasing the range of applicability without relying on experimental evidence for binary interaction parameters. This particular feature makes the COSMO-SAC method especially attractive for cases where the species are not defined in the simulator database, such as the ILs used in this section. It is important to highlight at this point that the methodology is entirely predictive, and no binary vapor-liquid data is required to adjust the activity coefficient parameters. The procedure followed here is similar to that used by Palomar and coworkers, who have successfully simulated different separation processes using ILs (Abranches et al., 2019; Ferro et al., 2012; Larriba et al., 2018; Santiago et al., 2018; Sosa et al., 2020).

The thermodynamic model requires rather complex quantum mechanical calculations for each component. This includes the COSMO volume, CSACVL in Aspen, as well as its charge distribution σ-profile, which may store up to 12 sigma profile points. The liquid activity coefficient is obtained as:

$$\ln \gamma_i = \frac{A_i}{a_{\text{eff}}} \sum_{\sigma_m} p_i(\sigma_m)[\ln \Gamma_s(\sigma_m) - \ln \Gamma_i(\sigma_m)] + \ln \gamma_i^{\text{SG}} \tag{3.75}$$

Where A_i is the molecular surface of component i, γ_i^{SG} is the Staverman-Guggenheim model for combinatorial contribution to γ_i, and the rest of the parameters have already been defined.

Regarding the component type, there are six major classes that can be dealt with in Aspen Plus (Al-Malah, 2017):

1. Conventional compounds: single species fluids (vapor or liquid). Typical components that may participate in VLE.
2. Solid: single species solids.
3. Non-conventional: solids that are not pure chemical species.
4. Pseudocomponents: components not included as conventional compounds which can be characterized using boiling point, molecular weight, specific gravity, and other properties.
5. Polymer: components used in polymer models.
6. Hypothetical liquid: a type of component mainly used in pyrometallurgical applications when modeling a component as a liquid when its properties should be extrapolated from solid properties.

HFCs are included in Aspen databases, so they are introduced as conventional compounds in the properties environment of Aspen Plus, whereas the ILs are introduced as pseudocomponents. To do so, molecular weight, normal boiling point (NBP), and density at 60 °F need to be specified. The remaining properties required to fully specify the component are then obtained from property estimation using the API (American Petroleum Institute) procedures with Aspen's modifications.

In addition to the properties retrieved from API procedures, several scalar and temperature-dependent properties were included in the properties specification environment to make the simulation thermodynamically consistent. The scalar properties include the critical temperature, the critical pressure, the critical volume, the critical compressibility factor, and Pitzer's acentric factor. Temperature-dependent properties include liquid density (DNLDIP in Aspen's environment), liquid heat capacity (CPLPO), liquid viscosity (MULAND or MULDIP), and vapor pressure (PLXANT). This correlations are defined below trough equations 3.76-3.80:

$$\text{DNLDIP:} \quad \rho = C_1/C_2^{1+(1-T/C_3)^{C_4}} \tag{3.76}$$

$$\text{CPLPO:} \quad C_P = C_1 + C_2T + C_3T^2 + C_4T^3 + \frac{C_5}{T^2} \tag{3.77}$$

$$\text{MULAND:} \quad \ln\mu = C_1 + \frac{C_2}{T} + C_3 \ln T \tag{3.78}$$

$$\text{MULDIP:} \quad \ln \mu = C_1 + \frac{C_2}{T} + C_3 \ln T + C_4 T^{C_5} \tag{3.79}$$

$$\text{PLXANT:} \quad \ln P_{\text{sat}} = C_1 + \frac{C_2}{T + C_3} + C_4 T + C_5 \ln T + C_6 T^{C_7} \text{ for } C_8 \leq C_9 \tag{3.80}$$

3.4.2 Life cycle assessment: SimaPro

Life cycle assessment (LCA) is a tool for quantifying the environmental performance of products by considering their whole life cycle, beginning with the manufacture of raw materials and concluding with the final disposal of the products, as well as any necessary material recycling. In this doctoral thesis, the LCA has carried out with the software SimaPro (version 9.0) (PRé Sustainability B.V., 2020).

The most important applications for an LCA are (Goedkoop et al., 2016):

- Identification of improvement opportunities through identifying environmental hot spots in the life cycle of a product.
- Analysis of the contribution of the life cycle stages to the overall environmental load, usually with the objective of prioritizing.
- Improvements on products or processes.
- Comparison between products for internal or external communication, and as a basis for environmental product declarations.
- The basis for standardized metrics and the identification of Key Performance Indicators used in companies for life cycle management and decision support.

LCA provides the quantitative and scientific basis for all these activities. In recent years, life cycle thinking has played an increasingly important role in environmental policymaking. Reputable institutions such as the World Resource Institute (WRI) have adopted life cycle thinking, and a growing number of different stakeholders are feeling pressure to lessen the environmental impact of global consumption.

An LCA is carried out following the steps reported in the ISO 14040:2006 standard (International Organization for Standardization, 2006) as shown in 3.8:

1. Goal and scope definition.
2. Life cycle inventory (LCI) analysis.
3. Life cycle impact assessment (LCIA).

4. Results interpretation.

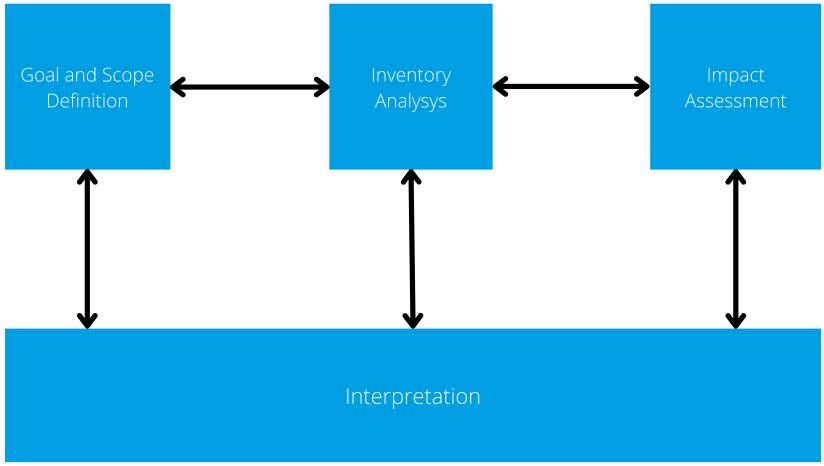

Figure 3.8: Steps of the LCA methodology according to ISO 14040.

The *goal and scope definition* of an LCA provides a description of the product system in terms of the system boundaries and a functional unit (Rebitzer et al., 2004). The functional unit is the critical basis that enables alternative goods, or services, to be compared and analyzed: the functional unit should relate to the functions of the product rather than to the physical product. For example, rather "annual lighting of a work area of 10 square meters with 30 lx" than "bulbs providing 30000 lm for one year". In this way, it is ensured that all obligatory properties – as well as the duration of the product performance – are addressed (Consequential-LCA, 2015).

LCI is a methodology for estimating the consumption of resources and the quantities of waste flows and emissions caused by or otherwise attributable to a product's life cycle (Rebitzer et al., 2004). It is the most demanding task when performing an LCA. The material and energy flows and other exchanges that happen during the life cycle of a product are modeled to show the product system and its total inputs and outputs from and to the natural environment. This results in a product system model and an inventory of environmental exchanges related to the functional unit.

SimaPro comes with the Ecoinvent 3 database (Wernet et al., 2016), covering over 10,000 processes and which has been used in this thesis for the LCI, taking into account that all the industrial processes are allocated in Spain. This database is the result of a joint effort by different Swiss institutions to update and integrate several life cycle inventory databases (Goedkoop et al., 2016).

LCIA provides indicators and a framework for analyzing the potential contributions of an inventory's resource extractions and wastes/emissions to a variety of potential consequences (Rebitzer et al., 2004). The result of the LCIA is an evaluation of a product life cycle, on

a functional unit basis, in terms of several impact categories. The LCIA performed in this thesis is carried out with the Centrum voor Millikunde Leiden (CML) methodology (Guinée et al., 1992), which has been recently suggested for studies with ILs (Maciel et al., 2019). CML is a procedure used to estimate the measure of environmental impact that is caused by the product. This method uses various impact categories, as described below. Normalization using European normalization factors (EU25) was used to convert the characterization results of all impact categories into dimensionless scores:

- *Global warming*: The characterization model as developed by the IPCC is selected to develop characterization factors. Factors are expressed as GWP for time horizon 100 years (GWP_{100}), in kg CO_2 eq./kg emission.
- *Depletion of abiotic resources*: comprises two impact categories, abiotic depletion of elements (ADP elements, ultimate reserves) and abiotic depletion of fossil fuels (ADP fossil fuels). ADP element is related to the extraction of minerals due to inputs in the system. The abiotic depletion factor (ADF) is determined for each extraction of minerals (kg antimony eq./kg extraction) based on concentration reserves and the rate of deaccumulation.
- *ADP fossil fuels* is related to the lower heating value (LHV) expressed in MJ per kg of m^3 fossil fuel. The reason for taking the LHV is that fossil fuels are considered to be fully substitutable.
- *Ozone layer depletion*: The characterization model was developed by the World Meteorological Organization (WMO) and defines the ODP of different gases (kg CFC-11 eq./kg emission).
- *Human toxicity*: expressed as human toxicity potential (HTP). It can be calculated using USES-LCA to describe the fate, exposure, and effects of toxic substances for an infinite time horizon. For each toxic substance, HTP is expressed as 1,4-dichlorobenzene eq./kg emission.
- *Freshwater aquatic ecotoxicity*: expressed as freshwater aquatic ecotoxicity potential (FAETP). The unit is 1,4-dichlorobenzene eq./kg emission. See the description of human toxicity.
- *Marine aquatic ecotoxicology*: expressed as marine aquatic ecotoxicology potential (MAETP). The unit is 1,4-dichlorobenzene eq./kg emission. See the description of human toxicity.
- *Terrestrial ecotoxicity*: expressed as terrestrial ecotoxicity potential (TETP). The unit is 1,4-dichlorobenzene eq./kg emission. See the description of human toxicity.
- *Photochemical oxidation*: Photochemical Ozone Creation Potential (POCP) for emission of substances to air is calculated with the United Nations Economic Commission for

Europe (UNECE) Trajectory model (including fate), and is expressed as kg ethylene eq. per kg emission.

- *Acidification*: Acidification Potential (AP) for emissions to air is calculated with the adapted RAINS 10 model, describing the fate and deposition of acidifying substances. AP is expressed as acidification potential (AP) with the unit kg SO_2 eq. per kg emission.
- *Eutrophication*: Eutrophication potential (EP) is based on the stoichiometric procedure of Guinée et al. (1992). EP is expressed with the unit kg $[PO_4]^{3-}$ eq. per kg emission.

4

Separation and recycling of fluorinated gases using advanced solvents

This first chapter of results aims to assess the feasibility of the selective recovery of hydrofluorocarbons from common refrigerant mixtures contained in waste refrigeration equipment using advanced solvents. To do so, the solubility of a selection of F-gases in different Ionic Liquids and Deep Eutectic solvents has been studied through the soft-SAFT EoS. Two process simulation studies are performed from the obtained results to estimate the approximate energy cost of the separation and recovery processes of R-410A and R-407F mixtures. Finally, a life cycle assessment is conducted for the separation of R-407 to compare the proposed separation processes with a direct comparison with the conventional F-gas production.

4.1 Introduction to advanced absorption processes

As widely exposed in Chapter 1, fluorinated greenhouse gas (F-gas) emissions declined for the first time between 2014 and 2015 and decreased by almost 5 percent in 2019 (European Environment Agency, 2021). This can be attributed in part to the EU-wide phase-down of hydrofluorocarbons (HFC) enforced by the F-gas Regulation (Regulation (EU) No 517/2014, 2014), which aims to limit F-gas emissions and prevent global warming. The F-Gas legislation, among other requirements, stipulates the recovery of HFCs from refrigeration and air conditioning systems and permits the continued use of *reclaimed* [1] and recycled refrigerants with a GWP over 2500 for an additional ten years after the service ban on the use of virgin product on January 1, 2020.

However, the vast majority of refrigerant combinations are close-boiling mixtures that typically exhibit azeotropic or near-azeotropic behavior, which makes conventional separation techniques such as distillation difficult to use to separate them. For these systems, only advanced separation systems constitute a viable option for recovering refrigerant mixtures, as standard separation methods will require a significant amount of energy, hence making the process incredibly expensive.

Absorption in liquid entrainers, adsorption on particulate materials, and membrane separation technologies appear as viable options for separating fluorocarbon mixtures. In addition, recent studies on the use of metal-organic frameworks (MOFs) have yielded positive results (Wanigarathna et al., 2020), and there has been some pioneering work on the use of polymer membrane (Pardo, Gutiérrez-Hernández, et al., 2021; Pardo et al., 2020; 2021).

This thesis has focused on using advanced absorption techniques with ionic liquids (ILs) as entrainers. The usage of ILs has attracted attention in several fields (see section 2.2.1 including separation (Han & Row, 2010; Kuzmina & Hallett, 2016; Pérez De Los Ríos & Hernández Fernández, 2014) and, more specifically, the separation and recovery of fluorinated refrigerants. ILs are used as entrainers in absorption and extractive distillation processes, the latter being a type of distillation in which a solvent, i.e., an IL, is added to the distillation column. This IL is selected so that one of the components, named B, is selectively attracted to it. Since the solvent has a significantly higher boiling point than the components being separated, the attracted component, B, has its volatility reduced. Thus, the other component, named A, becomes relatively more volatile and is easy to remove in the distillate. Note that an additional separation unit is required to separate B from the ILs. Deep Eutectic Solvents (DESs) are also gaining attention in this field as they have several advantages over conventional ILs, such as their easy preparation and accessibility from a relatively inexpensive cost (Durand et al., 2015), overcoming some of the limitations of ILs. In such designs, ILs and DESs' low vapor

[1] Reclamation refers to the reprocessing of a recovered F-gas to match the performance of a virgin substance, taking its intended application into account. The refrigerant is purified to an AHRI 700 standard (the quality necessary for *virgin* product), allowing it to be sold on the market as a regenerated product.

pressure values (Lei et al., 2013) are advantageous because there are no traces of them in the distillate, the bottoms stream can be easily recovered, and the selectivity of the separation may be high if the cation-anion combination is carefully chosen to match the mixture of interest.

To do so, it is crucial to study the interactions driving the physicochemical behavior of DESs and ILs. In the first part of this chapter, the mature soft-SAFT equation of state (EoS) (Blas & Vega, 1997) is used to assess the feasibility of the absorption of different F-gases in ILs and DESs. From the results obtained, two potential candidates are selected to separate two commercial blends of HFCs, R-410A, and R-407F, and a process flow diagram is built using Aspen Plus in a second part to estimate the approximate energy cost of the study and the feasibility to obtain a minimum purity of 98 wt % for each component. Although the idea of gas waste recycling seems to be, *a priori*, beneficial, the use of IL s in the F-gas recovery requires a deep study of its environmental impacts using a life-cycle approach, with a direct comparison with the conventional F-gas production. This is done in the final part of the chapter for one of the proposed separation schemes.

4.2 Phase behavior of fluorinated gases

In the first step, the phase behavior of several refrigerants and their mixtures is described using the soft-SAFT EoS. These gases include several common HFCs like difluoromethane, R-32, trifluoromethane, R-23, pentafluoroethane, R-125, and 1,1,1,2-tetrafluoroethane, R-134a, and perfluorocarbons like tetrafluoromethane, R-14. This selection is based on the usage of these gases in different refrigeration applications, where R-134a is the most used synthetic refrigerant (Zeiger et al., 2016), R-125 and R-32 conform a widely-used blend, R-410A, R-23 is frequently found in new equipment operating at very low temperatures (Linde GmbH, 2022), and R-14, a phased-out perfluorocarbon (PFC) because of its high GWP, which has become the most abundant PFC in the atmosphere, is included here for comparative purposes.

Refrigerants are modeled as several segments (m) of equal diameter (σ) and dispersive energy ($\varepsilon/k_{\mathrm{B}}$) of homonuclear chainlike molecules. The strong dipolar moments present in HFC molecules (Costa Cabral et al., 2001) have been modeled by mimicking two association sites of different nature (named type A and type B) with equal association energy ($\varepsilon^{\mathrm{HB}}/k_{\mathrm{B}}$) and volume ($K^{\mathrm{HB}}$). Although this model does not explicitly consider the polar nature of these molecules, it is useful for describing the main thermodynamic properties of fluorinated refrigerants with soft-SAFT (Albà et al., 2020b; Llovell et al., 2013a; Vilaseca et al., 2010). A-B interactions (self-association) between molecules of the same refrigerant and cross-association between different refrigerant molecules for binary mixtures (i.e., A-B' and A'-B interactions) are allowed.

For the cases of R-23 and R-32, their parameters have been readjusted given the fact that the original parametrization (Vilaseca et al., 2010) assumed a spherical model (i.e., $m = 1$) for

both molecules. Considering the acentric factor of R-23 ($\omega = 0.2820$) and R-32 ($\omega = 0.2769$) and the deviation induced by the original model, particularly at low temperatures, this restriction has been removed. The chain length parameter m has been kept constant (but different from unity) for both molecules, considering their similar size. At the same time, the association volume was maintained to match the same values as the rest of the family of HFCs. The remaining parameters were fitted without further restrictions.

Concerning R-14, it has been modeled as a non-associating molecule. Interestingly, some studies have demonstrated that perfluoroalkanes have a very high repulsive potential, which cannot be adequately represented using a Lennard-Jones (LJ) 12-6 attractive-repulsive potential (Lafitte et al., 2013), such as the one included in soft-SAFT. While a Mie potential, instead of a LJ, would allow to treat the repulsive exponent as an additional parameter, this would also require a modification of the soft-SAFT equation, which is out of the scope of this thesis. Instead, the solution implemented here has been to model the component allowing the m value to be different from one, despite the zero acentric factor of the molecule (A. Dias et al., 2009; A. M. A. Dias et al., 2004) (in this case, there is no discussion on its sphericity) to effectively account for the repulsive interactions. Other authors have also relaxed this constraint, obtaining similar results with other SAFT variants, like PC-SAFT (Aparicio, 2008).

The final set of parameters is given in Table 4.1, with the VLE representations in figures 4.1 (A) and (B). An excellent description of the phase envelope is found in a wide range of temperatures, up to 95% of the critical point. The critical point is slightly overestimated due to the absence of the renormalization-group treatment (Llovell & F. Vega, 2005), but this phenomenon is commonly found in mean-field theories such as soft-SAFT. Nonetheless, the relative average deviation with respect to the experimental data is very low for both the saturated liquid and vapor density calculations as well as for the vapor pressure (see Table 4.1).

Table 4.1: Soft-SAFT molecular parameters of the studied fluorinated refrigerants.

Compound	m	σ(Å)	ε/k_B(K)	ε^{HB}/k_B(K)	K^{HB}(Å^3)	AAD$_P$(%)	AAD$_D$(%)	Reference
R-14	2.195	3.167	124.7			4.508	1.481	This work
R-23	1.321	3.650	121.9	1470	24050	6.129	5.556	This work
R-32	1.321	3.529	144.4	1708	24050	8.109	1.208	This work
R-125	1.392	4.242	148.8	1685	24050	4.023	1.464	This work
R-134a	1.392	4.166	166.6	1862	24050	6.256	1.340	Albà et al. (2020b)

Some conclusions can be drawn from the representation of the VLE: first, the increase in the number and degree of halogenation leads to a higher molecular volume (i.e., volume occupied by the molecule) calculated as $m\sigma^3$. The increase in molecular volume results in lower liquid molar densities, which also means higher vapor molar densities and lower critical temperatures. This is clearly observable from R-32 (2-F), R-23 (3-F), and R-14 (4-F), all of them being single carbon molecules.

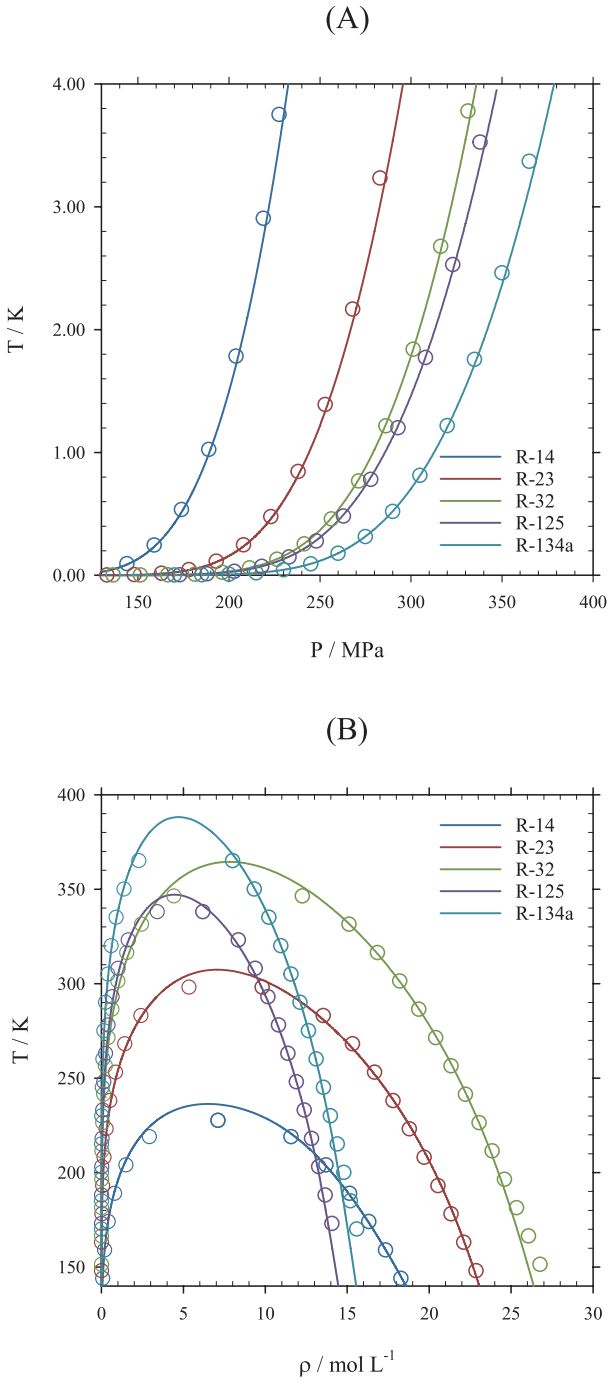

Figure 4.1: Vapor pressures (A) and coexistence densities (B) of the studied F-gases. Symbols represent the experimental data (Lemmon et al., 2018), and solid lines are the soft-SAFT calculations.

Another relevant aspect to consider is the dipole moment, influenced by the position of the fluorine atoms, which affects the VLE results. The molecules with higher dipole moments, such as R-134a and R-32 (2.058 and 1.978 D, respectively), also exhibit higher critical temperature points due to their higher capacity to interact with surrounding molecules. These conclusions will be expanded in further chapters of this thesis when analyzing the solubility in ILs (see section 4.4).

4.3 Molecular modeling of ionic liquids

4.3.1 Traditional ionic liquids

Traditional ionic liquids (ILs) are understood as those with well-known cations and anions, which have been extensively characterized in the literature. In this thesis, three *traditional* ionic liquids (ILs) have been considered : 1-ethyl-3-methylimidazolium bis(trifluoromethylsulfonyl)imide, [C_2mim][Tf_2N], 1-hexyl-3-methylimidazolium bis(trifluoromethylsulfonyl)imide, [C_6mim][Tf_2N], and 1-butyl-3-methylimidazolium hexafluorophosphate, [C_4mim][PF_6]. The choice is based on the availability of experimental solubility data with fluorinated gases, which seem to be promising due to the anion fluorination.

Traditional ILs are modeled as single chains in which the cations and anions are considered to be associated as ion pairs in the liquid state, assuming a very short time of dissociation until a new pair is formed (Del Pópolo & Voth, 2004). This assumption has been used in many contributions, obtaining a good description of the properties of ionic liquids (Andreu & Vega, 2008; Llovell et al., 2011). Specific associating sites have been defined to mimic the short-range and highly directional forces between the counterions. The number of associating sites, as well as the definition of the association scheme, is done considering previous research based on molecular dynamic simulations, quantum chemical calculations, experimental spectroscopic data, and previous experience with similar molecules. More specifically, [C_4mim][PF_6] has been modeled with a single associating site (named type C) mimicking the strong cation-anion interactions (Andreu & Vega, 2007; Llovell, Vilaseca, et al., 2012). The model proposed for [$C_x$mim][Tf_2N] ILs considers three association sites, representing the nitrogen atom interactions with the cation (site D) and two additional sites representing the charge delocalization due to the presence of the oxygen group (site E) (Llovell et al., 2011) as can be seen in Figure 4.2. Self-association interactions between different molecules of the same IL (C-C, and D-E) are explicitly considered. In addition, when describing the solubility behavior of HFCs in ILs, interactions with the refrigerant molecules (i.e., A-C, B-C, A-D, and B-E) are also taken into account.

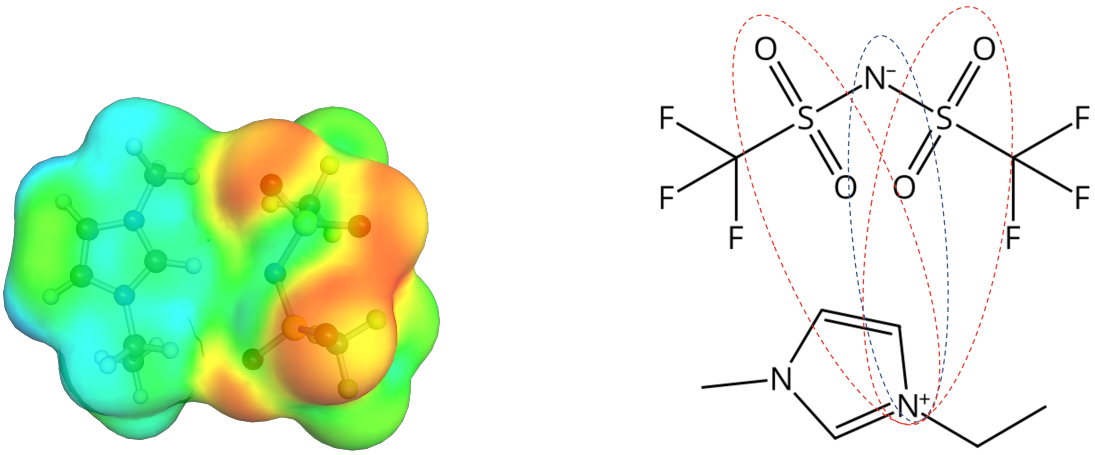

Figure 4.2: COSMO σ-surface charge density and sketch of the interactions used to model $[C_2mim][Tf_2N]$ molecule.

4.3.2 Fluorinated ionic liquids

Fluorinated Ionic liquids (FILs) are defined as ILs that contain chains of fluorinated anions of, at least, four carbons (Pereiro, Araújo, et al., 2013). They are far less common than *traditional* ILs, but their structure allows a high fluorinated absorption capacity (Pereiro, Araújo, et al., 2013; Pereiro, Pastoriza-Gallego, et al., 2013). FILs are described following similar patterns to those explained in the previous subsection, i.e., as homonuclear chainlike molecules with associations sites to describe the short-range interactions between anions and cations. The key aspect to consider is the delocalization of the anion's electric charge due to the presence of the fluorine atoms in the anion. Based on recent experimental measurements (Sosa et al., 2019), $[C_2mim][CF_3SO_3]$, $[C_2mim][C_4F_9SO_3]$, $[C_2py][C_4F_9SO_3]$ and $[C_2mim][C_4F_9CO_2]$ have been been modeled with soft-SAFT

$[C_2mim][C_4F_9SO_3]$, $[C_2py][C_4F_9SO_3]$ and $[C_2mim][C_4F_9CO_2]$ are modeled with three association sites (i.e., one D site plus two E sites, just as the $[C_2mim][Tf_2N]$ IL). For $[C_2py][C_4F_9SO_3]$ and $[C_2mim][C_4F_9CO_2]$ the two additional E sites come from the SO_3 presence, while a similar behavior is expected for $[C_2mim][C_4F_9CO_2]$ due to the presence of the CO_2 moiety (Ferreira, Araújo, et al., 2019; Pereiro et al., 2017). Only D-E interactions are allowed between different FILS. For $[C_2mim][CF_3SO_3]$ only one interaction site F is considered. The quasi-spherical shape of the $[CF_3SO_3]$ anion, similar to the behavior described in the IL with the $[PF_6]$ anion, results in a lower charge delocalization due to a much more centered electrostatic potential (Ferreira, Araújo, et al., 2019). Only F-F interactions are allowed between different FILs molecules, so this site has both a positive and negative nature.

A sketch of the interactions for all the FILs included in this thesis is depicted in Figure 4.3. The molecular parameters of all the ILs involved in this thesis are retrieved from previously

published works and are presented in Table 4.2. The reader is referred to Chapter 2 for further details on these solvents.

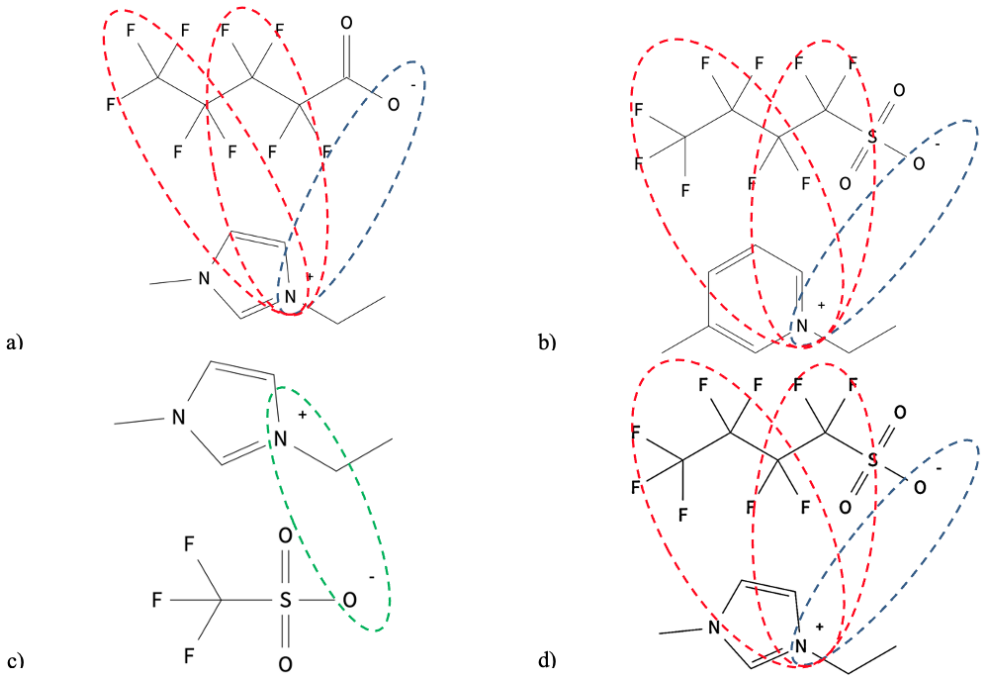

Figure 4.3: Sketch of the interactions used to model FILS: (a) $[C_2mim][C_4F_9CO_2]$, (b) $[C_2py][C_4F_9SO_3]$, (c) $[C_2mim][CF_3SO_3]$, and (d) $[C_2mim][C_4F_9SO_3]$.

Table 4.2: Soft-SAFT molecular parameters of the investigated ILs.

Compound	m	σ (Å)	ε/k_B (K)	ε^{HB}/k_B (K)	K^{HB} (Å^3)	Reference
$[C_2mim][Tf_2N]$	6.023	4.069	394.6	3450	3450	Llovell et al. (2011)
$[C_6mim][Tf_2N]$	6.338	4.334	404.2	3450	3450	Llovell et al. (2011)
$[C_4mim][PF_6]$	4.570	4.146	418.0	3450	3450	Andreu and Vega (2007)
$[C_2mim][CF_3SO_3]$	4.495	4.029	420.0	3450	2250	Ferreira, Llovell, et al. (2019)
$[C_2mim][C_4F_9SO_3]$	7.320	3.816	343.4	3850	2250	Pereiro et al. (2017)
$[C_2py][C_4F_9SO_3]$	7.320	3.889	359.4	3850	2250	Ferreira, Llovell, et al. (2019)
$[C_2mim]$ $[C_4F_9CO_2]$	7.233	3.762	338.8	3850	2250	Ferreira, Llovell, et al. (2019)

4.4 Solubility of F-gases in advanced solvents

The purpose of the following sections is to study the capacity of ILs and DESs to recover common refrigerant mixtures used in refrigeration systems. The fine-tunability of these solvents would allow, *a priori*, to design solvents that are selective for one of the species found in the quasi-azeotropic mixtures present in the refrigeration sector and with desirable properties such as low viscosity, low vapor pressure, and high thermal and chemical stability.

4.4.1 Solubility in traditional ionic liquids

In this section, a conductive modeling study of the capabilities of the previously reported *traditional* ILs in terms of refrigerants solubility and recovery capacity has been carried out with the soft-SAFT EoS using the molecular models described in previous sections.

First, based on the availability of experimental data, the solubility of the fluorinated refrigerants included in Table 4.1 in a widely-used traditional IL, [C_2mim][Tf_2N], has been compared at a selected working temperature of 303.15 K. This makes it possible to observe the influence of the structure and the degree of halogenation on the absorption capacity of ILs. New experimental data has been provided for some of these mixtures, thanks to a collaboration conducted during this Ph.D. thesis with the Associated Laboratory for Green Chemistry (LAQV) of the Network of Chemistry and Technology (REQUIMTE) lab from the Universidade Nova de Lisboa (Portugal). The results are included in Figure 4.4

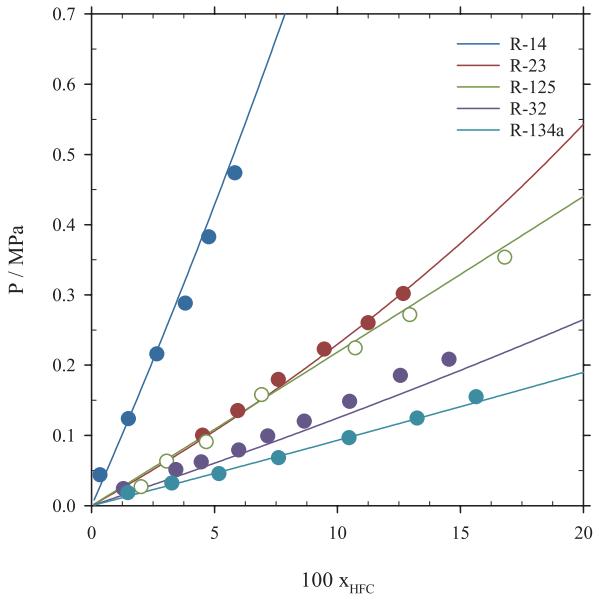

Figure 4.4: VLE of several F-gases in [C_2mim][Tf_2N] at 303.15 K. Symbols represent the experimental data from this work, empty symbols represent experimental data from Sosa et al. (2019) and solid lines are the soft-SAFT calculations.

As expected, it is confirmed that R-134a is the F-gas showing a higher solubility in [C_2mim][Tf_2N], followed by R-32, R-125, R-23, and R-14, in this order. The solubility of R-14 is the lowest because their molecules form a stable structure with neither dipole nor hydrogen-bonding associations. This lack of interaction makes the gas less soluble with ionic liquids with fluorinated structures.

The analysis of these results can be related to the ratio and position of fluorine/hydrogen atoms present in the F-gases structure. Hydrogen-containing fluorocarbons exhibit higher

solubilities because they can form more hydrogen bond combinations (H–F–H) with an IL, increasing the solubility. Also, it is noticeable that the molecule with the highest volume, R-134a, exhibits higher solubility, suggesting that steric effects do not play an important role. Concerning the position of the fluorine/hydrogen atoms, this modifies the dipole moment of these molecules. Interestingly, the solubility difference correlates with the magnitude of the dipole moments of R-134a (2.058 D), R-32 (1.978 D), R-23 (1.649 D), and R-14 (0 D). The only exception is R-125 (1.563 D), whose dipole moment is slightly lower than that of R-23. At the same time, its absorption is higher, possibly due to the higher volume and H-F-H possible combinations. In summary, it seems that the polarity is the dominant effect on the solubility in $[C_2mim][Tf_2N]$.

Concerning the soft-SAFT description, R-14 is predicted without further adjustments, reaching a very good agreement with the experimental data. For the rest of the compounds, and as mentioned in the previous section, a cross-association model has considered the association interaction between the refrigerant and $[C_2mim][Tf_2N]$, using equations 3.57 and 3.58. In addition, the energy and size binary parameters, ξ and η, have been used to quantitatively describe their solubility in $[C_2mim][Tf_2N]$. The full list of binary parameters is given in Table 4.3, including those from other ILs and FILs that will be addressed in the following sections.

Table 4.3: Binary and Energy Size Parameters for the Studied F-gases + Ionic Liquids systems.

Fluorinated gas	Ionic Liquid	ξ	η
R-14	$[C_2mim][Tf_2N]$	1.000	1.000
R-23	$[C_2mim][Tf_2N]$	1.189	0.925
R-32	$[C_2mim][Tf_2N]$	1.185	1.052
	$[C_6mim][Tf_2N]$	1.180	1.052
	$[C_4mim][PF_6]$	1.238	1.052
R-125	$[C_2mim][Tf_2N]$	1.236	1.052
	$[C_6mim][Tf_2N]$	1.230	1.052
	$[C_4mim][PF_6]$	1.266	1.070
R-134a	$[C_2mim][Tf_2N]$	1.165	1.035
	$[C_6mim][Tf_2N]$	1.165	1.038
	$[C_4mim][PF_6]$	1.220	1.052
	$[C_2mim][C_4F_9SO_3]$	1.140	1.049
	$[C_2mim][C_4F_9CO_2]$	1.146	1.049
	$[C_2mim][CF_3SO_3]$	1.220	1.035
	$[C_2mim][C_4F_9SO_3]$	1.157	1.049

In view of these results, in the following subsections, the attention has been focused on the prediction of the solubility of R-32, R-125, and R-134a in ILs, whose models are described in section 4.3.1.

4.4.2 Selection of the best solvent for the separation of R-32 and R-125

The first study shown is devoted to evaluate the technical viability of separating R-32 and R-125, both refrigerants forming the common blend R-410A, with the aim to recover R32 for further reuse, considering its moderate GWP. For this purpose, further analysis is carried out by predicting the separation performance of the gas-liquid separation, also conducted with soft-SAFT, with the selected traditional ILs. From this study, an IL candidate will be selected, and the possible interactions between the refrigerant gases and the IL will be ascertained by predicting the high-pressure phase behavior of ternary mixtures formed by the two HFCs and the selected IL. The results will guide the process design of section 4.5.3.

The solubility of R-32 and R-125 gases is represented in figures 4.5 (A) and (B). In both cases, size (η) and energy (ξ) binary parameters were fitted to the lowest temperature isotherm to predict the pressure-composition diagrams; then, the rest of the isotherms were predicted using those parameters. The full list of the optimized binary parameters for all the ionic liquids is included in Table 4.3.

Overall, the description of the solubility of these systems is very good at all temperatures, agreeing with the available experimental data (X. Liu, He, et al., 2015b; Shiflett et al., 2006; Shiflett & Yokozeki, 2006c; 2007; 2008). The optimized binary parameters have similar values regardless of the IL. In particular, the size binary parameter, η, is constant for all combinations of R-32 and R-125 except for the R-125 + [C_4mim][PF_6] mixture, whose value is slightly higher in order to capture the convex nature of the solubility curve at low temperatures. This means that the influence of the IL in the volume interactions (entropic effects) is almost negligible, allowing predictions of the solubility of these compounds in other ILs. The energy binary parameter, ξ, has similar values for the two [Tf_2N]-based ILs, indicating that the effect of the alkyl chain in the cation is minor in the description of the association interactions.

This information is helpful to check the transferability of these parameters to other compounds when no experimental data are available. A final comment concerns the value of the ξ parameter, which, in all cases, is remarkably higher than one, meaning the classical Lorentz-Berthelot combining rules underestimate the solubility of the refrigerant in the IL. This might be an indication that the model for the mixture is missing some interactions. Also, the size binary parameter is higher than one, increasing the miscibility of the refrigerant at high mole fractions.

From the results discussed above, Henry's constants (k_H), which relate the amount of gas dissolved in the liquid (x) to the vapor phase fugacity (as defined in equation 3.73) of the solute in equilibrium with the solvent (f^V) at infinite dilution and constant temperature, are calculated from the slope of the absorption isotherm at very low pressures:

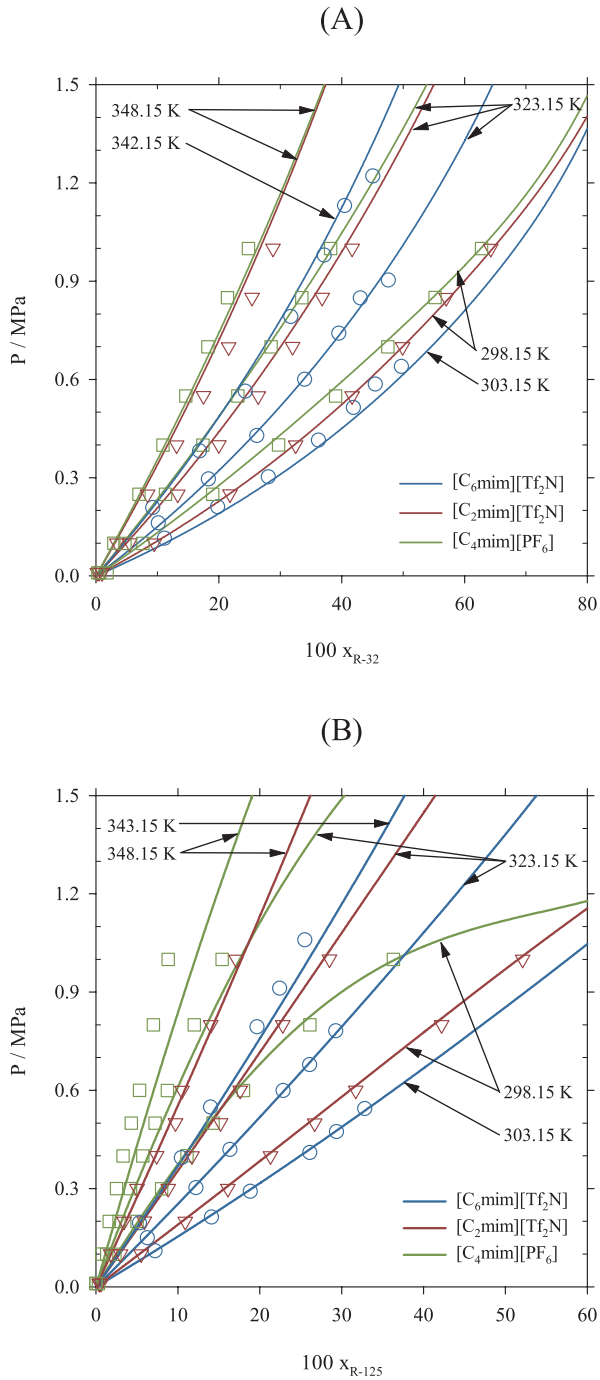

Figure 4.5: Solubility of R-32 (A) and R-125 (B) in $[C_6mim][Tf_2N]$, $[C_2mim][TF_2N]$, and $[C_4mim][PF_6]$. Lines are the soft-SAFT calculations, and symbols represent the experimental data from X. Liu, He, et al. (2015b), Shiflett et al. (2006), and Shiflett and Yokozeki (2006c), 2007, 2008.

$$k_{H_i}(T) = \lim_{x \to 0} \frac{f_i^V(P,T)}{x} \tag{4.1}$$

Figure 4.6 plots the calculated Henry's law constant of R-32 and R-125 in the ILs under study. As can be seen, the solubility of R-32 is higher than that of R-125 in all cases. Also, the ILs with the [Tf_2N] anion exhibit slightly higher absorption capacities than [C_4mim][PF_6], as they have lower Henry's constants.

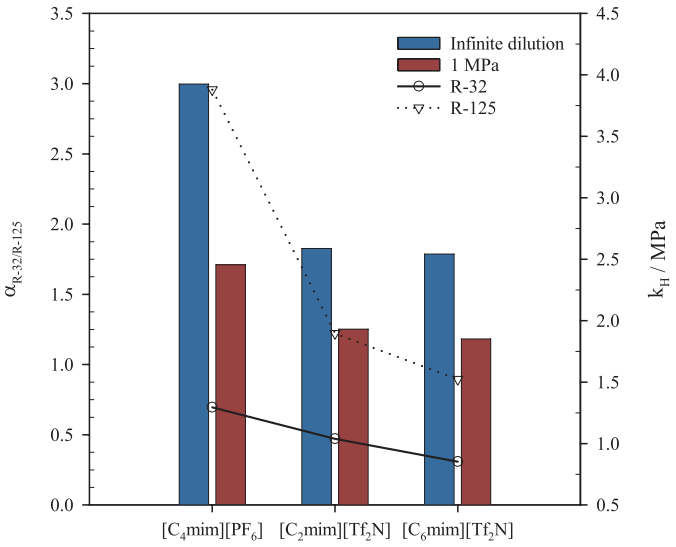

Figure 4.6: Selectivity (left axis) and Henry's law constants (right axis) in [C_4mim][PF_6] and [C_2mim][Tf_2N] at 298.15 K and [C_6mim][Tf_2N] at 303.15 K.

The theoretical performance of these ILs to separate R-410A compounds is firstly approached by defining the ideal selectivity, α, calculated at infinite dilution as:

$$\alpha_{\text{R-32/R-125}} = \frac{k_H^{R-125}}{k_H^{R-32}} \tag{4.2}$$

The selectivity values plotted in Figure 4.6 for each IL, follow the opposite trend to that observed in gas solubility, as the ideal selectivity is higher for [C_4mim][PF_6] than for the [Tf_2N]-based ILs. This is a consequence of the lower solubility of R-125 at low compositions of [C_4mim][PF_6]. This difference decreases at higher pressures, as it is shown by additionally plotting the ideal selectivity at 1.0 MPa, calculated from the VLE modeled data (Figure 4.5). At this pressure, which is likely to be employed in an extractive distillation process in order to increase gas absorption and reduce the amount of IL to be used, all three ILs provide similar selectivity values. Consequently, selecting the best IL to perform the separation becomes difficult if the comparison is made only in terms of absorption capacity and selectivity, as there are no significant differences among them. Mass transfer is another key factor affecting the

performance of gas separation processes (Mota-Martinez et al., 2018). Using [C_2mim][Tf_2N] would favor the separation because its viscosity (34 mPa s at 298 K) is twofold and tenfold lower than [C_6mim][Tf_2N] (71 mPa s at 298 K) and [C_4mim][PF_6] (329 mPa s at 298 K), respectively (Ahosseini & Scurto, 2008; Harris et al., 2005). Moreover, [PF_6] anion is less stable as it can hydrolyze in the presence of water (Wasserscheid et al., 2002). Therefore, [C_2mim][Tf_2N] is selected in this thesis to further assess the separation of R-32 from R-125 using ILs (see section 4.5.3).

Finally, the van't Hoff equation is used to obtain the enthalpy and entropy (equations 4.3 and 4.4) of dissolution of the mixtures (Blath et al., 2011) using the data obtained from soft-SAFT to evaluate the dependence of the solvation process on temperature.

$$\Delta H_{dis} = R \left(\frac{\partial \ln k_H}{\partial 1/T} \right)_p \tag{4.3}$$

$$\Delta S_{dis} = -R \left(\frac{\partial \ln k_H}{\partial \ln T} \right)_p \tag{4.4}$$

The results of the calculation of solvation enthalpies and entropies are presented in Table 4.4. The magnitude of the solvation enthalpies of R-32 and R-125 are within the typical range of physical sorption and are just slightly higher than that found for CO_2 sorption in these ILs (Cadena et al., 2004).

Table 4.4: Enthalpy and entropy of solvation of R-32 and R-125 in the selected ILs.

Ionic Liquid	HFC	ΔH (kJ mol^{-1})	ΔS (J mol^{-1} K^{-1})
[C2mim][Tf2N]	R-32	-21.5	-68.3
	R-125	-20.1	-63.8
[C6mim][Tf2N]	R-32	-20.5	-63.5
	R-125	-19.0	-59.0
[C4mim][PF6]	R-32	-18.8	-59.6
	R-125	-16.0	-50.7

The information gathered from the study of the binary systems is used to predict, in the absence of experimental data, the phase behavior of ternary mixtures formed by the two HFCs and the candidate IL, [C_2mim][Tf_2N], selected to perform the separation. The ternary diagram R-32 + R-125 + [C_2mim][Tf_2N] at 300 K is presented in Figure 4.7. Several isobars were calculated to assess the influence of pressure on the phase behavior of the mixture, and the corresponding liquid composition is indicated in the diagram. A region of immiscibility, i.e., liquid-liquid equilibrium (LLE), is found at high compositions of both refrigerants above 1.4 MPa, as expected from the information gathered in the binary systems. The three VLLE phase line has been estimated and indicated in the diagram with a dashed line. Similar diagrams

have been reported for the absorption into ILs of very soluble gases such as CO_2 and SO_2 (Shiflett & Yokozeki, 2010; Yokozeki & Shiflett, 2009).

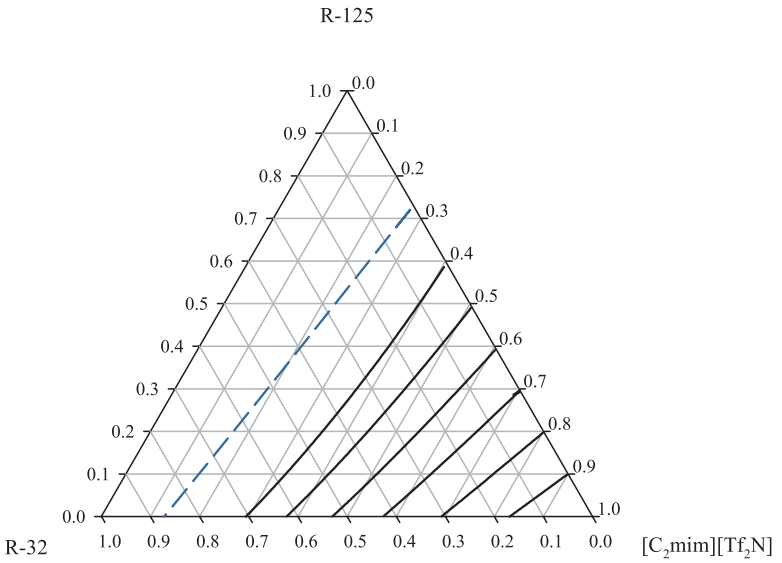

Figure 4.7: Isothermal ternary phase diagram predicted with soft-SAFT for the system R-32+R-125+[C_2mim][Tf_2N] at 300 K. The different curves represent predicted isobars at pressures ranging from 0.2 (bottom line) to 1.6 MPa (upper line) at 0.2 MPa intervals. The dashed blue line corresponds to the VLLE curve.

Using the ternary diagrams, the performance of the gas separation for a given inlet composition is reevaluated by defining the gaseous absorption selectivity, S, as follows (Yokozeki & Shiflett, 2007):

$$S_{R-32/R-125} = \frac{y_{R-125}/x_{R-125}}{y_{R-32}/x_{R-32}} \tag{4.5}$$

Where x and y denote the molar composition of R-32 and R-125 in the solvent liquid and vapor phases, respectively. This is a more realistic value than that obtained from Equation 4.2, as it includes the competition between the two HFCs. In Equation 4.5, the vapor compositions in equilibrium with the liquid are calculated as a function of the IL concentration in the feed (z_{IL}) and the operating pressure through an iterative process that involves solving the Rachford-Rice flash equation:

$$f\left(\frac{V}{F}\right) = \sum_{i=1}^{C} \frac{(K_i - 1)z_i}{1 + (K_i - 1)\frac{V}{F}} = 0 \tag{4.6}$$

With K_i, being the vapor-liquid relation and defined as:

$$y_i = K_i \cdot x_i \tag{4.7}$$

The separation performance for the mixture R-410A provided by [C_2mim][Tf_2N] at 300 K is presented in Figure 4.8. The predicted value of separation performance tends to the calculated ideal selectivity at infinite dilution and decreases, as expected, with pressure. Moreover, although lower pressures yield higher separation performances (closer to the ideal selectivity), this occurs at the expense of lower sorption capacity and, consequently, lower recovery. At higher pressures, the predicted LLE immiscibility region also limits the amount of gas that can be recovered. Nevertheless, very high-pressure operating conditions do not seem attractive because they incur in ∼25% separation performance drops for a given IL feed composition.

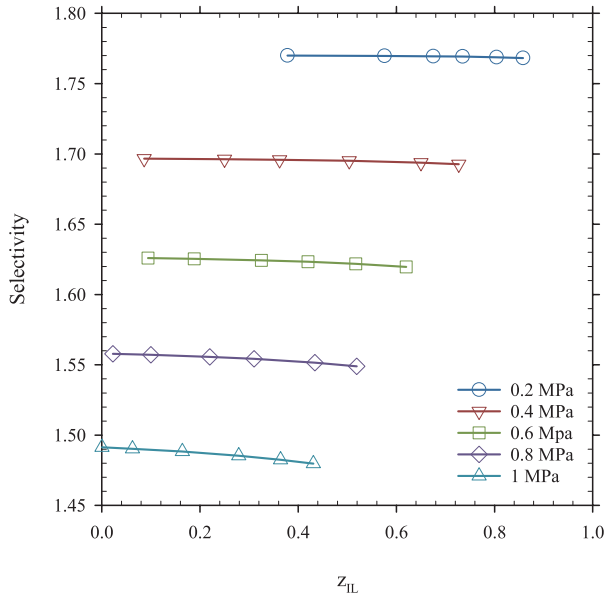

Figure 4.8: Predicted separation performance (Selectivity calculated as Equation **4.5**) for the recovery of R-32 from R-410A as a function of the [C_2mim][Tf_2N] feed mole fraction (z_{IL}).

4.4.3 Solubility study of R-134a in an extended variety of solvents

In the previous subsection, R-134a showed the highest solubility of all the studied F-gases. The interest behind this molecule is twofold: R-134a is an excellent refrigerant (used originally as a replacement of R-12, dichlorodifluoromethane), used in a wide variety of applications, and it is also used as a component of many of the existing HFC blends on the market, like R-407F.

The following subsection guides the study of the solubility of R-134a in the selected well-known traditional ionic liquids, just as for the R-32 + R-125 blend, but also extends this research to another family of ionic liquids named *fluorinated* ionic liquids and other types of solvents like fluorinated deep eutectic solvents (DESs).

Ionic liquids

As done for R-32 and R-125, the solubility of R-134a with *traditional* ionic liquids is represented in Figure 4.9. As expected, the R-134a solubility increases with pressure and decreases with temperature. Again, the description of the solubility is very good at all temperatures with a good fitting to the available experimental data (Ren & Scurto, 2009b). The size (η) and energy (ξ) binary parameters used for the fitting are included in Table 4.3.

The same conclusions can be drawn from this analysis as the other previously analyzed fluorinated gases. Regarding the anion effect, the solubility of R-134a in [C_6mim][Tf_2N] and [C_2mim][Tf_2N] at a particular pressure is markedly higher than [C_4mim][PF_6], as also observed from Figure 4.5 (A) and (B); ions with more disperse charge can be more easily solvated by some of the polar hydrofluorocarbons, making them miscible at lower temperatures and pressures (Ren & Scurto, 2009a; 2009b). Regarding the alkyl length, the solubility of R-134a is increased from [C_2mim] to [C_6mim], in line with the results observed for R-32 and R-125. The hexyl group increases the dispersion forces of the cation for better interaction with R-134a, thus increasing the solubility of the F-gas.

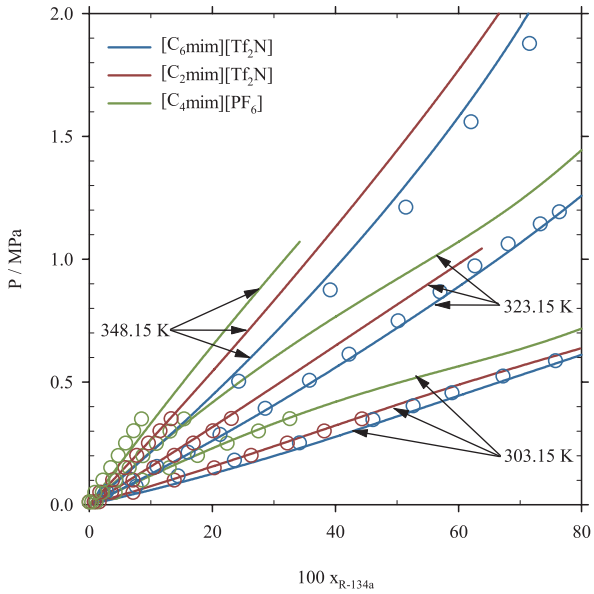

Figure 4.9: Solubility of R-134a in [C_6mim][Tf_2N], [C_2mim][TF_2N], and [C_4mim][PF_6]. Lines are the soft-SAFT calculations, and symbols represent the experimental data from Ren and Scurto (2009b).

Additionally, the solubility of R-134a has been studied to asses its solubility in a series of alternative FILs. The structural differences between the different fluorinated anions are accounted for in the values of the different molecular parameters, which are all listed in Table 4.2. The modeling results and their comparison with the experimental data are plotted in Figure 4.10, where the solubility of R-134a in [C_2mim][Tf_2N] has also been added for comparative purposes.

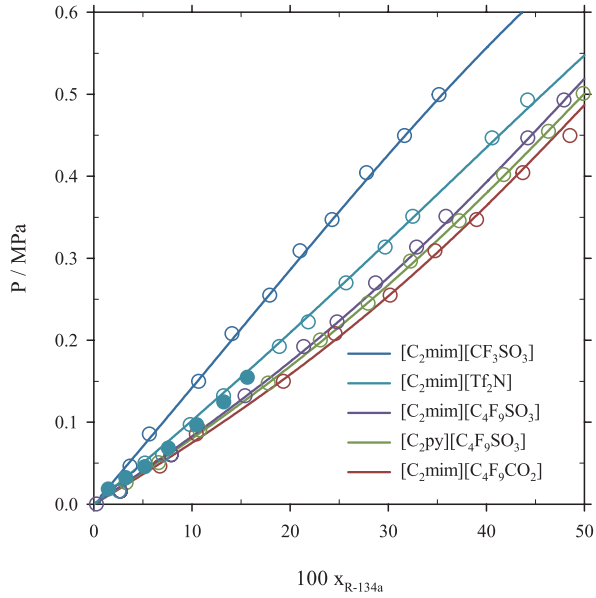

Figure 4.10: Pressure–composition diagram of R-134a in several FILs. Symbols represent the experimental data from this thesis, in collaboration with LAQV, REQUIMTE, empty symbols represent experimental data from Sosa et al. (2019), and solid lines are the soft-SAFT calculations.

The results show that, indeed, the inclusion of an alkyl fluorinated structure to the anion increases the solubility of the IL, with R-134a exhibiting the highest solubility in all anion structures with 9 fluorine atoms. This demonstrates that anions with longer fluorinated chains have a greater solubility for R-134a in comparison with $[C_2mim][Tf_2N]$, with 6 fluorine atoms and $[C_2mim][CF_3SO_3]$, with 3 fluorine atoms. Among the remaining FILs, the carboxylate anion seems to have slightly higher interactions than the sulfonate anion, hence increasing the solubility. The impact of the change of the cation (pyridinium vs. imidazolium) does not seem to be significant.

From a modeling perspective, the crossed associating interactions were predicted, while two binary parameters were necessary to obtain an accurate representation in the whole range of composition. The size binary parameter was fixed to a constant value of $\eta = 1.035$ for the anions containing fewer fluorine atoms ($[Tf_2N]^-$ and $[CF_3SO_3]^-$), while a higher value of $\eta = 1.050$ was used for the rest of anions. The binary parameters are listed in Table 4.3, with all the other binary parameters already presented. The energy binary parameter, ξ, is very similar in all cases, except for $[C_2mim][CF_3SO_3]$, whose value is higher. This difference is probably caused by using a single molecular association site to mimic the association interactions compared to the three-site choice of the rest of the molecules. Thus, the balance between dispersive and associative forces has to be compensated, and higher cross-dispersive energy is required. Overall, all values are higher than one, revealing again that the model is underpredicting the solubility. This result is consistent with previous studies on other ILs for HFCs and other gases using the soft-SAFT model (Llovell, Marcos, MacDowell, et al., 2012; Llovell,

Vilaseca, et al., 2012) and suggests that either the inclusion of the specific dipolar moment or an increment of association sites might be necessary for the model.

Alternative deep eutectic solvents

The last part of this section is based on the analysis of the solubility of R-134a, as in the previous subsection, in new Fluorinated DESs in order to compare their solubility performance with respect to the recently proposed FILs described above. For this purpose, six different DESs are combined using the original acids perfluorobutanesulfonic acid, $HC_4F_9SO_3$, and perfluoropentanoic acid, $HC_4F_9CO_2$, as HBDs and the 1-Ethyl-3-methylimidazolium chloride, [C_2mim][Cl], salt as HBA at different proportions. These DESs were synthesized and studied in this thesis for the first time.

DESs are modeled using a two-compounds approach, (Lloret et al., 2017; Ojeda & Llovell, 2018) considering both compounds forming the DES as independent entities and treating them as a mixture. One of the compounds is the [C_2mim][Cl] IL, which is modeled following as described in section 4.4.1 with one single association site of a dual nature, simulating the cation-anion interaction (i.e., one F site). In this case, there is no charge delocalization, and no additional sites are required. This can be clearly observed in Figure 4.11, where the charge distribution of this IL is shown on the left side. The quantum-chemical calculations have been performed using TmoleX (version 21.0.1) (Balasubramani et al., 2020).

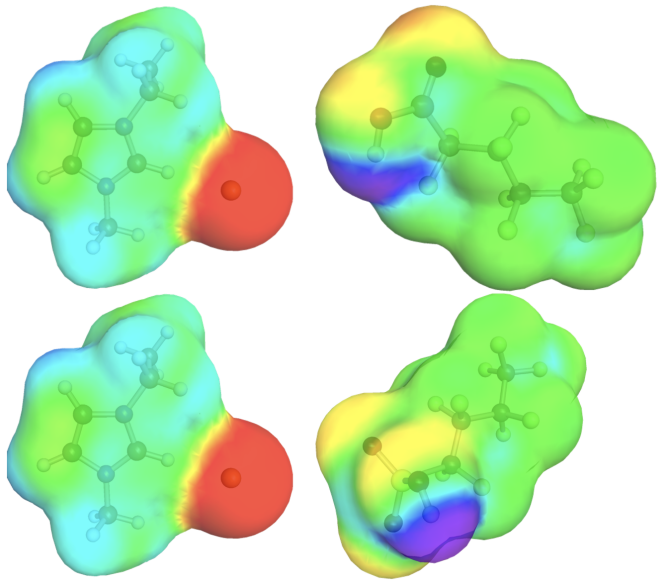

Figure 4.11: σ-surface diagrams (violet and red regions stand for positive and negative charges, respectively) for (top) [C_2mim][Cl]:[$HC_4F_9CO_2$] and (bottom) [C_2mim][Cl]:[$HC_4F_9SO_3$].

Concerning [$HC_4F_9SO_3$] and [$HC_4F_9CO_2$], these molecules have never been described with soft-SAFT. Their carboxylic acid nature suggests modeling them with only one associating site to mimic the formation of dimers that is characteristic of these fluids. Apparently, the charge distribution for both acids, also depicted in Figure 4.11, seems to confirm this fact, as only a clearly blue-colored area, representing a charged region, is observed over the OH^- group. However, Sadeqzadeh et al. (2016) noticed that in aqueous solutions of carboxylic acids, a large number of water molecules are expected to bond (by solvation) to the carboxylic acid (COOH) group. Although the DES mixture does not involve water, [C_2mim][Cl] is also expected to bond the COOH group, as this is the essence of the formation of the eutectic mixture. As done in this thesis and in other contributions for several SAFT versions (Ramdin et al., 2018; Ramos et al., 2011; Sadeqzadeh et al., 2016; Yushu et al., 2012), a higher number of sites have been incorporated to better reflect the formation of these clusters. Several attempts were made, and a three sites approach (one G site for the doubly bonded oxygen and two sites H and I for the hydroxyl group) has been chosen as it provides good agreement with the available data (see Figure 4.12).

Table 4.5: Molecular parameters of the IL and the acids conforming DESs.

Compound	m	σ (Å)	ε/k_B (K)	ε^{HB}/k_B (K)	k^{HB}(Å^3)	Reference
[C_2mim][Cl]	3.717	3.795	485.0	2200	2250	Mac Dowell et al. (2014)
$HC_4F_9CO_2$	2.403	4.550	298.5	2200	2250	This work
$HC_4F_9SO_3$	2.403	4.652	302.9	2200	2250	This work

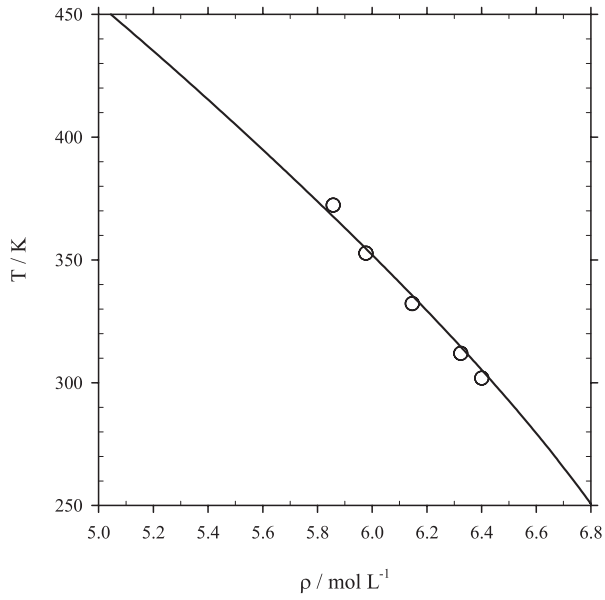

Figure 4.12: Saturated liquid density of $HC_4F_9CO_2$. Empty symbols represent experimental data from Sinitsyn et al. (1995), and solid lines are the soft-SAFT calculations.

Before studying the R-134a solubility, the experimental density and dynamic viscosity of

Table 4.6: FVT viscosity parameters of [C_2mim][Cl] and $HC_4F_9CO_2$ forming DESs.

Compound	α (J m^3 mol^{-1} kg^{-1})	B	L_v (Å)
[C_2mim][Cl]	33.5	0.0295	0.5297
$HC_4F_9CO_2$	60.5	0.0597	0.4152

DESs [C_2mim][Cl]:[$HC_4F_9CO_2$] at (1:1), (1:2), and (2:1) ratios were measured at the LAQV laboratory at Universidade NOVA de Lisboa, in the framework of collaborative work, in a range of temperatures from 293.15 to 353.15 K. The results are plotted in Figure 4.13 (A) and (B). Unfortunately, the values of density and viscosity of the DESs based on $HC_4F_9SO_3$ as HBD could not be measured due to bubble formation inside the equipment.

As shown in Figure 4.13 (A), the molar density increases with the concentration of the salt. Also, a linear decrease in the temperature is observed, as it commonly happens in all ILs and DESs. As explained, the two-compound approach is used here to model DESs, treating both compounds as independent species. The molecular parameters of [C_2mim][Cl] were available from a previous contribution (Mac Dowell et al., 2014). The parameters for [$HC_4F_9CO_2$] have been fitted to saturated liquid density experimental data (Sinitsyn et al., 1995) and are reported here for the first time. Then, the density of the DESs is calculated as a mixture. A binary temperature-independent parameter $\eta = 1.018$ is necessary to account for some minor deviations from the pure predictions ($\eta = 1$). It is interesting to note that the modeling does not degenerate with the change of composition, even if the nature of the two compounds is very different. Figure 4.13 (A) also includes the density of pure [C_2mim][Cl] for comparative purposes.

Once the soft-SAFT molecular parameters of both compounds are well established, the FVT is used to describe the viscosity of the DESs at all proportions. The Spider Web approach (Cané et al., 2017) is used, as no information on the viscosity of $HC_4F_9CO_2$ is available. Hence, the pure viscosity parameters of $HC_4F_9CO_2$ have been fitted to mixture data. The parameters of [C_2mim][Cl] have also been refined, as the model provided in a previous contribution (Mac Dowell et al., 2014) contained data with high uncertainty at low temperature, which has been discarded now. Table 4.6 presents the final set of parameters for both compounds. The description of the DESs' viscosities as a function of temperature is plotted in Figure 4.13 (B), showing good agreement with the data, except for the lowest temperatures at the (2:1) proportion, reaching an overall AAD in viscosity around 10%. The description of the viscosity of [C_2mim][Cl] is also included. No binary parameters are used in the approach, making it predictive for other different proportions.

In Figure 4.14, the pressure–composition diagrams describing the solubility of R-134a in [C_2mim][Cl]:$HC_4F_9CO_2$ and [C_2mim][Cl]:$HC_4F_9SO_3$ at three different proportions (1:1), (1:2), and (2:1) and 303.15 K are plotted, respectively. In both representations, the solubility of [C_2mim][$C_4F_9CO_2$] and [C_2mim][$C_4F_9SO_3$] have been added, respectively, for comparative

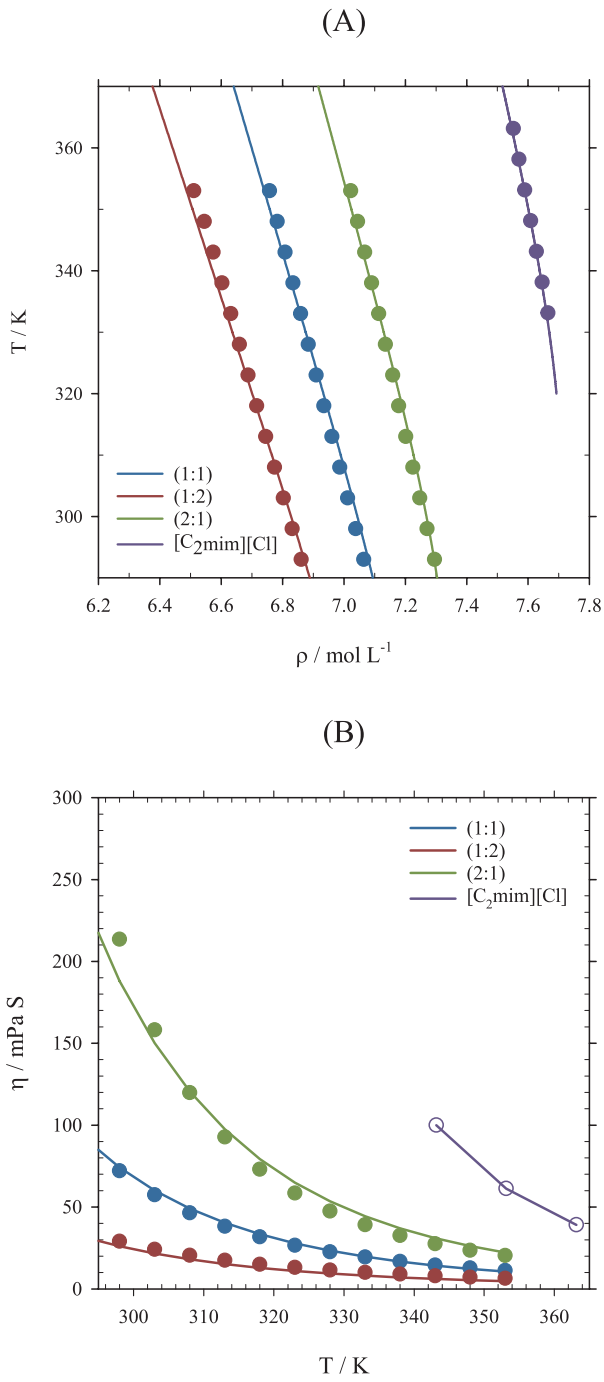

Figure 4.13: Density (A) and viscosity (B) of $[C_2mim][Cl]$:$[HC_4F_9CO_2]$ as a function of temperature. Both the density and the viscosity of pure $[C_2mim][Cl]$ are also included. Symbols represent the experimental data from this thesis, empty symbols represent experimental data from Mac Dowell et al. (2014) (density) and Seddon et al. (2002) (viscosity), and solid lines are the soft-SAFT calculations.

purposes. Unfortunately, all DESs exhibit a lower solubility compared to their equivalent FIL. Among DESs, the proportion (1:2) provides higher absorption values than the other proportions, although this is more evident when using $HC_4F_9SO_3$. The influence of $HC_4F_9CO_2$ seems to be less relevant, as the differences in solubility are minor, particularly at higher IL proportions.

The lines in both figures correspond to the soft-SAFT modeling of the mixture, which is treated as a ternary system between R-134a, [C_2mim][Cl], and the corresponding acid. The modeling was first applied to the R-134a + [C_2mim][Cl]:$HC_4F_9CO_2$ mixture. The binary parameter $\eta = 1.018$ from the DES was transferred here, while no binary interaction parameters had to be fitted for the interaction between the acid and R-134a. Finally, the binary parameters ξ and η, corresponding to the interaction between the halide salt and R-134a, were fitted to the (1:1) isotherm and transferred to the other two proportions in a predictive manner. The results obtained revealed a remarkable agreement between the experimental data and the modeling, not only at the fitted (1:1) ratio but also at the rest of the proportions. These results are encouraging, considering that only two temperature-independent binary parameters were fitted. A summary of all the binary parameters involved in this ternary system is given in Table 4.7.

Table 4.7: Binary energy and size parameters for the studied R-134a + DESs compounds.

Compound 1	Compound 2	ξ	η
[C_2mim][Cl]	$HC_4F_9CO_2$	1.000	1.018
[C_2mim][Cl]	$HC_4F_9SO_3$	1.000	1.018
[C_2mim][Cl]	R-134a	1.180	0.880
$HC_4F_9CO_2$	R-134a	1.000	1.000
$HC_4F_9SO_3$	R-134a	1.000	1.000

Concerning the description of the solubility data of R-134a in [C_2mim][Cl]:$HC_4F_9SO_3$ in Figure 4.14 (b), a novel approach has been followed because of the lack of DESs and pure $HC_4F_9SO_3$ density data. On the basis of the transferability of the parameters, a series of hypotheses were built to describe the ternary mixture and obtain the molecular parameters of [$HC_4F_9SO_3$]. First, it was assumed that no binary interaction parameters were necessary between the acid and R-134a, considering that the type of interaction would be similar to that of R-134a with $HC_4F_9CO_2$. Second, the association parameters and the chain length, m, of pure $HC_4F_9SO_3$ were also transferred from $HC_4F_9CO_2$, assuming that the nominal size and dispersive energy differences can be effectively taken into account in the segment diameter, σ, and dispersive energy, ε/k_B, parameters. Consequently, these two molecular parameters were fitted to the ternary mixture R-134a + DES using the (1:1) proportion data, as done before for [C_2mim][Cl]:$HC_4F_9SO_3$.

The results of this unusual yet effective parametrization are given in Table 4.5. As can be seen, the values obtained are similar but slightly higher for $HC_4F_9SO_3$, which is coherent with the expected increase in size (the molecular volume of the sulfonate ion is higher than the carboxylate) and energy. Besides, the increase is of the same order as the one found in

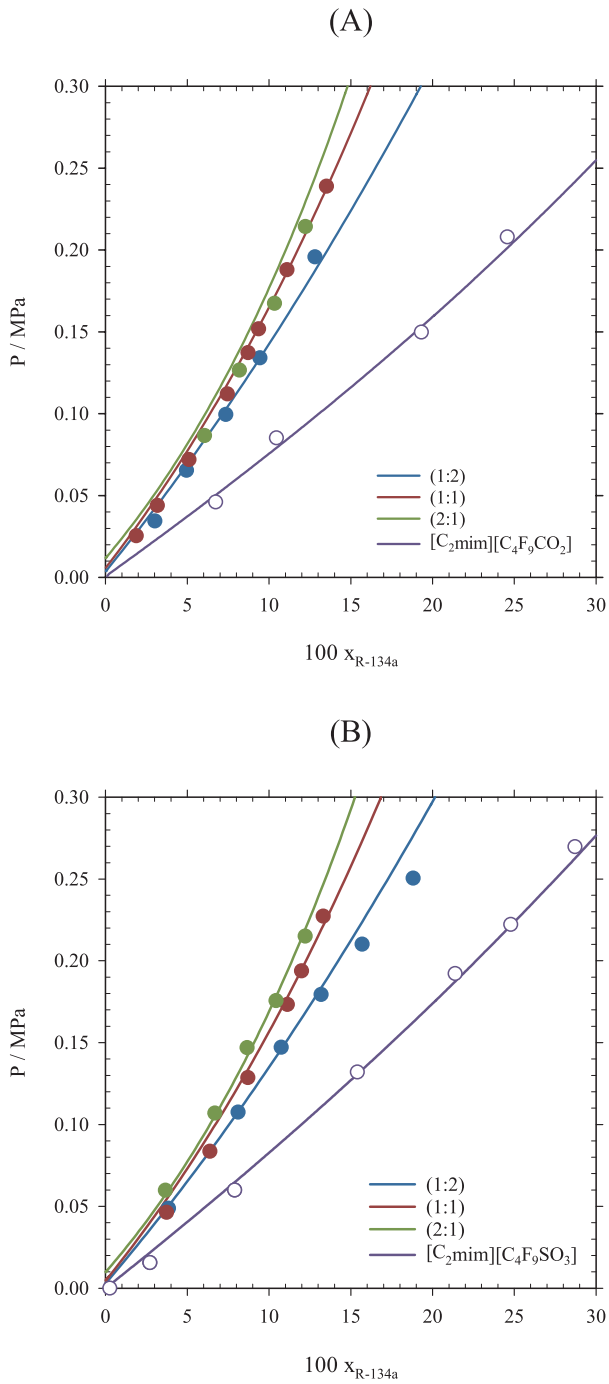

Figure 4.14: Pressure–composition diagrams at 303.15 K of R-134a with (a) $[C_2mim][Cl]:[HC_4F_9CO_2]$ and (b) $[C_2mim][Cl]:[HC_4F_9SO_3]$ at different molar ratios. The solubilities of R-134a in pure $[C_2mim][C_4F_9CO_2]$ and $[C_2mim][C_4F_9SO_3]$ are also included in panels (a) and (b), respectively. Symbols represent the experimental data from this thesis, empty symbols represent experimental data from Sosa et al. (2019), and solid lines are the soft-SAFT calculations.

the FILs, $[C_2mim][C_4F_9CO_2]$ and $[C_2mim][C_4F_9SO_3]$, so the physical meaning and coherence between parameters are preserved. More importantly, the model can accurately reproduce the solubility of R-134a in the DESs at the three different proportions, with no deterioration of the results when predicting the (1:2) and (2:1) ratios.

From the soft-SAFT calculations, it is possible to describe the density of $[C_2mim][Cl]$:$HC_4F_9SO_3$ in a fully predictive manner at any proportion. The results obtained at the (1:2), (1:1), and (2:1) ratios are plotted in Figure 4.15. The densities obtained follow, again, a decreasing linear trend with the temperature. Overall, they are higher than for the $[C_2mim][Cl]$:$HC_4F_9CO_2$ as was expected due to the higher weight of the molecule.

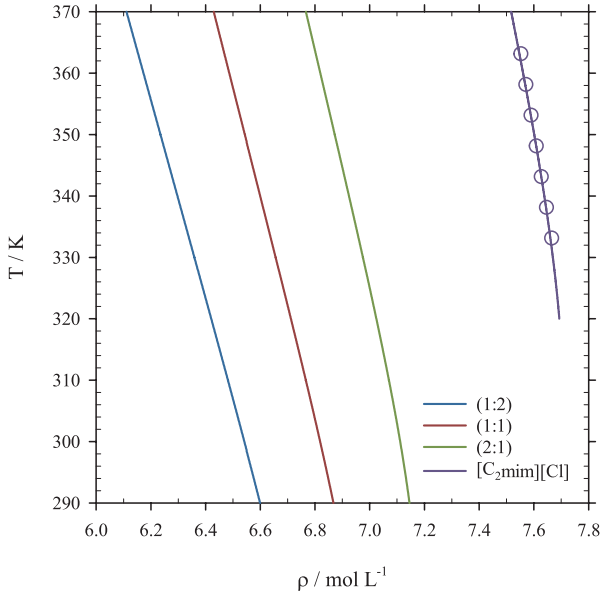

Figure 4.15: Soft-SAFT prediction for the density of $[C_2mim][Cl]$:$[HC_4F_9SO_3]$ as a function of temperature for different molar ratios. The density of pure $[C_2mim][Cl]$ is also included. Empty symbols represent experimental data from Mac Dowell et al. (2014), and solid lines are the soft-SAFT calculations.

Finally, from the description of the R-134a solubility in DESs, Henry's constants (k_H) have been predicted for the investigated DESs using equation 4.1.

The coefficients obtained with soft-SAFT are shown in Figure 4.16. The coefficients are higher than those found for $[C_2mim][C_4F_9CO_2]$ ($k_H = 0.73$ MPa) and $[C_2mim][C_4F_9SO_3]$ ($k_H = 0.81$ MPa), as it was expected as a consequence of the lower solubility of R-134a in the DESs. It can be noticed that the values for the $[C_2mim][Cl]$:$HC_4F_9CO_2$ are all very similar as a consequence of the similar trends in solubility observed at all proportions. Concerning $[C_2mim][Cl]$:$HC_4F_9SO_3$, the 1:2 ratio exhibits the lowest Henry's constant, indicating a higher solubility at infinite dilution.

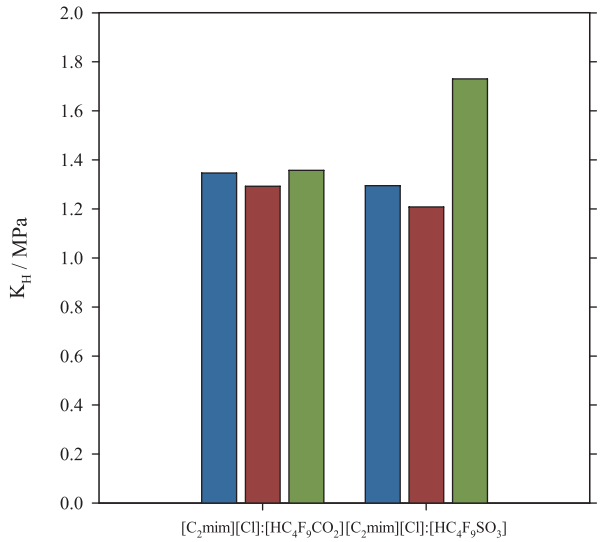

Figure 4.16: Calculated Henry's law constants for DESs for 1:2 (blue), 1:1 (red) and 2:1 (green) molar ratio.

4.5 Process design for separating fluorinated refrigerants using ionic liquids

As explained in previous sections, the refrigeration industry is currently transitioning to the next generation of low-GWP refrigerants, such as hydrofluoroolefins (HFOs) and HFO/HFC refrigerant blends, to replace HFCs in many applications (Booten et al., 2020). As some of the current HFCs will still be used in mixed blends with other compounds, there is an increasing interest in separating and recycling the compounds involved in current HFCs mixtures. Among them, R-32 is of particular interest, given the fact that it is found in several new formulations, such as R-463A, a mid-GWP (1494) blend developed as a non-flammable (A1) R-410A alternative, which is a mixture of R-32, R-125, R-1234yf, R-134a and CO_2. In addition, higher GWP HFCs, such as R-125, can be potentially utilized as new feedstocks for fluorinated polymers (Finberg & Shiflett, 2021) or even as a recycled refrigerant in new formulations since current legislation allows its usage as far as it is recycled.

The main issue related to the separation of these compounds is the fact that the vast majority of these blends include azeotropic or near-azeotropic mixtures, which cannot be split using traditional distillation methods, requiring an additional solvent (an entrainer) to alter the liquid phase in order to modify the volatility of each compound to have a more efficient separation. The entrainer absorbs one of the blend's components, allowing the other compound to be distilled out of the top of the column. The entrainer and the absorbed compound are separated in further stages, generally with a flash tank or a stripping column.

Several studies have addressed the viability of ILs as entrainers, primarily for aliphatic/aromatic hydrocarbon separation (Díaz et al., 2016; Ferro et al., 2015; S. García et

al., 2010), but also for HFCs mixtures. Being R-410A and R-407F two of the most common refrigerant mixtures used in the refrigeration sector, and given the fact that these blends contain R-32, R-125, and, for the R-407F case, R-134a, whose absorption in different solvents has been studied in detail in previous Sections, the technical viability of recovering its individual compounds for further reuse is evaluated next.

Two separation processes (an extractive distillation for the separation of R-410A and an absorption process for the separation of R-407F) are studied using the traditional IL $[C_2mim][Tf_2N]$ and the FIL $[C_2mim][C_4F_9CO_2]$ as solvents, respectively using Aspen Plus process simulator.

The selection of both solvents is based on the results obtained in this thesis. For R-410A, $[C_2mim][Tf_2N]$ IL showed a great selectivity and absorption capacity, and its low viscosity would favor the separation in terms of mass transfer phenomena. In the same line, $[C_2mim][C_4F_9CO_2]$ showed the greatest solubility in R-134a. Given the scarce amount of experimental data to adjust a model as required in process design, a novel methodology based on the COSMO-RS thermodynamic package integrated into Aspen Plus process simulator is used to achieve, as an objective, an R-32 purity of 98 wt %. More details regarding this selection are provided in the following subsections.

4.5.1 Property model specification and component definition in Aspen Plus

The absorption process has been modeled in Aspen Plus v11 (37.0.0.395) using the COSMO-SAC (**CO**nductor-like **S**creening **MO**del with **S**egment **A**ctivity **C**oefficient) property model (see section 3.4.1).

COSMO-RS calculations for each independent cation-anion conforming both ILs are performed. When available, the considered species were added from the COSMObase libraries. For the anion and cation, optimized structures were generated with TmoleX software v.21.0.1 (Balasubramani et al., 2020) using the triple-ζ valence potential (def-TZVP) basis with the Becke and Perdew (BP) functional at the density functional theory (DFT) level using the resolution of identity (RI) approximation and a convergence criterion of 10^{-6} Hartree, following the recommendations of other authors (Aldawsari et al., 2020; García-Gutiérrez et al., 2016; Sosa et al., 2020). COSMO files were then generated from the optimized structures by applying the COSMO solvation model at the same quantum-chemical computational level. The files were used as an input in COSMOThermX software v.21.0 (Dassault Systèmes, 2020) and its parametrization BP_TZVP_C30_1701 to perform COSMO-RS calculations to obtain the molecular volume and σ-profiles required by the fluid package. The σ-profile is represented in Figure 4.17, where the probability distribution (y-axes) of a molecular surface segment having a specific charge density (x-axes) is plotted. All six parameters are obtained using COSMO-RS

calculations. Note that the quantum-chemical calculations are only required for the ILs employed, as the model information for the F-gases is already included in Aspen Plus database.

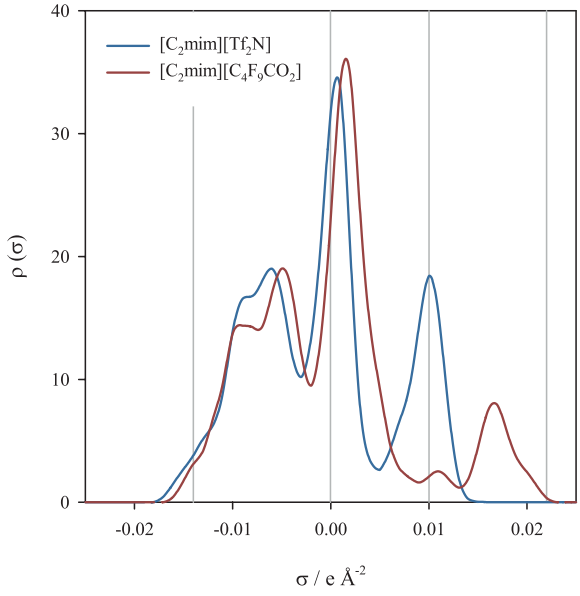

Figure 4.17: σ-profile for the molecules considered.

It should be noted that the σ-profile for the ILs considered is obtained as the sum of the cation and anion σ-profiles. The obtained σ-profiles are presented in Figure 4.17 and Table 4.8.

R-32, R-125, and R-134a F-gases are introduced as conventional components from the Aspen Plus database, whereas the ILs [C_2mim][$C_4F_9CO_2$] and [C_2mim][Tf_2N] are incorporated as pseudocomponents. The boiling point, critical temperature, critical pressure, critical compressibility factor, and acentric factor were all calculated using Valderrama and coworkers' modified Lydersen-Joback-Reid group contribution method (Valderrama et al., 2012). For the case of [C_2mim][Tf_2N], Shariati et al. (2013) provided new parameters for the critical properties and acentric factor using the Peng-Robinson equation of state and the differential evolution optimization. The temperature-dependent properties include heat capacity, viscosity, and density of the selected IL, which were retrieved from experimental data when available (Jacquemin et al., 2007; Paulechka et al., 2007; Schreiner et al., 2010; Vieira et al., 2015). When data was missing, it was estimated from Valderrama's group contribution method (Valderrama et al., 2011) based on the mass connectivity index (Valderrama & Rojas, 2010). The measurements were implemented in Aspen Plus and regressed in the desired range of temperature and pressure. Data regression is based on the Least Absolute Residuals (LAR) method together with the Levenberg–Marquardt algorithm. The negligible vapor pressure of the FIL was taken into account by setting the extended Antoine equation implemented in Aspen plus (equation 3.80) to an imaginary value of -1×10^{18} (García-Gutiérrez et al., 2016; Shiflett et

Table 4.8: σ-profile values for the $[C_2mim][Tf_2N]$ and the $[C_2mim][C_4F_9CO_2]$ molecules.

SGPRF-1												
	1	**2**	**3**	**4**	**5**	**6**	**7**	**8**	**9**	**10**	**11**	**12**
$[C_2mim][Tf_2N]$	0	0	0	0	0	0	0	0.02933	0.5117	1.585	2.708	3.818
$[C_2mim][C_4F_9CO_2]$	0	0	0	0	0	0	0	0	0.01700	0.5020	1.753	3.119
SGPRF-2												
	1	**2**	**3**	**4**	**5**	**6**	**7**	**8**	**9**	**10**	**11**	**12**
$[C_2mim][Tf_2N]$	5.163	6.280	8.911	13.90	16.55	16.80	18.02	19.01	16.83	12.22	10.20	13.40
$[C_2mim][C_4F_9CO_2]$	4.220	6.838	9.682	13.72	14.38	14.27	14.28	17.01	19.02	17.24	12.10	9.493
SGPRF-3												
	1	**2**	**3**	**4**	**5**	**6**	**7**	**8**	**9**	**10**	**11**	**12**
$[C_2mim][Tf_2N]$	21.33	31.84	33.53	20.35	7.644	3.381	2.641	4.178	6.604	9.345	14.46	18.42
$[C_2mim][C_4F_9CO_2]$	13.54	23.21	34.24	34.65	23.48	14.35	9.210	4.834	2.743	2.003	1.611	2.098
SGPRF-4												
	1	**2**	**3**	**4**	**5**	**6**	**7**	**8**	**9**	**10**	**11**	**12**
$[C_2mim][Tf_2N]$	15.31	7.754	2.167	0.2845	0.02950	0	0	0	0	0	0	0
$[C_2mim][C_4F_9CO_2]$	2.518	1.913	1.207	1.873	4.435	7.394	7.907	5.682	3.570	2.462	1.342	0.3600
SGPRF-5												
	1	**2**	**3**									
$[C_2mim][Tf_2N]$	0	0	0									
$[C_2mim][C_4F_9CO_2]$	0.01100	0	0									

al., 2011). Both the scalar properties and the coefficients for each correlated property model are available in Tables 4.9 and 4.10, respectively. The correlations for such properties are presented in section 3.4.1 in equations 3.76-3.80.

4.5.2 Property package validation

COSMO-RS-based simulation results were validated by comparing experimental solubility measurements (Shiflett & Yokozeki, 2006c; 2008; Sosa et al., 2019) with those calculated with Aspen Plus. The comparison was made for all three fluorinated gases forming the HFCs blends considered in the following simulations (i.e., R-32, R-125, and R-134a) by simulating a simple equilibrium flash model and setting the desired output pressure and temperature. It should be noted that COSMO-RS calculations are directly performed in Aspen Plus to obtain the desired properties (See section 3.1 in chapter 3).

As it can be seen from figures 4.18 and 4.19, COSMO-based Aspen predictions are capable of faithfully reproducing the gas solubility in the selected ILs and give acceptable deviations in terms of absolute average deviation for both [C_2mim][$C_4F_9CO_2$] (R-32 = 4.09%, R-125 = 18.79%, and R-134a = 12.00% for) and [C_2mim][Tf_2N] (R-32 = 9.97%, R-125 = 19.82%) ILs in the whole range of thermodynamic conditions for which experimental data have been reported. Although the prediction worsens with the length of the alkyl chain and the pressure, the observed error is constant in the whole range, and the results have comparable accuracy to those published by other authors in similar studies where the solubility of gases in ILs was predicted with COSMO-RS (García-Gutiérrez et al., 2016; Manan et al., 2009; Sosa et al., 2020).

4.5.3 R-410A separation process

This section focuses on evaluating the technical viability of the separation and recovery of the individual components of refrigerant blend R-410A, which will be phased out in air-conditioning applications (see Chapter 2). Based on the results obtained from section 4.4.1, the IL [C_2mim][Tf_2N] is selected, and a process simulation of the recovery unit through an extractive distillation process is performed to estimate the approximate energy cost of the separation process. As mentioned, the condition is to recover R-32 with a minimum of 98 wt % purity.

Following the scheme proposed by Shiflett and Yokozeki (2006b), 2014, the process consists of the main distillation column for the separation of R-32 and R-125 followed by a flash tank for the regeneration of [C_2mim][Tf_2N] and an IL recirculation including a pump with a heat exchanger to cool the IL before returning to the main column (see figure 4.20).

The inlet flow of R-410A introduced to the process was fixed to 10 $\mathrm{kg\,h^{-1}}$ and is considered an equimassic mixture of R-125 and R-32. A consistent heuristic in most simulations is that

Table 4.9: Scalar properties for $[C_2mim][C_4F_9CO_2]$ & $[C_2mim][Tf_2N]$.

Property	$[C_2mim][C_4F_9CO_2]$	$[C_2mim][Tf_2N]$
Molecular weight ($g\,mol^{-1}$)	374.21	391.31
Normal boiling point (K)	627.97	805.93
Density at 60°F $g\,cm^{-3}$	1.49616	1.4820
Critical temperature (K)	814.44	906.91
Critical pressure (bar)	15.285	29.160
Critical volume ($cm^3\,mol^{-1}$)	847.56	892.89
Critical compressibility factor	0.19131	0.21028
Pitzer acentric factor	0.71376	0.42230
COSMO Volume, ($Å^3$)	365.45	376.70

Table 4.10: Temperature-dependent properties for $[C_2mim][C_4F_9CO_2]$ & $[C_2mim][Tf_2N]$.

$[C_2mim][C_4F_9CO_2]$								
Parameter	Physical Property	Property Units	C1	C2	C3	C4	C5	T range (K)
CPLPO	Heat Capacity	$J\,kmol^{-1}\,K^{-1}$	566.7	41.14	-1.729	-4.120E-04	-6.000E-03	250 - 550
DNLDIP	Liquid density	$mol\,cm^{-3}$	4.690E-04	0.3119	1130	0.5964		250 - 500
MULDIP	Liquid viscosity	cP	-217.1	1383E+1	30.78			250 - 500
PLXANT	Vapor Pressure	bar	-1.0000E+18					200-600
$[C_2mim][Tf_2N]$								
CPLPO	Heat Capacity	$J\,kmol^{-1}\,K^{-1}$	35132E+1	491.20	-0.059570	5.4800E-05		0 - 1000
DNLDIP	Liquid density	$kmol\,m^{-3}$	0.35341	0.27578	1100.4	0.47778		-273.15 - 726.85
MULAND	Liquid viscosity	cP	-166.59	10367	23.745			250 - 500
PLXANT	Vapor Pressure	bar	-1.0000E+18					200-600

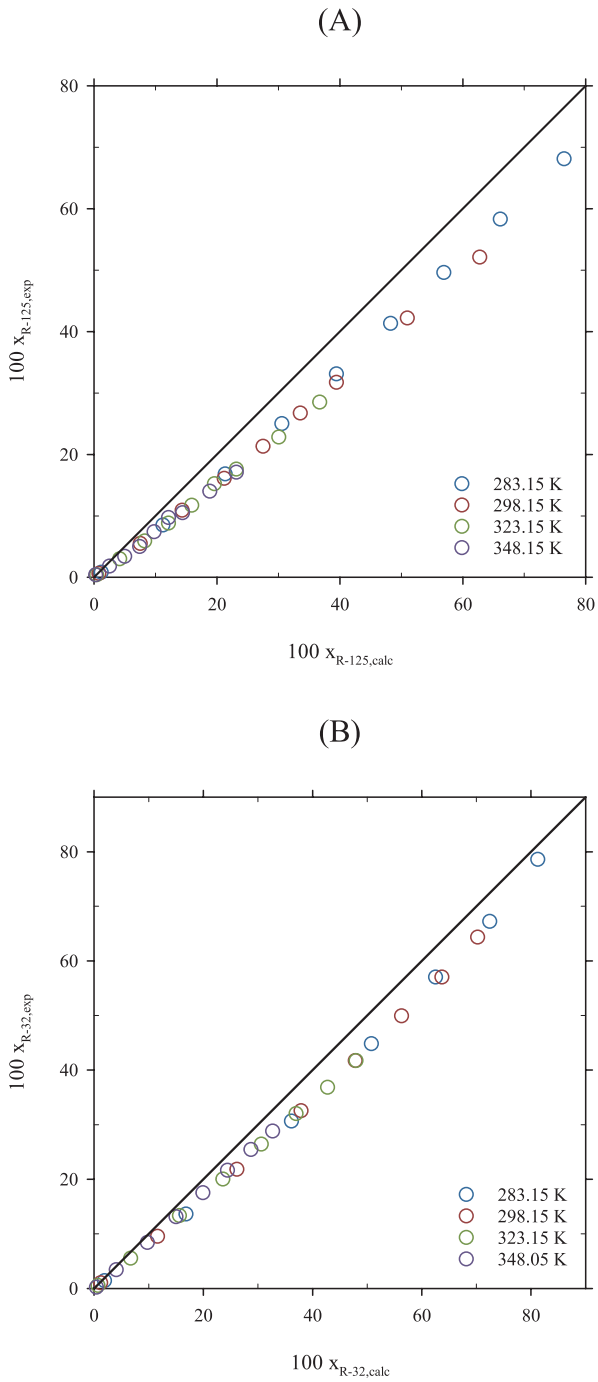

Figure 4.18: Validation of the solubility of several gases in $[C_2mim][Tf_2N]$. Prediction from the COSMO-RS-based simulation approach with experimental data from Shiflett and Yokozeki (2006c), 2008 for R-125 (A) and R-32 (B) at different temperatures.

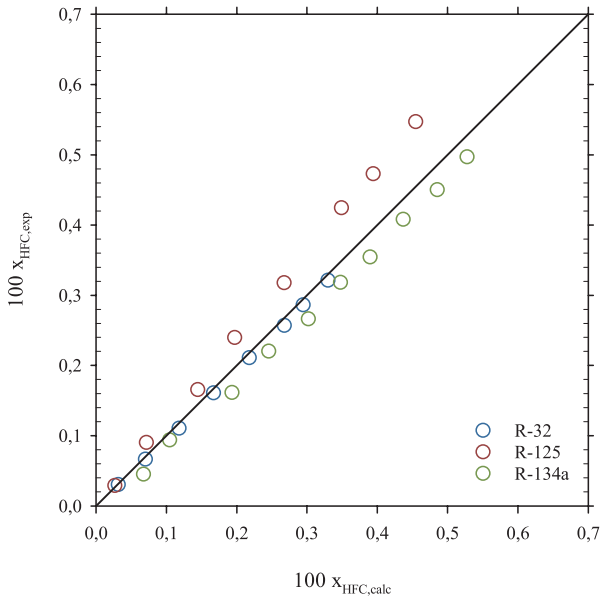

Figure 4.19: Validation of the solubility of several gases in $[C_2mim][C_4F_9CO_2]$. Prediction from the COSMO-RS-based simulation with experimental data from Sosa et al. (2019).

a liquid-phase refrigerant will result in a higher distillate purity compared to a vapor-phase feed (Finberg & Shiflett, 2021), so R-410A has been introduced at 20 °C and pressurized at 14 bar (vapor fraction = 0 as specification). The IL enters at the same pressure and temperature. Several configurations were tested to select the most appropriate column configuration to reach a purity of 98 wt % of R-32. Special care has also been put on the condenser and reboiler temperatures to avoid the need for a low-temperature thermostat and to avoid IL decomposition. Therefore, $T_{\text{condenser}} > 15°C$ and $T_{\text{reboiler}} < 200$ °C.

Several pre-calculations have shown that a column with 32 stages, including the reboiler and the condenser, is necessary to reach the purity requirements for R-32. The column operates at 1.4 MPa and has been modeled with the Aspen RadFrac module. Due to the non-ideal nature of the mixture, the column must be converged in two phases. In the first iteration, the highly non-ideal convergence method was selected, and the key components of the three-phase equilibrium were established. To make the column numerically more robust, a second iteration comprises a custom convergence method that uses the Newton-Raphson algorithm. A maximum of 200 iterations have been considered along with Powell's algorithm to find local minimums of functions. The IL and the refrigerant mixture have been fed through stages 2 (because the ionic liquid has essentially no measurable vapor pressure (Finberg & Shiflett, 2021)) and 18, respectively, with a molar reflux ratio of 4 and a $[C_2mim][Tf_2N]$ flow rate of 170.1 $\mathrm{kg\,h^{-1}}$ in order to meet the specified separation requirement.

The flash drums have been modeled with the Aspen two-outlet flash module, and the operating temperature has been set equal to the reboiler temperature (137.84 °C). The fluid is

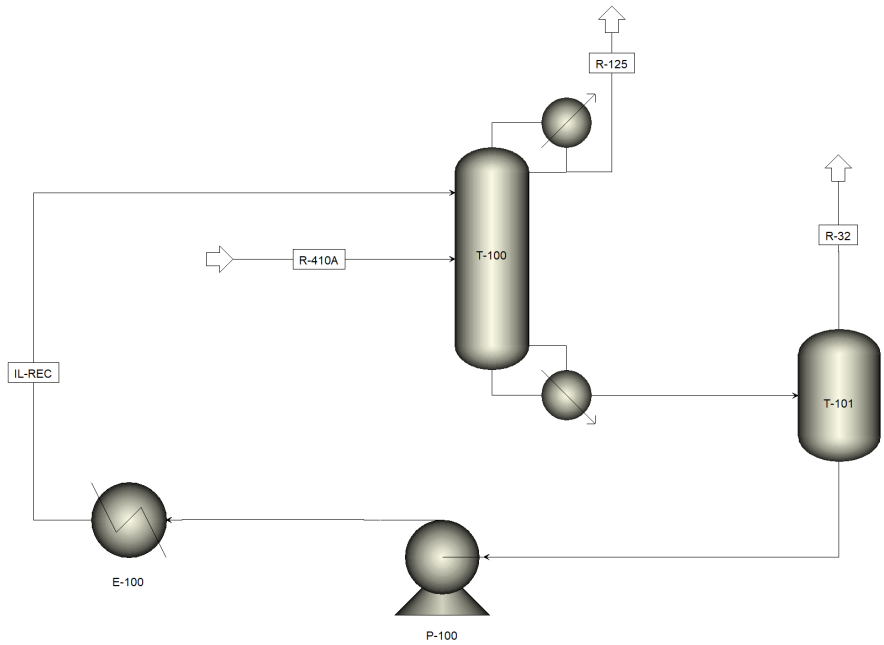

Figure 4.20: Main process flowsheet of a separation unit of the R-410A blend using [C_2mim][Tf_2N] as entrainer. The diagram contains a distillation column (T-100) for the removal of R-125, followed by a flash tank (T-101) to regenerate the IL and remove R-32. The IL recirculation line includes a pump with a heat exchanger to cool the IL before returning to the main column.

depressurized in the flash tank so that part of the fluid can be vaporized for further separation. No IL is vaporized, and gaseous R-32 is obtained through the flash drum's heads. The flash drum is operated adiabatically. The pressure drop is set at 13.99 bar.

Due to the pressure and temperature changes that the IL undergoes during the separation process, the solvent recycled must be pressurized again, and its temperature must be lowered to the feed temperature. For this purpose, a pump and heat exchanger are provided to recirculate the entire solvent used in the separation. The IL is then recirculated to the column with minimal traces of R-32 and R-125.

Table 4.11 shows the Aspen Plus simulation results for the separation of R-410A using [C_2mim][Tf_2N] as entrainer. To achieve complete separation, the distillate rate should equal the mass fraction of one component multiplied by the feed (i.e., $z_i F$), resulting in the component leaving the distillate. With the considered implementation, a recovery of 97.94% with respect to the initial feed of R-410A is obtained. R-32 is mostly absorbed in the IL and later recovered in the flash drum heads at 98 wt %, while R-125 exits at the top of the column with high purity (also 98 wt %), which makes the fluorinated gas reusable. Here, it is important to note that, although R-125 is a high GWP whose production has been phased-out in Europe ("Regulation (EU) No 517/2014 of the European Parliament and of the Council of 16 April

2014 on fluorinated greenhouse gases and repealing Regulation (EC) No 842/2006", 2014), recycling of this compound is permitted for reuse mixed with other lower GWP compounds.

Table 4.11: Aspen Plus simulation results for the separation of R-410A.

Feed	
Flow rate ($\mathrm{kg\,h^{-1}}$)	10.00
R-32 flow rate ($\mathrm{kg\,s^{-1}}$)	5.000
R-125 flow rate ($\mathrm{kg\,s^{-1}}$)	5.000
R-410A inlet temperature (°C)	25.00
[C_2mim][Tf_2N] flow rate ($\mathrm{kg\,h^{-1}}$)	170.1
[C_2mim][Tf_2N] inlet temperature (K)	25.00
Main Column	
Condenser temperature (°C)	25.08
Condenser heat duty (kW)	-0.8920
Distillate rate ($\mathrm{kg\,h^{-1}}$)	5.000
R-125 overhead mass fraction	0.9800
Reboiler temperature (°C)	137.8
Reboiler heat duty (kW)	8.731
Bottoms rate ($\mathrm{kg\,h^{-1}}$)	175.1
Operating pressure (MPa)	1.400
Theoretical stages	32
R-410A feed stage	2
[C_2mim][Tf_2N] feed stage	18
Flash Drum	
Outlet Pressure (MPa)	0.001000
Outlet temperature (°C)	138.2
R-32 overhead flow rate ($\mathrm{kg\,h^{-1}}$)	4.997
R-32 overhead mass fraction	0.9800
Cooler	
Net duty (kW)	-7.345
Pump	
Net Work Required (kW)	0.07708

Overall, the energy consumption of the process is moderate and within the same range as earlier simulations reported for the same mixture utilizing other imidazolium-based ionic liquids as entrainers (Shiflett & Yokozeki, 2006b) or the same as in this subsection (Finberg & Shiflett, 2021). Despite being relatively high, the L/G ratio of the fluorinated blend and the ionic liquid also falls within the same range as those reported in the literature. Note that in extractive distillation processes, it is common to use between 1 and up to even 30 times as much solvent as feed; thus, the solvent concentration in the middle section is often relatively high (Wankat, 2007).

A sensitivity analysis has also been conducted to test the effect of the pressure on the (L/G) ratio and on the R-32 recovery. This is graphically shown in Figure 4.21. The use of higher pressures would, in theory, require fewer theoretical stages (or packing height) to achieve the desired refrigerant purity due to the increase of the refrigerant solubility in the IL entrainer

(Finberg & Shiflett, 2021). Since the total number of stages was fixed in the considered implementation, this results in higher recoveries with the same (L/G) ratio. In any case, one must not forget that, apart from significant energy consumption and economic cost, an increase in the pressure results in an increase in T_{Reboiler}, which is limited by the thermal decomposition of the selected IL.

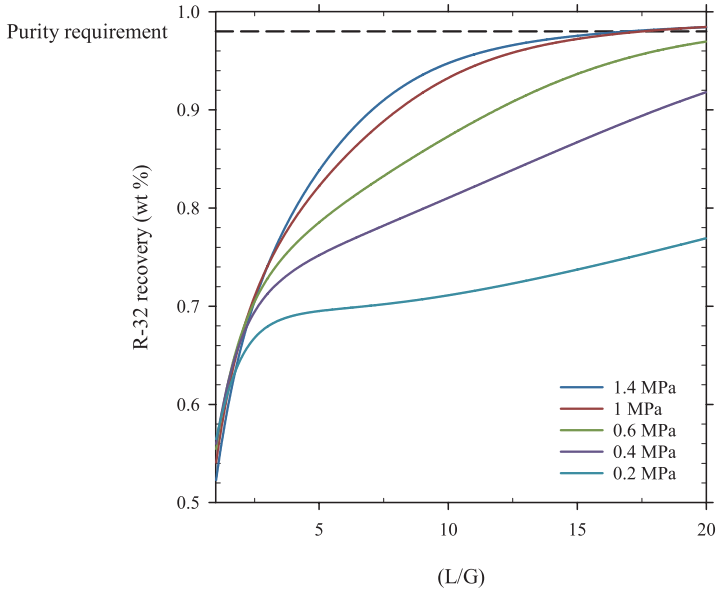

Figure 4.21: Influence of the pressure on the L/G ratio and on the recovery performance.

4.5.4 R-407F separation process

The flow diagram of the absorption process studied in this subsection is depicted in Figure 4.22. It consists of an absorption column for the separation of R-32 from the original R-407F blend using $[C_2mim][C_4F_9CO_2]$ as absorbent, followed by a flash tank for the regeneration and recycling of the FIL. The recirculation stream includes a pump (P-100) and a heat exchanger to cool down the FIL before returning to the main column. R-407F is assumed to arrive bottled at 8 bar and ambient temperature (25 °C) and is heated up to 45 °C (E-100) and fed countercurrently at a rate of 1000 $\mathrm{kg\,h^{-1}}$ in the absorption column (T-100) with the FIL at 14 °C and 8 bar.

R-125 and R-134a are selectively absorbed, and an enriched R-32 gas stream is released from the top of the absorber. The FIL solution with the absorbed R-125 and R-134a is fed into the flash drum (T-101). The FIL is then regenerated by a pressure swing (i.e., reducing the pressure to 0.01 bar) and cooled down to 14 °C (E-101) before it is recycled back to the absorption column for further reuse. The desorbed gases are released in the vapor stream of the flash drum.

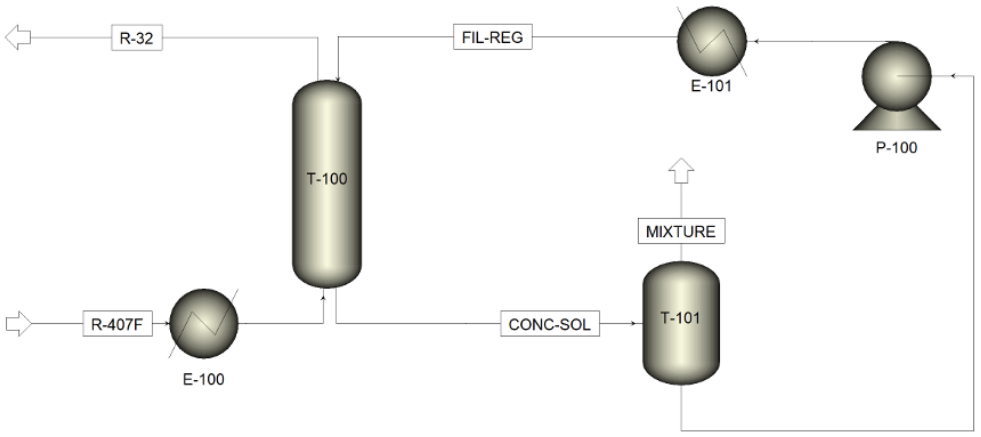

Figure 4.22: Complete Process Scheme Used for the separation of R-407F.

The absorber has been modeled using the RadFrac module available in Aspen Plus. The equilibrium approach, in which the liquid and vapor phases are assumed to be in equilibrium, is chosen together with the Petroleum/Wide-Boiling convergence algorithm. A purity of 98 wt % for R-32 is set as a design specification, using the FIL rate as a manipulated variable, to ensure adequate performance of the recycled refrigerant. The utilities used in the simulation for the duties of the pump and the two heat exchangers were electricity (pump P-100 and heater E-101) and low-pressure steam (heater E-100). A pump and driver efficiencies of 0.65 and 0.85 were considered, respectively (Sosa et al., 2020).

The main results for the Aspen Plus simulation are presented in Table 4.12. The results show that a column with 38 theoretical stages, the minimum number in which the module converged, is necessary to achieve an R-32 purity of 98 wt %.

Table 4.12: Main results of the Aspen Plus simulations for the separation of R-32 from the R-407F blend.

R-407F feed ($\mathrm{kg\,h^{-1}}$)	1000.00
R-32 separated (98 wt %) ($\mathrm{kg\,h^{-1}}$)	90.90
Fluorinated ionic liquid feed ($\mathrm{kg\,h^{-1}}$)	5774.07
R-32 recovery (%)	30.30
ratio L/G (kg FIL/kg R-407F)	5.77
Annual R-32 production (t R-32)	719.94
Absorber (T-100) theoretical stages	38
Absorber (T-100) operating pressure (bar)	8
Cooler electrical consumption (kWh)	7.03
Heater consumption (kWh)	4.64
Pump electrical consumption (kWh)	1.56

A working pressure of 8 bar has been fixed as a compromise between an acceptable R-32 recovery ratio and low energy consumption. Overall, the energy consumption of the process

is modest (see Table 4.12) given the relatively low operation flows and the moderate temperature operation range. Further insight will be given into this aspect in section 4.6.

A 30.3% recovery of R-32 is achieved using 5774 $\mathrm{kg\,h^{-1}}$ of FIL $[C_2mim][C_4F_9CO_2]$, which is also recovered and recycled. The recovery of R-32 obtained in a similar L/G ratio and pressure conditions is in the same range as those published by other authors for diluted mixtures of R-32 in argon using similar FILs (Sosa et al., 2020). Sensibly lower values of the L/G ratio are obtained (5.77) compared to similar absorption separation processes involving imidazolium-based ionic liquids for the capture of CO_2 and tetrafluoroethylene (11.7–70.0) (García-Gutiérrez et al., 2016; Shiflett et al., 2011). The results corroborate the adequacy of the FIL selected and provided, for the first time, a technology process for separating R-32 from a ternary mixture in an efficient-sustainable way.

4.6 Case study: LCA of the separation and recycling of fluorinated gases using IL

Based on the results obtained from the simulation presented in section 4.5.4, the environmental sustainability of the recovery process was analyzed with an LCA approach, comparing the obtained results with the conventional R-32 production. The LCA study follows the methodology proposed by B. Wu et al. (2019). The cradle-to-gate life cycle environmental impacts of the R-32 recovery (circular economy scenario) with FIL from the R-407F mixture and the R-32 industrial production (Benchmark scenario) were calculated with the software SimaPro (version 9.0).

The main objective of this section is to build an integrated LCA framework, comparing the life cycle environmental impacts among the recovery of the R-32 from used refrigerant mixtures using the FIL $[C_2mim][C_4F_9CO_2]$ and the R-32 industrial production. The scope of this study comprises (B. Wu et al., 2019):

1. The construction of the life cycle framework and LCI analysis for the two scenarios (R-32 recovery vs R-32 production).
2. A comparison of the LCIA of the studied scenarios.
3. An uncertainty analysis using Monte Carlo methodology to verify the robustness of the obtained results.
4. A sensitivity analysis to recognize the most important factors affecting the environmental impacts.

The system's boundary is shown in Figure 4.23 and includes all the processes of the R-32 recovery and R-32 production scenarios. It also includes transportation processes, which are omitted in the diagram to facilitate the interpretation. The process proposed is considered

a closed-loop recycling in which the recovered R-32 has the same quality and value as the produced R-32, so it can be recycled indefinitely without losing quality or functional (cooling) properties. Based on this assumption, allocation procedures for the burdens associated with avoiding the production of fresh R-32 and its incineration were not considered to simplify the LCA.

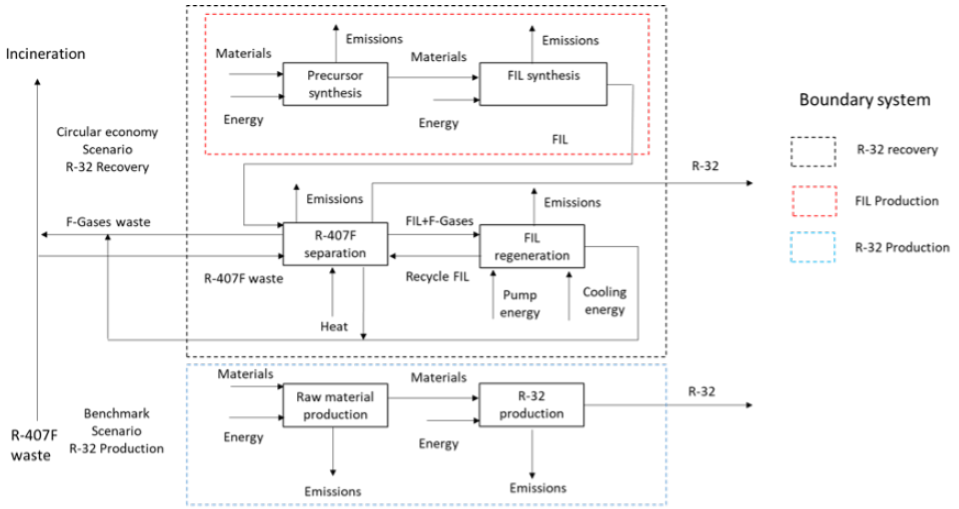

Figure 4.23: LCA system boundary of the R-32 recovery and production scenarios. The system boundary includes transportation processes, although they are omitted in the diagram to facilitate the diagram's interpretation.

The LCI of the R-32 recovery contains all the inputs and outputs (mass and energy), and the emissions associated with the precursors' production, FIL production, F-gases separation, and FIL regeneration. For precursors and FIL production, the LCI includes the upstream feedstock, auxiliary materials (i.e., catalyst), and energy consumption (i.e., cooling, heating...). The inventory of R-32 separation comprises the FIL inputs, losses, and energy consumption. The data for thermal energy (natural gas), electricity (electricity mix grid), chemical plants (chemical factory, organics), transportation (freight, lorry 16-32 t), and EoL of the wasted FIL (hazardous waste incineration) are obtained from Ecoinvent 3 (Wernet et al., 2016).

The precursors and the used FIL are not available in the LCI databases. The data for these compounds were obtained from the literature or process simulation (PS) (B. Wu et al., 2019). Following the assumptions of published works (Hischier et al., 2005; B. Wu et al., 2019), it was considered an emission to the air of 0.2% of input materials in those processes without information in Ecoinvent except for the FIL, which is considered to have a negligible vapor pressure. For the precursors' production, the theoretical energy needed is industrially upscaled through the use of conversion factors (Cuéllar-Franca et al., 2016; B. Wu et al., 2019). The theoretical heat needed in endothermic reactions is multiplied by a factor of 4.2, considering that the heat is obtained from natural gas. In the case of exothermic reactions, the theoretical heat generated is multiplied by a factor of 3.2, considering cooling electricity from the Spanish electricity mix (B. Wu et al., 2019).

4.6.1 Material and energy flow analysis

In order to understand the use of materials and their transformation during R-32 recovery, a material flow analysis (MFA) is carried out considering the separation of 1 kg of R-32 from the R-407F blend with a purity higher than 98 wt %. Figure 4.24 shows the results obtained from the MFA. According to the results of the simulated process (see section 4.5.4), the FIL is completely regenerated for further reuse. However, it is possible that, after prolonged use, the FIL may lose separation efficiency. For that reason, it has been established that the FIL will be replaced after one year (considering a total FIL mass in the close circuit of 5774 kg). The effect of this parameter on the LCA will be assessed in the sensitivity analysis section (section 4.6.4). On the basis of this assumption and the simulation results, 0.008 kg of $[C_2mim][C_4F_9CO_2]$ are needed to separate 1 kg of R-32. For the production of 0.008 kg of $[C_2mim][C_4F_9CO_2]$, 0.036 kg of raw materials are needed (derived from the production of the cation and anion precursors, $[C_2mim][Br]$ and C_4F_9COOH, respectively).

The material flow data for the $[C_2mim][Br]$ production was obtained from published data (B. Wu et al., 2019), while C_4F_9COOH production material flow data was estimated through PS based on the process reported by Kauck and Diesslin (1951). The mass of the used FIL ($[C_2mim][C_4F_9CO_2]$) is 22.2 wt % of the total raw materials used in the precursors' production. The total amount of waste emission in the $[C_2mim][C_4F_9CO_2]$ production process is 0.013 kg, accounting for 36.4 wt % of the total raw materials. It is important to highlight the use of water during FIL production, accounting for 33.5 wt % of the emissions related to FIL production. In the FIL use stage, 0.008 kg of waste related to the FIL replacement is produced, accounting for 22.9 wt % of the total waste emission. Hydrogen chloride and hydrogen are byproducts produced during the production of pentanoyl chloride and C_4F_9COOH, respectively, which can be considered as *avoided products* (B. Wu et al., 2019). These byproducts stand for 3.2 wt % of the raw materials introduced in the system.

Figure 4.25 shows the energy flow analysis (EFA) of the recovery of 1 kg of R-32 considering the electricity and heat consumption (e.g., mixing, heating, pressurization, cooling) during the production of precursors and FIL and R-32 recovery. The energy consumption inventory in the $[C_2mim][Br]$ production is obtained from published studies (B. Wu et al., 2019). The energy consumption data of the C_4F_9COOH production, FIL synthesis, and the R-32 recovery process are obtained with the PS carried out in this study (Table 4.13). The results of the EFA show that the electricity consumption was 69.8% in the R-32 recovery, 30.0% in the FIL precursor production, and 0.2% in the FIL production. In the case of heat consumption, a similar distribution was observed (60.9% was in the R-32 recovery, 21.6% in the FIL precursors production, and 17.5% in the FIL production). From the EFA results, it is clear that the decrease in electricity and heat consumption during the R-32 recovery is a promising strategy to reduce the total life cycle energy consumption.

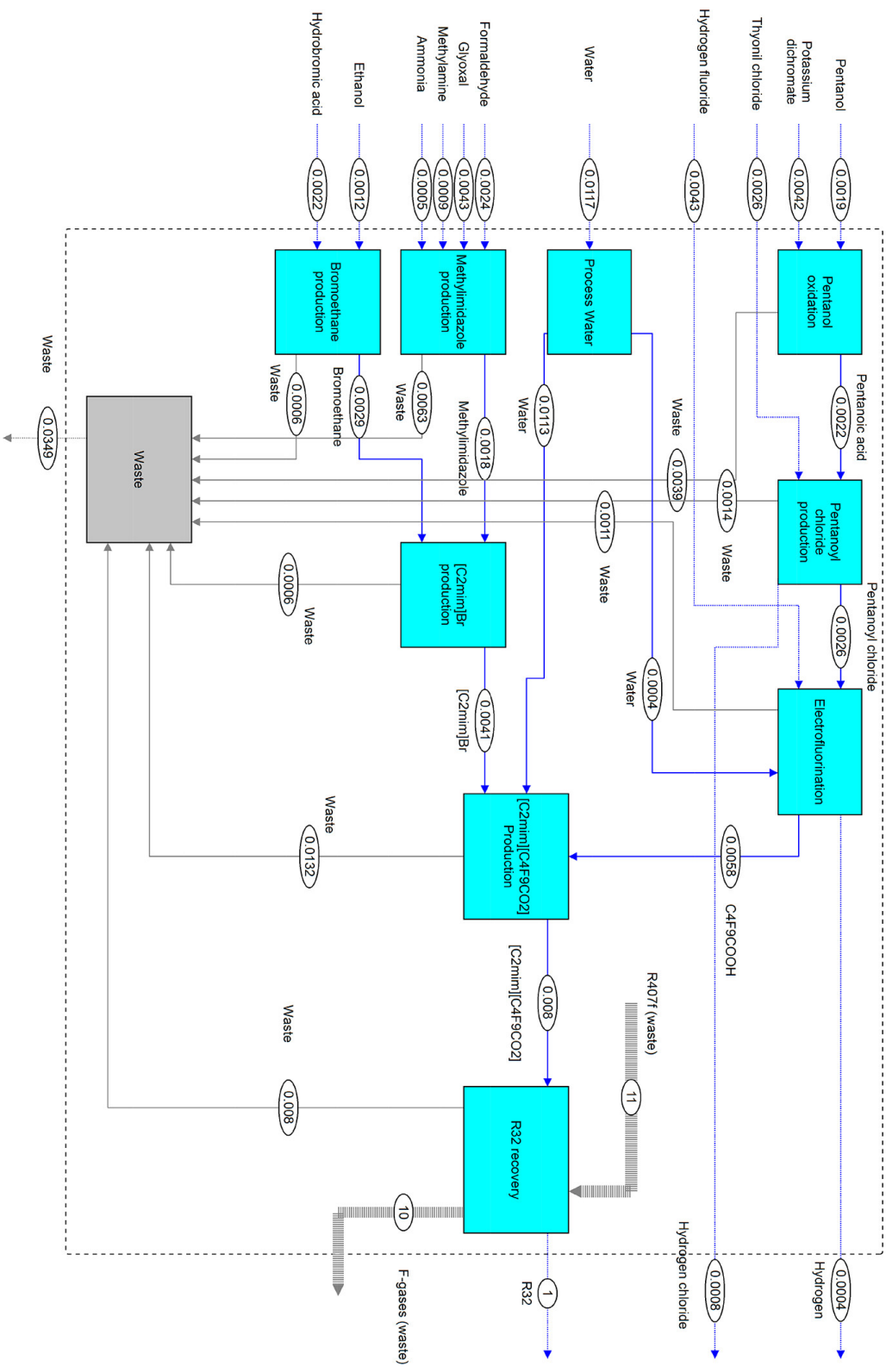

Figure 4.24: MFA for the recovery of 1 kg of R-32 using $[C_2mim][C_4F_9CO_2]$ as an absorbent. Units: kilogram. The thickness of the line shows the relative material flow.

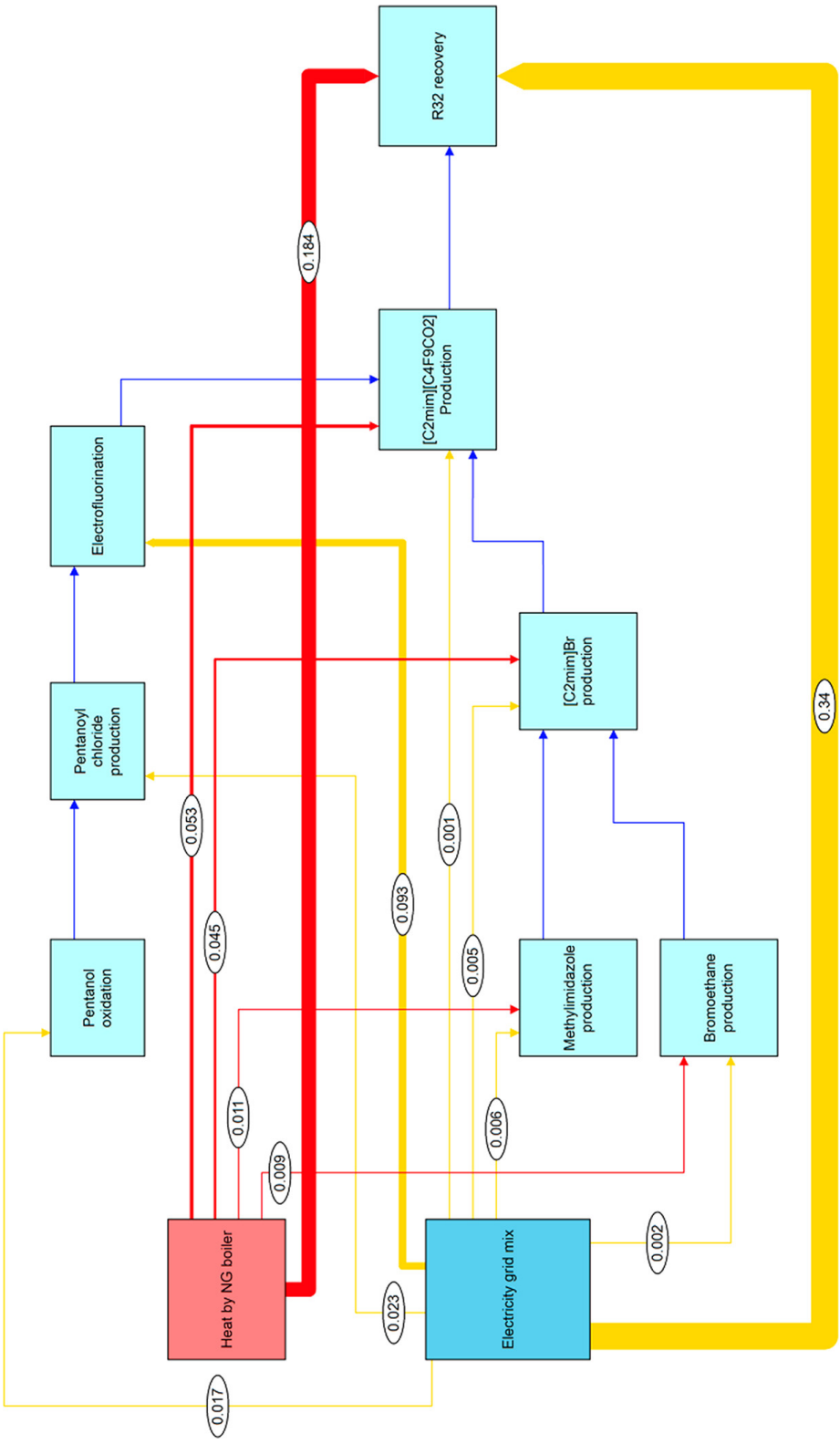

Figure 4.25: EFA for the recovery of 1 kg of R-32 using $[C_2mim][C_4F_9CO_2]$. Red arrows represent heat (MJ_{th}), while yellow arrows represent electricity (MJ_e). The thickness of the line shows the relative energy flow.

Table 4.13: LCI data for the production of 1kg of $[C_2mim][C_4F_9CO_2]$.

Inventory	Quantity	Unit	Data Source
Input			Vieira et al. (2015) and simulation work
$[C_2mim][Br]$	0.511	kg	
C_4F_9COOH	0.706	kg	
Water	1.411	kg	
Heat	6.63	MJ_{th}	
Electric Energy	0.12	MJ_e	
Output			
$[C_2mim][C_4F_9CO_2]$	1	kg	
Hydrogen bromide	0.216	kg	
Water	1.411	kg	
Input			Z. B. Liu (2018) and B. Wu et al. (2019)
N-methylimidazole	0.224	kg	
Bromoethane	0.357	kg	
Heat	5.57	MJ_{th}	
Electric Energy	0.594	MJ_e	
Output			
$[C_2mim][Br]$	0.511	kg	
Input			Righi et al. (2011) and B. Wu et al. (2019)
Glyoxal	0.531	kg	
Methylamine	0.114	kg	
Formaldehyde	0.297	kg	
Ammonia	0.064	kg	
Heat	1.4	MJ_{th}	
Electric Energy	0.7	MJ_e	
Output			
N-methylimidazole	0.224	kg	
Other	0.782	kg	
Input			Mehrkesh and Karunanithi (2013)
Ethanol	0.154	kg	
Hydrobromic Acid	0.273	kg	
Heat	1.12	MJ_{th}	
Electric Energy	0.254	MJ_e	
Output			
Bromoethane	0.357	kg	
Water	0.07	kg	
Input			Kauck and Diesslin (1951) and simulation
Pentanoyl chloride	0.322	kg	

Table 4.13 continued from previous page

Inventory	Quantity	Unit	Data Source
Hydrogen fluoride	0.535	kg	
Water	0,048		
Heat		MJ_{th}	
Electric Energy	11.596	MJ_e	
Output			
C_4F_9COOH	0.706	kg	
Water	0.07	kg	
Hydrogen fluoride	0.054	kg	
Hydrogen	0.049	kg	
Hydrogen chloride	0.097	kg	
Input			Larock (1999) and simulation
Pentanoic acid	0.273	kg	
Thionyl chloride	0.318	kg	
Heat		MJ_{th}	
Electric Energy	2.853	MJ_e	
Output			
Pentanoyl chloride	0.322	kg	
Sulphur dioxide	0.171	kg	
Hydrogen chloride	0.097	kg	
Input			Larock (1999) and simulation
Pentanol	0.236	kg	
Potassium dichromate	0.524	kg	
Heat		MJ_{th}	
Electric Energy	2.156	MJ_e	
Output			
Pentanoic acid	0.273	kg	
Chromium oxide	0.271	kg	
Potassium oxide	0.168	kg	
Water	0.048	kg	

4.6.2 Environmental impacts analysis of R-32 recovery

First, the distribution of the environmental impacts of the absorbent production (1 kg of FIL $[C_2mim][C_4F_9CO_2]$) in the different categories is provided in Figure 4.26 (A). The results show that the production of $[C_2mim][Br]$ and C_4F_9COOH has the largest contribution in all of the impact categories (contributions between 85 and 100%). Moreover, C_4F_9COOH has the most important contribution in all of the categories, excluding ADP (elements) (16.5%) and

HTP (14.9%). The impact category with the highest contribution is MAETP (94.3%), caused mainly by the emission of hydrogen fluoride. [C_2mim][Br] also has a severe contribution to the impact categories of the FIL production, ranging from 5 to 85%, depending on the category. [C_2mim][Br] has the most relevant contributions to the HTP (85.9%) and ADP (elements; 83.4%) categories.

As previously reported by B. Wu et al. (2019), the high contribution in the HTP category is attributed to the ethylene oxide emissions, which are considered toxic to humans. The contribution in the ADP (elements) is mainly caused by the extraction of bromine and chromium. However, the process energy (electricity and heat) accounts for the environmental impact in the range 0–14%, depending on the impact category. In the production of [C_2mim][$C_4F_9CO_2$], the transportation processes only account for 0.01–0.72% of the environmental impacts. Consequently, compared to the rest of the processes, the contribution of transportation to the life cycle impacts of the [C_2mim][$C_4F_9CO_2$] production can be omitted. The LCIA results of the FIL production are included in Table 4.14.

Second, the environmental impacts of the recovery process of 1 kg of R-32 using [C_2mim][$C_4F_9CO_2$] as an absorbent from wasted R-407F are estimated. The detailed contributions can be observed in Figure 4.26 (B). The results indicate that the use of the FIL in the separation process has the most significant contribution (58–99%) in most of the impact categories except in GWP (5.4%). It is worth mentioning that in the GWP category, 90% of the emissions are caused by the estimated fugitive emissions. The energy consumption (used for pumping, heating, cooling down, and regenerating the FIL) contributes to 0.11–34% of the environmental impact categories. The EoL of the wasted FIL contributes to 0.10–19% of the environmental impacts. Finally, the construction of the chemical plant facility contributes less than 3% to the environmental impact categories, and as observed during the FIL production, the transportation contribution to the environmental impacts is also residual (0.01–0.72%).

4.6.3 LCA comparison results of R-32 recovery with R-32 conventional production

The benchmark scenario for comparative purposes is the current scenario of R-32 production. The LCA of the production of R-32 was carried out according to the information obtained from the patent of Yuichi et al. (2002), where R-32 is produced from the reaction of dichloromethane with hydrogen fluoride and the available information in Ecoinvent for the production of the fluorinated gas 1,1-difluoroethane, R-152a.

The amount of raw materials needed was calculated through the stoichiometry of the reaction obtained from the patent, while the energy and ancillary materials consumption were obtained from the Ecoinvent database, assuming that R-152a and R-32 are relatively similar compounds due to the lack of available information for R-32.

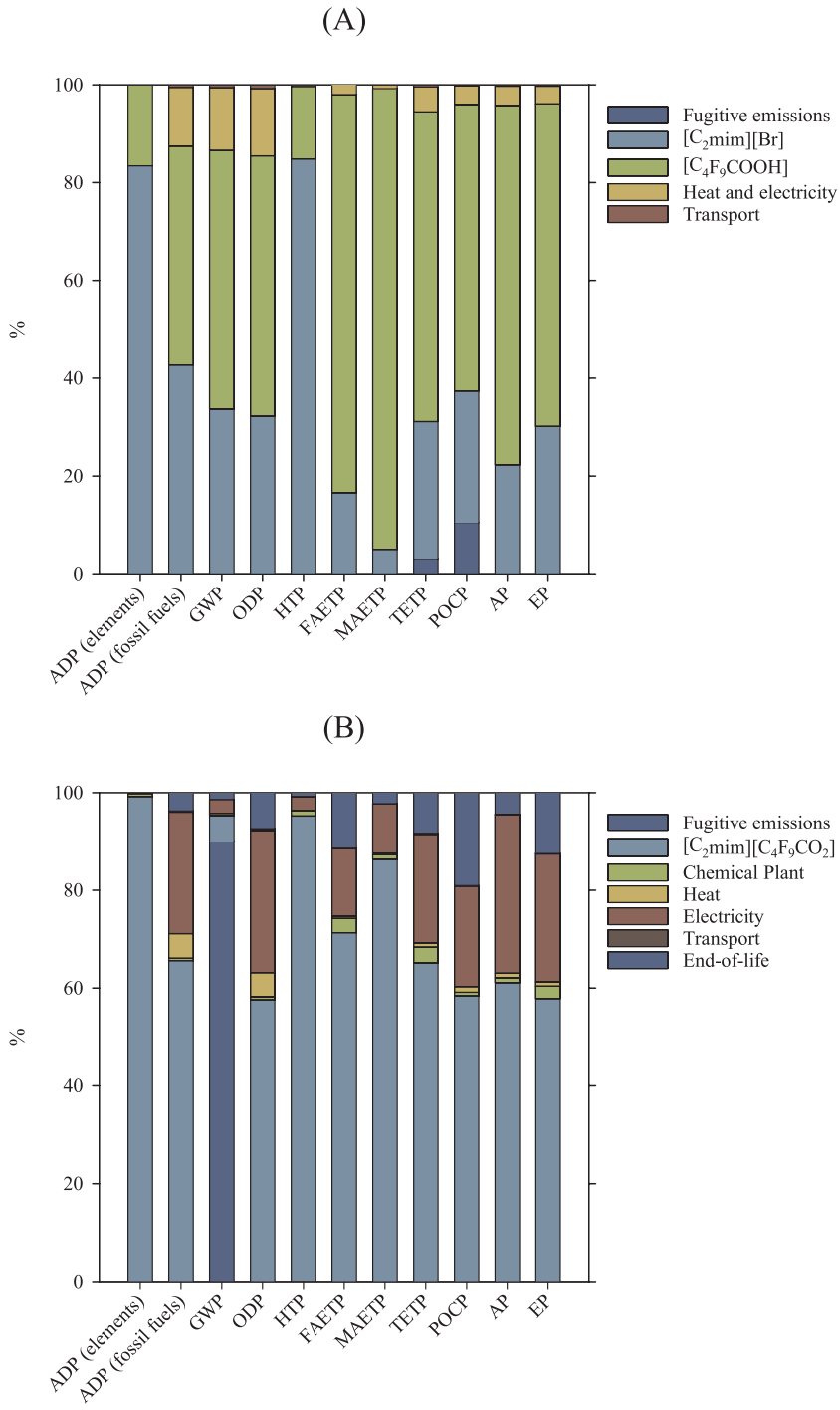

Figure 4.26: Characterization of the environmental impacts of (A) 1 kg of $[C_2mim][C_4F_9CO_2]$ production and (B) recovery of 1 kg of R-32 from R-407F with $[C_2mim][C_4F_9CO_2]$.

Table 4.14: Life cycle impact results of the production of 1 kg of $[C_2mim][C_4F_9CO_2]$.

Impact category	Units	Total	Fugitive emissions	$[C_2mim][Br]$	C_4F_9COOH	Heat	Electricity	Transport
ADP (elements)	kg Sb eq.	1.45×10^{-3}	0	1.21×10^{-3}	2.40×10^{-4}	8.33×10^{-8}	1.05×10^{-7}	1.44×10^{-7}
ADP (fossil fuels)	MJ	1.74×10^{2}	0	7.45×10^{1}	78.18	1.84×10^{1}	2.63	$8.36 \times 10^{-}1$
GWP	kg CO_2 eq.	9.99	0	3.38	5.31	1.08	2.11×10^{-1}	5.24×10^{-2}
ODP	kg CFC-11 eq.	1.37×10^{-6}	0	4.44×10^{-7}	7.34×10^{-7}	1.61×10^{-7}	2.86×10^{-8}	9.90×10^{-9}
HTP	kg 1,4-DB eq.	4.29×10^{1}	4.94×10^{-4}	3.64×10^{1}	6.38	5.75×10^{-2}	5.45×10^{-2}	1.69×10^{-2}
FAETP	kg 1,4-DB eq.	4.56	4.91×10^{-3}	7.51×10^{-1}	3.72	3.91×10^{-2}	4.68×10^{-2}	4.46×10^{-3}
MAETP	kg 1,4-DB eq.	5.28×10^{4}	9.68×10^{-4}	2.65×10^{3}	4.98×10^{4}	1.30×10^{2}	2.53×10^{2}	1.46×10^{1}
TETP	kg 1,4-DB eq.	1.77×10^{-2}	5.58×10^{-4}	4.98×10^{-3}	1.13×10^{-2}	3.46×10^{-4}	5.67×10^{-4}	7.26×10^{-5}
POCP	kg C_2H_4 eq.	$4.08 \times 10-3$	4.31×10^{-4}	$1.10 \times 10-3$	2.40×10^{-3}	9.80×10^{-5}	5.75×10^{-5}	8.55×10^{-6}
AP	kg SO_2 eq.	6.80×10^{-2}	0	1.52×10^{-2}	5.00×10^{-2}	1.28×10^{-3}	1.44×10^{-3}	1.69×10^{-4}
EP	kg PO_4 eq.	1.45×10^{-2}	0	4.39×10^{-3}	9.59×10^{-3}	2.61×10^{-4}	2.66×10^{-4}	3.72×10^{-5}

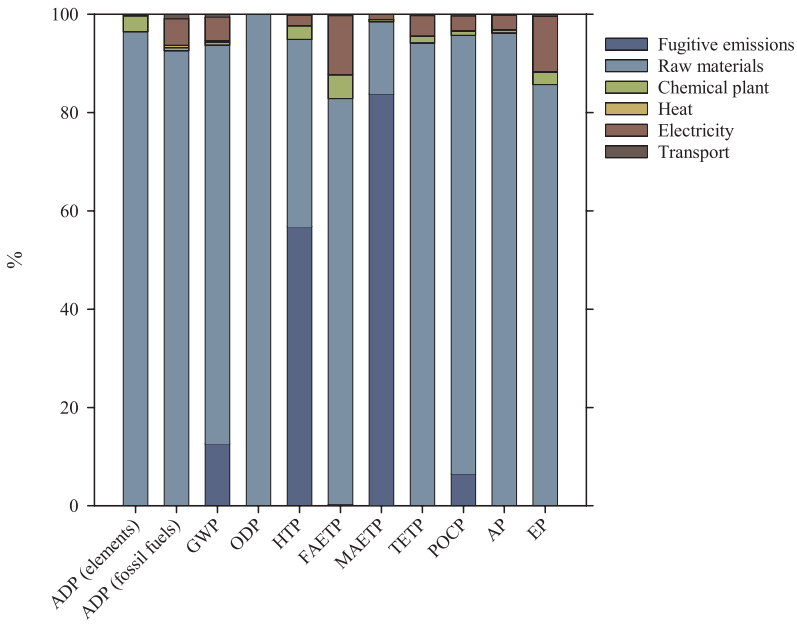

Figure 4.27: Characterization of the environmental impacts of conventional production of 1 kg of R-32.

Figure 4.27 shows the distribution of the impacts to produce 1 kg of R-32. It can be observed how the highest impact in most of the categories, except MAETP and HTP, is caused by hydrogen fluoride and dichloromethane raw materials, falling in the range 15–99% depending on the impact category. The fugitive emissions caused the most critical impacts in the HTP and MAETP categories, mainly due to hydrogen fluoride emissions, which is a well-known corrosive and toxic compound. The heat and electricity used in the R-32 production process caused 0.17–12% of the impacts, while the construction of the chemical plant and the transportation had a limited contribution (lower than 3.3% and 0.9% in all impact categories, respectively).

A comparison between the LCAs of the benchmark scenario (R-32 production) and the circular economy scenario (R-32 recovery process) was conducted (see Table 4.15), and the process inventories are shown in Tables 4.16 and 4.17, respectively. Comparing the results shown in Table 4.15, it can be observed that the circular economy recovery scenario has significantly lower environmental loads in all the impact categories than the benchmark production scenario, with a reduction in the range between 86% and 99%. This is caused due to higher use of raw materials and energy (heat and electricity) in the benchmark scenario compared to the circular economy scenario. The normalized environmental impacts, summarized in Table 4.15, show how the contribution with the highest impact is the MAETP category in both scenarios. The normalized results also suggest a better environmental performance for the circular economy scenario, which has lower environmental impacts by at least one order of magnitude.

Table 4.15: Characterization and normalized life cycle impact results of production and recovery of 1 kg of R-32*.

		Benchmark scenario		Circular economy scenario	
		R-32 production		R-32 recovery	
Impact category	Units	Charact.	Normal.	Charact.	Normal.
ADP (elements)	kg Sb eq.	1.39×10^{-4}	1.64×10^{-12}	1.17×10^{-5}	1.38×10^{-13}
ADP (fossil fuels)	MJ	1.15×10^{2}	3.65×10^{-12}	2.13	6.78×10^{-14}
GWP	kg CO_2 eq.	1.09×10^{1}	2.18×10^{-12}	1.5	2.99×10^{-13}
ODP	kg CFC-11 eq.	1.16×10^{-4}	1.30×10^{-12}	1.92×10^{-8}	2.15×10^{-16}
HTP	kg 1,4-DB eq.	9.37	1.21×10^{-12}	3.62×10^{-1}	4.67×10^{-14}
FAETP	kg 1,4-DB eq.	2.17	4.20×10^{-12}	5.13×10^{-2}	$9.90 \times 10-^{14}$
MAETP	kg 1,4-DB eq.	7.87×10^{4}	6.74×10^{-10}	4.91×10^{2}	4.21×10^{-12}
TETP	kg 1,4-DB eq.	3.63×10^{-2}	7.48×10^{-13}	2.19×10^{-4}	4.52×10^{-15}
POCP	kg C_2H_4 eq.	3.60×10^{-3}	4.25×10^{-13}	5.61×10^{-5}	6.63×10^{-15}
AP	kg SO_2 eq.	9.03×10^{-2}	3.21×10^{-12}	8.94×10^{-4}	3.17×10^{-14}
EP	kg PO_4 eq.	1.39×10^{-2}	1.05×10^{-12}	2.02×10^{-4}	1.53×10^{-14}

*Normalization obtained with European normalization factors (EU25).

Table 4.16: LCI data for the recovery of 1 kg of R-32 from R-407F.

Inventory	Quantity	Unit	Data source
Input			Simulation work
[C2mim][C4F9CO2]	0.008	kg	
R-407F	11.00	kg	
Heat	0.184	MJ_{th}	
Electric Energy	0.340	MJ_e	
Output			
R-32	1.00	kg	
[C2mim][C4F9CO2]	0.008	kg	
Mixture R-32/R-134a/R-125	10.00	kg	

Figure 4.28 shows the normalized environmental impact distribution of both scenarios, and it is observed how the highest impact in the MAETP category in the benchmark scenario is caused by the fugitive emissions, while in the circular economy scenario, it is caused by the use of the FIL.

Therefore, the results show that the environmental benefits of recycling the R-32 instead of producing new fresh R-32 are high. As an example, the GWP of the R-32 production is 10.9 kg CO_2 eq., while this value is much lower if the R-32 (1.50 kg CO_2 eq.) is recovered by the absorption process. According to these results, the carbon footprint of R-32 can be reduced up to 86%, promoting fluorinated gas recovery treatments for their recycling in a circular economy context. Other categories, such as ODP or toxicity, can be reduced by more than 99% and 96%, respectively, in the recovery scenario.

An uncertainty analysis for the two scenarios studied (R-32 production and recovery) was conducted to test the confidence level of the results reported in this work. The Monte Carlo

Table 4.17: LCI data for the production of 1 kg of R-32.

Inventory	Quantity	Unit	Data source
Input			Yuichi et al. (2002), Ecoinvent R-152 production and Simulation Work
Hydrogen fluoride	0.81	kg	
Dichloromethane	1.72	kg	
Chromium	0.002	MJ_{th}	
Heat	0.931		
Electric energy	3.920	MJ_e	
Output			
R-32	1.000	kg	
Hydrogen chloride	1.400	kg	

simulation (with 1000 iterations) results are presented in Figure 4.29. The results show that in all categories, the R-32 recovery scenario has a lower environmental load than the R-32 production scenario, which means it is certain that the recovery of R-32 with FIL is more environmentally benign than its new production. The results can further confirm the R-32 recovery LCA results reported in this work from a statistical aspect.

4.6.4 Sensitivity analysis

There is no information in the literature about the recyclability of FILs in HFC absorption processes. Many authors theoretically assumed that, due to its extremely low vapor pressure, FILs could be regenerated in absorption processes without losing absorption efficiency (Shiflett & Yokozeki, 2006b; Sosa et al., 2020). From experience with other regenerable IL-based absorbents in CO2 capture, it is plausible that, with time, the FIL could lose separation efficiency due to degradation processes or interactions with some impurities (J. Wu et al., 2019). In this subsection, a replacement of the whole FIL of the closed circuit (5774 kg of FIL) was considered after one year of use for the LCA study. Since the use of FIL affects the impacts of the life cycle of the R-32 recovery, a replacement after one year, six months, or one month of use was considered. The relative comparison of the life cycle impacts of R-32 recovery in these three scenarios is compared with the benchmark scenario (R-32 production) in Figure 4.30 (environmental impacts of the benchmark scenario were considered 100%).

The comparison indicates that the periodicity of the replacement of the FIL is not a critical factor in the sustainability of the circular economy approach. The ADP (elements) category is highly affected by replacing the FIL in a shorter time, reaching a similar impact than in the benchmark scenario if the FIL is replaced monthly. Additionally, HTP can reach 45% of the impact of the benchmark scenario, while the rest of the impact categories are below 24%, even if the FIL replacement is carried out monthly. According to these findings, the environmental impacts of R-32 recovery are slightly influenced by the FIL replacement time; a monthly period increases the environmental loads but still falls short of the environmental

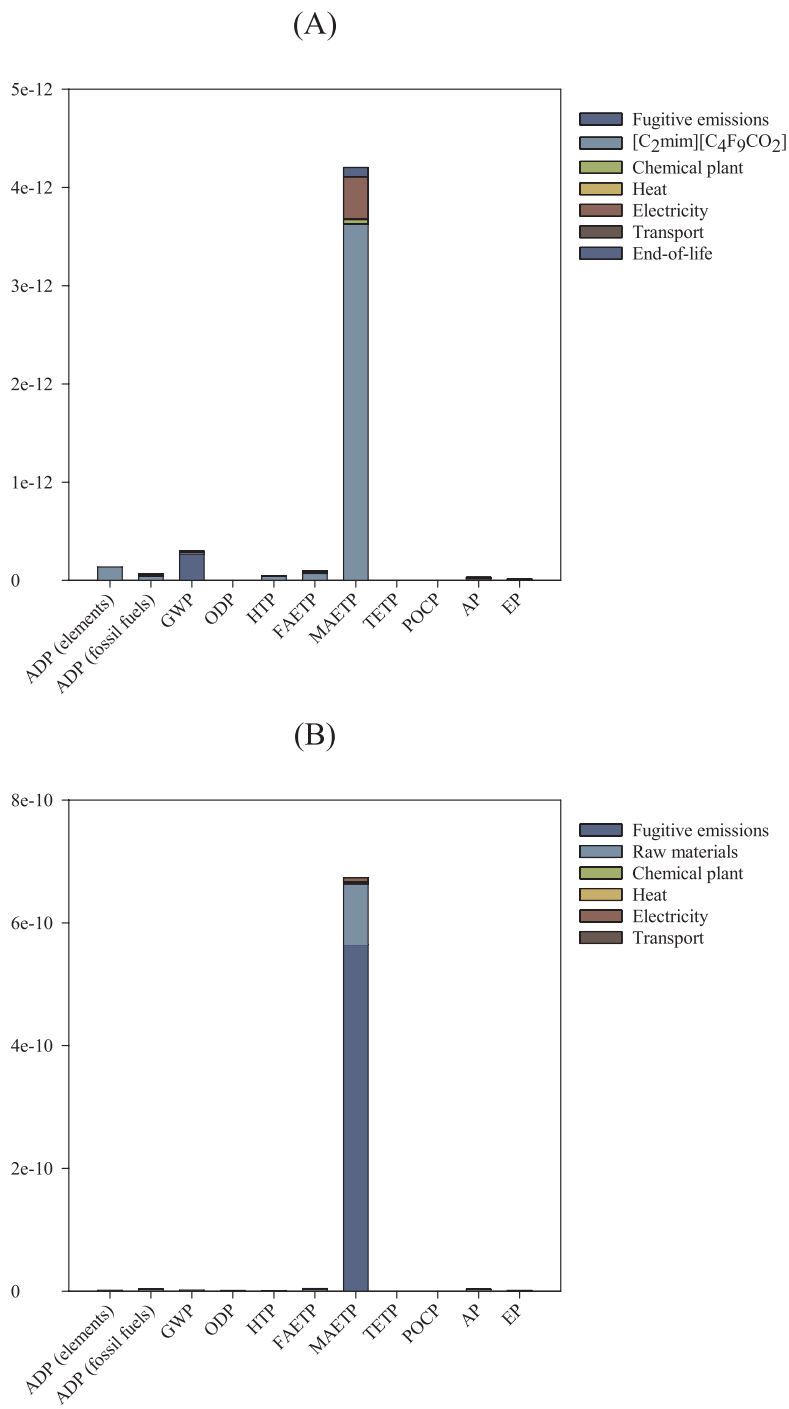

Figure 4.28: Distribution of the normalized environmental impacts of (A) conventional production of 1 kg of R-32 and (B) recovery of 1 kg of R-32 from R-407F with $[C_2mim][C_4F_9CO_2]$.

burdens of R-32 production, even in this very conservative scenario, in the majority of the impact categories.

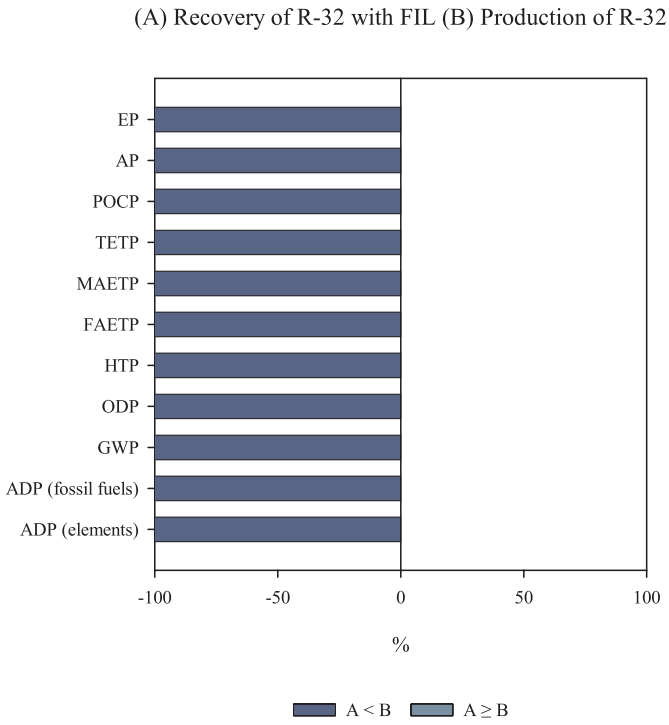

Figure 4.29: Uncertainty analysis for the recovery of R-32 with FIL (A) and comparison with R-32 production (B) (functional unit: 1 kg of R-32).

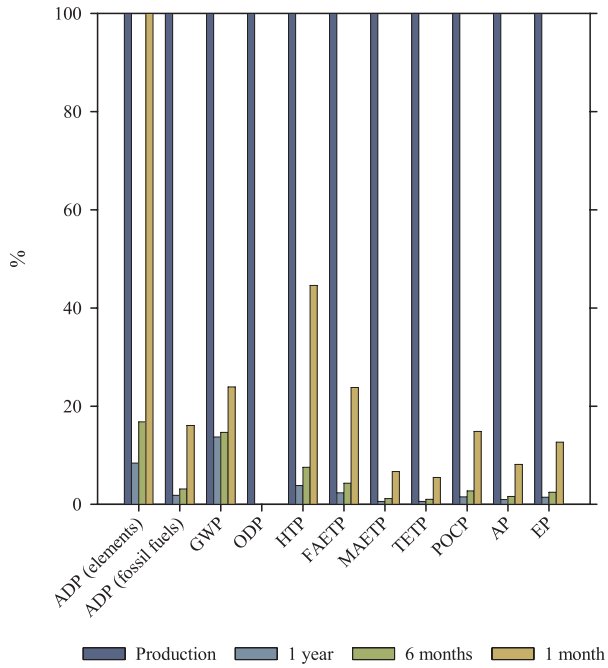

Figure 4.30: Sensitivity analysis of the replacement frequency of the FIL in the recovery process compared to the benchmark scenario. Impacts referred to the production of 1 kg of R-32.

5

Evaluation of alternative fluorinated fluids with low global warming impact

This chapter focuses on investigating alternative synthetic fluorinated fluids for currently used high global warming potential HFCs. The first section addresses the use of hydrofluoroolefins and their blends with hydrofluorocarbons by means of molecular dynamics simulations to gain insight into their thermophysical and transport properties. Then, the feasibility of using hydrofluoroethers as drop-in replacements for hydrofluorocarbons is studied with the polar soft-SAFT EoS. The performance of a series of hydrofluoroethers has been evaluated in terms of several key performance indicators.

Beyond the design of new technologies for the recovery of F-gases, the application of international treaties in the use of HFCs requires the design of new low-GWP working fluids so that these can become long-term solutions. This is currently an under-research topic, as widely exposed in Chapter 2, where hydrofluoroolefins (HFO) are catching the scientific community's attention because of their low-GWP value, especially 2,3,3,3-tetrafluoro-1-propene (R-1234yf) and *trans*-1,3,3,3-tetrafluoro1-propene (R-1234ze(*E*)). However, their use as a pure component causes concern due to their flammability and smaller volumetric cooling capacities than conventional HFC refrigerants. Refrigerant mixtures with mid-GWP values, like R-32, could represent a solution because of the resulting intermediate properties of the mixture, especially flammability and GWP.

According to a recent survey study (Zeiger et al., 2016), the majority of refrigeration systems installed in Europe are based on HFCs, and the most used synthetic refrigerants are R-134a, 404A (a mixture between R-125, R-143a, and R-134a), the 407 series (a mixture between R-125, R-32, and R-134a), R-410A (a mixture between R-125, and R-32), and R-507A (a mixture of R-143a and R-125).

The investigation of the performance of these refrigerant mixtures in possible technical applications calls for a comprehensive understanding of their thermodynamic and transport properties. However, the literature has only a small number of experimental studies of mixtures, including fluoropropenes, and the range of compositions and mixtures is extensive. To overcome this, molecule-based theoretical solutions, such as molecular simulations or advanced EoS, can provide valuable information, establishing themselves as a time- and cost-efficient alternative that yields reliable results.

5.1 Thermophysical characterization of fluorinated blends using molecular simulations

In the last decade, unsaturated fluorinated compounds like hydrofluoroolefins (HFO) have emerged as alternative refrigerants since they exhibit low GWP and null ozone depletion potential (ODP). However, despite having suitable thermophysical and transport properties and low toxicity, some of these refrigerants are somewhat flammable (safety class A2L), meaning their use as single compounds may be limited. In addition, none of them meets the required volumetric cooling capacity (VCC) of HFCs. Consequently, the direct substitution of an HFC by an HFO seems impossible, except in some specific cases (i.e., the substitution of R-134a by R-1234yf HFO in mobile air conditioning applications (Raabe & Maginn, 2010b)). Therefore, a mid-way solution consists of the development of new blends containing an HFO with a low/mid-GWP HFC. This has been widely discussed in Chapter 3, where the reader is referred to get deeper insight.

In this regard, the characterization and development of novel HFOs and their blends has been a matter of growing interest for the industry in recent years. At the same time, the scientific community searches for the right combination of thermophysical, environmental, and safety properties. Even though some studies have addressed the thermophysical properties of selected HFOs and their mixtures by means of computational techniques, this information is often limited to the pure compounds and the VLE behavior of the blends. Less information is found when describing the transport properties, which play an essential role in heat transfer and pressure drop characteristics and are therefore of paramount importance in the design of refrigerant equipment. This includes thermal conductivity for determining heat transfer coefficients, viscosity for fluid flow behavior, and convection characteristics. Surface tension is also of great importance despite being one of the less-studied properties for refrigerants and refrigerant-oil solutions (Zhelezny et al., 2014): it is required to correlate and predict heat transfer when a phase change occurs since it influences nucleate boiling and two-phase flow characteristics (Kim et al., 2004), which in turn is critical for identifying new low-GWP alternative refrigerants.

These properties are currently determined through manufacturers' specific correlations for each fluid (obtained from experimental data), extended corresponding states (Klein et al., 1997; McLinden et al., 2000) (as implemented in the NIST's Reference Fluid Thermodynamic Transport Property Database (REFPROP)), or the use of cubic or SAFT equations coupled with specific treatments for transport properties, such as the Free Volume Theory (Llovell et al., 2013b; Polishuk, 2012). Still, these methods rely on experimental data, which is exceptionally scarce for HFO-based blends. In this direction, molecular simulations can provide physical insight into studying the transport and interfacial properties to complement theoretical results without the need for experimental data and are expected to become crucial in studying such properties shortly.

In the following sections, Molecular Dynamics (MD) simulations have been employed to provide additional insight into the description of several alternative blends to R-410A and R-407F (two of the most widely used refrigerants in cooling, air conditioning, and heat pump (RACHP) applications), with particular emphasis in the description of heat capacity, viscosity, and surface tension. In particular, new interfacial property data of the selected 4^{th} generation blends, for which no experiments are yet available, are presented for the first time from the molecular simulation results. The studied blends include binary blends like R-454B and R-513A and ternary mixtures such as R-452B, which are all combinations between R-32, R-125, R-1234yf, and R-134a. All the properties have also been calculated with REFROP (v.10.0) for the sake of comparison.

5.1.1 Force field and simulation details

Force-field-based MD simulations were carried out using Large-scale Atomic/Molecular Massively Parallel Simulator (LAMMPS) code (Thompson et al., 2022). The force field parameters were taken from Raabe (2019) (R-1234yf, R-1233zd(E), R-32 and R-125) and Peguin et al. (2009) (R-134a) and are presented in Table 5.1. The structure of the compounds studied in this section and the nomenclature used for the different LJ atom types is shown in Figure 5.1

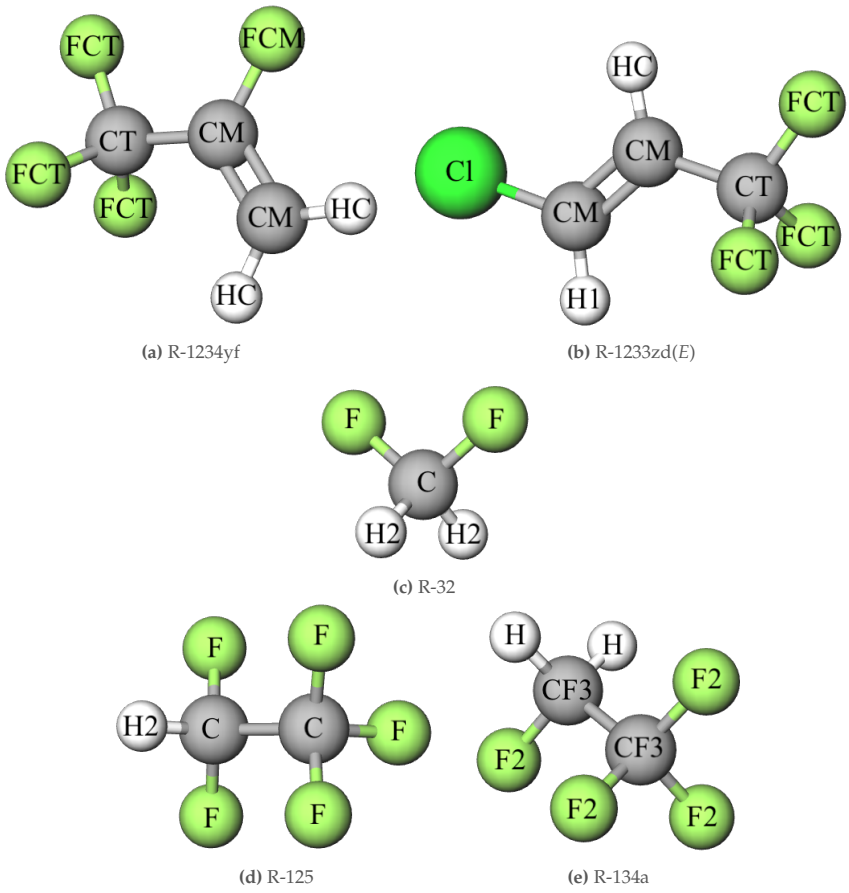

Figure 5.1: Structures of the molecules studied and nomenclature of the different LJ atom types.

The partial charges of the individual atoms have been obtained from the previously mentioned works, where the authors employed *ab-initio* simulations from geometries optimized at a given level of theory and basis sets using the CHELPG subroutine in Gaussian 16 (Frisch et al., 2016). The only exception is R-125, which had not been previously parameterized. Since the partial charges of R-125 had not been reported in those contributions, additional simulations for an isolated molecule were performed with the CHELPG fitting scheme at the HF/6-31G* level of theory in Gaussian. The partial charges of all the molecules employed in these simulations are shown in Table 5.2.

Table 5.1: Force field parameters.

Atom type	ϵ (kcal mol^{-1})	σ (Å)
FCT	0.05641	2.9400
FCM	0.05641	2.9000
CT	0.07426	3.4000
CM	0.09793	3.4000
HC	0.01569	2.6500
H1	0.01569	2.6500
Cl	0.2621	3.5500
C	0.1075	3.1500
F	0.08742	2.9400
H2	0.01569	2.2293
CF3	0.09340	3.6000
F2	0.04869	2.9200
H	0.01990	2.500
Bond	k_{bond} (kcal mol^{-1})	r_0 (Å)
CM=CM	676.3	1.331
CM-CT	317.4	1.511
CT-FCT	371.3	1.353
CM-HC	388.6	1.086
CM-FCM	445.4	1.33
CM-H1	388.6	1.086
CM-Cl	227.8	1.734
C-F	368.9	1.369
C-H2	351.8	1.094
C-C	317.4	1.511
CF3-CF3	317.4	1.529
CF3-F2	368.9	1.360
CF3-H	368.9	1.090
Bend	k_{bend} (kcal mol^{-1} rad^{-2})	θ (deg)
HC-CM=CM	36.33	120.6
FCT-CT-FCT	87.80	107.5
CM-CT-FCT	74.80	111.3
HC-CM-HC	29.29	118.7
CM=CM-FCM	50.49	122.6
FCM-CM-CT	50.09	124.1
CM=CM-CT	50.09	124.1

Table 5.1 continued from previous page

CM=CM-H1	36.33	120.6	
CM=CM-Cl	67.07	122.9	
H1-CM-Cl	36.45	113.8	
HC-CM-CT	32.31	115.1	
F-C-H2	59.69	108.6	
H2-C-H2	35.00	113.6	
F-C-F	87.80	108.7	
H2-C-C	32.31	115.1	
F-C-C	74.80	111.3	
CF3-CF3-H	18.77	110.7	
CF3-CF3-F2	25.02	109.5	
H-CF3-H	16.52	107.8	
H-CF3-F2	20.02	107.0	
F2-CF3-F2	38.54	109.1	
Dihedral	K_1 (kcal mol^{-1})	K_2 (kcal mol^{-1})	K_3 (kcal mol^{-1})
FCT-CT-CM-FCM	0	0	0.4989
FCT-CT-CM=CM	0	0	0.2843
FCM-CM=CM-HC	0	13.30	0
CT-CM=CM-HC	0	13.78	0
HC-CM=CM-HC	0	0	14.25
FCT-CT-CM-HC	0	0	0.3559
HC-CM=CM-H1	-14.25	0	0
HC-CM=CM-Cl	14.25	0	0
Cl-CM=CM-CT	-14.25	0	0
H1-CM=CM-CT	-14.25	0	0
H2-C-C-F	0	0.3559	0
F-C-C-F	0	0.4989	0
F2-CF3-CF3-F2	0.007790	-0.09737	40.42
F2-CF3-CF3-H	0.006319	0.03958	4.231

The intermolecular energy of the system includes a bond stretching, an angle bending, and a torsion term, as shown in equations 3.19 and 3.20. Dihedrals are considered with a cosine torsion series (Optimized Potentials for Liquid Simulations (OPLS) style) as in equation 3.21. Note that the K_4 constant for the OPLS dihedral style is omitted as it is 0 for all dihedrals. For the case of R-134a, the intramolecular energy is represented by the sum of the bending and the torsion term since bonds are considered rigid.

Regarding the intramolecular interactions, they are considered as the contributions of the

Table 5.2: Partial charges for all the molecules employed in MD simulations.

	R-1234yf		R-1233zd(*E*)		R-32		R-125		R-134a	
#	Atom	q_i (e)	Atom	q_i (e)	Atom	q_i (e)	Atom	q_i (e)	Atom	q_i (e)
1	CM	-0.41911	CM	-0.0042700	C	0.43960	C	0.29317	CF3	0.53400
2	CM	0.19743	CM	-0.35183	F	-0.26138	C	0.53245	CF3	0.0020000
3	CT	0.63064	CT	0.97116	H2	0.041580	F	-0.19592	F2	-0.19150
4	HC	0.20473	Cl	-0.075830			F	-0.19592	F2	-0.19150
5	HC	0.20473	H1	-0.28846			F	-0.15794	F2	-0.19150
6	FCM	-0.18254	HC	-0.28846			F	-0.19825	H	0.11500
7	FCT	-0.21196	FCT	-0.28846			F	-0.19825	H	0.11500
8	FCT	-0.21196	FCT	0.15783			H2	0.12067	F2	-0.19150
9	FCT	-0.21196	FCT	0.16832						

van der Waals and electrostatic interactions, the latter described by a pairwise-additive 12-6 LJ potential (equation 3.22) and the odder represented by the coulombic potential as in equation 3.24.

Systems were created differently according to the desired calculated property. Once this was done, simulations were conducted as follows: (i) energy minimization of the system (ii) NVT thermalization to drag the system to the working temperature using the Langevin thermostat (Schneider & Stoll, 1978), (iii) NVT equilibration using the Nosé-Hoover thermostat (Nosé, 1984) and (iv) NVT production with the Nosé-Hoover thermostat to allow the system to achieve the equilibrium state to compute thermophysical properties. All simulations were evolved using a timestep of 1 fs with pair interactions calculated using a spherical cutoff of 22 Å and long-range coulombic interactions computed through the Particle-Particle/Particle-Mesh (PPPM) method (Hockney & Eastwood, 1988). This cutoff was selected as an alternative to heterogeneous tail corrections to the LJ potential (Duque & Vega, 2004; Janeček, 2006; Martínez-Ruiz et al., 2015).

For phase equilibria calculations, the initial configuration was built by placing N molecules in a parallelepiped box of $45 \times 45 \times 225$ Å^3 divided into two symmetric regions to place sensibly large vapor and liquid phases. When dealing with binary and ternary blends, the box size was increased to $60 \times 60 \times 300$Å^3 to improve the phase space sampling in mixtures. The number of atoms, N, was set in order to match the coexistence densities ρ_L and ρ_V at each temperature.

50 ns were run from which the last 10 ns were considered production. Coexistence densities were calculated from the $\rho(z)$-profile built averaging the number of molecules in 1Å bins along the z direction during the last 6 ns. Vapor pressures were similarly obtained by averaging the per-atom stress tensor in 1 bin elementary volumes to build the pressure tensor profile $P(z)$-profile. This profile is diagonal with $P_{xx}(Z) = P_{yy}(Z) = P_{zz}(Z)$ in each bulk phase region, thus the vapor pressure could be obtained by averaging those three components at the vapor region:

$$P(z) = \frac{1}{3}\left(P_{xx}(z) + P_{yy}(z) + P_{zz}(z)\right) \tag{5.1}$$

By integration of the aforementioned $P(z)$-profile along the z-direction, one can obtain the surface tension directly, as in the Irving and Kirkwood formulation (Irving & Kirkwood, 1950) or via the global pressure tensor by using the Kirkwood and Buff formulation (Kirkwood & Buff, 1949), as done in this thesis:

$$\gamma = \frac{L_z}{2}\left[P_{zz} - \frac{P_{xx} + P_{yy}}{2}\right] \tag{5.2}$$

For the calculation of isobaric heat capacity, C_p, a set of homogeneous squared boxes of $65 \times 65 \times 65$ Å^3 were built with N atoms and equilibrated with 0.1 ns, followed by 1 ns production time. The number of atoms was, again, obtained from the liquid and vapor densities obtained from phase equilibria calculations. C_p was determined from simulations in the NpT ensemble from the slope of the intermolecular energy by fitting a straight line to the simulation results at 5 successive temperatures at a time (i.e., $T - 2\Delta T$, $T - \Delta T$, T, $T + \Delta T$ and $T + 2\Delta T$, in total 5 ns) to ensure that the heat capacity grows linearly with temperature, as explained before.

The derivative of the volume within the temperature range and the ideal contribution obtained from bibliographic sources (see Table 5.3) were then added to the obtained slope as in equation 3.39.

Table 5.3: Bibliographic sources for the determination of ideal heat capacities.

System	Type of data	Source
R-1234yf	Experimental, correlated	Kano et al. (2010)
R-1233zd(*E*)	Experimental, correlated	Hulse et al. (2012)
R-32	Correlated	Outcalt and McLinden (1995)
R-125	Correlated (technical report)	EI du Pont de Nemours and Co (2004a)
R-134a	Correlated (technical report)	EI du Pont de Nemours and Co (2004b)

Regarding the viscosity calculation, a time decomposition method for the calculation of shear viscosity from the Green-Kubo (GK) relations has been used in this doctoral thesis. The main foundations and the procedure is widely exposed in section 3.2.5.

5.1.2 Pure refrigerant compounds

As a first step, VLE MD simulations were performed for the HFOs and HFCs conforming the refrigerant blends, R-1234yf, R-1233zd(*E*), R-32, R-125, and R-134a, at three different temperatures along the saturation line, with the purpose to evaluate the predictive capabilities of the

selected force fields. Simulations close to the critical point were not performed to avoid errors in the calculation of equilibrium properties.

Once equilibrated, two vapor-liquid interfaces were clearly identified (see Figure 5.2), and the density profiles were calculated by averaging the number of molecules in 1 Å bins.

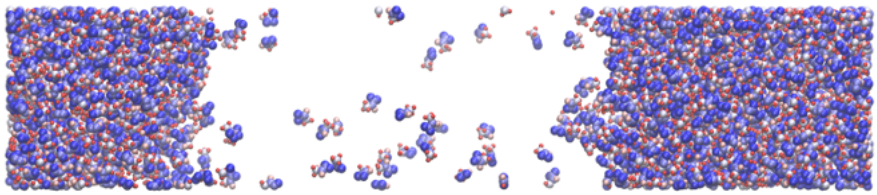

Figure 5.2: Snapshot of the simulation box at equilibrium.

The corresponding vapor-liquid coexistence curves were calculated by collecting the saturated density profiles at different temperatures. Additional properties, such as vapor pressure and surface tension, were also given by building the pressure tensor profile from the per-atom stress tensor. Finally, the vapor and liquid heat capacity and the liquid viscosity were also provided for a complete analysis. The results of all these properties are represented in Figure 5.3.

Overall, the predicted saturated densities and pressures obtained with MD simulations are in good agreement with those calculated with REFPROP, validating the approach used in this work to compute these properties. Similarly, the predicted surface tensions obtained from molecular simulations are in excellent agreement with REFPROP calculations, thus reinforcing the modeling of the selected compounds and their validity in predicting other thermophysical properties. Only slight deviations are observed in the saturated liquid densities, where MD simulations tend to overestimate the results for low temperatures.

Regarding liquid viscosity calculations, MD simulations accurately reproduce the values from REFPROP, with the exception of R-1233zd(*E*), where the obtained viscosity is underestimated in comparison with REFPROP. However, it should be noted that these results are fully predictive, as no data for transport properties has been used by Raabe et al. to correlate the force field. On top of that, in REFPROP, the viscosity for HFO compounds is described by an *extended corresponding states (ECS) approach*, which tends to overestimate the viscosity of both R-1233zd(*E*) and R-1234yf. Overall, good agreement is found given the low deviations for all the other compounds in a wide temperature range, validating the force field.

As for the heat capacity results, the approach used to calculate them can reproduce the REFPROP values for both phases in a whole temperature range. On the other hand, the simulations tend to overestimate the heat capacities at low temperatures, the same as for the saturated liquid densities. To achieve a better agreement with both properties, the interaction energies (i.e., ϵ LJ parameter) should be reduced, which would significantly affect the accuracy of the results for the vapor pressure. Consequently, it is preferred to keep the original

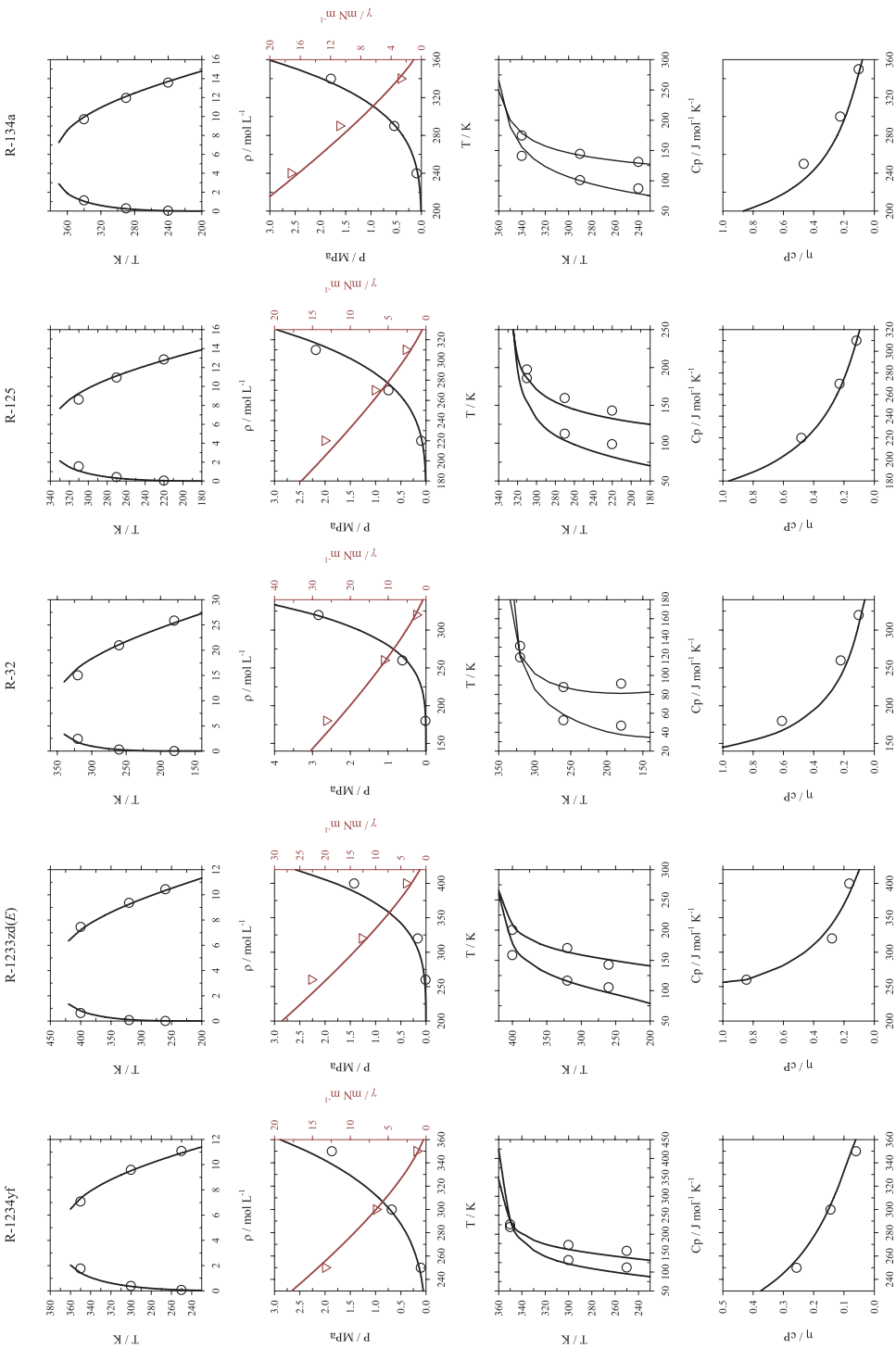

Figure 5.3: Vapor-liquid coexistence curves (first row), vapor pressures and surface tensions (second row), vapor and liquid isobaric heat capacities (third row), and liquid viscosities (fourth row) for R-1234yf, R-1233zd(*E*), R-32, R-125, and R-134a. Symbols represent MD simulation results, and solid lines are REFPROP calculations.

force field proposed by Raabe and coworkers, given the good balance found for all properties studied, being conscious of these observed minor deviations.

5.1.3 Low temperature refrigerants

Low-temperature refrigerants include refrigerants with high cooling capacity (between 265 and 318 K). Currently, R407-F is commonly used, although pure R-134a also seems adequate for certain applications. In this section, the results for the R407-F (GWP = 1965) and R-134a (GWP = 1530), high and mid-GWP refrigerants, are compared with R-513A (GWP = 673.5), a low GWP alternative azeotropic mixture[1] with a mass ratio of R-1234yf and R-134a of 56 to 44. R-513A is sold under the OPTEON^{TM} brand to replace R-134a in positive displacement, direct expansion, medium and low-temperature commercial and industrial chillers, as well as flooded and/or centrifugal chillers. As R-134a, ASHRAE classifies R-513A as a nontoxic and nonflammable fluid (A1); therefore, flammability is not an issue. Both refrigerants have similar boiling points (-26.4 °C for R-134a and -29.9 °C for R-513A), so R-513A can also be used in food conservation systems (Mota-Babiloni, Makhnatch, Khodabandeh, & Navarro-Esbrí, 2017). Figure 5.4 compares the VLE behavior and surface tension of the beforementioned blends. Note that for R-513A, no correlated surface tension data were available in REFPROP; therefore, it has not been included here.

Overall, the results are in excellent agreement, and both three refrigerants show similar properties. However, the most significant differences are found in the surface tension values. A low surface tension reduces the liquid surface stability, which may have a negative effect on heat transfer due to an increase in droplet formation and entrainment. In this case, the R-407F shows a lower value for this property, while R-513A seems a better substitute for R-134a.

Regarding the heat capacity and viscosity calculations, the results are included in Figure 5.5. Both R-513A and R-134a show very similar behavior, with the most significant differences found in the lower heat capacity compared to R-407F. Still, the differences are minor, and both refrigerants are able to work under these conditions. Again, the results are in good agreement with the REFPROP calculations.

5.1.4 High temperature refrigerants

The second group of refrigerants comprises those within a mid-temperature range, generally employed for air-cooling. R-410A is the dominant refrigerant in residential heat pumps. Two low-GWP refrigerants are proposed here as replacements: R-452B and R-454B, originally named DR-55 and DR-5A, respectively. They are both indicated for usage in residential, light

[1] The average glide of 0.1 °C is considered negligible

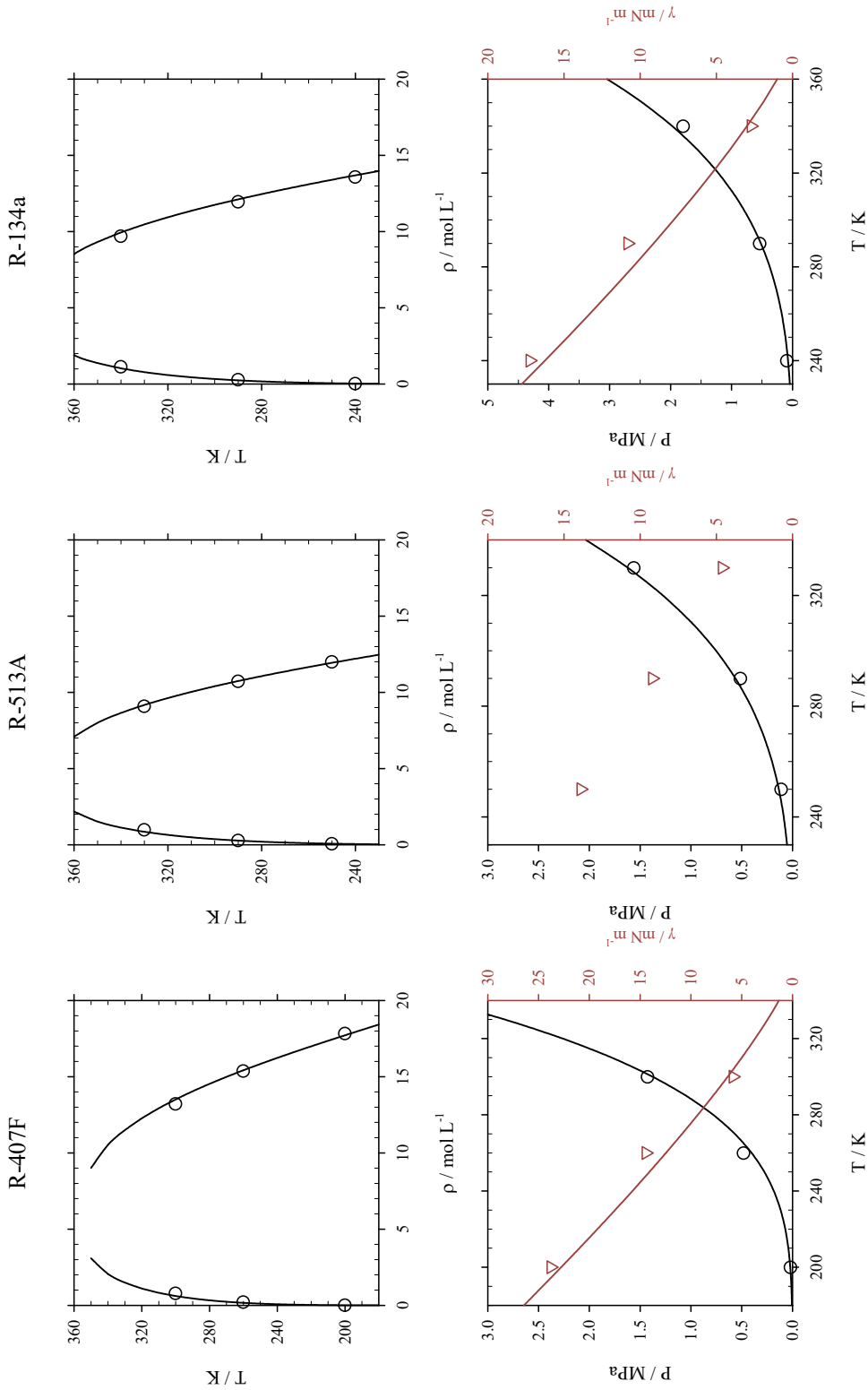

Figure 5.4: Vapor-liquid coexistence curves (first row), vapor pressures and surface tensions (second row) for R-407F, R-513A, and R-134a. Symbols represent MD simulation results, and solid lines are REFPROP calculations. If no solid line is plotted, there is no available correlated data in REFPROP.

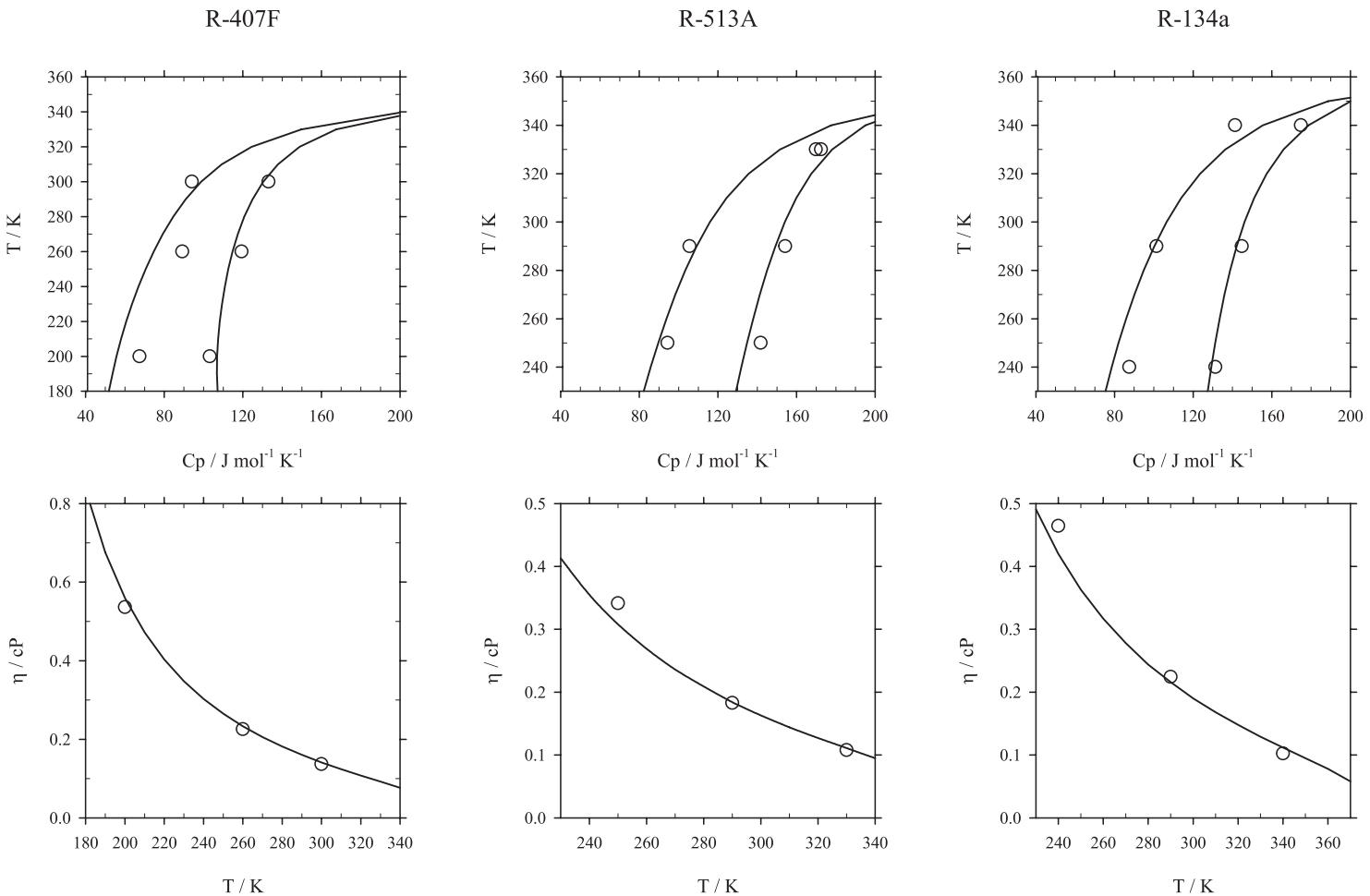

Figure 5.5: Heat capacities (first row) and viscosities (second row) for R-407F, R-513A, and R-134a. Symbols represent MD simulation results, and solid lines are REFPROP predictions.

commercial, and commercial positive displacement devices, direct expansion (DX) chillers and AC, and window units and portable AC, among others.

R-452B is also sold under the OPTEON^{TM} brand as a replacement for *the same functionality* as R-410A. It comprises a mixture of R-32, R-125, and R-1234yf in a 67/7/26 wt % ratio and is classified as a mildly-flammable refrigerant (A2L). R-454B, on the other hand, is a binary mixture of R-32 and R-1234yf in a 68.9/31.1 wt % ratio and is also classified as an A2L refrigerant.

Figure 5.6 compares the VLE behavior and surface tension of both refrigerant alternatives with R-410A. Like in the previous case, the correlated surface tension data from REFPROP for both R-452B and R-454B were unavailable. As for the other group of refrigerants, the MD simulations results match the values correlated with REFPROP, with only slight differences observed near the critical temperature: MD simulations tend to slightly underestimate the coexistence densities for R-454B and R-452B and thus predict a lower critical point. Some conclusions can be drawn from these results: first, the alternatives have slightly higher critical temperatures and have wider saturation domes than R-410A. This should allow the alternatives to perform somewhat better at higher ambient temperatures (Sieres et al., 2021). On the other hand, slight differences are observed with respect to the value of the vapor density at saturation for the two alternative mixtures with respect to R-410A, with R-452B and R-454B having a lower density. This is undesired, as a low vapor density (or a high specific volume) will require a bigger compressor.

Finally, in Figure 5.7, the comparison is presented for heat capacity and viscosity. Overall good agreement is achieved, with the highest deviations found for the viscosity of R-452B with respect to the calculations from REFPROP. In this case, there are no significant differences between the blends: all of them exhibit low viscosities and high heat capacities, which are all desired properties: a low viscosity refrigerant will require less energy for its circulation through the refrigeration system, and a high heat capacity lowers the required mass flow rate.

5.2 Drop-in assessment of hydrofluoroethers in organic Rankine cycles

Although the determination of thermophysical properties is essential for the design of new refrigerants, in a second step, it is necessary to evaluate the theoretical performance of the possible candidates in the systems to be substituted. In this sense, the use of computational tools allows this step to be carried out in a quick cost-efficient way.

This section evaluates the theoretical performance of another family of fluorinated fluids, hydrofluoroethers (HFE), as potential substitutes for pentafluoropropane, R-245fa, in a low-grade waste heat recovery Organic Rankine Cycle (ORC). The choice is based on the condition of a lower GWP than the benchmark fluid. The soft-SAFT EoS (Alkhatib et al., 2020) has been

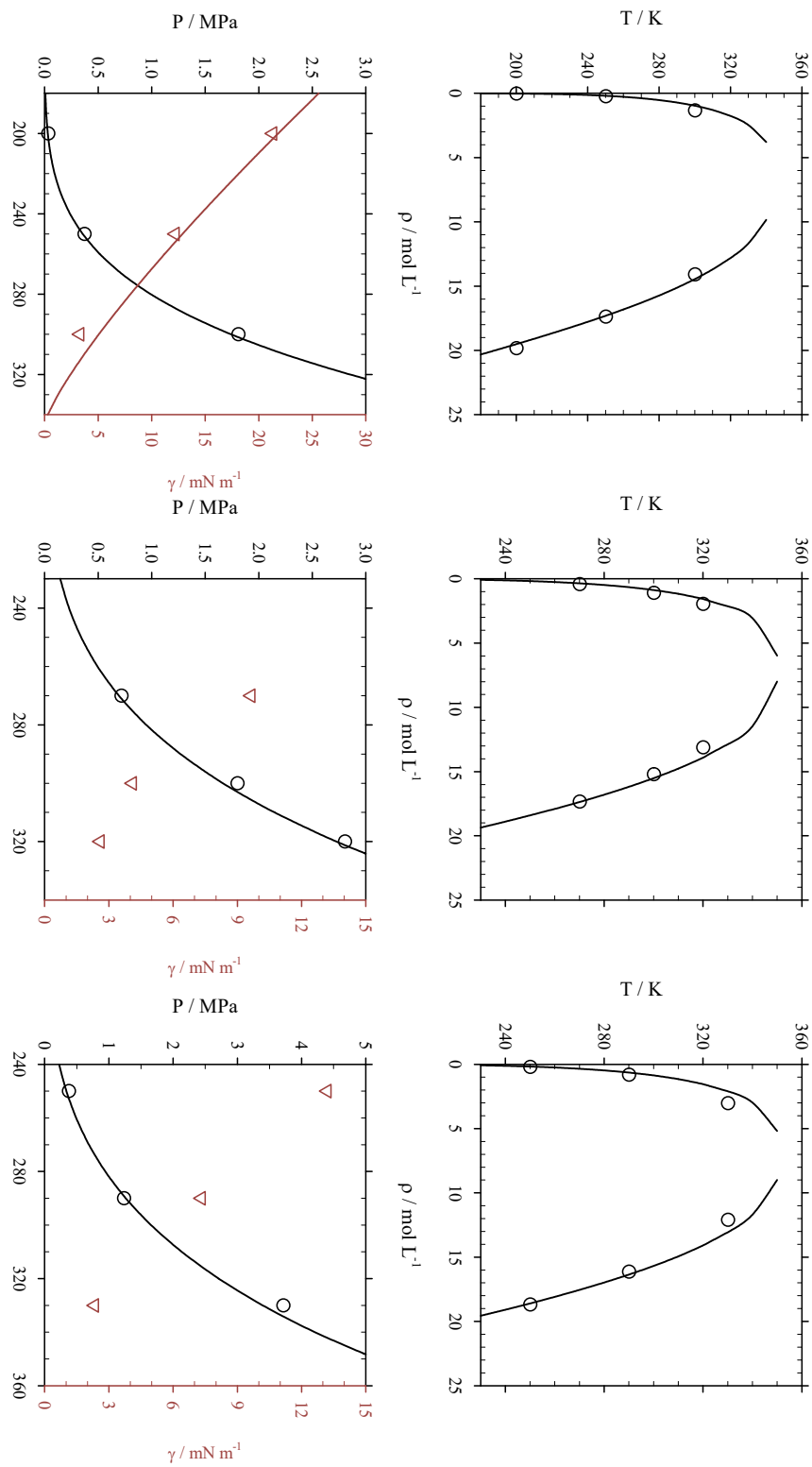

Figure 5.6: Vapor-liquid coexistence curves (first row), vapor pressures and surface tensions (second row) for R-410A, R-452B, and R-454B. Symbols represent MD simulation results, and solid lines are REFPROP predictions. If no solid line is plotted, there is no available correlated data in REFPROP.

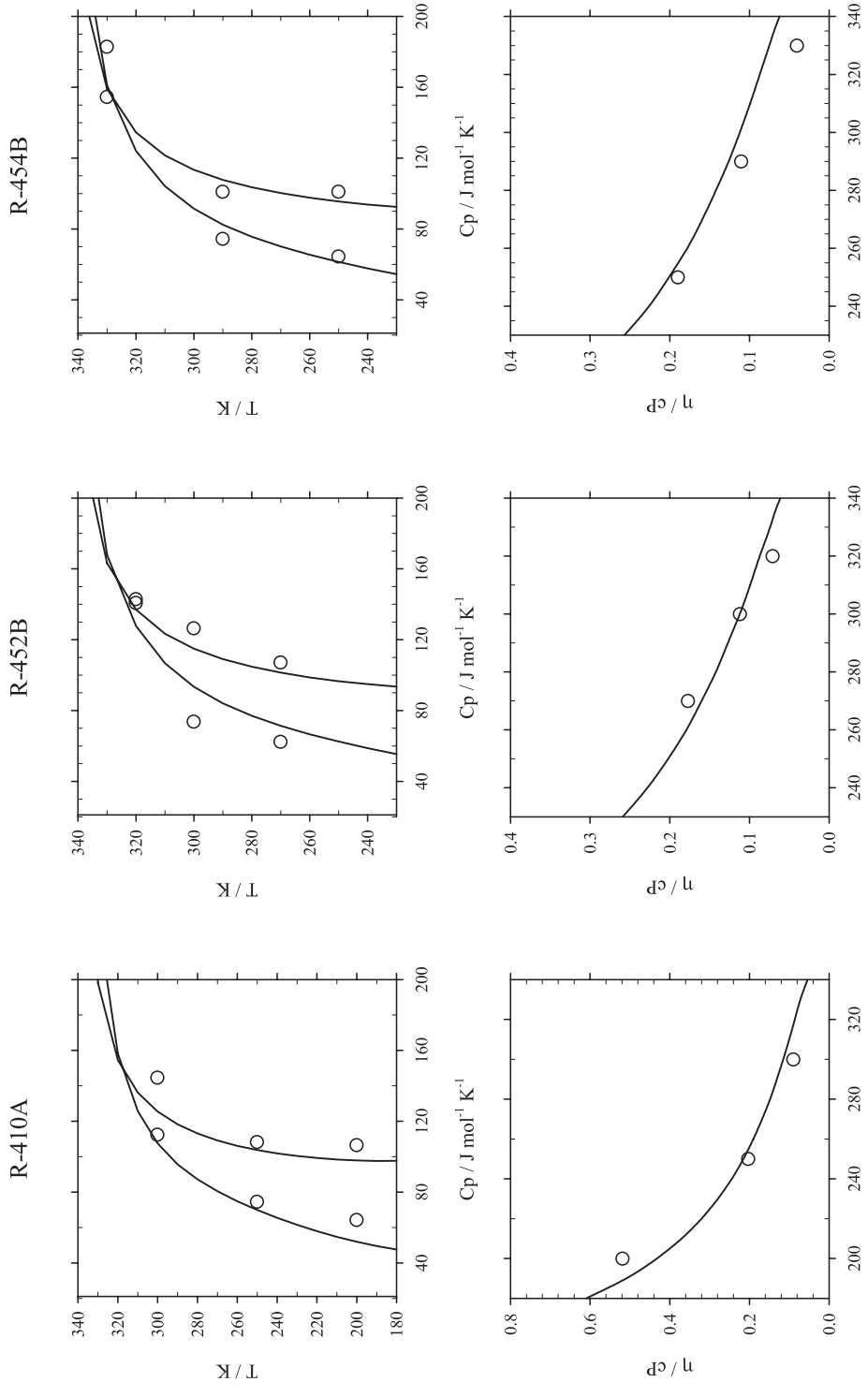

Figure 5.7: Heat capacities (first row) and viscosities (second row) for R-410A, R-452B, and R-454B. Symbols represent MD simulation results, and solid lines are REFPROP predictions.

used for the first time to model these compounds, specifically including the impact of the permanent dipole of these molecules for a more realistic and reliable prediction of their thermophysical behavior. Based on such optimization, the performance of each compound has been evaluated in terms of thermal efficiency and cooling water, heating fluid, and working fluid consumption, providing new insight into the feasibility of using HFEs as drop-in replacements for ORCs.

5.2.1 Thermophysical characterization of hydrofluoroethers

Benchmark R-245fa and all HFEs are represented as homonuclear non-associating LJ chainlike fluids in the polar soft-SAFT framework, explicitly considering their dipole moment caused by the electronegative fluorine and oxygen atoms, and their asymmetric molecular structure, which is a key feature affecting its thermodynamic properties. For these fluids, the association contribution, A^{assoc} from equation 3.47 has been omitted in an effort to avoid an overparametrization that would not represent the key physical interactions occurring in those molecules, based on the fact that polar interactions are dominant. Consequently, a total of five molecular parameters are used to describe these molecules: the LJ segment diameter (σ_i), chain length (m_i), and LJ segments dispersive energy (ε_i), and the dipole moment (μ) and the fraction of segments affected by the polar moment (x_p).

Further validation of the parametrization is carried out by studying binary mixtures with some additional compounds, such as ethers and alcohols. Hence, an adequate molecular model must also be proposed for these molecules. Acetone and ethyl acetate follow the same pattern as HFEs, being modeled as homonuclear chains with specific dipole moments. However, hydrogen bonding interactions are dominant in alcohols due to the presence of a hydroxyl group and cannot be omitted. In this work, methanol and 1-propanol are modeled, for the first time, using a combination of dipole + association terms to consider both the permanent dipolar and hydrogen bonding interactions, adding two additional parameters, $\varepsilon^{\text{HB}}$for the square-well energy parameter of an association site, and K^{HB} for the volume of association, to the parametrization of these specific compounds.

Dipole moments, μ, for HFE-143a, HFE-245mf, HFE-245mc, HFE-7000, HFE-7100, acetone, ethyl acetate, methanol, and 1-propanol were retrieved from Aspen Plus Database (v.12.1). For the remaining ones, DFT (Density Functional Theory) calculations were employed for their estimation. Optimized structures were generated with TmoleX software v.21.0.1 (Balasubramani et al., 2020) at the gas phase using the triple-ζ valence potential (def-TZVP) basis with the Becke and Perdew (BP) functional using the resolution of identity (RI) approximation and a convergence criterion of 10^{-6} Hartree. Next, a second optimization was performed using the TZVDP-FINE level; a more computationally-demanding level considered the best

Table 5.4: Selection of working fluids studied as R-245fa replacement.

Name	Other identifiers	CAS	Molecular weight	Boiling point (K)	Critical Temperature (K)	Critical Pressure (MPa)	Enthalpy of vaporization at 293.15 K ($kJ\,kg^{-1}$)	Flammability limits[c]	GWP[d]
1,1,1,3,3-Pentafluoropropane	R-245fa	460-73-1	134.1	288.3	427.1	3.654	192.5	Non-flammable	962.0
Trifluoromethyl Methyl Ether	HFE-143a	421-14-7	100.0	248.9	377.9	3.642	180.6	10.5%-21.5% (dry air)	616.0
Methyl pentafluoroethyl ether	HFE-245mc	22410-44-2	150.1	278.8	406.8	2.886	152.6	10.5%-13.5% (dry air)	747.0
2,2,2-Trifluoroethyl difluoromethyl ether	HFE-245mf	1885-48-9	150.1	302.4	444.9	3.428	186.5	Non-flammable	878.0
Hexafluoroisopropyl methyl ether	HFE-356mmz	13171-18-1	182.1	322.4	459.6	2.699	172.1	5.25%-15.0% (dry air)	8.100
Methyl Perfluorobutyl Ether	HFE-7100	163702-07-6	250.1	332.7	458.0	2.220	139.0	Non-flammable	490.5
Ethyl Perfluorobutyl Ether	HFE-7200	163702-05-4	264.1	349.3	482.0	1.976	131.8	Non-flammable	34.30
1,1,1,2,2,3,4,5,5,5-Decafluoro-3-methoxy-4-(trifluoromethyl)pentane	HFE-7300	132182-92-4	350.1	375.4	497.0	1.454	133.5	Non-flammable	405.0
3-Ethoxy-1,1,1,2,3,4,4,5,5,6,6,6-dodecafluoro-2-(trifluoromethyl)hexane	HFE-7500	297730-93-9	414.1	412.3	559.0	1.625	111.7	Non-flammable	13.00

[a] Reference Lemmon et al. (2018).
[b] Calculated with the Watson equation with the parameters provided by the NIST TDE Lemmon et al. (2018).
[c] Defined as the lowest and greatest concentrations of a combustible substance capable of producing a flash fire in the presence of an ignition source under specified conditions. References 3M Company (2008), 2009a, 2009b, 2009c, 2021 and Kondo et al. (2006).
[d] Global Warming potential. Reference IPCC (2021).

quality calculation method currently available (Dassault Systèmes, 2020). Density functionals have been reported to be quite good at predicting dipole moments, with low Root Mean Squared errors compared to the reference values (Hait & Head-Gordon, 2018).

Finally, surface tension calculations were also performed through the use of the density gradient theory (DGT) and coupled into the polar soft-SAFT EoS.

The rest of the polar soft-SAFT molecular parameters, including m, σ, ε, x_p, as well as K^{HB}, and $\varepsilon^{\mathrm{HB}}$ for the alcohols, were fitted to the available experimental saturated liquid density and vapor pressure data. A careful analysis of the values obtained and how they are related to the structural features of these compounds is given below. The optimized polar soft-SAFT molecular parameters for the nine studied HFEs, as well as the average deviations obtained from the experimental saturated liquid density (AAD_D) and vapor pressure (AAD_P), are presented in Table 5.5.

Table 5.5: Optimized polar soft-SAFT molecular parameters for the selected HFE working fluids.

Compound	m	σ (Å)	$\varepsilon/k_{\mathrm{B}}$ (K)	$\mu \times 10^{-30}$ (C m)	x_p	AAD_P (%)	AAD_D (%)
R-245fa	2.479	3.675	197.1	5.166	0.800	1.593	0.596
HFE-143a	1.784	3.894	167.9	8.333	0.550	1.541	1.25
HFE-245mf	3.309	3.400	179.6	5.440	0.525	5.568	1.17
HFE-245mc	2.051	4.126	179.0	9.290	0.500	1.938	0.462
HFE-356mmz	2.681	3.965	175.4	9.856	0.425	1.585	0.822
HFE-7000	2.324	4.259	181.3	9.910	0.500	1.739	0.505
HFE-7100	2.283	4.575	204.9	9.900	0.625	2.696	0.166
HFE-7200	2.113	4.916	214.6	11.21	0.675	3.243	0.162
HFE-7300	2.636	4.775	250.6	8.049	0.650	4.035	0.0300
HFE-7500	3.940	4.392	198.3	9.435	0.500	5.659	2.73

The physical meaning of these parameters, which is related to the size and energy of the molecule, allows for the extraction of molecular features and comprehension of their impact on macro-level properties. It can be noticed that the volume of the molecule, reproduced by $m\sigma^3$, increases with the size of the refrigerant. However, this increase cannot be strictly related to the carbon chain length (a common approach done for other families, such as n-alkanes or 1-alkanols (Pàmies & Vega, 2001)) due to the influence of the number and position of fluorine atoms located in the molecule. For this reason, a direct relationship between the m chain length parameter and the number of carbons cannot be correlated, being the volume comparison a more appropriate descriptor (Albà et al., 2021).

Another relevant aspect is the existing correlation between the effective dipole (expressed as the dipole moment value multiplied by the fraction of the molecule affected by this dipole, x_p) and the segment diameter, σ. This is appreciated in Table 5.5 and, visually, in Figure 5.8. The polar effect is clearly influenced by the presence of fluorine atoms connected to the main carbon chain, described with SAFT through a higher diameter. Indeed, the size of

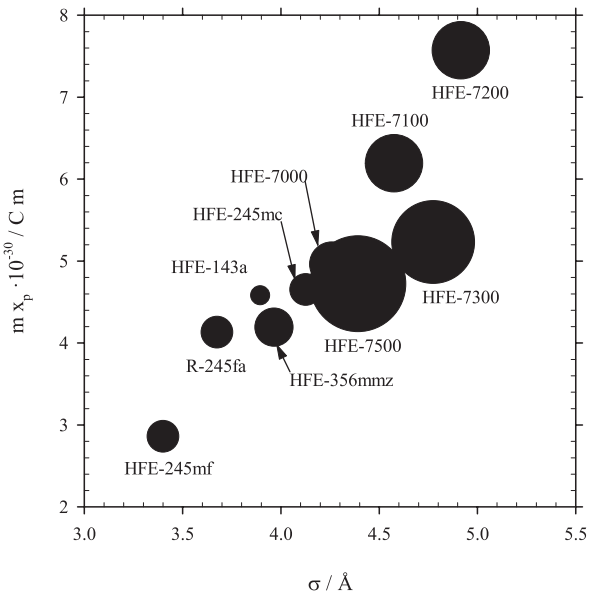

Figure 5.8: Effect of the product of the dipole moment. μ, and the polar fraction of the molecule on the segment diameter σ. Note that the size of the symbols reflects the number of fluorine atoms in the molecule.

the filled circles in 5.8 indicates the number of fluorine atoms in each molecule. Still, some discrepancies are observed as a consequence of the exact location of these atoms. For example, HFE-143a contains only 3 F-atoms but located on one specific side of the molecule, increasing the asymmetry and the polarity (as shown in the σ-surface diagrams in Figure 5.9). Contrarily, HFE-7500 has 15 F-atoms, but they are quite symmetrically distributed along the molecule, resulting in a more electroneutral molecule compared to other HFEs of the 7000-series.

To further understand the significance of explicitly accounting for the polarity of the refrigerants explored herein, the relative contribution of the different terms (Reference, Chain, and Polar) to the residual Helmholtz free energy (equation 3.47) was calculated at saturated liquid conditions for all fluids at T = 273.15 K. Note that the ideal contribution has also been estimated, and proven to be dominant at the established conditions, but has not been included in the figure for a better appreciation of the polarity effect among the residual terms. The results, displayed in Figure 5.10, reveal that the polar term has a significant impact in all the compounds, with contributions ranging from 27% to 53%, except for HFE-7300 (16%), differing from a recent publication carried out with PC-SAFT (Vinš et al., 2021). It can be seen that, for fluids with equivalent degrees of fluorination (HFE-356mmz vs. HFE-7100, HFE-143a vs. HFE-245mf/mc, or HFE-7200 vs. HFE-7300), the polar contribution diminishes as the carbon chain increases. This can be associated with a more symmetrical charge distribution, as observed from the σ-surface diagrams in Figure 5.9. In any case, it is clear that the polar term will affect the thermodynamic properties, such as vapor pressure or enthalpy of vaporization, although it is difficult to separate this explicit effect from the rest of the contributions since all of them are interrelated (Albà et al., 2021).

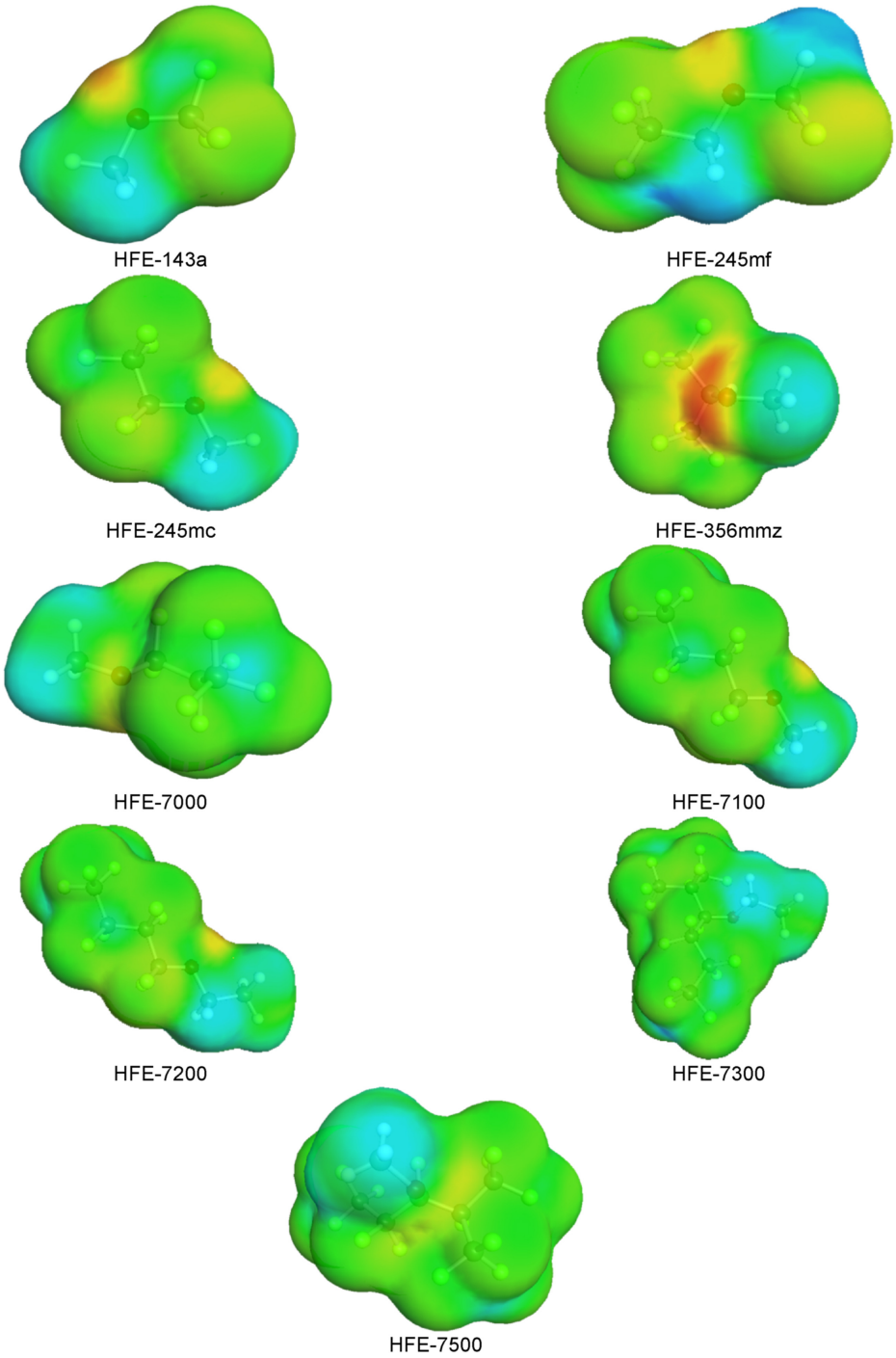

Figure 5.9: σ-surfaces for the HFEs investigated predicted by conductor-like screening model for real solvents (COSMO-RS) analysis. Green zones reveal non-polar regions, blue regions show H-bond donors (electropositive area), and red regions depict H-bond acceptors (electronegative area).

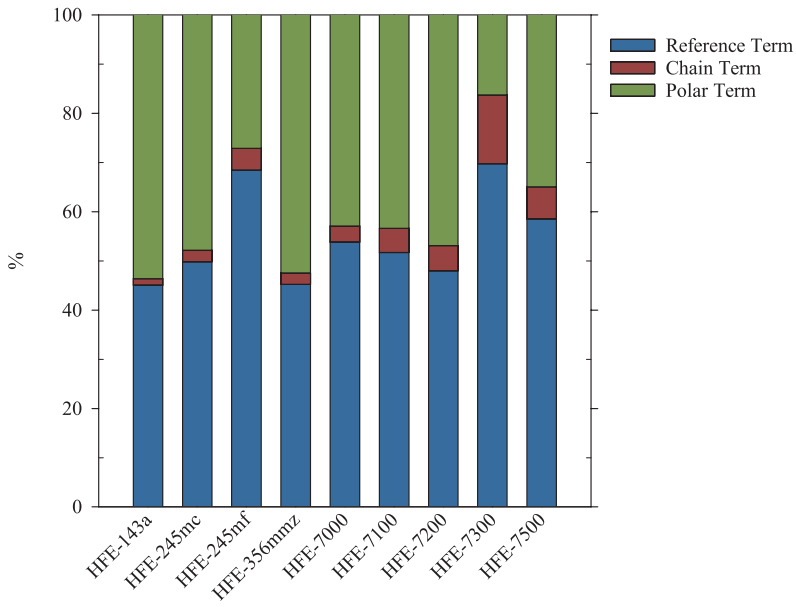

Figure 5.10: Relative term contribution to the residual Helmholtz free energy predicted with polar soft-SAFT at T = 273.15 K and saturation conditions for the liquid phase of the HFEs characterized in this work.

The parameters presented can accurately reproduce the phase equilibria diagrams of all fluids, as provided in Figure 5.11 (A) for the vapor pressure and the saturated vapor-liquid densities (B). The average absolute deviation (AAD) for the vapor pressure is below 2% in most cases, with the exceptions of HFE-245mf, HFE-7100, and HFE-7500, still in an acceptable range between 2.5 and 6%. The comparison of the vapor pressures reveals that HFE-245mc and HFE-143a can achieve higher evaporation temperatures than R-245fa at the same conditions, which is expected to improve the cycle thermal efficiency (J. Yang et al., 2018a). Similar behavior is observed for HFE-245mf, HFE-7000, and HFE-356mmz at moderate working pressures. Finally, high molecular weight HFEs, such as HFE-7500 and HFE-7300, exhibit lower saturation pressures and high normal boiling points, being a clear disadvantage when choosing an ORC working fluid, since it is necessary to increase the temperature to avoid working under atmospheric pressure, with a negative impact on the thermal efficiency. The results are consistent with the vaporization enthalpies shown in Table 5.4, where these components have the lowest values.

The saturated liquid density is even better described, as shown in Figure 5.11 (B), with an AAD below 1% with the exception of HFE-245mf and HFE-7500, both below 3%. Interestingly, vapor densities are also predicted in very good agreement with the available experimental information. Coexistence densities also play an essential role, particularly in the sizing of the equipment (Eyerer et al., 2019); although the functional design of the ORC is beyond the scope of this work, the behavior is comparable to what has previously been observed for the vapor pressures: HFE-245mc and HFE-143a exhibit higher vapor densities, leading to lower volume

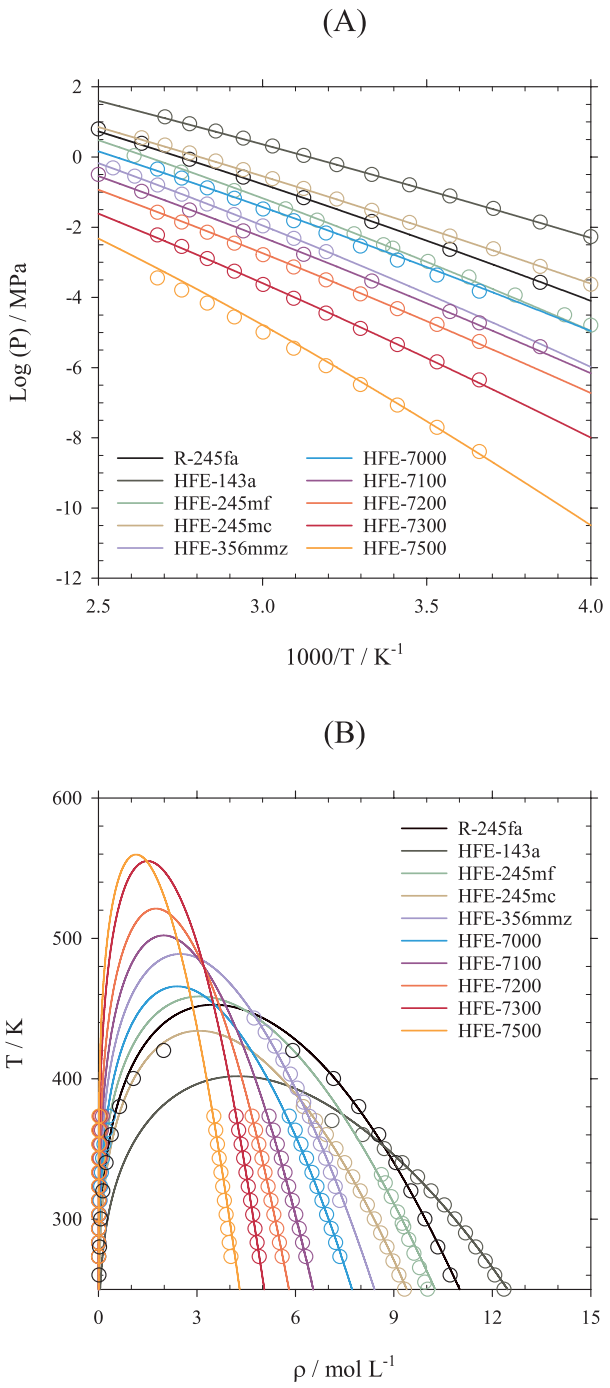

Figure 5.11: Vapor pressures (A) and coexisting densities (B) for the working fluids studied as replacements in ORC. Symbols represent the experimental data (see references in Table 5.5), and solid lines are the polar soft-SAFT calculations.

flow rates at equal mass flow. This would eventually reduce the cost of the system as the size of the heat exchangers would not have to be increased to limit the pressure drops, as it occurs

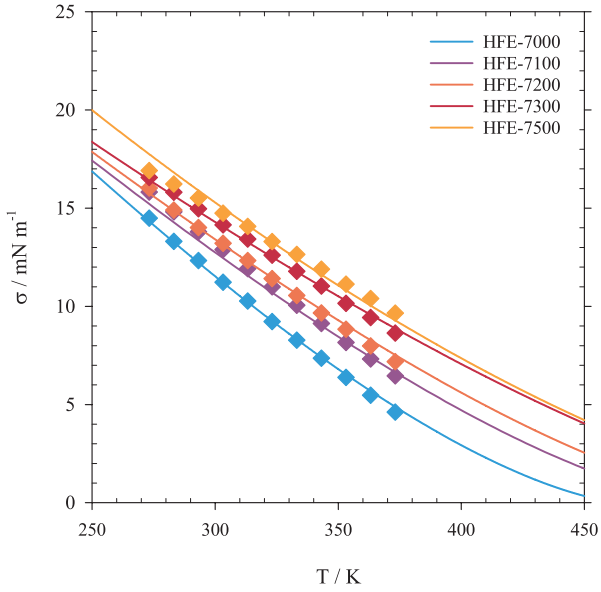

Figure 5.12: Surface tensions for some of the hydrofluoroethers studied in this work. Symbols represent the experimental data (Rausch et al., 2015), and solid lines are the soft-SAFT calculations.

Table 5.6: Optimized influence parameter (c) for the 3M's Novec engineered fluids and its deviation from experimental values.

Compound	$c \times 10^{-8}$ (Jm^5mol^{-2})	(%)
HFE-7000	3.259	1.654
HFE-7100	4.661	2.520
HFE-7200	6.637	1.519
HFE-7300	8.418	1.024
HFE-7500	1.220	2.509

in low-vapor density fluids with high volume flow rates (Quoilin et al., 2013).

The thermodynamic characterization of pure HFEs has been completed by calculating the surface tension of the fluids for which experimental data are available (Rausch et al., 2015). The results are shown in Figure 5.12. Even if the influence parameter c is adjusted to data, as indicated in Section 3.3.3, the correct description of the slope of the surface tension can only be achieved if the right balance between the van der Waals and the polar forces is given. The description of the surface tension is, in all cases, excellent using a temperature-independent influence parameter (AAD lower than 2.6%, see Table 5.6), corroborating the validity of the molecular parameters presented in Table 5.5.

Further validation of the adequacy of the selected molecular parameters, as well as the impact of the polar contribution in those compounds, is provided by describing the phase behavior of binary systems with other molecules. Reported experimental data of alcohols or acetates are commonly encountered in binary combinations with HFEs, as these mixtures

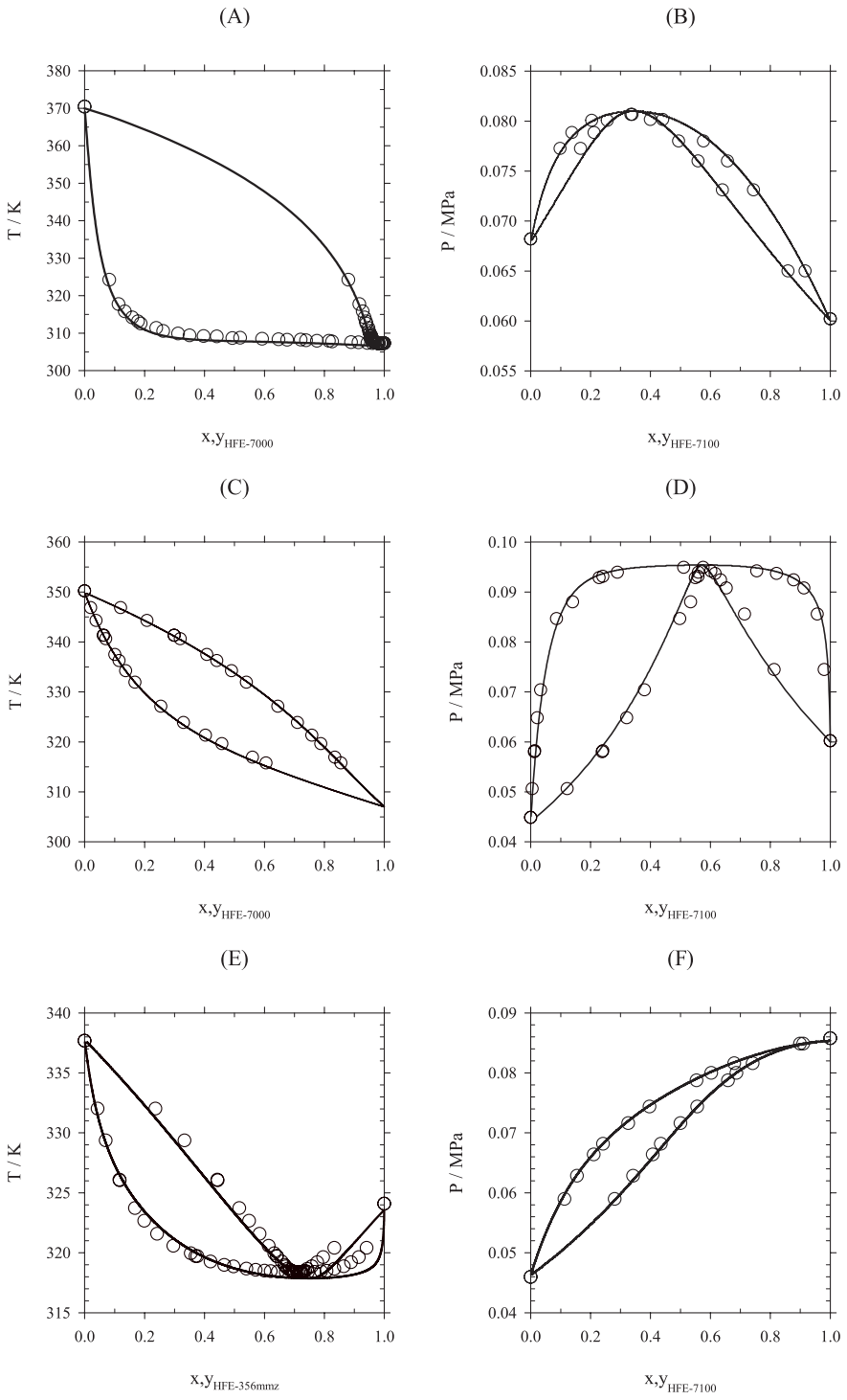

Figure 5.13: Binary VLE for HFE-7000 + 1-propanol (A) and Ethyl Acetate (C), HFE-7100 + acetone (B), methanol (D) and ethyl acetate (F), and HFE-356mmz + methanol (E). Symbols represent the experimental data (Hiaki & Kawai, 1999; Řehák et al., 2017; Tochigi et al., 2001) and solid lines are the polar soft-SAFT calculations. Isotherm plots are performed at 318.15 K (B,D) and at 328.15 K (F), and isobaric plots are all at 0.1013 MPa. One binary parameter (ξ) was used for the fitting, with values of 1.005 (A), 0.986 (B), 1.020 (C), 0.982 (D), 1.070 (E), and 0.990 (F).

Table 5.7: Optimized polar soft-SAFT molecular parameters for selected alcohols and ethers.

Compound	m	σ (Å)	ε/k_B (K)	ε^{HB}/k_B (K)	K^{HB}(Å^3)	$\mu \times 10^{-30}$ (C m)	x_p	AAD_P (%)	AAD_D (%)
Acetone[a]	1.849	3.827	275.7	n.a	n.a	9.610	0.3330	1.640	0.9100
Methanol	1.123	3.748	214.3	3436	4099	5.504	0.3500	1.088	0.4920
Ethyl Acetate	2.797	3.620	247.2	n.a	n.a	5.940	0.4750	1.687	0.6150
1-propanol	1.981	3.826	263.0	3249	2250	5.600	0.3380	1.128	0.3120

[a] Molecular parameters retrieved from Alkhatib and Vega (2021)

are present in advanced cleaning solvents (Muñoz-Rujas et al., 2018; Sekiya & Misaki, 2000). Figure 5.13 shows the VLE of HFE-7000, HFE-7100, and HFE-356mmz with solvents such as acetone, methanol, ethyl acetate, or 1-propanol, whose molecular parameters are presented in Table 5.7. In all cases, a very good representation of the nonideal behavior of these mixtures is achieved, with only some slight deviations for the HFE-356mmz + methanol at the azeotropic concentration. These results are obtained by using a single energy binary parameter, ξ, described as $\varepsilon_{ij} = \xi \cdot \sqrt{\varepsilon_{ii}\varepsilon_{jj}}$ to quantitatively fit the experimental data. However, a closer examination indicates that they are all close to unity. It is important to notice that a value of one means that the system is predicted using the combining rules without any additional correction. While the use of this parameter is typically required to account for structural differences among molecules, the inclusion of the polar-polar contributions allows for a decrease in this degree of correction. Here, a pure prediction ($\xi = 1$), not shown for clarity, is even capable of qualitatively reproducing the different azeotropes and complex behavior in all systems.

5.2.2 Organic Rankine cycle process simulation

The scheme of the modeled single ORC is shown in Figure 5.14, with the corresponding T-S diagram. This basic configuration comprises a feed pump, an evaporator, an expander, and a condenser. The saturated liquid is pressurized in the pump and evaporated in the evaporator exchanger in the considered implementation. The saturated vapor is pushed through an expander and a condenser, where it is cooled and liquefied, restarting the cycle.

A 2 K subcooling temperature was set in the condenser to ensure a complete liquid phase at the input of the pump to avoid damage. However, superheating was not considered at the evaporator's outlet because droplets in metastable pure vapor state are not expected under saturated conditions (H. Chen et al., 2010; Demuth, 1983; Hung, 2001). Following Jang and Lee's study (Jang & Lee, 2018), heat and head losses were assumed to be negligible, and the working fluid efficiencies were supposed to be constant.

Also, the volumetric expansion ratio (ER) (i.e., the variation of the working fluid's specific volume during the expansion) was limited to 5 to achieve the scroll expander's maximal isentropic efficiency. Finally, the condenser and evaporator were modeled with a pinch temperature of more than 5 K to ensure proper heat transmission between the two fluids (Jang &

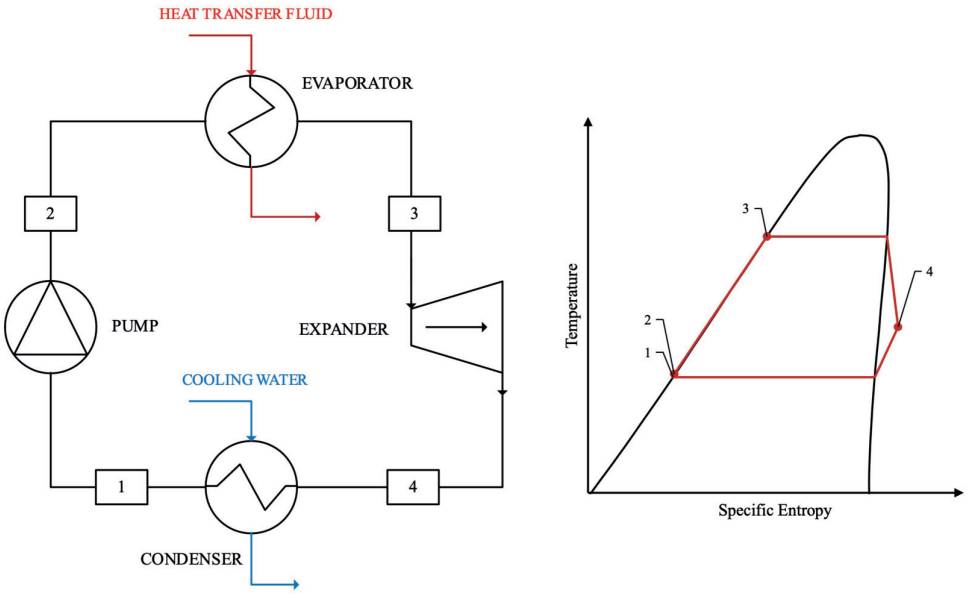

Figure 5.14: Schematic diagram of the studied ORC (left) and T-S diagram (right).

Lee, 2018; Q. Wang et al., 2019). Cooling water (CW) was considered as the cooling fluid at an inlet temperature of 291.15 K and a pressure of 304 kPa, whereas DOWTHERM A, a synthetic organic heat transfer fluid designed for high-temperature heat transfer applications, was chosen as the Heating Fluid (HF) at an inlet temperature of 473.15 K and the same pressure as the cooling fluid.

Overall, the cycle must deliver more than 2 kW of electric power. Isentropic and mechanical efficiencies are assumed to be 65% and 90% for the expander, and 50% and 70% for the pump, respectively. To simplify the model, heat transfer efficiencies were not considered for the condenser and the evaporator. All the performance criteria and constraints are summarized in Table 5.8.

The main objective of an ORC process is to deliver maximum electricity production with the lowest service fluid consumption (i.e., mass flows of CW and HF required). This is determined not only by the fluid choice but also by the selected operating conditions. Consequently, a thermodynamic analysis is proposed, and fluid properties at each point of the ORC have been calculated based on the aforementioned considerations for steady-state conditions. Under these circumstances, the energy balance at the evaporator can be written as:

$$\dot{m}_{\mathrm{HF}} \cdot (h_{\mathrm{HF,in}} - h_{\mathrm{HF,out}}) = \dot{m}_{\mathrm{ORC}} \cdot (h_3 - h_2) \tag{5.3}$$

$$h_2 = h_1 + \frac{h_{2,\mathrm{isen}} - h_1}{\eta_{\mathrm{isen,pump}}} \tag{5.4}$$

Table 5.8: Performance criteria, constraints, and component efficiencies of the ORC.

Isentropic efficiency of the expander (%)	65
Mechanical efficiency of the expander (%)	90
Isentropic efficiency of the feed pump (%)	50
Mechanical efficiency of the feed pump (%)	70
HF Inlet temperature (K)	473.15
CW Inlet temperature (K)	291.15
Subcooling temperature (K)	2
Pinch point temperature difference (K)	>5
Volumetric expansion ratio	<5
Inlet pressure for cooling/heating fluids (KPa)	304
Net electric power (kW)	>2

where $\dot{m}_{\text{HF}}$ and $\dot{m}_{\text{ORC}}$ are the mass flows ($\text{kg}\,\text{s}^{-1}$) of the heating and working fluids, respectively, $h_{\text{HF,in}}$ and $h_{\text{HF,out}}$ are the inlet, and outlet evaporator enthalpies ($\text{kJ}\,\text{kg}^{-1}$) of the heating fluid, h_3 and h_2 are the enthalpies of the ORC working fluid at the specified points (see Figure 5.14), and $\eta_{\text{isen,pump}}$ is the isentropic efficiency of the pump. Likewise, an equivalent energy balance is calculated for the condenser:

$$\dot{m}_{\text{CW}} \cdot (h_{\text{CW,in}} - h_{\text{CW,out}}) = \dot{m}_{\text{ORC}} \cdot (h_1 - h_4) \tag{5.5}$$

$$h_4 = h_3 - (h_3 - h_{4,\text{isen}}) \cdot \eta_{\text{isen,exp}} \tag{5.6}$$

Therein, $\dot{m}_{\text{CW}}$ refers to the mass flow of cooling water ($\text{kg}\,\text{s}^{-1}$) and $h_{\text{CW,in}}$ and $h_{\text{CW,out}}$ are the inlet and outlet enthalpies ($\text{kJ}\,\text{kg}^{-1}$) for the cooling water at the condenser, while $\eta_{\text{isen,exp}}$ is the isentropic efficiency of the expander.

The net power of the system (kW) (equation 5.9) is obtained from the pump power consumption (equation 5.7) and the power generated by the expander (equation 5.8):

$$W_{\text{p}} = \dot{m}_{\text{ORC}} \cdot \frac{h_2 - h_1}{\eta_{\text{mec,pump}}} \tag{5.7}$$

$$W_{\text{exp}} = \dot{m}_{\text{ORC}} \cdot (h_3 - h_4) \cdot \eta_{\text{mec,pump}} \tag{5.8}$$

$$W_{\text{net}} = W_{\text{p}} - W_{\text{exp}} \tag{5.9}$$

Where $\eta_{\text{mec,pump}}$ and $\eta_{\text{mec,exp}}$ are the mechanical efficiencies of the pump and the expander, respectively.

Finally, the thermal efficiency (equation 5.10) indicates the amount of energy received by the working fluid in the evaporator that is converted into net work produced:

$$\eta_{\text{ORC}} = \frac{W_{\text{exp}} - W_{\text{p}}}{Q_{\text{evap}}} \tag{5.10}$$

$$Q_{\text{evap}} = \dot{m}_{\text{ORC}} \cdot (h_3 - h_2) \tag{5.11}$$

The cycle's energy balances are solved iteratively, with the evaporation and condensation temperatures (T_3 and T_4, respectively) and the working fluid, heating fluid, and cooling water flow rates as manipulated variables.

An Aspen Plus (v.12.1) model of the ORC proposed has been used to determine the operating conditions for each fluid, following the iterative scheme depicted in Figure 5.15. The physicochemical thermodynamic properties at the conditions resulting from this evaluation are calculated using polar soft-SAFT. First, the evaporating temperature (T_3) is set by imposing a value that provides a difference with the inlet heating fluid temperature of at least 5 K, with a maximum value of 90% of the working fluid's critical temperature. This additional restriction is established to avoid errors in the calculation of the fluid properties with polar soft-SAFT, which, as explained in previous chapters, as other mean-field theories, overestimates the calculations near the critical region. Once T_3 is fixed, the cycle's maximum pressure, P_2, is automatically obtained, as it equals the vapor saturation pressure at T_3 (no head losses in the condenser or the evaporator have been considered). Likewise, a condensation temperature (T_4) is given under the constraint of the volumetric ER criteria, which must be below 5. Analogously, the minimum cycle's pressure, P_4, is calculated as the liquid's saturation pressure at T_4 and must not be lower than atmospheric pressure (Jang & Lee, 2018). Next, the value of the mass flow rate of the working fluid is iterated until it satisfies the net electrical power set out in Table 5.8. Finally, the flow rates of the heating and cooling service fluids are determined by iteratively solving the energy balances in the condenser and evaporator, under the constraint that the calculated output fluid temperatures must not go below the pinch point.

5.2.3 Organic Rankine cycle drop-in assessment results

Once the parametrization of HFEs has been validated, saturated mass entropies and enthalpies have been predicted using the same set of parameters (Table 5.5), as this is key information to assess their adequacy in ORCs. While the residual term has been predicted with polar soft-SAFT, the ideal term has been obtained from the Aspen Properties database, using the REFPROP property package included in version 12.1. Enthalpy and entropy values are referenced to 200 $\text{kJ}\,\text{kg}^{-1}$ and 1 $\text{kJ}\,\text{kg}^{-1}\,\text{K}^{-1}$ respectively for saturated liquid at 273.15 K. A

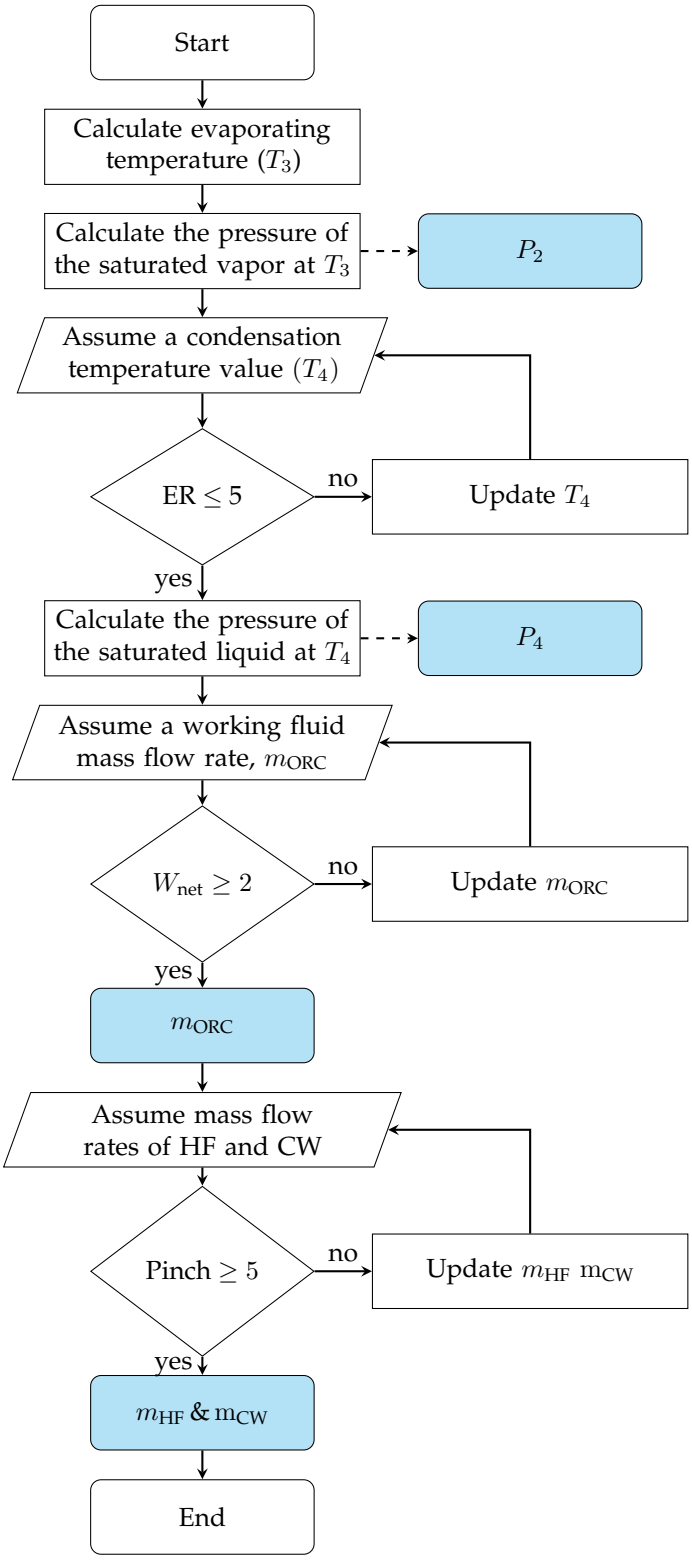

Figure 5.15: ORC calculation algorithm.

summary of the results for some of the most promising working fluids is represented in Figure 5.16 (A & C), while the remaining ones are included in Figure 5.16 (B & D) for clarity.

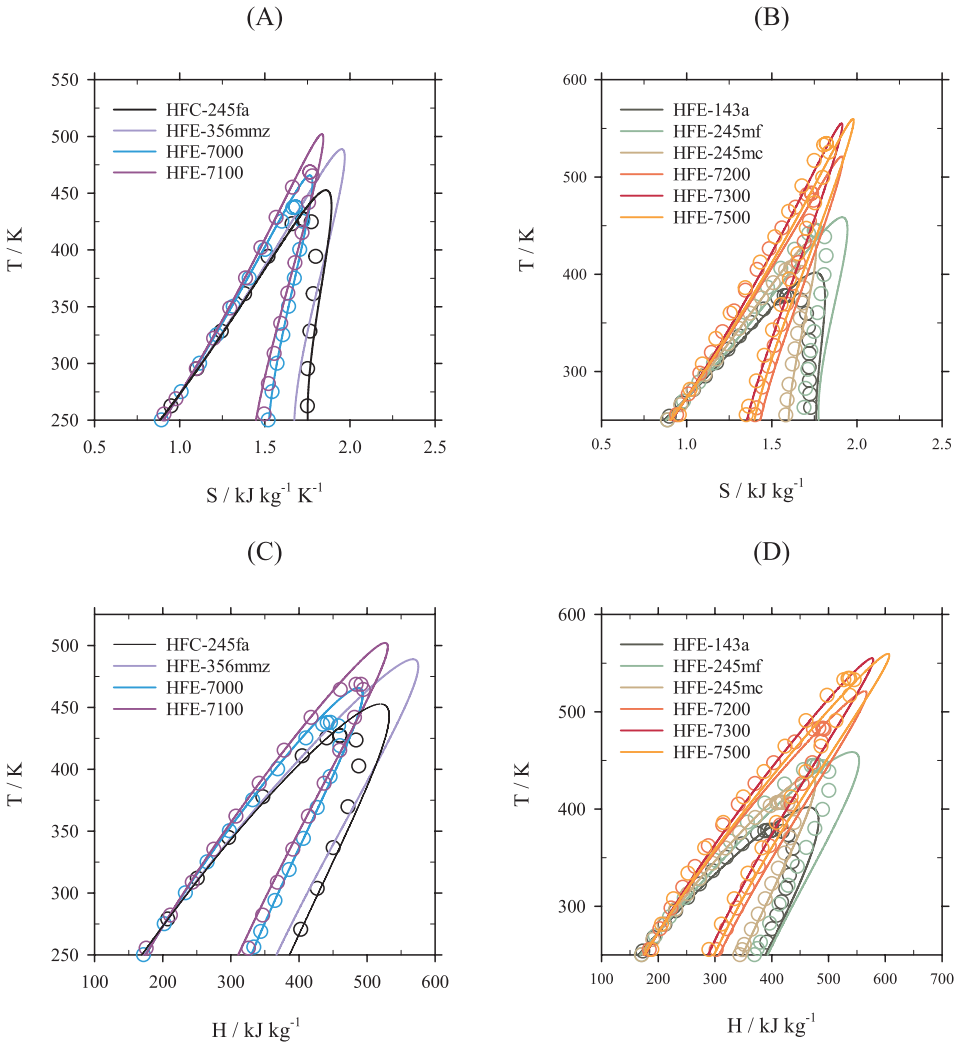

Figure 5.16: Saturated mass entropies (top) and enthalpies (bottom) for a selection of working fluids studied as ORC's working fluid replacements. Symbols represent the calculations by REFPROP (Lemmon et al., 2018), and solid lines are the polar soft-SAFT EoS.

The results reveal that all the studied compounds exhibit either a near-zero or a positive slope ($\mathrm{d}S/\mathrm{d}t$) in the vapor saturation curve, indicating a near-isentropic (R-245fa and HFE-143a) or a dry (HFE-7000 or HFE-7100) fluid behavior, respectively. Both behaviors are recommended for ORC applications since no superheating is required to avoid condensation during the isentropic expansion (Petr & Raabe, 2015; Tchanche et al., 2011). Indeed, it is even possible to predict the transition from wet to dry fluids as a function of the operating conditions chosen using SAFT approaches (Albornoz et al., 2018; Garrido et al., 2012), although this is out of the scope of this thesis. The predictions obtained with the soft-SAFT models are in agreement

with the REFPROP correlations for the fluids for which data are available. Significant deviations are noticed in the high-temperature range of the vapor phase, particularly for the base case (R-245fa). This is caused by the overprediction of the critical point, a common drawback of SAFT mean-field approaches. It is important to note that R-245fa parameters were transferred from the work of Albà et al. (2021), in which the molecular parameters had been fitted to a lower temperature range. While it is possible to reduce these deviations by reparametrizing this compound at a higher temperature range, in this study, these parameters were kept for consistency, given the marginal improvement that would be achieved. In any case, and as shown in the previous section, the soft-SAFT characterization ensures a good description of the range of temperature and pressure working conditions of the ORC.

Next, the information gathered for all HFEs, along with the benchmark HFC, is used to optimize the ORC represented in Figure 5.14, based on the choice of several Key Performance Indicators (KPIs). These include the cycle thermal efficiency (η_{ORC}), as defined by equation 5.10, and the service fluids (i.e., CW, and HF) and working fluid mass flow rates. The choice is based on the search for reducing the energy inputs coming from the mass flows, while η_{ORC} is typically seen as an ORC system's performance metric (J. Yang et al., 2018a). The main results of the optimization are reported in Table 5.9.

Fixing a constant net work output, the calculated η_{ORC} for all fluids is given in Figure 5.17.

While the benchmark R-245fa shows the greatest performance (9.80%), the low molecular weight compounds, HFE-143a and HFE-245mc, exhibit cycle yields that are comparable to the reference (8.74% and 8.52%, respectively). This is because, as stated in section 5.2.1, these fluids have thermodynamic properties that make them suitable for use in ORCs, such as a high vapor pressure or vaporization enthalpy. Nonetheless, with the exception of HFE-7500, no significant changes in the cycle efficiency are seen across the different HFE working fluids provided in this study at the established conditions. This exception is justified since this compound has a lower vapor pressure and much greater boiling point values than the other fluids evaluated, resulting in worse performance when compared to the alternatives.

A comparison between the soft-SAFT predicted efficiencies and those estimated in the previous bibliography for some specific compounds (i.e., R-245fa, HFE-7000, and HFE-7100) reveal slightly higher values than those of Jang and Lee (2018) (4-5%), slightly lower values than the results of H. Wang et al. (2017) (12-13%) and similar results to the molecular dynamic simulations done by Petr and Raabe (2015) (7.5%). This comparison must be taken with care, as the methodologies adopted by the different authors differ from each other, as well as the performance constraints and component efficiencies (different evaporation temperature, mass flows, or condensing temperatures). In any case, the results presented in this thesis fall within the range of expected values and do not prevent the qualitative comparison presented in this section.

Table 5.9: Optimized operational parameters in the modeled ORC for the selected HFE.

	R-245fa	HFE-143a	HFE-245mf	HFE-245mc	HFE-356mmz	HFE-7000	HFE-7100	HFE-7200	HFE-7300	HFE-7500
T_1 (K)	324.15	296.15	337.15	309.15	353.15	335.15	354.15	407.15	406.15	410.15
P_1 (kPa)	376.92	574.27	361.00	312.84	285.27	267.42	201.24	496.93	247.90	101.30
T_2 (K)	325.39	297.45	338.25	310.21	354.15	336.02	354.85	408.83	406.97	410.45
P_2 (kPa)	1600.0	1674.0	1467.0	1283.0	1157.0	1076.0	836.00	1568.0	881.00	362.00
T_3 (K)	384.02	340.13	399.60	366.14	413.66	393.88	414.90	468.15	468.12	468.03
P_3 (kPa)	1600.0	1674.0	1467.0	1283.0	1157.0	1076.0	836.00	1568.0	881.00	362.00
T_4 (K)	345.58	304.03	367.50	334.18	388.55	368.66	395.96	444.23	451.17	458.87
P_4 (kPa)	376.92	574.27	361.00	312.84	285.27	267.42	201.24	496.93	247.90	101.30
$T_{\mathrm{HF,in}}$ (K)	473.15	473.15	473.15	473.15	473.15	473.15	473.15	473.15	473.15	473.15
$T_{\mathrm{HF,out}}$ (K)	331.10	303.17	343.44	315.84	359.20	341.83	360.23	456.59	459.21	462.34
$\dot{m}_{\mathrm{HF}}$ (kg s^{-1})	0.12500	0.13000	0.14500	0.11700	0.17400	0.15200	0.18200	1.9710	1.8960	2.3270
$T_{\mathrm{CW,in}}$ (K)	291.15	291.15	291.15	291.15	291.15	291.15	291.15	291.15	291.15	291.15
$T_{\mathrm{CW,out}}$ (K)	329.86	298.40	349.19	314.29	370.57	349.10	379.08	412.40	459.21	408.42
$\dot{m}_{\mathrm{CW}}$ (kg s^{-1})	0.19000	1.2560	0.13400	0.32700	0.098000	0.14500	0.092000	0.023000	0.062000	0.018000
$\dot{m}_{\mathrm{ORC}}$ (kg s^{-1})	0.15670	0.20330	0.16940	0.18650	0.19260	0.22570	0.24230	0.47020	0.39310	0.35490
ER	4.9557	3.2877	4.8671	4.9270	4.9400	4.9397	5.0051	4.9879	4.9612	4.0352
Q_{evap} (kW)	35.247	44.562	38.366	36.005	40.036	38.958	39.871	72.292	56.670	52.517
Q_{cond} (kW)	31.263	39.978	34.964	32.381	36.642	35.405	36.640	64.960	51.545	50.204
W_{p} (kW)	0.35671	0.61987	0.42823	0.52114	0.42585	0.45207	0.23920	1.4574	0.61695	0.20495
W_{exp} (kW)	3.8107	4.5158	3.3322	3.5899	3.3231	3.4823	3.0582	7.5170	5.0285	2.2114
η_{ORC} (%)	9.7994	8.7428	7.5691	8.5231	7.2366	7.7782	7.0705	8.3820	7.7805	3.8205

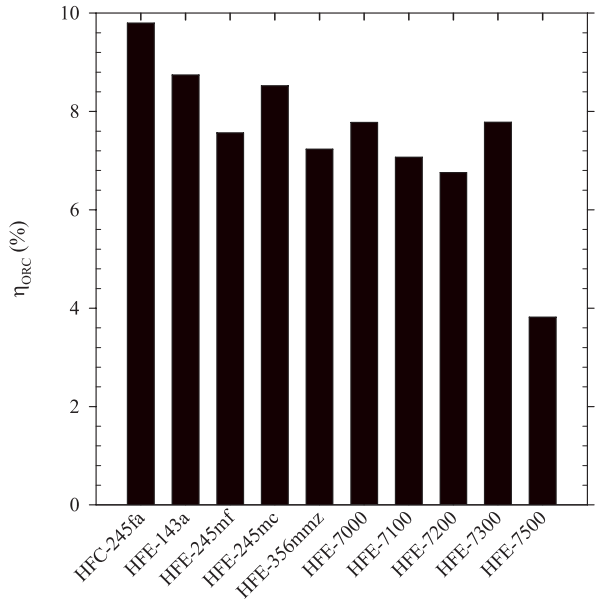

Figure 5.17: Cycle thermal efficiencies for the studied working fluids.

Figure 5.18 compares the required cooling, heating, and working fluid mass flow rates for all the studied cases at the constraint imposed.

In contrast to the results obtained for thermal efficiencies, evident differences are found among all cases. The first apparent conclusion is the low suitability of high molecular weight HFE-7200, HFE-7300, and, again, HFE-7500 to become alternative substitutes to R-245fa due to their high demand for the heating fluid and working fluid flow rates. This is again related to their high boiling point and low enthalpy of vaporization. Although this facilitates a low CW demand at moderate pressure conditions, they require a higher heat demand to produce 2 kW of electricity and, consequently, a higher flow rate of working fluid and HF.

At the other end of the scale, and despite being the top-performing fluids in terms of thermal efficiency, the low molecular weight HFE-143a and, to a lesser extent, HFE-245mc, also have a severe energy penalty in terms of service fluids needs. In this case, they have the lowest boiling points and, therefore, require a higher cooling water flow rate because they exhibit the lowest condensation temperatures, regardless of having a latent heat very close to the benchmark working fluid.

The remaining fluids present a balanced amount of mass flow rates, which are similar to the R-245fa benchmark case. At this stage, it is also important to include the GWP criteria in the selection. While all the fluids evaluated in this thesis have lower GWPs than the benchmark, HFE-245mf represents a minor decrement and, as far as it does not show a clear improvement, is also discarded at this stage.

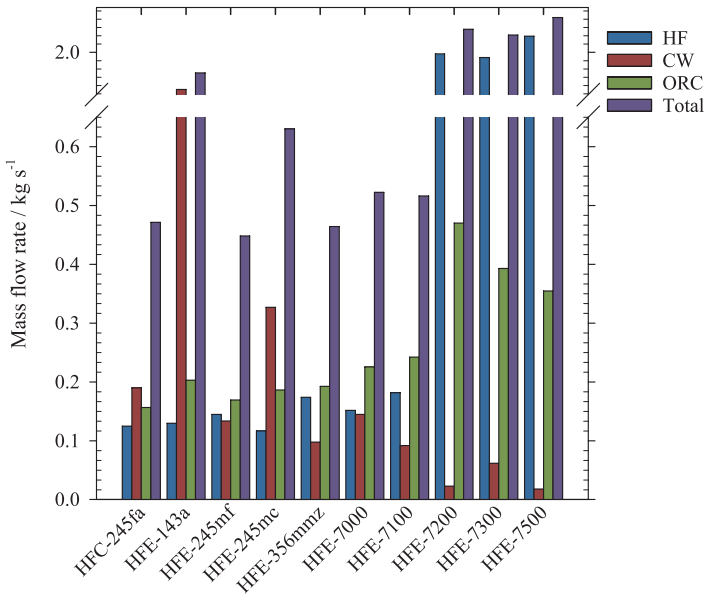

Figure 5.18: ORC mass flowrate comparison for the selected working fluids.

According to the findings of this investigation, HFE-7000, HFE-7100, and HFE-356mmz are the best alternatives in single-stage ORCs with low-temperature heat sources in terms of thermal efficiency and service fluids consumption. This conclusion partially agrees with the suggestion of Jang and Lee (2018), who also recommended the first two options to build a cycle with minimal cooling water usage and moderate maximum pressures, allowing for cost reductions in electricity production. Among the three possibilities, HFE-7000 provides the highest thermal efficiency, while HFE-356mmz requires lower mass flow rates. Again, a key factor to consider is the GWP reduction compared to HFC-245a. While HFE-7000 and HFE-7100 reduce the GWP by 40.12% and 49.06%, respectively, HFE-356mmz provides an astonishing 99.15% reduction. Consequently, the latest one represents one of the most promising choices for the future.

Despite all these facts, it is important to keep in mind that the obtained cycle thermal efficiency is lower than that of R-245fa, as it is shown in Figure 5.17, due to lower vaporization enthalpies, vapor pressures, and critical pressures compared to the benchmark HFC. Indeed, none of the alternatives reaches the same efficiency. This is a clear sign that further improvements will be necessary, undoubtedly pushing this analysis toward the study of working fluid mixtures.

6

Conclusions and Future Work

Based on the objectives of this doctoral thesis, in which new ecotechnological recovery and recycling methods are explored using a multiscale simulation approach to recover fluorinated working fluids to develop novel, circular economy-based initiatives to facilitate the phase-out of the F-gases affected by the new legislation resulting from the Kigali Amendment, the key findings obtained are discussed hereunder

6.1 Conclusions

This thesis's primary goal is to develop novel circular economy-based initiatives through a multiscale simulation approach to facilitate the phase-out of F-gases affected by the new legislation resulting from the Kigali Amendment. In such an approach, several multiscale tools ranging from quantum-based calculations to macroscopic process simulations, have been used to gather information at different simulation scales to (i) design and optimize recovery ecotechnological methods to recycle fluorinated working fluids from high-GWP commercial mixtures using advanced solvents and (ii) describe the physicochemical behavior of alternative low-GWP compatible working fluids to replace the affected F-gases in a wide range of applications.

The main conclusions drawn from the analysis of the results obtained in this work are highlighted below:

1. A molecular model for several F-gases has been built within the soft-SAFT framework employing a relatively simple coarse-grained approach. These include R-32, R-23, R-125, and R-134a, based on their usage in different refrigeration applications, as well as the R-14 perfluorocarbon for comparative purposes.

   (a) An excellent description of the phase envelope is found in a wide range of temperatures, up to 95% of the critical point.

   (b) The increase in the number and degree of halogenation leads to lower molecular volumes. This decrease results in lower molecular densities, higher vapor molar densities, and lower critical temperatures.

   (c) The molecules with higher dipole moments also exhibit higher critical temperatures due to their capacity to interact with surrounding molecules.

2. A conductive study modeling the solubility of the fluorinated refrigerants has been carried out in terms of their solubility and recovery capacity in a widely-used imidazolium-based ionic liquid, $[C_2mim][Tf_2N]$, at a selected working temperature of 303.15 K based on the availability of experimental data.

   (a) F-gases with more hydrogens in their chain have more absorption capacity due to hydrogen bonding between molecules. With this, R-134a is the gas showing a higher solubility in $[C_2mim][Tf_2N]$, followed by R-32, R-125, R-23, and R-14, whose solubility is the lowest because their molecules form a stable structure with neither a dipole nor hydrogen-bonding associations.

   (b) A proportional trend between a higher chain length/volume (entropic effect) and a higher dipole moment (enthalpic effect) was found to increase the solubility in $[C_2mim][Tf_2N]$.

3. Three imidazolium-based ILs containing two fluorinated anions, [C_2mim][Tf_2N], [C_6mim[Tf_2N], and [C_4mim][PF_6] named in this thesis *traditional* ionic liquids, have been selected to address the absorption and separation of R-32 and R-125, the two hydrofluorocarbons conforming the R-410A blend.

   (a) *Traditional* ionic liquids have been modeled as single chains with a certain amount of association sites representing the cation-anion interactions, assuming a very short time of dissociation until a new pair is formed.

   (b) An excellent representation of the solubility curves is achieved at all compositions and temperature conditions.

   (c) The enthalpy and entropy of solvation, Henry's constants, and the selectivity of these mixtures have been evaluated and compared. The ideal selectivity is higher for [C_4mim][PF_6] than for the [Tf_2N]-based ionic liquids. This is a consequence of the lower solubility of R-125 at low compositions of [C_4mim][PF_6].

   (d) Although results do not reveal significant differences from a thermodynamic perspective, [C_2mim][Tf_2N] has been selected as the most promising solvent considering mass transfer and viscosity aspects.

   (e) A ternary mixture is predicted to build the thermodynamic diagram and evaluate the competitive selectivity. The results reveal low selectivity values in a range between 1 and 2 at 300 K.

4. In a similar way, four different ILs with variable amounts of fluorine atoms in the anion, named *fluorinated* ionic liquids in this thesis, were selected to perform a thermodynamic characterization of the solubility of R-134a. The results reveal that the anion structures with nine fluorine atoms improve the solubility of R-134a in comparison to [C_2mim][Tf_2N], with six fluorine atoms. The carboxylate anion [$C_4F_9CO_2$] and the sulfonate anion, [$C_4F_9SO_3$], show higher solubilities in this order.

5. The analysis of the solubility of R-134a has been completed by studying new deep eutectic solvents based on the precursors of the promising anions [$C_4F_9CO_2$] and [$C_4F_9SO_3$], $HC_4F_9CO_2$ and $HC_4F_9SO_3$ as HBDs and [C_2mim][Cl] as HBA.

   (a) DESs were modeled here for the first time using a two-component approach considering both compounds forming the DES as independent entities and treating them as a mixture. A novel approach was used to find the molecular parameters of $HC_4F_9SO_3$ based on the parameter transferability between the two acids. An excellent description was found for the ternary systems at all proportions fitting only two temperature-independent binary parameters that remained equal for all DESs mixtures.

(b) Combining different molar ratios, the results revealed that higher proportions of the acid provided higher solubility when mixing.

(c) DES did not favor the solubility of R-134a, which decreased with respect to the previously studied FILs.

6. Two separation processes have been studied for the separation of R-410A and R-407F using the *traditional* IL [C_2mim][Tf_2N] and the FIL [C_2mim][$C_4F_9CO_2$] respectively, according to the results obtained, using Aspen Plus process simulator. Given the scarce amount of experimental data, a novel methodology based on the COSMO-RS thermodynamic package integrated into the Aspen Plus process simulator was used.

(a) An extractive distillation process was built for the separation of R-410A. A column with 32 stages, followed by a flash tank, was modeled to achieve a purity of 98 wt % of R-32. A recovery of 97.94% concerning the initial feed of R-32 is obtained.

(b) An absorption process was carried out to separate R-32 from the R-407F commercial blend. An absorption column with 38 theoretical stages, followed by a flash tank, was necessary to achieve a 98 wt % purity for R-32. The obtained L/G ratio of 5.77 is considerably lower than other absorption separation methods.

7. Based on the results obtained from the simulation of the recovery of R-407F, the environmental sustainability of the recovery process was analyzed with an LCA approach, comparing the obtained results with the conventional R-32 production.

(a) The LCA revealed that the R-32 recovery from R-407F has considerably lower environmental impacts than the production of R-32, with a GWP reduction of 86%.

(b) The results evidence that the FIL production and the fugitive emissions in the FIL use stage are the main hotspots dominating the life cycle of the R-32 recovery scenario. The production stage of FIL contributes more than 57% to most of the impact categories, while the fugitive emissions are the main ones responsible for the impact in the GWP category.

(c) Sensitivity analysis results show that decreasing the time of FIL replacement has a significant impact in the ADP (elements) and HTP categories, but still, the impacts are generally lower than in the R-32 production scenario in most of the categories.

8. Force-field-based molecular dynamic simulations have been employed to provide insight into the thermodynamical description of several alternative blends to R-407F and R-410A.

(a) VLE MD simulations were performed for the HFO and the HFCs conforming the mixtures. The calculated properties include saturated density profiles, vapor pressures, surface tensions, vapor and liquid heat capacity, and liquid viscosity. The

predicted properties with MD simulations were in good agreement with REFPROP calculations, validating the force field used and the simulation results.

(b) R-513A blend and R-134a as a single compound were compared with the behavior of R-407F. The predicted properties are in excellent agreement with the results obtained with REFPROP calculations, with the most significant differences obtained in the surface tension values. The results show that R-513A and R-134a exhibit higher values for the surface tensions, which may result in an enhanced heat transfer due to a decrease in droplet formation and entrainment.

(c) R-410A was compared with R-452B and R-454B. Both alternatives exhibit higher critical temperatures and wider saturation domes than R-410A, in contrast with the lower vapor pressures observed with respect to R-410A.

9. The suitability of nine HFEs as prospective replacements for R-245fa working fluids in low-grade waste heat recovery ORCs has been assessed, proposing a study based on different key performance indicators (KPIs) related to energy efficiency.

(a) A solid and robust model has been built using the soft-SAFT EoS with the explicit inclusion of the polar interactions present in such fluids, which have proven to strongly impact their physicochemical behavior.

(b) The results have shown a similar performance in terms of efficiency for all the studied fluids at the process conditions considered (except for HFE-7500), lower in all cases than the benchmark R-245fa.

(c) Significant differences have been detected in the required service fluids flow rates. High molecular weight working fluids, such as HFE-7200, HFE-7300, and HFE-7500, have been excluded as suitable alternatives due to their elevated normal boiling points and low vaporization enthalpy, being incompatible with the ORC studied in this work, as they demand large amounts of working and heating fluids. Low molecular weight HFE-143a and HFE-245mc suffer a substantial energy penalty in terms of cooling water demands due to their low boiling points. HFE-245mf is discarded in the final stage since it has a high GWP value, representing a minor decrease compared to the benchmark case.

(d) HFE-356mmz, HFE-7000, and HFE-7100 are considered possible replacements for R-245fa in a simple ORC design, with the first two having the best environmental (HFE-356mmz) and technical (HFE-7000) performance.

6.2 Future Work

To further extend the results presented in this work, some strategies and investigation lines are given below:

1. A deeper understanding of multicomponent mixtures must be performed to extend the design of separation processes to other ternary commercial blends.

2. The separation of R-134a using DES does not improve the results obtained with the FILs studied. However, these conclusions are limited to specific F-gas in some particular conditions. While DESs are still a hot topic and present many advantages concerning ILs, a future work would extend the solubility study of more HFCs, such as R-32 and R-125, on a broader family of eutectic mixtures of FILs with perfluorinated acids.

3. The thermophysical characterization of the binary and ternary blends presented in Chapter 5 using molecular dynamics must be completed using the soft-SAFT EoS for a full comparison of both methodologies. Additional molecular simulations would be desirable for further properties and new mixtures of fluids.

4. Although the methodology presented in this thesis for studying alternative working fluids in ORC applies to mixtures; only pure HFEs have been studied. The results show that some of these gases are promising alternatives to R-245fa, even though none of the alternatives meet its overall efficiency in ORC applications. A future line of research would correspond to the study of the efficiency of binary mixtures of HFEs mixed with 3rd generation working fluids, with a moderate GWP, or even with 4th generation refrigerants such as HFOs.

5. The results presented in this doctoral thesis can guide a new line of investigation, where artificial neural networks may be utilized to forecast new parameters for SAFT models or molecular simulation's force fields to predict the thermodynamic behavior of other potential working fluid alternatives.

A

Papers published in indexed journals and contributions to scientific meetings

A.1 Papers published during the development of this thesis

1. Asensio-Delgado, S., **Jovell, D.**, Zarca, G., Urtiaga, A., & Llovell, F. (2020). Thermodynamic and process modeling of the recovery of R410A compounds with ionic liquids. *International Journal of Refrigeration*, *118*, 365–375. https://doi.org/10.1016/j.ijrefrig.2020.04.013.

2. **Jovell, D.**, B. Gómez, S., Zakrzewska, M. E., Nunes, A. V., Araújo, J. M., Pereiro, A. B., & Llovell, F. (2020). Insight on the solubility of R134a in fluorinated ionic liquids and deep eutectic solvents. *Journal of Chemical & Engineering Data*, *65*(10), 4956–4969. https://doi.org/10.1021/acs.jced.0c00588.

3. **Jovell, D.**, O. Pou, J., Llovell, F., & Gonzalez-Olmos, R. (2022). Life Cycle Assessment of the Separation and Recycling of Fluorinated Gases Using Ionic Liquids in a Circular Economy Framework. *ACS Sustainable Chemistry & Engineering*, *10*(1), 71–80. https://doi.org/10.1021/acssuschemeng.1c04723.

4. **Jovell, D.**, Gonzalez-Olmos, R., & Llovell, F. (2022). A computational drop-in assessment of hydrofluoroethers in Organic Rankine Cycles. *Energy*, *254*, 124319. https://doi.org/10.1016/j.energy.2022.124319.

5. **Jovell, D.**, Alonso, G., Gonzalez-Olmos, R., Gamallo, P., Quinteros-Lama, H., & Llovell, F. (In preparation). Thermophysical characterization of fluorinated blends using molecular simulations.

A.2 Contributions to scientific meetings

1. Ojeda, R.M., Lloret, J.O., **Jovell, D**, Vega, L. F., & Llovell, F., (2018, June 26-28). Physicochemical characterization of Deep Eutectic Solvents as alternative solvents for gas recovery [Oral Presentation]. The 26th Thermodynamics Conference, Punta Umbría, Spain.

2. **Jovell, D.**, Albà, C.G., & Llovell, F. (2019, May 16-17). Understanding the thermodynamic behavior of fluorinated refrigerants using soft-SAFT [Poster Presentation]. Jornada Doctorands IQS, Barcelona, Spain.

3. **Jovell, D.**, Albà, C.G., & Llovell, F. (2019, June 19-21). Process design and energy optimization of the separation of fluorinated refrigerants using ionic liquids with Aspen Plus [Oral Presentation]. ANQUE-ICCE-CIBIQ, Santander, Spain.

4. **Jovell, D.**, Alonso, G., Gamallo, P., & Llovell, F. (2021, June 20-25). Thermophysical Behaviour of Fluorinated Blends Using Molecular Dynamics Simulations combined with

soft-SAFT [Oral Presentation]. 21st Symposium on Thermophysical Properties, Boulder, CO, United States of America.

5. **Jovell, D.**, Alonso, G., Araújo, J. M. M., Pereiro, A. B., & Llovell, F. (2021, June 20-25). Addressing the Capacity of Fluorinated Ionic Liquids and Deep Eutectic Solvents for the Separation and Recovery of Refrigerants [Oral Presentation]. 21st Symposium on Thermophysical Properties, Boulder, CO, United States of America.

6. **Jovell, D.**, Gómez, S., Araújo, J. M. M., Pereiro,. A. B., & Llovell, F. (2021, June 5-9). Characterization of the Absorption of F-gases in new Fluorinated Ionic Liquids and Deep Eutectic Solvents with soft-SAFT [Oral Presentation]. 31st European Symposium on Applied Thermodynamics, Paris, France.

7. **Jovell, D.**, Gonzalez-Olmos, R., & Llovell, F. (2022, June 17-21). Thermodynamic characterization and energy analysis of hydrofluoroethers in Organic Rankine Cycles using soft-SAFT [Oral Presentation]. 32nd European Symposium on Applied Thermodynamics, Graz, Austria.

8. **Jovell, D.**, Demirbek, M.G., Alencar, L.V., Alkhatib, I.I.I., Vega, L.F., & Llovell, F. (2022, September 7-9). Thermophysical Characterization of Deep Eutectic Solvents for Practical Applications in Greenhouse Gas Capture and Separation [Oral Presentation]. The 27th Thermodynamics Conference, Bath, United Kingdom.

9. **Jovell, D.**, González-Olmos, R., Quinteros-Lama, H., & Llovell, F. (2022, November 13-18). Thermophysical Characterisation and Drop-in Assessment of Hydrofluoroethers in Organic Rankine Cycles [Oral Presentation]. 2022 AIChE Annual Meeting, Phoenix, AZ, United States of America.

10. **Jovell, D.**, Pou, J.O., González-Olmos, R., & Llovell, F. (2022, November 13-18). Design and Environmental Assessment of an Ionic-Liquid-Based R407F Refrigerant Separation Process [Oral Presentation]. 2022 AIChE Annual Meeting, Phoenix, AZ, United States of America.

References

3M Company. (2008). *Technical Data 3M™ Novec™ 7500 Engineered Fluid* (tech. rep.). https://multimedia.3m.com/mws/media/65496O/3m-novec-7500-engineered-fluid.pdf%7B%5C&%7Dfn=prodinfo%7B%5C_%7Dnvc7500.pdf

3M Company. (2009a). *Technical Data 3M™ Novec™ 7100 Engineered Fluid* (tech. rep.). https://multimedia.3m.com/mws/media/199818O/3m-novec-7100-engineered-fluid.pdf

3M Company. (2009b). Technical Data 3M™ Novec™ 7200 Engineered Fluid. https://multimedia.3m.com/mws/media/199819O/3m-novec-7200-engineered-fluid-en.pdf%7B%5C&%7Dfn=prodinfo%7B%5C_%7Dnvc7200.pdf

3M Company. (2009c). *Technical Data 3M™ Novec™ 7300 Engineered Fluid* (tech. rep.). https://multimedia.3m.com/mws/media/338713O/3m-novec-7300-engineered-fluid.pdf

3M Company. (2021). *Technical Data 3M™ Novec™ 7000 Engineered Fluid* (tech. rep.). https://multimedia.3m.com/mws/media/121372O/3m-novec-7000-engineered-fluid-tds.pdf

Abbott, A. P., Boothby, D., Capper, G., Davies, D. L., & Rasheed, R. K. (2004). Deep Eutectic Solvents Formed between Choline Chloride and Carboxylic Acids: Versatile Alternatives to Ionic Liquids. *Journal of the American Chemical Society*, *126*(29), 9142–9147. https://doi.org/10.1021/ja048266j

Abbott, A. P., Capper, G., Davies, D. L., & Rasheed, R. K. (2004). Ionic Liquid Analogues Formed from Hydrated Metal Salts. *Chemistry - A European Journal*, *10*(15), 3769–3774. https://doi.org/10.1002/chem.200400127

Abbott, A. P., Capper, G., Davies, D. L., Rasheed, R. K., & Tambyrajah, V. (2003). Novel solvent properties of choline chloride/urea mixtures. *Chemical Communications*, (1), 70–71. https://doi.org/10.1039/b210714g

Abbott, A. P., Capper, G., & Gray, S. (2006). Design of Improved Deep Eutectic Solvents Using Hole Theory. *ChemPhysChem*, *7*(4), 803–806. https://doi.org/10.1002/cphc.200500489

Abbott, A. P., Harris, R. C., & Ryder, K. S. (2007). Application of Hole Theory to Define Ionic Liquids by their Transport Properties. *The Journal of Physical Chemistry B*, *111*(18), 4910–4913. https://doi.org/10.1021/jp0671998

Abbott, A. P., Harris, R. C., Ryder, K. S., D'Agostino, C., Gladden, L. F., & Mantle, M. D. (2011). Glycerol eutectics as sustainable solvent systems. *Green Chem.*, *13*(1), 82–90. https://doi.org/10.1039/C0GC00395F

Abedin, R., Heidarian, S., Flake, J. C., & Hung, F. R. (2017). Computational Evaluation of Mixtures of Hydrofluorocarbons and Deep Eutectic Solvents for Absorption Refrigeration Systems. *Langmuir*, *33*(42), 11611–11625. https://doi.org/10.1021/acs.langmuir.7b02003

Abedin, R., Shen, Y., Flake, J. C., & Hung, F. R. (2020). Deep Eutectic Solvents Mixed with Fluorinated Refrigerants for Absorption Refrigeration: A Molecular Simulation Study. *The Journal of Physical Chemistry B*, *124*(22), 4536–4550. https://doi.org/10.1021/acs.jpcb.0c01860

Abrams, D. S., & Prausnitz, J. M. (1975). Statistical thermodynamics of liquid mixtures: A new expression for the excess Gibbs energy of partly or completely miscible systems. *AIChE Journal*, *21*(1), 116–128. https://doi.org/10.1002/aic.690210115

Abranches, D. O., Larriba, M., Silva, L. P., Melle-Franco, M., Palomar, J. F., Pinho, S. P., & Coutinho, J. A. (2019). Using COSMO-RS to design choline chloride pharmaceutical eutectic solvents. *Fluid Phase Equilibria*, *497*, 71–78. https://doi.org/10.1016/j.fluid.2019.06.005

Ahosseini, A., & Scurto, A. M. (2008). Viscosity of imidazolium-based ionic liquids at elevated pressures: Cation and anion effects. *International Journal of Thermophysics*, *29*(4), 1222–1243. https://doi.org/10.1007/s10765-008-0497-7

Ahrenberg, M., Beck, M., Neise, C., Keßler, O., Kragl, U., Verevkin, S. P., & Schick, C. (2016). Vapor pressure of ionic liquids at low temperatures from AC-chip-calorimetry. *Physical Chemistry Chemical Physics*, *18*(31), 21381–21390. https://doi.org/10.1039/C6CP01948J

Aidt, M. (2020). Climate Emergency Declaration. Retrieved September 19, 2022, from https://climateemergencydeclaration.org/

Albà, C. G., Alkhatib, I. I. I., Llovell, F., & Vega, L. F. (2021). Assessment of Low Global Warming Potential Refrigerants for Drop-In Replacement by Connecting their Molecular Features to Their Performance. *ACS Sustainable Chemistry & Engineering*, *9*(50), 17034–17048. https://doi.org/10.1021/acssuschemeng.1c05985

Albà, C. G., Vega, L. F., & Llovell, F. (2020a). A consistent thermodynamic molecular model of n-hydrofluoroolefins and blends for refrigeration applications. *International Journal of Refrigeration*, *113*, 145–155. https://doi.org/10.1016/j.ijrefrig.2020.01.008

Albà, C. G., Vega, L. F., & Llovell, F. (2020b). Assessment on Separating Hydrofluoroolefins from Hydrofluorocarbons at the Azeotropic Mixture R513A by Using Fluorinated Ionic Liquids: A Soft-SAFT Study. *Industrial & Engineering Chemistry Research*, *59*(29), 13315–13324. https://doi.org/10.1021/acs.iecr.0c02331

Albornoz, J., Mejía, A., Quinteros-Lama, H., & Garrido, J. M. (2018). A rigorous and accurate approach for predicting the wet-to-dry transition for working mixtures in organic Rankine cycles. *Energy*, *156*, 509–519. https://doi.org/10.1016/j.energy.2018.05.074

Aldawsari, J. N., Adeyemi, I. A., Bessadok-Jemai, A., Ali, E., AlNashef, I. M., & Hadj-Kali, M. K. (2020). Polyethylene glycol-based deep eutectic solvents as a novel agent for natural gas sweetening (E. Jabbari, Ed.). *PLOS ONE*, *15*(9), e0239493. https://doi.org/10.1371/journal.pone.0239493

Alkhatib, I. I. I., Albà, C. G., Darwish, A. S., Llovell, F., & Vega, L. F. (2022). Searching for Sustainable Refrigerants by Bridging Molecular Modeling with Machine Learning.

Industrial & Engineering Chemistry Research, *61*(21), 7414–7429. https://doi.org/10.1021/acs.iecr.2c00719

Alkhatib, I. I. I., Pereira, L. M. C., Torne, J., & Vega, L. F. (2020). Polar soft-SAFT: theory and comparison with molecular simulations and experimental data of pure polar fluids. *Physical Chemistry Chemical Physics*, *22*(23), 13171–13191. https://doi.org/10.1039/D0CP00846J

Alkhatib, I. I. I., & Vega, L. F. (2021). Quantifying the effect of polarity on the behavior of mixtures of n-alkanes with dipolar solvents using polar soft-statistical associating fluid theory (Polar soft-SAFT). *AIChE Journal*, *67*(3), e16649. https://doi.org/10.1002/aic.16649

Allal, A., Boned, C., & Baylaucq, A. (2001). Free-volume viscosity model for fluids in the dense and gaseous states. *Physical Review E*, *64*(1), 011203. https://doi.org/10.1103/PhysRevE.64.011203

Allal, A., Moha-ouchane, M., & Boned, C. (2001). A New Free Volume Model for Dynamic Viscosity and Density of Dense Fluids Versus Pressure and Temperature. *Physics and Chemistry of Liquids*, *39*(1), 1–30. https://doi.org/10.1080/00319100108030323

Allen, M. P., & Tildesley, D. J. (2017). *Computer Simulation of Liquids: Second Edition*. Oxford University Press USA - OSO.

Al-Malah, K. I. M. (2017). *Aspen Plus: Chemical Engineering Applications*. John Wiley & Sons, Inc.

Amde, M., Liu, J.-F., & Pang, L. (2015). Environmental Application, Fate, Effects, and Concerns of Ionic Liquids: A Review. *Environmental Science & Technology*, *49*(21), 12611–12627. https://doi.org/10.1021/acs.est.5b03123

Andersen, H. C. (1973). Cluster expansions for hydrogen-bonded fluids. I. Molecular association in dilute gases. *The Journal of Chemical Physics*, *59*(9), 4714–4725. https://doi.org/10.1063/1.1680684

Andersen, H. C. (1974). Cluster expansions for hydrogen bonded fluids. II. Dense liquids. *The Journal of Chemical Physics*, *61*(12), 4985–4992. https://doi.org/10.1063/1.1681838

Anderson, J. L., Dixon, J. K., Maginn, E. J., & Brennecke, J. F. (2006). Measurement of SO2 Solubility in Ionic Liquids. *The Journal of Physical Chemistry B*, *110*(31), 15059–15062. https://doi.org/10.1021/jp063547u

Andreu, J. S., & Vega, L. F. (2007). Capturing the solubility behavior of CO2 in ionic liquids by a simple model. *Journal of Physical Chemistry C*, *111*(43), 16028–16034. https://doi.org/10.1021/jp074353x

Andreu, J. S., & Vega, L. F. (2008). Modeling the solubility behavior of CO2, H2, and Xe in [Cn-mim] [Tf2N] ionic liquids. *Journal of Physical Chemistry B*, *112*(48), 15398–15406. https://doi.org/10.1021/jp807484g

Aparicio, S. (2008). Phase equilibria in perfluoroalkane + alkane binary systems from PC-SAFT equation of state. *Journal of Supercritical Fluids*, *46*(1), 10–20. https://doi.org/10.1016/j.supflu.2008.02.017

Aparicio, S., Atilhan, M., & Karadas, F. (2010). Thermophysical Properties of Pure Ionic Liquids: Review of Present Situation. *Industrial & Engineering Chemistry Research*, *49*(20), 9580–9595. https://doi.org/10.1021/ie101441s

Aprea, C., Greco, A., & Maiorino, A. (2017a). An experimental investigation of the energetic performances of HFO1234yf and its binary mixtures with HFC134a in a household refrigerator. *International Journal of Refrigeration*, *76*, 109–117. https://doi.org/10.1016/j.ijrefrig.2017.02.005

Aprea, C., Greco, A., Maiorino, A., & Masselli, C. (2018). The drop-in of HFC134a with HFO1234ze in a household refrigerator. *International Journal of Thermal Sciences*, *127*, 117–125. https://doi.org/10.1016/j.ijthermalsci.2018.01.026

Aprea, C., Greco, A., & Maiorino, A. (2016). An experimental investigation on the substitution of HFC134a with HFO1234YF in a domestic refrigerator. *Applied Thermal Engineering*, *106*, 959–967. https://doi.org/10.1016/j.applthermaleng.2016.06.098

Aprea, C., Greco, A., & Maiorino, A. (2017b). Comparative performance analysis of HFO1234ze/HFC134a binary mixtures working as a drop-in of HFC134a in a domestic refrigerator. *International Journal of Refrigeration*, *82*, 71–82. https://doi.org/10.1016/j.ijrefrig.2017.07.001

Asensio-Delgado, S., Pardo, F., Zarca, G., & Urtiaga, A. (2020a). Enhanced absorption separation of hydrofluorocarbon/hydrofluoroolefin refrigerant blends using ionic liquids. *Separation and Purification Technology*, *249*, 117136. https://doi.org/10.1016/j.seppur.2020.117136

Asensio-Delgado, S., Pardo, F., Zarca, G., & Urtiaga, A. (2020b). Vapor–Liquid Equilibria and Diffusion Coefficients of Difluoromethane, 1,1,1,2-Tetrafluoroethane, and 2,3,3,3-Tetrafluoropropene in Low-Viscosity Ionic Liquids. *Journal of Chemical & Engineering Data*, *65*(9), 4242–4251. https://doi.org/10.1021/acs.jced.0c00224

Asensio-Delgado, S., Pardo, F., Zarca, G., & Urtiaga, A. (2021). Absorption separation of fluorinated refrigerant gases with ionic liquids: Equilibrium, mass transport, and process design. *Separation and Purification Technology*, *276*, 119363. https://doi.org/10.1016/j.seppur.2021.119363

Asensio-Delgado, S., Pardo, F., Zarca, G., & Urtiaga, A. (2022). Machine learning for predicting the solubility of high-GWP fluorinated refrigerants in ionic liquids. *Journal of Molecular Liquids*, *367*, 120472. https://doi.org/10.1016/j.molliq.2022.120472

Standard Test Method for Concentration Limits of Flammability of Chemicals (Vapors and Gases) (Standard). (2010). American Society for Testing and Materials. West Conshohocken, PA, USA.

Bai, L., He, M., Liu, X., & Ye, Z. (2019). A new activity coefficient model for the solution of molecular solute + ionic liquid. *Fluid Phase Equilibria*, *493*, 144–152. https://doi.org/10.1016/j.fluid.2019.04.016

Balasubramani, S. G., Chen, G. P., Coriani, S., Diedenhofen, M., Frank, M. S., Franzke, Y. J., Furche, F., Grotjahn, R., Harding, M. E., Hättig, C., Hellweg, A., Helmich-Paris, B.,

Holzer, C., Huniar, U., Kaupp, M., Marefat Khah, A., Karbalaei Khani, S., Müller, T., Mack, F., … Yu, J. M. (2020). TURBOMOLE: Modular program suite for ab initio quantum-chemical and condensed-matter simulations. *The Journal of Chemical Physics*, *152*(18), 184107. https://doi.org/10.1063/5.0004635

Ben-Naim, A. (1987). *Solvation thermodynamics*. Plenum Press.

Bhattacharjee, A., Luís, A., Santos, J. H., Lopes-da-Silva, J. A., Freire, M. G., Carvalho, P. J., & Coutinho, J. A. (2014). Thermophysical properties of sulfonium- and ammonium-based ionic liquids. *Fluid Phase Equilibria*, *381*, 36–45. https://doi.org/10.1016/j.fluid.2014.08.005

Bhatti, M. S. (1999). A historical look at chlorofluorocarbon refrigerants. *ASHRAE Transactions*, *105*, 1186.

Biczak, R., Pawłowska, B., Bałczewski, P., & Rychter, P. (2014). The role of the anion in the toxicity of imidazolium ionic liquids. *Journal of Hazardous Materials*, *274*, 181–190. https://doi.org/10.1016/j.jhazmat.2014.03.021

Bittner, B., Wrobel, R. J., & Milchert, E. (2012). Physical properties of pyridinium ionic liquids. *The Journal of Chemical Thermodynamics*, *55*, 159–165. https://doi.org/10.1016/j.jct.2012.06.018

Bivens, D. B., & Minor, B. H. (1998). Fluoroethers and other next generation fluids. *International Journal of Refrigeration*, *21*(7), 567–576. https://doi.org/10.1016/S0140-7007(98)00027-9

Bivens, D. B., Minor, B. H., & Sievert, A. C. (1996). *Method for preparation of imidazole ionic liquids by microwave* (WO9640834).

Blas, F. J., & Vega, L. F. (1997). Thermodynamic behaviour of homonuclear and heteronuclear lennard-jones chains with association sites from simulation and theory. *Molecular Physics*, *92*(1), 135–150. https://doi.org/10.1080/002689797170707

Blath, J., Christ, M., Deubler, N., Hirth, T., & Schiestel, T. (2011). Gas solubilities in room temperature ionic liquids – Correlation between RTiL-molar mass and Henry's law constant. *Chemical Engineering Journal*, *172*(1), 167–176. https://doi.org/10.1016/j.cej.2011.05.084

Bobbo, S., Nicola, G. D., Zilio, C., Brown, J. S., & Fedele, L. (2018). Low GWP halocarbon refrigerants: A review of thermophysical properties. *International Journal of Refrigeration*, *90*, 181–201. https://doi.org/10.1016/j.ijrefrig.2018.03.027

Boisset, A., Jacquemin, J., & Anouti, M. (2013). Physical properties of a new Deep Eutectic Solvent based on lithium bis[(trifluoromethyl)sulfonyl]imide and N-methylacetamide as superionic suitable electrolyte for lithium ion batteries and electric double layer capacitors. *Electrochimica Acta*, *102*, 120–126. https://doi.org/10.1016/j.electacta.2013.03.150

Bolaji, B. O. (2011). Performance investigation of ozone-friendly R404A and R507 refrigerants as alternatives to R22 in a window air-conditioner. *Energy and Buildings*, *43*(11), 3139–3143. https://doi.org/10.1016/j.enbuild.2011.08.011

Bongiorno, V., & Davis, H. T. (1975). Modified Van der Waals theory of fluid interfaces. *Physical Review A*, *12*(5), 2213–2224. https://doi.org/10.1103/PhysRevA.12.2213

Booten, C. W., Nicholson, S. R., Mann, M. K., & Abdelaziz, O. (2020). *Refrigerants: Market Trends and Supply Chain Assessment* (tech. rep.). United States. https://doi.org/10.2172/1599577

Brown, J. S., Zilio, C., & Cavallini, A. (2010). Thermodynamic properties of eight fluorinated olefins. *International Journal of Refrigeration*, *33*(2), 235–241. https://doi.org/10.1016/j.ijrefrig.2009.04.005

Cadena, C., Anthony, J. L., Shah, J. K., Morrow, T. I., Brennecke, J. F., & Maginn, E. J. (2004). Why is CO2 so Soluble in Imidazolium-Based Ionic Liquids? *Journal of the American Chemical Society*, *126*(16), 5300–5308. https://doi.org/10.1021/ja039615x

Cahn, J. W., & Hilliard, J. E. (1958). Free Energy of a Nonuniform System. I. Interfacial Free Energy. *The Journal of Chemical Physics*, *28*(2), 258–267. https://doi.org/10.1063/1.1744102

Calm, J. M. (2008). The next generation of refrigerants – Historical review, considerations, and outlook. *International Journal of Refrigeration*, *31*(7), 1123–1133. https://doi.org/10.1016/j.ijrefrig.2008.01.013

Camper, D., Becker, C., Koval, C., & Noble, R. (2006). Diffusion and Solubility Measurements in Room Temperature Ionic Liquids. *Industrial & Engineering Chemistry Research*, *45*(1), 445–450. https://doi.org/10.1021/ie0506668

Cané, E., Llovell, F., & Vega, L. F. (2017). Accurate viscosity predictions of linear polymers from n-alkanes data. *Journal of Molecular Liquids*, *243*, 115–123. https://doi.org/10.1016/j.molliq.2017.08.033

Carey, V. P. (1999). *Statistical Thermodynamics and Microscale Thermophysics*. Cambridge University Press. https://doi.org/10.1017/CBO9780511626395

Carrier, W. H., & Waterfill, R. W. (1924). Comparison of thermodynamic characteristics of various refrigerating fluids. *Refrigerating Engineering*.

Castro, P. J., Redondo, A. E., Sosa, J. E., Zakrzewska, M. E., Nunes, A. V. M., Araújo, J. M. M., & Pereiro, A. B. (2020). Absorption of Fluorinated Greenhouse Gases in Deep Eutectic Solvents. *Industrial & Engineering Chemistry Research*, *59*(29), 13246–13259. https://doi.org/10.1021/acs.iecr.0c01893

Çengel, Y. A. (2018). *Thermodynamics: An Engineering Approach*. McGraw-Hill Education Includes bibliographical references and index.

Chandler, D., & Pratt, L. R. (1976). Statistical mechanics of chemical equilibria and intramolecular structures of nonrigid molecules in condensed phases. *The Journal of Chemical Physics*, *65*(8), 2925–2940. https://doi.org/10.1063/1.433529

Chapman, S., & Cowling, T. G. (1990). *The Mathematical Theory of Non-uniform Gases: An Account of the Kinetic Theory of Viscosity, Thermal Conduction and Diffusion in Gases* (D. Burnett, Ed.). Cambridge University Press.

Chapman, W. G., Gubbins, K. E., Jackson, G., & Radosz, M. (1989). SAFT: Equation-of-state solution model for associating fluids. *Fluid Phase Equilibria*, *52*(100), 31–38. https://doi.org/10.1016/0378-3812(89)80308-5

Chapman, W. G., Gubbins, K. E., Joslin, C. G., & Gray, C. G. (1986). Theory and simulation of associating liquid mixtures. *Fluid Phase Equilibria*, *29*(100), 337–346. https://doi.org/10.1016/0378-3812(86)85033-6

Chapman, W. G., Gubbins, K. E., Jackson, G., & Radosz, M. (1990). New Reference Equation of State for Associating Liquids. *Industrial and Engineering Chemistry Research*, *29*(8), 1709–1721. https://doi.org/10.1021/ie00104a021

Chapman, W. G., Jackson, G., & Gubbins, K. E. (1988). Phase equilibria of associating fluids. *Molecular Physics*, *65*(5), 1057–1079. https://doi.org/10.1080/00268978800101601

Chen, H., Goswami, D. Y., & Stefanakos, E. K. (2010). A review of thermodynamic cycles and working fluids for the conversion of low-grade heat. *Renewable and Sustainable Energy Reviews*, *14*(9), 3059–3067. https://doi.org/10.1016/j.rser.2010.07.006

Chen, L., Sharifzadeh, M., Mac Dowell, N., Welton, T., Shah, N., & Hallett, J. P. (2014). Inexpensive ionic liquids: [HSO4]–based solvent production at bulk scale. *Green Chemistry*, *16*(6), 3098–3106. https://doi.org/10.1039/C4GC00016A

Chen, Q., Du, L., Guan, X., Guo, Z., Gao, R., Li, W., & Chen, G. (2020). Measurement of Saturated Vapor Pressure and Compressed Liquid Density for 1,1,1,3,3,3-Hexafluoroisopropylmethyl Ether. *Journal of Chemical & Engineering Data*, *65*(10), 4790–4797. https://doi.org/10.1021/acs.jced.0c00232

Chen, Y., & Mu, T. (2019). Thermal Stability of Ionic Liquids BT - Encyclopedia of Ionic Liquids. In S. Zhang (Ed.). Springer Singapore. https://doi.org/10.1007/978-981-10-6739-6_103-1

Chung, T. H., Ajlan, M., Lee, L. L., & Starling, K. E. (1988). Generalized multiparameter correlation for nonpolar and polar fluid transport properties. *Industrial & Engineering Chemistry Research*, *27*(4), 671–679. https://doi.org/10.1021/ie00076a024

Climate Change: Evidence and Causes: Update 2020. (2020). The National Academies Press. https://doi.org/10.17226/25733

Cohen, M. H., & Turnbull, D. (1959). Molecular Transport in Liquids and Glasses. *The Journal of Chemical Physics*, *31*(5), 1164–1169. https://doi.org/10.1063/1.1730566

Comuñas, M., Baylaucq, A., Plantier, F., Boned, C., & Fernández, J. (2004). Influence of the number of CH2-CH2-O groups on the viscosity of polyethylene glycol dimethyl ethers at high pressure. *Fluid Phase Equilibria*, *222-223*, 331–338. https://doi.org/10.1016/j.fluid.2004.06.034

Consequential-LCA. (2015). Defining the functional unit. Retrieved September 22, 2022, from https://consequential-lca.org/clca/the-functional-unit/define-the-functional-unit/

Constable, G., & Somerville, B. (2003). *A Century of Innovation: Twenty Engineering Achievements that Transformed our Lives*. The National Academies Press. https://doi.org/10.17226/10726

Costa Cabral, B. J., Guedes, R. C., Pai-Panandiker, R. S., & Nieto de Castro, C. A. (2001). Hydrogen bonding and the dipole moment of hydrofluorocarbons by density functional theory. *Physical Chemistry Chemical Physics*, *3*(19), 4200–4207. https://doi.org/10.1039/b102879k

Costello, M. G., Flynn, R. M., & Owens, J. G. (2004). Fluoroethers and Fluoroamines. *Kirk-othmer encyclopedia of chemical technology*. Wiley. https://doi.org/10.1002/0471238961.0612211506122514.a01.pub2

Cuéllar-Franca, R. M., García-Gutiérrez, P., Taylor, S. F., Hardacre, C., & Azapagic, A. (2016). A novel methodology for assessing the environmental sustainability of ionic liquids used for CO2 capture. *Faraday Discussions*, *192*, 283–301. https://doi.org/10.1039/C6FD00054A

Cui, Y., Li, C., Yin, J., Li, S., Jia, Y., & Bao, M. (2017). Design, synthesis and properties of acidic deep eutectic solvents based on choline chloride. *Journal of Molecular Liquids*, *236*, 338–343. https://doi.org/10.1016/j.molliq.2017.04.052

D'Agostino, C., Gladden, L. F., Mantle, M. D., Abbott, A. P., Ahmed, Essa, I., Al-Murshedi, A. Y. M., & Harris, R. C. (2015). Molecular and ionic diffusion in aqueous – deep eutectic solvent mixtures: probing inter-molecular interactions using PFG NMR. *Physical Chemistry Chemical Physics*, *17*(23), 15297–15304. https://doi.org/10.1039/C5CP01493J

Dai, Y., Witkamp, G.-J., Verpoorte, R., & Choi, Y. H. (2015). Tailoring properties of natural deep eutectic solvents with water to facilitate their applications. *Food Chemistry*, *187*, 14–19. https://doi.org/10.1016/j.foodchem.2015.03.123

Dassault Systèmes. (2020, November 2). *BIOVIA COSMOtherm* (Version 21.0). http://www.3ds.com

de Groot, S. R., & Mazur, P. (1984). *Non-equilibrium Thermodynamics*. Dover Publications.

Deiters, U. K. (1997). Some remarks on the nomenclature of refrigerants. *Fluid Phase Equilibria*, *132*(1-2), 265–270. https://doi.org/10.1016/S0378-3812(96)03232-3

Del Pópolo, M. G., & Voth, G. A. (2004). On the Structure and Dynamics of Ionic Liquids. *The Journal of Physical Chemistry B*, *108*(5), 1744–1752. https://doi.org/10.1021/jp0364699

Demuth, O. J. (1983). *Preliminary assessment of condensation behavior for hydrocarbon-vapor expansions which cross the saturation line near the critical point* (tech. rep.). EG; G Idaho, Inc., Idaho Falls (USA).

Deorukhkar, O. A., Rahangdale, T. B., & Mahajan, Y. S. (2016). Entrainer selection approach for distillation column. *International Journal of Chemical Engineering Research*, *8*(1), 29–38.

Devecioğlu, A. G., & Oruç, V. (2015). Characteristics of Some New Generation Refrigerants with Low GWP. *Energy Procedia*, *75*, 1452–1457. https://doi.org/10.1016/j.egypro.2015.07.258

Di Nicola, G., Brandoni, C., Di Nicola, C., & Giuliani, G. (2012). Triple point measurements for alternative refrigerants. *Journal of Thermal Analysis and Calorimetry*, *108*(2), 627–631. https://doi.org/10.1007/s10973-011-1944-4

Dias, A., Llovell, F., Coutinho, J. A., Marrucho, I., & Vega, L. F. (2009). Thermodynamic characterization of pure perfluoroalkanes, including interfacial and second order derivative properties, using the crossover soft-SAFT EoS. *Fluid Phase Equilibria*, *286*(2). https://doi.org/10.1016/j.fluid.2009.08.018

Dias, A. M. A., Pàmies, J. C., Coutinho, J. A., Marrucho, I. M., & Vega, L. F. (2004). SAFT Modeling of the Solubility of Gases in Perfluoroalkanes. *The Journal of Physical Chemistry B*, *108*(4), 1450–1457. https://doi.org/10.1021/jp036225o

Díaz, I., Palomar, J., Rodríguez, M., de Riva, J., Ferro, V., & González, E. J. (2016). Ionic liquids as entrainers for the separation of aromatic–aliphatic hydrocarbon mixtures by extractive distillation. *Chemical Engineering Research and Design*, *115*, 382–393. https://doi.org/10.1016/j.cherd.2016.07.012

Diedenhofen, M., & Klamt, A. (2010). COSMO-RS as a tool for property prediction of IL mixtures-A review. *Fluid Phase Equilibria*, *294*(1-2), 31–38. https://doi.org/10.1016/j.fluid.2010.02.002

Dolezalek, F. (1908). Zur Theorie der binären Gemische und konzentrierten Lösungen. *Zeitschrift für Physikalische Chemie*, *64U*(1), 727–747. https://doi.org/doi:10.1515/zpch-1908-6443

Dong, L., Zheng, D., & Wu, X. (2012). Working Pair Selection of Compression and Absorption Hybrid Cycles through Predicting the Activity Coefficients of Hydrofluorocarbon + Ionic Liquid Systems by the UNIFAC Model. *Industrial & Engineering Chemistry Research*, *51*(12), 4741–4747. https://doi.org/10.1021/ie202029d

Doubek, M., & Vacek, V. (2022). SAFT Equations of State for Low GWP Hydrofluoroethers Heat Transfer Fluids. *International Journal of Thermophysics*, *43*(9), 138. https://doi.org/10.1007/s10765-022-03063-4

Duque, D., Pàmies, J. C., & Vega, L. F. (2004). Interfacial properties of Lennard-Jones chains by direct simulation and density gradient theory. *The Journal of Chemical Physics*, *121*(22), 11395–11401. https://doi.org/10.1063/1.1818679

Duque, D., & Vega, L. F. (2004). Some issues on the calculation of interfacial properties by molecular simulation. *The Journal of Chemical Physics*, *121*(17), 8611. https://doi.org/10.1063/1.1802672

Durand, E., Lecomte, J., & Villeneuve, P. (2015). Are emerging deep eutectic solvents (DES) relevant for lipase-catalyzed lipophilizations? *OCL*, *22*(4), D408. https://doi.org/10.1051/ocl/2015026

E, W., & Lu, J. (2011). Multiscale modeling. *Scholarpedia*, *6*(10), 11527.

Earle, M. J., & Seddon, K. R. (2000). Ionic liquids. Green solvents for the future. *72*(7), 1391–1398. https://doi.org/doi:10.1351/pac200072071391

EI du Pont de Nemours and Co. (2004a). *Thermodynamic properties of HFC-125* (tech. rep.).

EI du Pont de Nemours and Co. (2004b). *Thermodynamic properties of HFC-134a* (tech. rep.).

El Achkar, T., Greige-Gerges, H., & Fourmentin, S. (2021). Basics and properties of deep eutectic solvents: a review. *Environmental Chemistry Letters*, *19*(4), 3397–3408. https://doi.org/10.1007/s10311-021-01225-8

Environmental Studies Board, & National Research Council. (1982). *Causes and effects of stratospheric ozone reduction: An update*. National Academies Press.

Errington, J., & Panagiotopoulos, A. (1998). Phase equilibria of the modified Buckingham exponential-6 potential from Hamiltonian scaling grand canonical Monte Carlo. *Journal of Chemical Physics*, *109*(3), 1093–1100. https://doi.org/10.1063/1.476652

Errington, J., & Panagiotopoulos, A. (1999a). A new intermolecular potential model for the n-alkane homologous series. *Journal of Physical Chemistry B*, *103*(30), 6314–6322. https://doi.org/10.1021/jp990988n

Errington, J., & Panagiotopoulos, A. (1999b). New intermolecular potential models for benzene and cyclohexane. *Journal of Chemical Physics*, *111*(21), 9731–9738. https://doi.org/10.1063/1.480308

European Environment Agency. (2021). Hydrofluorocarbon phase-down in Europe. Retrieved August 31, 2022, from https://www.eea.europa.eu/ims/hydrofluorocarbon-phase-down-in-europe

European Environment Agency. (2022). Annual European Union greenhouse gas inventory 1990–2020 and inventory report 2022 Submission to the UNFCCC Secretariat. https://www.eea.europa.eu//publications/annual-european-union-greenhouse-gas-1

Eyerer, S., Dawo, F., Kaindl, J., Wieland, C., & Spliethoff, H. (2019). Experimental investigation of modern ORC working fluids R1224yd(Z) and R1233zd(E) as replacements for R245fa. *Applied Energy*, *240*, 946–963. https://doi.org/10.1016/j.apenergy.2019.02.086

Eyerer, S., Wieland, C., Vandersickel, A., & Spliethoff, H. (2016). Experimental study of an ORC (Organic Rankine Cycle) and analysis of R1233zd-E as a drop-in replacement for R245fa for low temperature heat utilization. *Energy*, *103*, 660–671. https://doi.org/10.1016/j.energy.2016.03.034

Farman, J. C., Gardiner, B. G., & Shanklin, J. D. (1985). Large losses of total ozone in Antarctica reveal seasonal ClOx/NOx interaction. *Nature*, *315*(6016), 207–210. https://doi.org/10.1038/315207a0

Faúndez, C. A., Barrientos, L. A., & Valderrama, J. O. (2013). Modeling and thermodynamic consistency of solubility data of refrigerants in ionic liquids. *International Journal of Refrigeration*, *36*(8), 2242–2250. https://doi.org/10.1016/j.ijrefrig.2013.06.006

Faúndez, C. A., Campusano, R. A., & Valderrama, J. O. (2020). Misleading results on the use of artificial neural networks for correlating and predicting properties of fluids. A case on the solubility of refrigerant R-32 in ionic liquids. *Journal of Molecular Liquids*, *298*, 112009. https://doi.org/10.1016/j.molliq.2019.112009

Faúndez, C. A., Valderrama, J. O., & Campusano, R. A. (2020). Henry's law constant as a function of temperature and pressure to calculate the solubility of difluoromethane

(R-32) in ionic liquids. *International Journal of Refrigeration*, *119*, 401–409. https://doi.org/https://doi.org/10.1016/j.ijrefrig.2020.05.024

Ferreira, M. L., Araújo, J. M., Pereiro, A. B., & Vega, L. F. (2019). Insights into the influence of the molecular structures of fluorinated ionic liquids on their thermophysical properties. A soft-SAFT based approach. *Physical Chemistry Chemical Physics*, *21*(12), 6362–6380. https://doi.org/10.1039/c8cp07522k

Ferreira, M. L., Llovell, F., Vega, L. F., Pereiro, A. B., & Araújo, J. M. (2019). Systematic study of the influence of the molecular structure of fluorinated ionic liquids on the solubilization of atmospheric gases using a soft-SAFT based approach. *Journal of Molecular Liquids*, *294*, 111645. https://doi.org/10.1016/j.molliq.2019.111645

Ferreira, M. L., Pastoriza-Gallego, M. J., Araújo, J. M. M., Canongia Lopes, J. N., Rebelo, L. P. N., M. Piñeiro, M., Shimizu, K., & Pereiro, A. B. (2017). Influence of Nanosegregation on the Phase Behavior of Fluorinated Ionic Liquids. *The Journal of Physical Chemistry C*, *121*(9), 5415–5427. https://doi.org/10.1021/acs.jpcc.7b00516

Ferro, V. R., Ruiz, E., De Riva, J., & Palomar, J. (2012). Introducing process simulation in ionic liquids design/selection for separation processes based on operational and economic criteria through the example of their regeneration. *Separation and Purification Technology*, *97*, 195–204. https://doi.org/10.1016/j.seppur.2012.02.026

Ferro, V., de Riva, J., Sanchez, D., Ruiz, E., & Palomar, J. (2015). Conceptual design of unit operations to separate aromatic hydrocarbons from naphtha using ionic liquids. COSMO-based process simulations with multi-component "real" mixture feed. *Chemical Engineering Research and Design*, *94*, 632–647. https://doi.org/10.1016/j.cherd.2014.10.001

Fierro, E. N., Faúndez, C. A., & Muñoz, A. S. (2021). Influence of thermodynamically inconsistent data on modeling the solubilities of refrigerants in ionic liquids using an artificial neural network. *Journal of Molecular Liquids*, *337*, 116417. https://doi.org/10.1016/j.molliq.2021.116417

Finberg, E. A., & Shiflett, M. B. (2021). Process Designs for Separating R-410A, R-404A, and R-407C Using Extractive Distillation and Ionic Liquid Entrainers. *Industrial & Engineering Chemistry Research*, *60*(44), 16054–16067. https://doi.org/10.1021/acs.iecr.1c02891

Florindo, C., Oliveira, F. S., Rebelo, L. P. N., Fernandes, A. M., & Marrucho, I. M. (2014). Insights into the Synthesis and Properties of Deep Eutectic Solvents Based on Cholinium Chloride and Carboxylic Acids. *ACS Sustainable Chemistry & Engineering*, *2*(10), 2416–2425. https://doi.org/10.1021/sc500439w

Flynn, R. M., Costello, M. G., & Bulinski, M. J. (2011). *Methods of using hydrofluoroethers as heat transfer fluids* (WO2011053628).

Fouad, W. A., & Vega, L. F. (2018a). Next generation of low global warming potential refrigerants: Thermodynamic properties molecular modeling. *AIChE Journal*, *64*(1), 250–262. https://doi.org/10.1002/aic.15859

Fouad, W. A., & Vega, L. F. (2018b). Transport properties of HFC and HFO based refrigerants using an excess entropy scaling approach. *The Journal of Supercritical Fluids*, *131*(July 2017), 106–116. https://doi.org/10.1016/j.supflu.2017.09.006

Fox, D. M., Gilman, J. W., Morgan, A. B., Shields, J. R., Maupin, P. H., Lyon, R. E., De Long, H. C., & Trulove, P. C. (2008). Flammability and Thermal Analysis Characterization of Imidazolium-Based Ionic Liquids. *Industrial & Engineering Chemistry Research*, *47*(16), 6327–6332. https://doi.org/10.1021/ie800665u

Francisco, M., van den Bruinhorst, A., Zubeir, L. F., Peters, C. J., & Kroon, M. C. (2013). A new low transition temperature mixture (LTTM) formed by choline chloride+lactic acid: Characterization as solvent for CO2 capture. *Fluid Phase Equilibria*, *340*, 77–84. https://doi.org/10.1016/j.fluid.2012.12.001

Fredlake, C. P., Crosthwaite, J. M., Hert, D. G., Aki, S. N. V. K., & Brennecke, J. F. (2004). Thermophysical Properties of Imidazolium-Based Ionic Liquids. *Journal of Chemical & Engineering Data*, *49*(4), 954–964. https://doi.org/10.1021/je034261a

Freitas, A. C. D., Cunico, L. P., Aznar, M., & Guirardello, R. (2013). Modeling vapor liquid equilibrium of ionic liquids + gas binary systems at high pressure with cubic equations of state. *Brazilian Journal of Chemical Engineering*, *30*(1), 63–73. https://doi.org/10.1590/S0104-66322013000100008

Frenkel, D., & Smit, B. (2001). *Understanding Molecular Simulation: From Algorithms to Applications*. Elsevier Science.

Frisch, M. J., Trucks, G. W., Schlegel, H. B., Scuseria, G. E., Robb, M. a., Cheeseman, J. R., Scalmani, G., Barone, V., Petersson, G. a., Nakatsuji, H., Li, X., Caricato, M., Marenich, a. V., Bloino, J., Janesko, B. G., Gomperts, R., Mennucci, B., Hratchian, H. P., Ortiz, J. V., … Fox, D. J. (2016). Gaussian 16, Revision C.01.

Galán Sánchez, L., Meindersma, G., & de Haan, A. (2007). Solvent Properties of Functionalized Ionic Liquids for CO2 Absorption. *Chemical Engineering Research and Design*, *85*(1), 31–39. https://doi.org/10.1205/cherd06124

García, G., Aparicio, S., Ullah, R., & Atilhan, M. (2015). Deep Eutectic Solvents: Physicochemical Properties and Gas Separation Applications. *Energy & Fuels*, *29*(4), 2616–2644. https://doi.org/10.1021/ef5028873

García, S., Larriba, M., García, J., S. Torrecilla, J., & Rodríguez, F. (2010). Liquid-Liquid Extraction of Toluene from Heptane Using 1-Alkyl-3-methylimidazolium Bis(trifluoromethylsulfonyl)imide Ionic Liquids. *Journal of Chemical & Engineering Data*, *56*(1), 113–118. https://doi.org/10.1021/je100982h

García-Gutiérrez, P., Jacquemin, J., McCrellis, C., Dimitriou, I., Taylor, S. F. R., Hardacre, C., & Allen, R. W. K. (2016). Techno-Economic Feasibility of Selective CO2 Capture Processes from Biogas Streams Using Ionic Liquids as Physical Absorbents. *Energy & Fuels*, *30*(6), 5052–5064. https://doi.org/10.1021/acs.energyfuels.6b00364

Garrido, J. M., Quinteros-Lama, H., Mejía, A., Wisniak, J., & Segura, H. (2012). A rigorous approach for predicting the slope and curvature of the temperature–entropy saturation

boundary of pure fluids. *Energy*, *45*(1), 888–899. https://doi.org/10.1016/j.energy.2012.06.073

Gasser, R. P. H., & Richards, W. G. (1995). *An Introduction to statistical thermodynamics*. World Scientific Publishing.

Gathergood, N., Garcia, M. T., & Scammells, P. J. (2004). Biodegradable ionic liquids: Part I. Concept, preliminary targets and evaluation. *Green Chemistry*, *6*(3), 166–175. https://doi.org/10.1039/B315270G

Ghareh Bagh, F. S., Mjalli, F. S., Hashim, M. A., Hadj-Kali, M. K. O., & AlNashef, I. M. (2013). Solubility of Sodium Salts in Ammonium-Based Deep Eutectic Solvents. *Journal of Chemical & Engineering Data*, *58*(8), 2154–2162. https://doi.org/10.1021/je400045d

Goedkoop, M., Oele, M., Leijting, J., Ponsioen, T., & Meijer, E. (2016). *Introduction to LCA with SimaPro* (tech. rep.). Pré Sustainability B.V. Amersfoort, The Netherlands.

Goodwin, A. R. H., Defibaugh, D. R., & Weber, L. A. (1998). Vapor Pressure of 2-(Difluoromethoxy)-1,1,1-trifluoroethane CHF2-O-CH2CF3 (HFE-245). *Journal of Chemical & Engineering Data*, *43*(5), 846–848. https://doi.org/10.1021/je980056x

Gubbins, K. E., & Twu, C. H. (1978). Thermodynamics of polyatomic fluid mixtures—I theory. *Chemical Engineering Science*, *33*(7), 863–878. https://doi.org/10.1016/0009-2509(78)85176-8

Guggenheim, E. A. (1952). *Mixtures; the theory of the equilibrium properties of some simple classes of mixtures, solutions and alloys.* Clarendon Press.

Guinée, J. B., Huppes, G., Lankreijer, R. M., Udo de Haes, H. A., Wegener Sleeswijk, A., Ansems, A. M. M., Eggels, P. G., van Duin, R., & de Goede, H. P. (1992). *Environmental life cycle assessment of products.* (R. Heijungs, Ed.). https://openaccess.leidenuniv.nl/handle/1887/8061

Haile, J. M. (1992). *Molecular dynamics simulation : elementary methods*. John Wiley.

Hait, D., & Head-Gordon, M. (2018). How Accurate Is Density Functional Theory at Predicting Dipole Moments? An Assessment Using a New Database of 200 Benchmark Values. *Journal of Chemical Theory and Computation*, *14*(4), 1969–1981. https://doi.org/10.1021/acs.jctc.7b01252

Haley, J. D., & McCabe, C. (2017). Predicting the phase behavior of fluorinated organic molecules using the GC-SAFT-VR equation of state. *Fluid Phase Equilibria*, *440*, 111–121. https://doi.org/10.1016/j.fluid.2017.01.013

Han, D., & Row, K. H. (2010). Recent Applications of Ionic Liquids in Separation Technology. https://doi.org/10.3390/molecules15042405

Harris, K. R., Woolf, L. A., & Kanakubo, M. (2005). Temperature and pressure dependence of the viscosity of the ionic liquid 1-butyl-3-methylimidazolium hexafluorophosphate. https://doi.org/10.1021/je050147b

Hayyan, A., Ali Hashim, M., Mjalli, F. S., Hayyan, M., & AlNashef, I. M. (2013). A novel phosphonium-based deep eutectic catalyst for biodiesel production from industrial

low grade crude palm oil. *Chemical Engineering Science*, *92*, 81–88. https://doi.org/10.1016/j.ces.2012.12.024

Hayyan, A., Mjalli, F. S., AlNashef, I. M., Al-Wahaibi, T., Al-Wahaibi, Y. M., & Hashim, M. A. (2012). Fruit sugar-based deep eutectic solvents and their physical properties. *Thermochimica Acta*, *541*, 70–75. https://doi.org/10.1016/j.tca.2012.04.030

Hayyan, A., Mjalli, F. S., AlNashef, I. M., Al-Wahaibi, Y. M., Al-Wahaibi, T., & Hashim, M. A. (2013). Glucose-based deep eutectic solvents: Physical properties. *Journal of Molecular Liquids*, *178*, 137–141. https://doi.org/10.1016/j.molliq.2012.11.025

Henderson, D. (Ed.). (1992). Fundamentals of Inhomogeneous Fluids. CRC Press.

Henne, A. L., & Renoll, M. W. (1936). Fluoro Derivatives of Ethane and Ethylene. IV. *Journal of the American Chemical Society*, *58*(6), 887–889. https://doi.org/10.1021/ja01297a008

Henne, A. L., & Waalkes, T. P. (1946). Fluorinated Derivatives of Propane and Propylene. VI. *Journal of the American Chemical Society*, *68*(3), 496–497. https://doi.org/10.1021/ja01207a041

Heredia-Aricapa, Y., Belman-Flores, J., Mota-Babiloni, A., Serrano-Arellano, J., & García-Pabón, J. J. (2020). Overview of low GWP mixtures for the replacement of HFC refrigerants: R134a, R404A and R410A. *International Journal of Refrigeration*, *111*, 113–123. https://doi.org/10.1016/j.ijrefrig.2019.11.012

Hess, B. (2001). Determining the shear viscosity of model liquids from molecular dynamics simulations. *The Journal of Chemical Physics*, *116*(1), 209–217. https://doi.org/10.1063/1.1421362

Hiaki, T., & Kawai, A. (1999). Vapor–liquid equilibria determination for a hydrofluoroether with several alcohols. *Fluid Phase Equilibria*, *158-160*, 979–989. https://doi.org/10.1016/S0378-3812(99)00064-3

Higashi, Y. (1999). Vapor-Liquid Equilibrium, Coexistence Curve, and Critical Locus for Pentafluoroethane + 1,1,1-Trifluoroethane (R125/R143a). *Journal of Chemical & Engineering Data*, *44*(2), 333–337. https://doi.org/10.1021/je980266+

Higashi, Y., Hayasaka, S., Shirai, C., & Akasaka, R. (2015). Measurements of PρT properties, vapor pressures, saturated densities, and critical parameters for R 1234ze(Z) and R 245fa. *International Journal of Refrigeration*, *52*, 100–108. https://doi.org/10.1016/j.ijrefrig.2014.12.007

Higashi, Y., Tanaka, K., & Ichikawa, T. (2010). Critical Parameters and Saturated Densities in the Critical Region for trans -1,3,3,3-Tetrafluoropropene (HFO-1234ze(E)). *Journal of Chemical & Engineering Data*, *55*(4), 1594–1597. https://doi.org/10.1021/je900696z

Hinchliffe, A. (2005). *Molecular Modelling for Beginners* (2nd ed.). Wiley.

Hischier, R., Hellweg, S., Capello, C., & Primas, A. (2005). Establishing life cycle inventories of chemicals based on differing data availability. *International Journal of Life Cycle Assessment*, *10*, 59–67. https://doi.org/10.1065/lca2004.10.181.7

Hockney, R. W., & Eastwood, J. W. (1988). *Computer Simulation Using Particles* (1st ed.). CRC Press. https://doi.org/10.1201/9780367806934

Hogenboom, D. L., Webb, W., & Dixon, J. A. (1967). Viscosity of Several Liquid Hydrocarbons as a Function of Temperature, Pressure, and Free Volume. *The Journal of Chemical Physics*, *46*(7), 2586–2598. https://doi.org/10.1063/1.1841088

Hou, Y., Gu, Y., Zhang, S., Yang, F., Ding, H., & Shan, Y. (2008). Novel binary eutectic mixtures based on imidazole. *Journal of Molecular Liquids*, *143*(2-3), 154–159. https://doi.org/10.1016/j.molliq.2008.07.009

HØye, J. S., & Olaussen, K. (1980). Statistical mechanical model with chemical reaction. *Physica A: Statistical Mechanics and its Applications*, *104*(3), 435–446. https://doi.org/10.1016/0378-4371(80)90006-0

Hulse, R. J., Basu, R. S., Singh, R. R., & Thomas, R. H. (2012). Physical properties of HCFO-1233zd(E). *Journal of Chemical and Engineering Data*, *57*(12), 3581–3586. https://doi.org/10.1021/je300776s

Hung, T. C. (2001). Waste heat recovery of organic Rankine cycle using dry fluids. *Energy Conversion and Management*, *42*(5), 539–553. https://doi.org/10.1016/S0196-8904(00)00081-9

Husband, W. W., & Beyene, A. (2008). Low-grade heat-driven Rankine cycle, a feasibility study. *International Journal of Energy Research*, *32*(15), 1373–1382. https://doi.org/10.1002/er.1442

Ibrahim, R. K., Hayyan, M., AlSaadi, M. A., Ibrahim, S., Hayyan, A., & Hashim, M. A. (2019). Physical properties of ethylene glycol-based deep eutectic solvents. *Journal of Molecular Liquids*, *276*, 794–800. https://doi.org/10.1016/j.molliq.2018.12.032

IEA. (2021). Greenhouse Gas Emissions from Energy: Overview. Retrieved January 24, 2022, from https://www.iea.org/reports/greenhouse-gas-emissions-from-energy-overview

International Organization for Standardization. (2006). Environmental management - Life cycle assessment - Principles and framework. https://www.iso.org/standard/37456.html

IPCC. (2021). *Climate Change 2021: The Physical Science Basis. Contribution of Working Group I to the Sixth Assessment Report of the Intergovernmental Panel on Climate Change* (tech. rep.). Cambridge University Press. In Press.

Irving, J. H., & Kirkwood, J. G. (1950). The Statistical Mechanical Theory of Transport Processes. IV. The Equations of Hydrodynamics. *The Journal of Chemical Physics*, *18*(6), 817–829. https://doi.org/10.1063/1.1747782

Jacquemin, J., Husson, P., Majer, V., & Costa Gomes, M. F. (2007). Influence of the Cation on the Solubility of CO2 and H2 in Ionic Liquids Based on the Bis(trifluoromethylsulfonyl)imide Anion. *Journal of Solution Chemistry*, *36*(8), 967–979. https://doi.org/10.1007/s10953-007-9159-9

Jalili, A. H., Rahmati-Rostami, M., Ghotbi, C., Hosseini-Jenab, M., & Ahmadi, A. N. (2009). Solubility of H2S in Ionic Liquids [bmim][PF6], [bmim][BF4], and [bmim][Tf2N]. *Journal of Chemical & Engineering Data*, *54*(6), 1844–1849. https://doi.org/10.1021/je8009495

Janeček, J. (2006). Long Range Corrections in Inhomogeneous Simulations. *The Journal of Physical Chemistry B*, *110*(12), 6264–6269. https://doi.org/10.1021/jp056344z

Jang, Y., & Lee, J. (2018). Optimizations of the organic Rankine cycle-based domestic CHP using biomass fuel. *Energy Conversion and Management*, *160*, 31–47. https://doi.org/10.1016/j.enconman.2018.01.025

Jog, P. K., Sauer, S. G., Blaesing, J., & Chapman, W. G. (2001). Application of Dipolar Chain Theory to the Phase Behavior of Polar Fluids and Mixtures. *Industrial & Engineering Chemistry Research*, *40*(21), 4641–4648. https://doi.org/10.1021/ie010264+

Jordan, A., & Gathergood, N. (2015). Biodegradation of ionic liquids – a critical review. *Chemical Society Reviews*, *44*(22), 8200–8237. https://doi.org/10.1039/C5CS00444F

Joslin, C. G., Gray, C. G., Chapman, W. G., & Gubbins, K. E. (1987). Theory and simulation of associating liquid mixtures. II. *Molecular Physics*, *62*(4), 843–860. https://doi.org/10.1080/00268978700102621

Kano, Y., Kayukawa, Y., Fujii, K., & Sato, H. (2010). Ideal-Gas Heat Capacity for 2,3,3,3-Tetrafluoropropene (HFO-1234yf) Determined from Speed-of-Sound Measurements. *International Journal of Thermophysics*, *31*(11-12), 2051–2058. https://doi.org/10.1007/s10765-010-0885-7

Karakatsani, E. K., Economou, I. G., Kroon, M. C., Peters, C. J., & Witkamp, G.-J. (2007). tPC-PSAFT Modeling of Gas Solubility in Imidazolium-Based Ionic Liquids. *The Journal of Physical Chemistry C*, *111*(43), 15487–15492. https://doi.org/10.1021/jp070556+

Kauck, E. A., & Diesslin, A. R. (1951). Some Properties of Perfluorocarboxylic Acids. *Industrial & Engineering Chemistry*, *43*(10), 2332–2334. https://doi.org/10.1021/ie50502a044

Kayukawa, Y., Hasumoto, M., Hondo, T., Kano, Y., & Watanabe, K. (2003). Thermodynamic Property Measurements for Trifluoromethyl Methyl Ether and Pentafluoroethyl Methyl Ether. *Journal of Chemical & Engineering Data*, *48*(5), 1141–1151. https://doi.org/10.1021/je025657

Khazalpour, S., Yarie, M., Kianpour, E., Amani, A., Asadabadi, S., Seyf, J. Y., Rezaeivala, M., Azizian, S., & Zolfigol, M. A. (2020). Applications of phosphonium-based ionic liquids in chemical processes. *Journal of the Iranian Chemical Society*, *17*(8), 1775–1917. https://doi.org/10.1007/s13738-020-01901-6

Kim, M. H., Pettersen, J., & Bullard, C. W. (2004). Fundamental process and system design issues in CO2 vapor compression systems. *Progress in Energy and Combustion Science*, *30*(2), 119–174. https://doi.org/10.1016/j.pecs.2003.09.002

Kirkwood, J. G., & Buff, F. P. (1949). The Statistical Mechanical Theory of Surface Tension. *The Journal of Chemical Physics*, *17*(3), 338–343. https://doi.org/10.1063/1.1747248

Kitanovski, A., Plaznik, U., Tomc, U., & Poredoš, A. (2015). Present and future caloric refrigeration and heat-pump technologies. *International Journal of Refrigeration*, *57*, 288–298. https://doi.org/10.1016/j.ijrefrig.2015.06.008

Klamt, A., & Schüürmann, G. (1993). COSMO: A new approach to dielectric screening in solvents with explicit expressions for the screening energy and its gradient. *Journal of*

the Chemical Society, Perkin Transactions 2, (5), 799–805. https://doi.org/10.1039/P29930000799

Klamt, A. (1995). Conductor-like screening model for real solvents: A new approach to the quantitative calculation of solvation phenomena. *Journal of Physical Chemistry*, *99*(7), 2224–2235. https://doi.org/10.1021/j100007a062

Klamt, A. (2005). *COSMO-RS : from quantum chemistry to fluid phase thermodynamics and drug design*. Elsevier Science & Technology.

Klamt, A., Eckert, F., & Arlt, W. (2010). COSMO-RS: An Alternative to Simulation for Calculating Thermodynamic Properties of Liquid Mixtures. *Annual Review of Chemical and Biomolecular Engineering*, *1*(1), 101–122. https://doi.org/10.1146/annurev-chembioeng-073009-100903

Klamt, A., Jonas, V., Bürger, T., & C. W. Lohrenz, J. (1998). Refinement and Parametrization of COSMO-RS. *The Journal of Physical Chemistry A*, *102*(26), 5074–5085. https://doi.org/10.1021/jp980017s

Klein, S., McLinden, M., & Laesecke, A. (1997). An improved extended corresponding states method for estimation of viscosity of pure refrigerants and mixtures. *International Journal of Refrigeration*, *20*(3), 208–217. https://doi.org/10.1016/S0140-7007(96)00073-4

Kondo, S., Urano, Y., Takizawa, K., Takahashi, A., Tokuhashi, K., & Sekiya, A. (2006). Flammability limits of multi-fluorinated compounds. *Fire Safety Journal*, *41*(1), 46–56. https://doi.org/10.1016/j.firesaf.2005.08.002

Kubo, R. (1957). Statistical-Mechanical Theory of Irreversible Processes. I. General Theory and Simple Applications to Magnetic and Conduction Problems. *Journal of the Physical Society of Japan*, *12*(6), 570–586. https://doi.org/10.1143/jpsj.12.570

Kujak, S., & Schultz, K. (2016). Insights into the next generation HVAC&R refrigerant future. *Science and Technology for the Built Environment*, *22*(8), 1226–1237. https://doi.org/10.1080/23744731.2016.1203239

Kuzmina, O., & Hallett, J. P. (Eds.). (2016). *Application, Purification, and Recovery of Ionic Liquids*. Elsevier Inc. https://doi.org/10.1016/C2012-0-06616-1

Lafitte, T., Apostolakou, A., Avendaño, C., Galindo, A., Adjiman, C. S., Müller, E. A., & Jackson, G. (2013). Accurate statistical associating fluid theory for chain molecules formed from Mie segments. *Journal of Chemical Physics*, *139*(15). https://doi.org/10.1063/1.4819786

Lai, N. A. (2014). Equations of state for HFO-1234ze(E) and their application in the study on refrigeration cycle. *International Journal of Refrigeration*, *43*, 194–202. https://doi.org/10.1016/j.ijrefrig.2013.11.011

Lapeña, D., Lomba, L., Artal, M., Lafuente, C., & Giner, B. (2019). The NADES glyceline as a potential Green Solvent: A comprehensive study of its thermophysical properties and effect of water inclusion. *The Journal of Chemical Thermodynamics*, *128*, 164–172. https://doi.org/10.1016/j.jct.2018.07.031

Larock, R. C. (1999). *Comprehensive organic transformations: a guide to functional group preparations* (2nd ed.). Wiley-VCH.

Larriba, M., de Riva, J., Navarro, P., Moreno, D., Delgado-Mellado, N., García, J., Ferro, V. R., Rodríguez, F., & Palomar, J. (2018). COSMO-based/Aspen Plus process simulation of the aromatic extraction from pyrolysis gasoline using the {[4empy][NTf2] + [emim][DCA]} ionic liquid mixture. *Separation and Purification Technology*, *190*, 211–227. https://doi.org/10.1016/j.seppur.2017.08.062

Lee, B. G., Park, J. Y., Lim, J. S., Cho, S. Y., & Park, K. Y. (1999). Phase Equilibria of Chlorofluorocarbon Alternative Refrigerant Mixtures. *Journal of Chemical & Engineering Data*, *44*(2), 190–192. https://doi.org/10.1021/je980180g

Lee, Y., & Jung, D. (2012). A brief performance comparison of R1234yf and R134a in a bench tester for automobile applications. *Applied Thermal Engineering*, *35*, 240–242. https://doi.org/10.1016/j.applthermaleng.2011.09.004

Lei, Z., Dai, C., & Chen, B. (2013). Gas Solubility in Ionic Liquids. *Chemical Reviews*, *114*(2), 1289–1326. https://doi.org/10.1021/cr300497a

Lei, Z., Dai, C., Zhu, J., & Chen, B. (2014). Extractive distillation with ionic liquids: A review. *AIChE Journal*, *60*(9), 3312–3329. https://doi.org/10.1002/aic.14537

Lei, Z., Li, C., & Chen, B. (2003). Extractive Distillation: A Review. *Separation & Purification Reviews*, *32*(2), 121–213. https://doi.org/10.1081/SPM-120026627

Lemmon, E. W., Bell, I. H., Huber, M. L., & McLinden, M. O. (2018). NIST Standard Reference Database 23: Reference Fluid Thermodynamic and Transport Properties-REFPROP, Version 10.0, National Institute of Standards and Technology. https://doi.org/10.18434/T4/1502528

Lepre, L. F., Andre, D., Denis-Quanquin, S., Gautier, A., Pádua, A. A. H., & Costa Gomes, M. (2019). Ionic Liquids Can Enable the Recycling of Fluorinated Greenhouse Gases. *ACS Sustainable Chemistry & Engineering*, *7*(19), 16900–16906. https://doi.org/10.1021/acssuschemeng.9b04214

Ley 16/2013, de 29 de octubre, por la que se establecen determinadas medidas en materia de fiscalidad medioambiental y se adoptan otras medidas tributarias y financieras. (2013). *Boletín Oficial del Estado*, *260*, 87528–87568. https://www.boe.es/eli/es/l/2013/10/29/16

Li, X., Hou, M., Han, B., Wang, X., & Zou, L. (2008). Solubility of CO2 in a Choline Chloride + Urea Eutectic Mixture. *Journal of Chemical & Engineering Data*, *53*(2), 548–550. https://doi.org/10.1021/je700638u

Lim, J. S., Park, J.-Y., Lee, B.-G., & Lee, Y.-W. (2002). Phase equilibria of 1,1,1-trifluoroethane (HFC-143a) + 1,1,1,2-tetrafluoroethane (HFC-134a), and + 1,1-difluoroethane (HFC-152a) at 273.15, 293.15, 303.15, and 313.15 K. *Fluid Phase Equilibria*, *193*(1), 29–39. https://doi.org/10.1016/S0378-3812(01)00632-X

Lin, S. T., Mathias, P. M., Song, Y., Chen, C. C., & Sandler, S. I. (2002). Improvements of Phase-Equilibrium Predictions for Hydrogen-Bonding Systems from a New Expression for COSMO Solvation Models. *AIChE Annual Meeting, Indianapolis, IN*, 3–8.

Lin, S.-T., & Sandler, S. I. (2002). A Priori Phase Equilibrium Prediction from a Segment Contribution Solvation Model. *Industrial & Engineering Chemistry Research*, *41*(5), 899–913. https://doi.org/10.1021/ie001047w

Linde GmbH. (2022). HFC Gases: R-23. Retrieved August 18, 2022, from https://www.linde-gas.se/en/products%7B%5C_%7Dren/refrigerants/hfc%7B%5C_%7Dgases/r23/index.html

Liu, X., He, M., Lv, N., Qi, X., & Su, C. (2015a). Solubilities of R-161 and R-143a in 1-Hexyl-3-methylimidazolium bis(trifluoromethylsulfonyl)imide. *Fluid Phase Equilibria*, *388*, 37–42. https://doi.org/10.1016/j.fluid.2014.12.026

Liu, X., He, M., Lv, N., Qi, X., & Su, C. (2015b). Vapor-liquid equilibrium of three hydrofluorocarbons with [HMIM][Tf2N]. *Journal of Chemical and Engineering Data*, *60*(5), 1354–1361. https://doi.org/10.1021/je501069b

Liu, X., Lv, N., Su, C., & He, M. (2016). Solubilities of R32, R245fa, R227ea and R236fa in a phosphonium-based ionic liquid. *Journal of Molecular Liquids*, *218*, 525–530. https://doi.org/10.1016/j.molliq.2016.02.041

Liu, X., Nguyen, M. Q., Xue, S., Song, C., & He, M. (2019). Vapor–liquid equilibria and interdiffusion coefficients for working pairs for absorption refrigeration systems composed of [HMIM][BF4] and fluorinated propanes. *International Journal of Refrigeration*, *104*, 34–41. https://doi.org/10.1016/j.ijrefrig.2019.04.023

Liu, X., Pan, P., Yang, F., & He, M. (2018). Solubilities and diffusivities of R227ea, R236fa and R245fa in 1-hexyl-3-methylimidazolium bis(trifluoromethylsulfonyl)imide. *The Journal of Chemical Thermodynamics*, *123*, 158–164. https://doi.org/https://doi.org/10.1016/j.jct.2018.04.004

Liu, X., Qi, X., Lv, N., & He, M. (2015). Gaseous absorption of fluorinated ethanes by ionic liquids. *Fluid Phase Equilibria*, *405*, 1–6. https://doi.org/10.1016/j.fluid.2015.07.001

Liu, X., Wang, T., & He, M. (2019). Investigation on the condensation process of HFO refrigerants by molecular dynamics simulation. *Journal of Molecular Liquids*, *288*, 111034. https://doi.org/10.1016/j.molliq.2019.111034

Liu, Z. B. (2018). *Method for preparation of imidazole ionic liquids by microwave* (CN108129391A2018).

Lloret, J. O., Vega, L. F., & Llovell, F. (2017). Accurate description of thermophysical properties of Tetraalkylammonium Chloride Deep Eutectic Solvents with the soft-SAFT equation of state. *Fluid Phase Equilibria*, *448*, 81–93. https://doi.org/10.1016/j.fluid.2017.04.013

Llovell, F., & F. Vega, L. (2005). Global Fluid Phase Equilibria and Critical Phenomena of Selected Mixtures Using the Crossover Soft-SAFT Equation. *The Journal of Physical Chemistry B*, *110*(3), 1350–1362. https://doi.org/10.1021/jp0551465

Llovell, F., Marcos, R. M., MacDowell, N., & Vega, L. F. (2012). Modeling the absorption of weak electrolytes and acid gases with ionic liquids using the soft-SAFT approach. *Journal of Physical Chemistry B*, *116*(26), 7709–7718. https://doi.org/10.1021/jp303344f

Llovell, F., Marcos, R. M., & Vega, L. F. (2013a). Free-volume theory coupled with soft-SAFT for viscosity calculations: Comparison with molecular simulation and experimental data. *Journal of Physical Chemistry B*, *117*(27), 8159–8171. https://doi.org/10.1021/jp401307t

Llovell, F., Marcos, R. M., & Vega, L. F. (2013b). Transport properties of mixtures by the soft-SAFT + Free-volume theory: Application to mixtures of n-alkanes and hydrofluorocarbons. *Journal of Physical Chemistry B*, *117*(17), 5195–5205. https://doi.org/10.1021/jp401754r

Llovell, F., Valente, E., Vilaseca, O., & Vega, L. F. (2011). Modeling complex associating mixtures with [Cnmim][Tf2N] ionic liquids: Predictions from the soft-SAFT equation. *Journal of Physical Chemistry B*, *115*(15), 4387–4398. https://doi.org/10.1021/jp112315b

Llovell, F., Vilaseca, O., & Vega, L. F. (2012). Thermodynamic Modeling of Imidazolium-Based Ionic Liquids with the [PF 6] Anion for Separation Purposes. *Separation Science and Technology*, *47*(2), 399–410. https://doi.org/10.1080/01496395.2011.635625

Lo, E. S. (1961). *Fluorine-containing polymers and preparation thereof* (US3178399A).

Lovelock, J. E., Maggs, R. J., & Wade, R. J. (1973). Halogenated hydrocarbons in and over the Atlantic. https://doi.org/10.1038/241194a0

Luckas, M., Lucas, K., Deiters, U., & Gubbins, K. E. (1986). Integrals over pair- and triplet-correlation functions for the Lennard-Jones (12–6)-fluid. *Molecular Physics*, *57*(2), 241–253. https://doi.org/10.1080/00268978600100191

Ma, Y., Liu, Z., & Tian, H. (2013). A review of transcritical carbon dioxide heat pump and refrigeration cycles. *Energy*, *55*, 156–172. https://doi.org/10.1016/j.energy.2013.03.030

Maalem, Y., Zarfa, A., Tamene, Y., Fedali, S., & Madani, H. (2020). Prediction of thermodynamic properties of the ternary azeotropic mixtures. *Fluid Phase Equilibria*, *517*, 112613. https://doi.org/10.1016/j.fluid.2020.112613

Mac Dowell, N., Llovell, F., Sun, N., Hallett, J. P., George, A., Hunt, P. A., Welton, T., Simmons, B. A., & Vega, L. F. (2014). New Experimental Density Data and Soft-SAFT Models of Alkylimidazolium ([CnC1im]+) Chloride (Cl-), Methylsulfate ([MeSO4]-), and Dimethylphosphate ([Me2PO4]-) Based Ionic Liquids. *Journal of Physical Chemistry B*, *118*(23), 6206–6221. https://doi.org/10.1021/jp501619y

Maciel, V. G., Wales, D. J., Seferin, M., Ugaya, C. M. L., & Sans, V. (2019). State-of-the-art and limitations in the life cycle assessment of ionic liquids. https://doi.org/10.1016/j.jclepro.2019.01.133

Manan, N. A., Hardacre, C., Jacquemin, J., Rooney, D. W., & Youngs, T. G. A. (2009). Evaluation of Gas Solubility Prediction in Ionic Liquids using COSMOthermX. *Journal of Chemical & Engineering Data*, *54*(7), 2005–2022. https://doi.org/10.1021/je800857x

Martínez-Ruiz, F. J., Moreno-Ventas Bravo, A. I., & Blas, F. J. (2015). Liquid-liquid interfacial properties of a symmetrical Lennard-Jones binary mixture. *The Journal of Chemical Physics*, *143*(10), 104706. https://doi.org/10.1063/1.4930276

Martins, M. A., Pinho, S. P., & Coutinho, J. A. (2019). Insights into the Nature of Eutectic and Deep Eutectic Mixtures. *Journal of Solution Chemistry*, *48*(7), 962–982. https://doi.org/10.1007/s10953-018-0793-1

Matsuo, S., Tanaka, Y., Takada, N., Yamamoto, H., & Sekiya, A. (1998). Gaseous Thermal Conductivities of Fluorinated Methyl Ethyl Ethers. *Journal of Chemical & Engineering Data*, *43*(3), 473–476. https://doi.org/10.1021/je9702854

McLinden, M. O., Brown, J. S., Brignoli, R., Kazakov, A. F., & Domanski, P. A. (2017). Limited options for low-global-warming-potential refrigerants. *Nature Communications*, *8*(1), 14476. https://doi.org/10.1038/ncomms14476

McLinden, M. O., & Didion, D. (1987). CFCs: Quest for Alternatives. *ASHRAE Journal*, *29*(12), 32–42.

McLinden, M. O., & Huber, M. L. (2020). (R)Evolution of Refrigerants. *Journal of Chemical & Engineering Data*, *65*(9), 4176–4193. https://doi.org/10.1021/acs.jced.0c00338

McLinden, M. O., Kazakov, A. F., Steven Brown, J., & Domanski, P. A. (2014). A thermodynamic analysis of refrigerants: Possibilities and tradeoffs for Low-GWP refrigerants. *International Journal of Refrigeration*, *38*, 80–92. https://doi.org/10.1016/j.ijrefrig.2013.09.032

McLinden, M. O., Klein, S. A., & Perkins, R. A. (2000). An extended corresponding states model for the thermal conductivity of refrigerants and refrigerant mixtures. *International Journal of Refrigeration*, *23*(1), 43–63. https://doi.org/10.1016/S0140-7007(99)00024-9

McLinden, M. O., Seeton, C. J., & Pearson, A. (2020). New refrigerants and system configurations for vapor-compression refrigeration. *Science*, *370*(6518), 791–796. https://doi.org/10.1126/science.abe3692

McQuarrie, D. A. (1976). *Statistical mechanics*. Harper & Row.

Mehrkesh, A., & Karunanithi, A. T. (2013). Energetic Ionic Materials: How Green Are They? A Comparative Life Cycle Assessment Study. *ACS Sustainable Chemistry & Engineering*, *1*(4), 448–455. https://doi.org/10.1021/sc3001383

Meindersma, G. W., Quijada-Maldonado, E., Jongmans, M. T. G., Hernandez, J. P. G., Schuur, B., & de Haan, A. B. (2016). Extractive Distillation with Ionic Liquids: Pilot Plant Experiments and Conceptual Process Design. In H. Rodríguez (Ed.). Springer Berlin Heidelberg. https://doi.org/10.1007/978-3-662-48520-0_2

Mejía, A., & Segura, H. (2004). Interfacial Behavior in Type IV Systems. *International Journal of Thermophysics*, *25*(5), 1395–1414. https://doi.org/10.1007/s10765-004-5746-9

Meng, X., Qiu, G., Wu, J., & Abdulagatov, I. M. (2013). Viscosity measurements for 2,3,3,3-tetrafluoroprop-1-ene (R1234yf) and trans-1,3,3,3-tetrafluoropropene (R1234ze(E)).

The Journal of Chemical Thermodynamics, *63*, 24–30. https://doi.org/10.1016/j.jct.2013.03.013

Midgley, T., & Henne, A. L. (1930). Organic Fluorides as Refrigerants. *Industrial & Engineering Chemistry*, *22*(5), 542–545. https://doi.org/10.1021/ie50245a031

Minnick, D. L., & Shiflett, M. B. (2019). Solubility and Diffusivity of Chlorodifluoromethane in Imidazolium Ionic Liquids: [emim][Tf2N], [bmim][BF4], [bmim][PF6], and [emim][TFES]. *Industrial & Engineering Chemistry Research*, *58*(25), 11072–11081. https://doi.org/10.1021/acs.iecr.9b02419

Molina, M. J., & Rowland, F. S. (1974). Stratospheric sink for chlorofluoromethanes: chlorine atom-catalysed destruction of ozone. *Nature*, *249*(5460), 810–812. https://doi.org/10.1038/249810a0

Monnery, W. D., Svrcek, W. Y., & Mehrotra, A. K. (1995). Viscosity: A critical review of practical predictive and correlative methods. *The Canadian Journal of Chemical Engineering*, *73*(1), 3–40. https://doi.org/https://doi.org/10.1002/cjce.5450730103

Morais, A. R. C., Harders, A. N., Baca, K. R., Olsen, G. M., Befort, B. J., Dowling, A. W., Maginn, E. J., & Shiflett, M. B. (2020). Phase Equilibria, Diffusivities, and Equation of State Modeling of HFC-32 and HFC-125 in Imidazolium-Based Ionic Liquids for the Separation of R-410A. *Industrial & Engineering Chemistry Research*, *59*(40), 18222–18235. https://doi.org/10.1021/acs.iecr.0c02820

Moreno, D., Ferro, V. R., de Riva, J., Santiago, R., Moya, C., Larriba, M., & Palomar, J. (2018). Absorption refrigeration cycles based on ionic liquids: Refrigerant/absorbent selection by thermodynamic and process analysis. *Applied Energy*, *213*, 179–194. https://doi.org/10.1016/j.apenergy.2018.01.034

Morrison, G., & McLinden, M. O. (1993). Azeotropy in refrigerant mixtures: Azéotropie dans les mélanges de frigorigènes. *International Journal of Refrigeration*, *16*(2), 129–138. https://doi.org/10.1016/0140-7007(93)90069-K

Morrison, H. G., Sun, C. C., & Neervannan, S. (2009). Characterization of thermal behavior of deep eutectic solvents and their potential as drug solubilization vehicles. *International Journal of Pharmaceutics*, *378*(1-2), 136–139. https://doi.org/10.1016/j.ijpharm.2009.05.039

Mota-Babiloni, A., Navarro-Esbrí, J., Molés, F., Cervera, Á. B., Peris, B., & Verdú, G. (2016). A review of refrigerant R1234ze(E) recent investigations. *Applied Thermal Engineering*, *95*, 211–222. https://doi.org/10.1016/j.applthermaleng.2015.09.055

Mota-Babiloni, A. (2016). *Analysis of fluoride fluids with low global warming impact in vapour compression systems. Experimental evaluation of different alternatives for commercial refrigeration* (Doctoral dissertation). Universitat Politècnica de València. https://doi.org/10.4995/Thesis/10251/62680

Mota-Babiloni, A., Makhnatch, P., & Khodabandeh, R. (2017). Recent investigations in HFCs substitution with lower GWP synthetic alternatives: Focus on energetic performance

and environmental impact. *International Journal of Refrigeration*, *82*, 288–301. https://doi.org/10.1016/j.ijrefrig.2017.06.026

Mota-Babiloni, A., Makhnatch, P., Khodabandeh, R., & Navarro-Esbrí, J. (2017). Experimental assessment of R134a and its lower GWP alternative R513A. *International Journal of Refrigeration*, *74*, 682–688. https://doi.org/10.1016/j.ijrefrig.2016.11.021

Mota-Babiloni, A., Mastani Joybari, M., Navarro-Esbrí, J., Mateu-Royo, C., Barragán-Cervera, Á., Amat-Albuixech, M., & Molés, F. (2020). Ultralow-temperature refrigeration systems: Configurations and refrigerants to reduce the environmental impact. *International Journal of Refrigeration*, *111*, 147–158. https://doi.org/10.1016/j.ijrefrig.2019.11.016

Mota-Babiloni, A., Navarro-Esbrí, J., Barragán, Á., Molés, F., & Peris, B. (2014). Drop-in energy performance evaluation of R1234yf and R1234ze(E) in a vapor compression system as R134a replacements. *Applied Thermal Engineering*, *71*(1), 259–265. https://doi.org/10.1016/j.applthermaleng.2014.06.056

Mota-Martinez, M. T., Brandl, P., Hallett, J. P., & Mac Dowell, N. (2018). Challenges and opportunities for the utilisation of ionic liquids as solvents for CO2 capture. *Molecular Systems Design and Engineering*, *3*(3), 560–571. https://doi.org/10.1039/c8me00009c

Muñoz Rujas, N. (2018). *Investigación sobre propiedades de nuevos fluidos industriales de bajo impacto ambiental como sustitutivos de gases fluorados para reducción del cambio climático* (Doctoral dissertation). Universidad de Burgos. https://doi.org/10.36443/10259/5069

Muñoz-Rujas, N., Aguilar, F., García-Alonso, J. M., & Montero, E. A. (2018). High pressure density and speed of sound of hydrofluoroether fluid 1,1,1,2,2,3,4,5,5,5-decafluoro-3-methoxy-4-(trifluoromethyl)-pentane (HFE-7300). *The Journal of Chemical Thermodynamics*, *121*, 1–7. https://doi.org/10.1016/j.jct.2018.02.003

Murata, J., Yamashita, S., Akiyama, M., Katayama, S., Hiaki, T., & Sekiya, A. (2002). Vapor Pressures of Hydrofluoroethers. *Journal of Chemical & Engineering Data*, *47*(4), 911–915. https://doi.org/10.1021/je010322y

Nair, V. (2021). HFO refrigerants: A review of present status and future prospects. *International Journal of Refrigeration*, *122*, 156–170. https://doi.org/10.1016/j.ijrefrig.2020.10.039

NASA. (2022). Climate change: Vital signs of the planet. Retrieved January 21, 2022, from https://climate.nasa.gov/

Neubauer, M., Wallek, T., & Lux, S. (2022). Deep eutectic solvents as entrainers in extractive distillation – A review. *Chemical Engineering Research and Design*, *184*, 402–418. https://doi.org/10.1016/j.cherd.2022.06.019

Neufeld, P. D., Janzen, A. R., & Aziz, R. A. (1972). Empirical Equations to Calculate 16 of the Transport Collision Integrals Ω(l, s)* for the Lennard-Jones (12–6) Potential. *The Journal of Chemical Physics*, *57*(3), 1100–1102. https://doi.org/10.1063/1.1678363

Niedermeyer, H., Ashworth, C., Brandt, A., Welton, T., & Hunt, P. A. (2013). A step towards the a priori design of ionic liquids. *Physical Chemistry Chemical Physics*, *15*(27), 11566–11578. https://doi.org/10.1039/C3CP50521A

Nosé, S. (1984). A molecular dynamics method for simulations in the canonical ensemble. *Molecular Physics*, *52*(2), 255–268. https://doi.org/10.1080/00268978400101201

Nunes, R. J., Saramago, B., & Marrucho, I. M. (2019). Surface Tension of dl-Menthol:Octanoic Acid Eutectic Mixtures. *Journal of Chemical & Engineering Data*, *64*(11), 4915–4923. https://doi.org/10.1021/acs.jced.9b00424

Ohta, H., Morimoto, Y., Widiatmo, J. V., & Watanabe, K. (2001). Liquid-Phase Thermodynamic Properties of New Refrigerants: Pentafluoroethyl Methyl Ether and Heptafluoropropyl Methyl Ether. *Journal of Chemical & Engineering Data*, *46*(5), 1020–1024. https://doi.org/10.1021/je0002538

Ojeda, R. M., & Llovell, F. (2018). Soft-SAFT Transferable Molecular Models for the Description of Gas Solubility in Eutectic Ammonium Salt-Based Solvents. *Journal of Chemical & Engineering Data*, *63*(7), 2599–2612. https://doi.org/10.1021/acs.jced.7b01103

Outcalt, S. L., & McLinden, M. O. (1995). Equations of state for the thermodynamic properties of R32 (difluoromethane) and R125 (pentafluoroethane). *International Journal of Thermophysics*, *16-16*(1), 79–89. https://doi.org/10.1007/BF01438959

Paduszyński, K., & Domańska, U. (2014). Viscosity of Ionic Liquids: An Extensive Database and a New Group Contribution Model Based on a Feed-Forward Artificial Neural Network. *Journal of Chemical Information and Modeling*, *54*(5), 1311–1324. https://doi.org/10.1021/ci500206u

Pàmies, J. C., & Vega, L. F. (2001). Vapor-Liquid Equilibria and Critical Behavior of Heavy n-Alkanes Using Transferable Parameters from the Soft-SAFT Equation of State. *Industrial & Engineering Chemistry Research*, *40*(11), 2532–2543. https://doi.org/10.1021/ie000944x

Pardo, F., Gutiérrez-Hernández, S. V., Hermida-Merino, C., Araújo, J. M. M., Piñeiro, M. M., Pereiro, A. B., Zarca, G., & Urtiaga, A. (2021). Integration of Stable Ionic Liquid-Based Nanofluids into Polymer Membranes. Part II: Gas Separation Properties toward Fluorinated Greenhouse Gases. https://doi.org/10.3390/nano11030582

Pardo, F., Zarca, G., & Urtiaga, A. (2020). Separation of Refrigerant Gas Mixtures Containing R32, R134a, and R1234yf through Poly(ether-block-amide) Membranes. *ACS Sustainable Chemistry & Engineering*, *8*(6), 2548–2556. https://doi.org/10.1021/acssuschemeng.9b07195

Pardo, F., Zarca, G., & Urtiaga, A. (2021). Effect of feed pressure and long-term separation performance of Pebax-ionic liquid membranes for the recovery of difluoromethane (R32) from refrigerant mixture R410A. *Journal of Membrane Science*, *618*, 118744. https://doi.org/10.1016/j.memsci.2020.118744

Parvaneh, K., Rasoolzadeh, A., & Shariati, A. (2019). Modeling the phase behavior of refrigerants with ionic liquids using the QC-PC-SAFT equation of state. *Journal of Molecular Liquids*, *274*, 497–504. https://doi.org/10.1016/j.molliq.2018.10.116

Paulechka, Y., Blokhin, A., Kabo, G., & Strechan, A. (2007). Thermodynamic properties and polymorphism of 1-alkyl-3-methylimidazolium bis(triflamides). *The Journal of Chemical Thermodynamics*, *39*(6), 866–877. https://doi.org/10.1016/j.jct.2006.11.006

Pearson, A. (2008). Refrigeration with ammonia. *International Journal of Refrigeration*, *31*(4), 545–551. https://doi.org/10.1016/j.ijrefrig.2007.11.011

Pearson, A. (2020). Why Zeotropes Upset Me. *ASHRAE Journal*, *62*(3), 75.

Peguin, R. P. S., Kamath, G., Potoff, J. J., & da Rocha, S. R. P. (2009). All-Atom Force Field for the Prediction of Vapor-Liquid Equilibria and Interfacial Properties of HFA134a. *The Journal of Physical Chemistry B*, *113*(1), 178–187. https://doi.org/10.1021/jp806213w

Pereiro, A. B., Araújo, J., Esperança, J., Marrucho, I., & Rebelo, L. (2012). Ionic liquids in separations of azeotropic systems – A review. *The Journal of Chemical Thermodynamics*, *46*, 2–28. https://doi.org/10.1016/j.jct.2011.05.026

Pereiro, A. B., Araújo, J. M. M., Martinho, S., Alves, F., Nunes, S., Matias, A., Duarte, C. M. M., Rebelo, L. P. N., & Marrucho, I. M. (2013). Fluorinated Ionic Liquids: Properties and Applications. *ACS Sustainable Chemistry & Engineering*, *1*(4), 427–439. https://doi.org/10.1021/sc300163n

Pereiro, A. B., Llovell, F., Araújo, J. M. M., Santos, A. S. S., Rebelo, L. P. N., Piñeiro, M. M., & Vega, L. F. (2017). Thermophysical Characterization of Ionic Liquids Based on the Perfluorobutanesulfonate Anion: Experimental and Soft-SAFT Modeling Results. *ChemPhysChem*, *18*(15), 2012–2023. https://doi.org/10.1002/cphc.201700327

Pereiro, A. B., Pastoriza-Gallego, M. J., Shimizu, K., Marrucho, I. M., Lopes, J. N. C., Piñeiro, M. M., & Rebelo, L. P. N. (2013). On the Formation of a Third, Nanostructured Domain in Ionic Liquids. *The Journal of Physical Chemistry B*, *117*(37), 10826–10833. https://doi.org/10.1021/jp402300c

Pereiro, A. B., Tomé, L. C., Martinho, S., Rebelo, L. P. N., & Marrucho, I. M. (2013). Gas Permeation Properties of Fluorinated Ionic Liquids. *Industrial & Engineering Chemistry Research*, *52*(14), 4994–5001. https://doi.org/10.1021/ie4002469

Pérez De Los Ríos, A., & Hernández Fernández, F. J. (Eds.). (2014). *Ionic Liquids for Separation of Metal Ions and Organic Compounds from Aqueous Solutions*. Elsevier Ltd. https://doi.org/10.1016/B978-0-444-63257-9.00004-3

Peric, B., Sierra, J., Martí, E., Cruañas, R., Garau, M. A., Arning, J., Bottin-Weber, U., & Stolte, S. (2013). (Eco)toxicity and biodegradability of selected protic and aprotic ionic liquids. *Journal of Hazardous Materials*, *261*, 99–105. https://doi.org/10.1016/j.jhazmat.2013.06.070

Petkovic, M., Seddon, K. R., Rebelo, L. P. N., & Silva Pereira, C. (2011). Ionic liquids: a pathway to environmental acceptability. *Chemical Society Reviews*, *40*(3), 1383–1403. https://doi.org/10.1039/C004968A

Petr, P., & Raabe, G. (2015). Evaluation of R-1234ze(Z) as drop-in replacement for R-245fa in Organic Rankine Cycles – From thermophysical properties to cycle performance. *Energy*, *93*, 266–274. https://doi.org/10.1016/j.energy.2015.09.035

Philippi, F., Rauber, D., Eliasen, K. L., Bouscharain, N., Niss, K., Kay, C. W. M., & Welton, T. (2022). Pressing matter: why are ionic liquids so viscous? *Chemical Science*, *13*(9), 2735–2743. https://doi.org/10.1039/D1SC06857A

Piña-Martinez, A., Lasala, S., Privat, R., Falk, V., & Jaubert, J.-N. (2021). Design of Promising Working Fluids for Emergent Combined Cooling, Heating, and Power (CCHP) Systems. *ACS Sustainable Chemistry & Engineering*, *9*(35), 11807–11824. https://doi.org/10.1021/acssuschemeng.1c03362

Plechkova, N. V., & Seddon, K. R. (2008). Applications of ionic liquids in the chemical industry. *Chemical Society Reviews*, *37*(1), 123–150. https://doi.org/10.1039/b006677j

Polishuk, I. (2012). Modeling of Viscosities in Extended Pressure Range Using SAFT + Cubic EoS and Modified Yarranton–Satyro Correlation. *Industrial & Engineering Chemistry Research*, *51*(41), 13527–13537. https://doi.org/10.1021/ie3021208

Polishuk, I. (2017). Implementation of CP-PC-SAFT for Predicting Thermodynamic Properties and Gas Solubility in 1-Alkyl-3-methylimidazolium Bis(trifluoromethylsulfonyl)imide Ionic Liquids without Fitting Binary Parameters. *Industrial & Engineering Chemistry Research*, *56*(27), 7845–7857. https://doi.org/10.1021/acs.iecr.7b01846

PRé Sustainability B.V. (2020, August). *SimaPro* (Version 9.4.2). https://wwww.simapro.com/

Pye, C. C., Ziegler, T., van Lenthe, E., & Louwen, J. N. (2009). An implementation of the conductor-like screening model of solvation within the Amsterdam density functional package — Part II. COSMO for real solvents. *Canadian Journal of Chemistry*, *87*(7), 790–797. https://doi.org/10.1139/V09-008

Qiu, G. (2012). Selection of working fluids for micro-CHP systems with ORC. *Renewable Energy*, *48*, 565–570. https://doi.org/10.1016/j.renene.2012.06.006

Quijada-Maldonado, E., Aelmans, T., Meindersma, G., & de Haan, A. (2013). Pilot plant validation of a rate-based extractive distillation model for water–ethanol separation with the ionic liquid [emim][DCA] as solvent. *Chemical Engineering Journal*, *223*, 287–297. https://doi.org/10.1016/j.cej.2013.02.111

Quijada-Maldonado, E., Meindersma, G. W., & de Haan, A. B. (2016). Pilot plant study on the extractive distillation of toluene–methylcyclohexane mixtures using NMP and the ionic liquid [hmim][TCB] as solvents. *Separation and Purification Technology*, *166*, 196–204. https://doi.org/10.1016/j.seppur.2016.04.041

Quoilin, S., Broek, M. V. D., Declaye, S., Dewallef, P., & Lemort, V. (2013). Techno-economic survey of Organic Rankine Cycle (ORC) systems. *Renewable and Sustainable Energy Reviews*, *22*, 168–186. https://doi.org/10.1016/j.rser.2013.01.028

Raabe, G. (2012). Molecular Modeling of Fluoropropene Refrigerants. *The Journal of Physical Chemistry B*, *116*(19), 5744–5751. https://doi.org/10.1021/jp300991t

Raabe, G. (2013a). Molecular Simulation Studies on the Thermophysical Properties of the Refrigerant Blend R-445A. *Journal of Chemical & Engineering Data*, *58*(12), 3470–3476. https://doi.org/10.1021/je400738r

Raabe, G. (2013b). Molecular simulation studies on the vapor-liquid phase equilibria of binary mixtures of R-1234yf and R-1234ze(E) with R-32 and CO2. *Journal of Chemical and Engineering Data*, *58*(6), 1867–1873. https://doi.org/10.1021/je4002619

Raabe, G. (2014). Molecular Dynamics Studies on Liquid-Phase Dynamics and Structures of Four Different Fluoropropenes and Their Binary Mixtures with R-32 and CO2. *The Journal of Physical Chemistry B*, *118*(1), 240–254. https://doi.org/10.1021/jp409408k

Raabe, G. (2015). Molecular Simulation Studies on the Vapor–Liquid Equilibria of the cis - and trans -HCFO-1233zd and the cis - and trans -HFO-1336mzz. *Journal of Chemical & Engineering Data*, *60*(8), 2412–2419. https://doi.org/10.1021/acs.jced.5b00286

Raabe, G. (2016). Molecular simulation studies in hydrofluoroolefine (HFO) working fluids and their blends. *Science and Technology for the Built Environment*, *22*(8), 1077–1089. https://doi.org/10.1080/23744731.2016.1206796

Raabe, G. (2017). *Molecular Simulation Studies on Thermophysical Properties With Application to Working Fluids* (1st ed.). Springer, Singapore. https://doi.org/10.1007/978-981-10-3545-6

Raabe, G. (2019). Molecular simulation studies on refrigerants past – present – future. *Fluid Phase Equilibria*, *485*, 190–198. https://doi.org/10.1016/j.fluid.2018.12.022

Raabe, G. (2020). Parameterization Approach for a Systematic Extension of the Hydrofluoroolefin Force Field to Fluorinated Butenes and Hydrochlorofluoroolefin Compounds. *Journal of Chemical & Engineering Data*, *65*(3), 1234–1242. https://doi.org/10.1021/acs.jced.9b00588

Raabe, G., & Maginn, E. J. (2010a). A Force Field for 3,3,3-Fluoro-1-propenes, Including HFO-1234yf. *The Journal of Physical Chemistry B*, *114*(31), 10133–10142. https://doi.org/10.1021/jp102534z

Raabe, G., & Maginn, E. J. (2010b). Molecular Modeling of the Vapor-Liquid Equilibrium Properties of the Alternative Refrigerant 2,3,3,3-Tetrafluoro-1-propene (HFO-1234yf). *The Journal of Physical Chemistry Letters*, *1*(1), 93–96. https://doi.org/10.1021/jz900070h

Rajendran, P., Sidney, S., Ramakrishnan, I., & Dhasan, M. L. (2021). Experimental studies on the performance of mobile air conditioning system using environmental friendly HFO-1234yf as a refrigerant. *Proceedings of the Institution of Mechanical Engineers, Part E: Journal of Process Mechanical Engineering*, *235*(3), 731–742. https://doi.org/10.1177/0954408919881236

Ramdin, M., Jamali, S. H., van den Broeke, L. J., Buijs, W., & Vlugt, T. J. (2018). CO2 solubility in small carboxylic acids: Monte Carlo simulations and PC-SAFT modeling. *Fluid Phase Equilibria*, *458*, 1–8. https://doi.org/10.1016/j.fluid.2017.11.001

Ramdin, M., W. de Loos, T., & J.H. Vlugt, T. (2012). State-of-the-Art of CO2 Capture with Ionic Liquids. *Industrial & Engineering Chemistry Research*, *51*(24), 8149–8177. https://doi.org/10.1021/ie3003705

Ramos, M. C. D., Haley, J. D., Westwood, J. R., & McCabe, C. (2011). Extending the GC-SAFT-VR approach to associating functional groups: Alcohols, aldehydes, amines and carboxylic acids. *Fluid Phase Equilibria*, *306*(1), 97–111. https://doi.org/10.1016/j.fluid.2011.03.026

Rausch, M. H., Kretschmer, L., Will, S., Leipertz, A., & Fröba, A. P. (2015). Density, Surface Tension, and Kinematic Viscosity of Hydrofluoroethers HFE-7000, HFE-7100, HFE-7200, HFE-7300, and HFE-7500. *Journal of Chemical & Engineering Data*, *60*(12), 3759–3765. https://doi.org/10.1021/acs.jced.5b00691

Rebitzer, G., Ekvall, T., Frischknecht, R., Hunkeler, D., Norris, G., Rydberg, T., Schmidt, W.-P., Suh, S., Weidema, B., & Pennington, D. (2004). Life cycle assessment. *Environment International*, *30*(5), 701–720. https://doi.org/10.1016/j.envint.2003.11.005

Reghem, P., Baylaucq, A., Comuñas, M., Fernández, J., & Boned, C. (2005). Influence of the molecular structure on the viscosity of some alkoxyethanols. *Fluid Phase Equilibria*, *236*(1-2), 229–236. https://doi.org/10.1016/j.fluid.2005.02.009

Regulation (EC) No 842/2006 of the European Parliament and of the Council of 17 May 2006 on certain fluorinated greenhouse gases (Text with EEA relevance). (2006). *Official Journal of the European Union*, *161*, 1–11. http://data.europa.eu/eli/reg/2006/842/oj

Regulation (EU) No 517/2014 of the European Parliament and of the Council of 16 April 2014 on fluorinated greenhouse gases and repealing Regulation (EC) No 842/2006. (2014). *Official Journal of the European Union*, 195–230. http://eur-lex.europa.eu/eli/reg/2014/517/oj

Řehák, K., Klajmon, M., Strejc, M., & Morávek, P. (2017). Isothermal Vapor–Liquid Equilibria for Binary Mixtures of Methyl Nonafluorobutyl Ether + Acetone, Cyclopentyl Methyl Ether, Ethyl Acetate, n-Heptane, Methanol, and Toluene. *Journal of Chemical & Engineering Data*, *62*(11), 3878–3888. https://doi.org/10.1021/acs.jced.7b00599

Reid, R. C., Prausnitz, J. M., & Poling, B. E. (1987). *The properties of gases and liquids*. McGraw Hill Book Co.,New York, NY.

Ren, W., M. Scurto, A., B. Shiflett, M., & Yokozeki, A. (2009). *Phase Behavior and Equilibria of Ionic Liquids and Refrigerants: 1-Ethyl-3-methyl-imidazolium Bis(trifluoromethylsulfonyl)imide ([EMIm][Tf2N]) and R-134a*. https://doi.org/10.1021/bk-2009-1006.ch006

Ren, W., & Scurto, A. M. (2009a). Global phase behavior of imidazolium ionic liquids and compressed 1,1,1,2-tetrafluoroethane (R-134a). *AIChE Journal*, *55*(2), 486–493. https://doi.org/10.1002/aic.11657

Ren, W., & Scurto, A. M. (2009b). Phase equilibria of imidazolium ionic liquids and the refrigerant gas, 1,1,1,2-tetrafluoroethane (R-134a). *Fluid Phase Equilibria*, *286*(1), 1–7. https://doi.org/10.1016/j.fluid.2009.07.007

Rey-Castro, C., & Vega, L. F. (2006). Transport Properties of the Ionic Liquid 1-Ethyl-3-Methylimidazolium Chloride from Equilibrium Molecular Dynamics Simulation. The Effect of Temperature. *The Journal of Physical Chemistry B*, *110*(29), 14426–14435. https://doi.org/10.1021/jp062885s

Ribeiro, M. C. C. (2012). High Viscosity of Imidazolium Ionic Liquids with the Hydrogen Sulfate Anion: A Raman Spectroscopy Study. *The Journal of Physical Chemistry B*, *116*(24), 7281–7290. https://doi.org/10.1021/jp302091d

Riffat, S., Afonso, C., Oliveira, A., & Reay, D. (1997). Natural refrigerants for refrigeration and air-conditioning systems. *Applied Thermal Engineering*, *17*(1), 33–42. https://doi.org/10.1016/1359-4311(96)00030-0

Righetti, G., Zilio, C., & Longo, G. A. (2015). Comparative performance analysis of the low GWP refrigerants HFO1234yf, HFO1234ze(E) and HC600a inside a roll-bond evaporator. *International Journal of Refrigeration*, *54*, 1–9. https://doi.org/10.1016/j.ijrefrig.2015.02.010

Righi, S., Morfino, A., Galletti, P., Samorì, C., Tugnoli, A., & Stramigioli, C. (2011). Comparative cradle-to-gate life cycle assessments of cellulose dissolution with 1-butyl-3-methylimidazolium chloride and N-methyl-morpholine-N-oxide. *Green Chem.*, *13*(2), 367–375. https://doi.org/10.1039/C0GC00647E

Ripple, D., & Matar, O. (1993). Viscosity of the saturated liquid phase of six halogenated compounds and three mixtures. *Journal of Chemical & Engineering Data*, *38*(4), 560–564. https://doi.org/10.1021/je00012a021

Ruh, R. P., Davis, R. A., & Broadworth, M. R. (1959). *Fluorination of trichloroethylene* (US2885427A).

Sadeqzadeh, M., Papaioannou, V., Dufal, S., Adjiman, C. S., Jackson, G., & Galindo, A. (2016). The development of unlike induced association-site models to study the phase behaviour of aqueous mixtures comprising acetone, alkanes and alkyl carboxylic acids with the SAFT-γ Mie group contribution methodology. *Fluid Phase Equilibria*, *407*, 39–57. https://doi.org/10.1016/j.fluid.2015.07.047

Sánchez, D., Cabello, R., Llopis, R., Arauzo, I., Catalán-Gil, J., & Torrella, E. (2017). Energy performance evaluation of R1234yf, R1234ze(E), R600a, R290 and R152a as low-GWP R134a alternatives. *International Journal of Refrigeration*, *74*, 269–282. https://doi.org/10.1016/j.ijrefrig.2016.09.020

Santiago, R., Bedia, J., Moreno, D., Moya, C., De Riva, J., Larriba, M., & Palomar, J. (2018). Acetylene absorption by ionic liquids: A multiscale analysis based on molecular and process simulation. *Separation and Purification Technology*, *204*, 38–48. https://doi.org/10.1016/j.seppur.2018.04.060

Schneider, T., & Stoll, E. (1978). Molecular-dynamics study of a three-dimensional one-component model for distortive phase transitions. *Physical Review B*, *17*(3), 1302–1322. https://doi.org/10.1103/PhysRevB.17.1302

Schreiner, C., Zugmann, S., Hartl, R., & J. Gores, H. (2010). Fractional Walden Rule for Ionic Liquids: Examples from Recent Measurements and a Critique of the So-Called Ideal KCl Line for the Walden Plot. *Journal of Chemical & Engineering Data*, *55*(5), 1784–1788. https://doi.org/10.1021/je900878j

Sears, F. W., Salinger, G. L., & Lee, J. E. (1975). *Thermodynamics, Kinetic Theory, and Statistical Thermodynamics*. Addison-Wesley Publishing Company.

Seddon, K. R., Stark, A., & Torres, M.-J. (2002). Viscosity and Density of 1-Alkyl-3-methylimidazolium Ionic Liquids. *Clean solvents* (pp. 34–49). American Chemical Society. https://doi.org/10.1021/bk-2002-0819.ch004

Sekiya, A., & Misaki, S. (1996). A continuing search for new refrigerants. *CHEMTECH*, *26*(12). https://www.osti.gov/biblio/419608

Sekiya, A., & Misaki, S. (2000). The potential of hydrofluoroethers to replace CFCs, HCFCs and PFCs. *Journal of Fluorine Chemistry*, *101*(2), 215–221. https://doi.org/10.1016/S0022-1139(99)00162-1

Shahbaz, K., Baroutian, S., Mjalli, F., Hashim, M., & AlNashef, I. (2012). Densities of ammonium and phosphonium based deep eutectic solvents: Prediction using artificial intelligence and group contribution techniques. *Thermochimica Acta*, *527*, 59–66. https://doi.org/10.1016/j.tca.2011.10.010

Shahbaz, K., Mjalli, F. S., Hashim, M. A., & AlNashef, I. M. (2011). Using Deep Eutectic Solvents Based on Methyl Triphenyl Phosphunium Bromide for the Removal of Glycerol from Palm-Oil-Based Biodiesel. *Energy & Fuels*, *25*(6), 2671–2678. https://doi.org/10.1021/ef2004943

Shannon, M. S., Tedstone, J. M., Danielsen, S. P. O., Hindman, M. S., Irvin, A. C., & Bara, J. E. (2012). Free Volume as the Basis of Gas Solubility and Selectivity in Imidazolium-Based Ionic Liquids. *Industrial & Engineering Chemistry Research*, *51*(15), 5565–5576. https://doi.org/10.1021/ie202916e

Shariati, A., Ashrafmansouri, S. S., Osbuei, M. H., & Hooshdaran, B. (2013). Critical properties and acentric factors of ionic liquids. *Korean Journal of Chemical Engineering*, *30*(1), 187–193. https://doi.org/10.1007/s11814-012-0118-9

Shariati, A., & Peters, C. J. (2003). High-pressure phase behavior of systems with ionic liquids: measurements and modeling of the binary system fluoroform+1-ethyl-3-methylimidazolium hexafluorophosphate. *The Journal of Supercritical Fluids*, *25*(2), 109–117. https://doi.org/10.1016/S0896-8446(02)00160-2

Shiflett, M. B., Corbin, D. R., Elliott, B. A., & Yokozeki, A. (2013). Sorption of trifluoromethane in zeolites and ionic liquid. *The Journal of Chemical Thermodynamics*, *64*, 40–49. https://doi.org/10.1016/j.jct.2013.04.018

Shiflett, M. B., Harmer, M. A., Junk, C. P., & Yokozeki, A. (2006). Solubility and diffusivity of difluoromethane in room-temperature ionic liquids. *Journal of Chemical and Engineering Data*, *51*(2), 483–495. https://doi.org/10.1021/je050386z

Shiflett, M. B., Shiflett, A. D., & Yokozeki, A. (2011). Separation of tetrafluoroethylene and carbon dioxide using ionic liquids. *Separation and Purification Technology*, *79*(3), 357–364. https://doi.org/10.1016/j.seppur.2011.03.023

Shiflett, M. B., & Yokozeki, A. (2006a). Gaseous Absorption of Fluoromethane, Fluoroethane, and 1,1,2,2-Tetrafluoroethane in 1-Butyl-3-Methylimidazolium Hexafluorophosphate. *Industrial & Engineering Chemistry Research*, *45*(18), 6375–6382. https://doi.org/10.1021/ie060192s

Shiflett, M. B., & Yokozeki, A. (2006b). Separation of difluoromethane and pentafluoroethane by extractive distillation using ionic liquid. *Chimica Oggi*, *24*(2), 28–30.

Shiflett, M. B., & Yokozeki, A. (2006c). Solubility and diffusivity of hydrofluorocarbons in room-temperature ionic liquids. *AIChE Journal*, *52*(3), 1205–1219. https://doi.org/10.1002/aic.10685

Shiflett, M. B., & Yokozeki, A. (2007). Solubility Differences of Halocarbon Isomers in Ionic Liquid [emim][Tf2N]. *Journal of Chemical & Engineering Data*, *52*(5), 2007–2015. https://doi.org/10.1021/je700295e

Shiflett, M. B., & Yokozeki, A. (2008). Binary vapor-liquid and vapor-liquid-liquid equilibria of hydrofluorocarbons (HFC-125 and HFC-143a) and hydrofluoroethers (HFE-125 and HFE-143a) with ionic liquid [emim][Tf2N]. *Journal of Chemical and Engineering Data*, *53*(2), 492–497. https://doi.org/10.1021/je700588d

Shiflett, M. B., & Yokozeki, A. (2010). Separation of carbon dioxide and sulfur dioxide using room-temperature ionic liquid [bmim][MeSO4]. *Energy and Fuels*, *24*(2), 1001–1008. https://doi.org/10.1021/ef900997b

Shiflett, M. B., & Yokozeki, A. (2014). *Utilizing ionic liquids for hydrofluorocarbon separation* (US8628644B2).

Sicard, A. J., & Baker, R. T. (2020). Fluorocarbon Refrigerants and their Syntheses: Past to Present. *Chemical Reviews*, *120*(17), 9164–9303. https://doi.org/10.1021/acs.chemrev.9b00719

Sieres, J., Ortega, I., Cerdeira, F., & Álvarez, E. (2021). Drop-in performance of the low-GWP alternative refrigerants R452B and R454B in an R410A liquid-to-water heat pump. *Applied Thermal Engineering*, *182*, 116049. https://doi.org/10.1016/j.applthermaleng.2020.116049

Singh, B. S., Lobo, H. R., & Shankarling, G. S. (2012). Choline chloride based eutectic solvents: Magical catalytic system for carbon–carbon bond formation in the rapid synthesis of β-hydroxy functionalized derivatives. *Catalysis Communications*, *24*, 70–74. https://doi.org/10.1016/j.catcom.2012.03.021

Singh, J. K., Sharma, R. K., Ghosh, P., Kumar, A., & Khan, M. L. (2018). Imidazolium Based Ionic Liquids: A Promising Green Solvent for Water Hyacinth Biomass Deconstruction. https://doi.org/10.3389/fchem.2018.00548

Sinitsyn, E. N., Mikhalevich, L. A., Yankovskaya, O. P., Gulezkaya, I. F., Ivakin, V. B., Muratov, G. N., & Ermakov, G. V. (1995). Thermophysical Properties of Liquid Fluoroorganic Compounds.

Smiglak, M., Reichert, W. M., Holbrey, J. D., Wilkes, J. S., Sun, L., Thrasher, J. S., Kirichenko, K., Singh, S., Katritzky, A. R., & Rogers, R. D. (2006). Combustible ionic liquids by design: is laboratory safety another ionic liquid myth? *Chemical Communications*, (24), 2554–2556. https://doi.org/10.1039/B602086K

Smith, E. L., Abbott, A. P., & Ryder, K. S. (2014). Deep Eutectic Solvents (DESs) and Their Applications. *Chemical Reviews*, *114*(21), 11060–11082. https://doi.org/10.1021/cr300162p

Smith, W. R., Jirsák, J., Nezbeda, I., & Qi, W. (2017). Molecular simulation of caloric properties of fluids modelled by force fields with intramolecular contributions: Application to heat capacities. *The Journal of Chemical Physics*, *147*(3), 34508. https://doi.org/10.1063/1.4993572

Solomon, S., Garcia, R. R., Rowland, F. S., & Wuebbles, D. J. (1986). On the depletion of Antarctic ozone. *Nature*, *321*(6072), 755–758. https://doi.org/10.1038/321755a0

Sosa, J. E., Ribeiro, R. P. P. L., Castro, P. J., Mota, J. P. B., Araújo, J. M. M., & Pereiro, A. B. (2019). Absorption of Fluorinated Greenhouse Gases Using Fluorinated Ionic Liquids. *Industrial & Engineering Chemistry Research*, *58*(45), 20769–20778. https://doi.org/10.1021/acs.iecr.9b04648

Sosa, J. E., Santiago, R., Hospital-Benito, D., Costa Gomes, M., Araújo, J. M. M., Pereiro, A. B., & Palomar, J. (2020). Process Evaluation of Fluorinated Ionic Liquids as F-Gas Absorbents. *Environmental Science & Technology*, *54*(19), 12784–12794. https://doi.org/10.1021/acs.est.0c05305

Sosa, J. E., Santiago, R., Redondo, A. E., Avila, J., Lepre, L. F., Gomes, M. C., Araújo, J. M. M., Palomar, J., & Pereiro, A. B. (2022). Design of Ionic Liquids for Fluorinated Gas Absorption: COSMO-RS Selection and Solubility Experiments. *Environmental Science & Technology*, *56*(9), 5898–5909. https://doi.org/10.1021/acs.est.2c00051

Stell, G., Rasaiah, J. C., & Narang, H. (1972). Thermodynamic perturbation theory for simple polar fluids, I. *Molecular Physics*, *23*(2), 393–406. https://doi.org/10.1080/00268977200100381

Sujatha, I., & Venkatarathnam, G. (2018). Performance d'un système frigorifique à absorption de vapeur opérant avec des hydrofluorocarbures et des hydrofluorooléfines comme frigorigènes et du liquide ionique [hmim][TF2N] comme absorbant. *International Journal of Refrigeration*, *88*, 370–382. https://doi.org/10.1016/j.ijrefrig.2018.03.004

Swope, W. C., Andersen, H. C., Berens, P. H., & Wilson, K. R. (1982). A computer simulation method for the calculation of equilibrium constants for the formation of physical clusters of molecules: Application to small water clusters. *The Journal of Chemical Physics*, *76*(1), 637–649. https://doi.org/10.1063/1.442716

Takada, N., Tamai, R., Yamamoto, H., Sekiya, A., Tsukida, N., & Takeyasu, H. (1999). Fundamental Study of Fluorinated Ethers as New Generation Blowing Agents. *Journal of Cellular Plastics*, *35*(5), 389–402. https://doi.org/10.1177/0021955X9903500502

Takada, N., Matsuo, S., Tanaka, Y., & Sekiya, A. (1998). Gaseous thermal conductivities of new hydrofluoroethers (HFEs). *Journal of Fluorine Chemistry*, *91*(1), 81–85. https://doi.org/10.1016/S0022-1139(98)00202-4

Takahashi, K., Matsumi, Y., Wallington, T., & Hurley, M. (2002). Atmospheric chemistry of CF3CFHOCF3: kinetics of the reaction with Cl atoms and fate of CF3CFO( )OCF3 radicals. *Chemical Physics Letters*, *352*(3-4), 202–208. https://doi.org/10.1016/S0009-2614(01)01443-9

Tanaka, K., Akasaka, R., Sakaue, E., Ishikawa, J., & Kontomaris, K. K. (2016). Thermodynamic Properties of cis -1,1,1,4,4,4-Hexafluoro-2-butene (HFO-1336mzz(Z)): Measurements of the pρT Property and Determinations of Vapor Pressures, Saturated Liquid and Vapor Densities, and Critical Parameters. *Journal of Chemical & Engineering Data*, *61*(7), 2467–2473. https://doi.org/10.1021/acs.jced.6b00169

Tanaka, K., & Higashi, Y. (2010a). P ρ T Property Measurements for trans -1,3,3,3-Tetrafluoropropene (HFO-1234ze(E)) in the Gaseous Phase. *Journal of Chemical & Engineering Data*, *55*(11), 5164–5168. https://doi.org/10.1021/je100707s

Tanaka, K., & Higashi, Y. (2010b). Thermodynamic properties of HFO-1234yf (2,3,3,3-tetrafluoropropene). *International Journal of Refrigeration*, *33*(3), 474–479. https://doi.org/10.1016/j.ijrefrig.2009.10.003

Tanaka, K., Higashi, Y., & Akasaka, R. (2010). Measurements of the Isobaric Specific Heat Capacity and Density for HFO-1234yf in the Liquid State. *Journal of Chemical & Engineering Data*, *55*(2), 901–903. https://doi.org/10.1021/je900515a

Tanaka, K., Ishikawa, J., & Kontomaris, K. K. (2017). Thermodynamic properties of HFO-1336mzz(E) (trans-1,1,1,4,4,4-hexafluoro-2-butene) at saturation conditions. *International Journal of Refrigeration*, *82*, 283–287. https://doi.org/10.1016/j.ijrefrig.2017.06.012

Tanaka, K., Takahashi, G., & Higashi, Y. (2010a). Measurements of the Isobaric Specific Heat Capacities for trans -1,3,3,3-Tetrafluoropropene (HFO-1234ze(E)) in the Liquid Phase. *Journal of Chemical & Engineering Data*, *55*(6), 2267–2270. https://doi.org/10.1021/je900799e

Tanaka, K., Takahashi, G., & Higashi, Y. (2010b). Measurements of the Vapor Pressures and p ρ T Properties for trans -1,3,3,3-Tetrafluoropropene (HFO-1234ze(E)). *Journal of Chemical & Engineering Data*, *55*(6), 2169–2172. https://doi.org/10.1021/je900756g

Tang, B., & Row, K. H. (2013). Recent developments in deep eutectic solvents in chemical sciences. *Monatshefte für Chemie - Chemical Monthly*, *144*(10), 1427–1454. https://doi.org/10.1007/s00706-013-1050-3

Tao, D.-J., Hu, W.-J., Chen, F.-F., Chen, X.-S., Zhang, X.-L., & Zhou, Y. (2014). Low-Viscosity Tetramethylguanidinum-Based Ionic Liquids with Different Phenolate Anions: Synthesis, Characterization, and Physical Properties. *Journal of Chemical & Engineering Data*, *59*(12), 4031–4038. https://doi.org/10.1021/je500631j

Tchanche, B. F., Lambrinos, G., Frangoudakis, A., & Papadakis, G. (2011). Low-grade heat conversion into power using organic Rankine cycles – A review of various applications. *Renewable and Sustainable Energy Reviews*, *15*(8), 3963–3979. https://doi.org/10.1016/j.rser.2011.07.024

Thompson, A. P., Aktulga, H. M., Berger, R., Bolintineanu, D. S., Brown, W. M., Crozier, P. S., in 't Veld, P. J., Kohlmeyer, A., Moore, S. G., Nguyen, T. D., Shan, R., Stevens, M. J., Tranchida, J., Trott, C., & Plimpton, S. J. (2022). LAMMPS - a flexible simulation tool for particle-based materials modeling at the atomic, meso, and continuum scales. *Computer Physics Communications*, *271*, 108171. https://doi.org/10.1016/j.cpc.2021.108171

Thuy Pham, T. P., Cho, C.-W., & Yun, Y.-S. (2010). Environmental fate and toxicity of ionic liquids: A review. *Water Research*, *44*(2), 352–372. https://doi.org/10.1016/j.watres.2009.09.030

Tochigi, K., Satou, T., Kurihara, K., Ochi, K., Yamamoto, H., Mochizuki, Y., & Sako, T. (2001). Vapor-Liquid Equilibrium Data for the Four Binary Systems Containing Fluorocarbon, Hydrofluorocarbon, and Fluorinated Ethers at 101.3 kPa. *Journal of Chemical & Engineering Data*, *46*(4), 913–917. https://doi.org/10.1021/je000192d

Tousignant, L., & Tuma, P. E. (2000). *Hydrofluoroether as a heat-transfer fluid* (WO2001027217A1).

Tsai, W. T. (2005). Environmental risk assessment of hydrofluoroethers (HFEs). *Journal of Hazardous Materials*, *119*(1-3), 69–78. https://doi.org/10.1016/j.jhazmat.2004.12.018

Tuma, P. E. (2000). *Hydrofluoroethers as heat-transfer fluids in low temperature processes requiring sterilization* (US6303080B1).

Tuma, P. E. (2001). Using Segregated HFEs as Heat Transfer Fluids - Avoiding problems in system design. Retrieved October 6, 2022, from https://www.acota.co.uk/wp-content/uploads/2018/11/tech%7B%5C_%7DHFE%7B%5C_%7DChemProc%7B%5C_%7DFeb01.pdf

Tuma, P. E. (2006). Evaporator/boiler design for thermosyphons utilizing segregated hydrofluoroether working fluids. *Twenty-Second Annual IEEE Semiconductor Thermal Measurement And Management Symposium*, 69–77. https://doi.org/10.1109/stherm.2006.1625209

Tuma, P. E., & Tousignant, L. (2000). New "green" heat transfer fluids. *Solid State Technology*, *43*(6), 175. ink.gale.com/apps/doc/A63298787/AONE?u=anon%7B~%7Da79eeffa%7B%5C&%7Dsid=googleScholar%7B%5C&%7Dxid=77a3efd2

Twu, C. H., & Gubbins, K. E. (1978). Thermodynamics of polyatomic fluid mixtures—II: Polar, quadrupolar and octopolar molecules. *Chemical Engineering Science*, *33*(7), 879–887. https://doi.org/10.1016/0009-2509(78)85177-X

Ungerer, P., Nieto-Draghi, C., Rousseau, B., Ahunbay, G., & Lachet, V. (2007). Molecular simulation of the thermophysical properties of fluids: From understanding toward quantitative predictions. *Journal of Molecular Liquids*, *134*(1-3), 71–89. https://doi.org/10.1016/j.molliq.2006.12.019

Ungerer, P., Tavitian, B., & Boutin, A. (2005). *Applications of Molecular Simulation in the Oil and Gas Industry: Monte Carlo Methods*. Editions Technip.

United Nations. (2016). Amendment to the Montreal Protocol on Substances that Deplete the Ozone Layer.

United States Environmental Protection Agency. (2022). SNAP Regulations. Retrieved June 17, 2022, from https://www.epa.gov/snap/snap-regulations

Valderrama, J. O., Faúndez, C. A., & Campusano, R. (2019). An overview of a thermodynamic consistency test of phase equilibrium data. Application of the versatile VPT equation of state to check data of mixtures containing a gas solute and an ionic liquid solvent. *The Journal of Chemical Thermodynamics*, *131*, 122–132. https://doi.org/10.1016/j.jct.2018.09.019

Valderrama, J. O., Forero, L. A., & Rojas, R. E. (2012). Critical Properties and Normal Boiling Temperature of Ionic Liquids. Update and a New Consistency Test. *Industrial & Engineering Chemistry Research*, *51*(22), 7838–7844. https://doi.org/10.1021/ie202934g

Valderrama, J. O., & Robles, P. A. (2007). Critical properties, normal boiling temperatures, and acentric factors of fifty ionic liquids. *Industrial and Engineering Chemistry Research*, *46*(4), 1338–1344. https://doi.org/10.1021/ie0603058

Valderrama, J. O., & Rojas, R. E. (2009). Critical properties of ionic liquids. Revisited. *Industrial and Engineering Chemistry Research*, *48*(14), 6890–6900. https://doi.org/10.1021/ie900250g

Valderrama, J. O., & Rojas, R. E. (2010). Mass connectivity index, a new molecular parameter for the estimation of ionic liquid properties. *Fluid Phase Equilibria*, *297*(1), 107–112. https://doi.org/10.1016/j.fluid.2010.06.015

Valderrama, J. O., Toro, A., & Rojas, R. E. (2011). Prediction of the heat capacity of ionic liquids using the mass connectivity index and a group contribution method. *Journal of Chemical Thermodynamics*, *43*(7), 1068–1073. https://doi.org/10.1016/j.jct.2011.02.014

van der Waals, J. D. (1894). Thermodynamische Theorie der Kapillarität unter Voraussetzung stetiger Dichteänderung. *Zeitschrift für Physikalische Chemie*, *13U*(1), 657–725. https://doi.org/doi:10.1515/zpch-1894-1338

Vega, L. F., Vilaseca, O., Llovell, F., & Andreu, J. S. (2010). Modeling ionic liquids and the solubility of gases in them: Recent advances and perspectives. *Fluid Phase Equilibria*, *294*(1-2), 15–30. https://doi.org/10.1016/j.fluid.2010.02.006

Velders, G. J. M., Andersen, S. O., Daniel, J. S., Fahey, D. W., & McFarland, M. (2007). The importance of the Montreal Protocol in protecting climate. *Proceedings of the National Academy of Sciences*, *104*(12), 4814–4819. https://doi.org/10.1073/pnas.0610328104

Velders, G. J., Fahey, D. W., Daniel, J. S., Andersen, S. O., & McFarland, M. (2015). Future atmospheric abundances and climate forcings from scenarios of global and regional hydrofluorocarbon (HFC) emissions. *Atmospheric Environment*, *123*, 200–209. https://doi.org/10.1016/j.atmosenv.2015.10.071

Ventura, S. P. M., e Silva, F. A., Gonçalves, A. M. M., Pereira, J. L., Gonçalves, F., & Coutinho, J. A. P. (2014). Ecotoxicity analysis of cholinium-based ionic liquids to Vibrio fischeri marine bacteria. *Ecotoxicology and Environmental Safety*, *102*, 48–54. https://doi.org/https://doi.org/10.1016/j.ecoenv.2014.01.003

Vieira, N. S., Reis, P. M., Shimizu, K., Cortes, O. A., Marrucho, I. M., Araújo, J. M., Esperança, J. M., Lopes, J. N., Pereiro, A. B., & Rebelo, L. P. (2015). A thermophysical and structural characterization of ionic liquids with alkyl and perfluoroalkyl side chains. *RSC Advances*, *5*(80), 65337–65350. https://doi.org/10.1039/c5ra13869h

Vijande, J., Piñeiro, M. M., Bessières, D., Saint-Guirons, H., & Legido, J. L. (2004). Description of PVT behaviour of hydrofluoroethers using the PC-SAFT EOS. *Phys. Chem. Chem. Phys.*, *6*(4), 766–770. https://doi.org/10.1039/B312223A

Vilaseca, O., Llovell, F., Yustos, J., Marcos, R. M., & Vega, L. F. (2010). Phase equilibria, surface tensions and heat capacities of hydrofluorocarbons and their mixtures including the critical region. *Journal of Supercritical Fluids*, *55*(2), 755–768. https://doi.org/10.1016/j.supflu.2010.10.015

Vinš, V., Aminian, A., Celný, D., Součková, M., Klomfar, J., Čenský, M., & Prokopová, O. (2021). Surface tension and density of dielectric heat transfer fluids of HFE type-experimental data at 0.1 MPa and modeling with PC-SAFT equation of state and density gradient theory. *International Journal of Refrigeration*, *131*, 956–969. https://doi.org/10.1016/j.ijrefrig.2021.06.029

Viswanath, D. S., Ghosh, T. K., Prasad, D. H. L., Dutt, N. V. K., & Rani, K. Y. (2007). *Viscosity of Liquids: Theory, Estimation, Experiment, and Data* (Springer Science & Business Media, Ed.). Springer.

Wang, C., Luo, H., Luo, X., Li, H., & Dai, S. (2010). Equimolar CO2 capture by imidazolium-based ionic liquids and superbase systems. *Green Chemistry*, *12*(11), 2019. https://doi.org/10.1039/c0gc00070a

Wang, C., Luo, X., Zhu, X., Cui, G., Jiang, D.-e., Deng, D., Li, H., & Dai, S. (2013). The strategies for improving carbon dioxide chemisorption by functionalized ionic liquids. *RSC Advances*, *3*(36), 15518. https://doi.org/10.1039/c3ra42366b

Wang, H., Li, H., Wang, L., & Bu, X. (2017). Thermodynamic Analysis of Organic Rankine Cycle with Hydrofluoroethers as Working Fluids. *Energy Procedia*, *105*, 1889–1894. https://doi.org/10.1016/j.egypro.2017.03.554

Wang, J., Wolf, R. M., Caldwell, J. W., Kollman, P. A., & Case, D. A. (2004). Development and testing of a general amber force field. *Journal of Computational Chemistry*, *25*(9), 1157–1174. https://doi.org/https://doi.org/10.1002/jcc.20035

Wang, Q., Wu, W., & He, Z. (2019). Thermodynamic analysis and optimization of a novel organic Rankine cycle-based micro-scale cogeneration system using biomass fuel. *Energy Conversion and Management*, *198*, 111803. https://doi.org/10.1016/j.enconman.2019.111803

Wang, T., Liu, X., He, M., & Zhang, Y. (2020). Molecular dynamics simulation of thermophysical properties and condensation process of R1233zd(E). *International Journal of Refrigeration*, *112*, 341–347. https://doi.org/10.1016/j.ijrefrig.2019.12.029

Wanigarathna, D. K. J. A., Gao, J., & Liu, B. (2020). Metal organic frameworks for adsorption-based separation of fluorocompounds: a review. *Materials Advances*, *1*(3), 310–320. https://doi.org/10.1039/D0MA00083C

Wankat, P. C. (2007). *Separation Process Engineering: Includes Mass Transfer Analysis* (4th ed.). Prentice Hall.

Wasserscheid, P., Van Hal, R., & Bösmann, A. (2002). 1-n-butyl-3-methylimidazolium ([bmim]) octylsulfate - An even 'greener' ionic liquid. *Green Chemistry*, *4*(4), 400–404. https://doi.org/10.1039/b205425f

Weiss, S., & Arlt, R. (1987). On the modelling of mass transfer in extractive distillation. *Chemical Engineering and Processing: Process Intensification*, *21*(2), 107–113. https://doi.org/https://doi.org/10.1016/0255-2701(87)80013-2

Wernet, G., Bauer, C., Steubing, B., Reinhard, J., Moreno-Ruiz, E., & Weidema, B. (2016). The ecoinvent database version 3 (part I): overview and methodology. *The International Journal of Life Cycle Assessment*, *21*(9), 1218–1230. https://doi.org/10.1007/s11367-016-1087-8

Wertheim, M. S. (1984a). Fluids with highly directional attractive forces. I. Statistical thermodynamics. *Journal of Statistical Physics*, *35*(1), 19–34. https://doi.org/10.1007/BF01017362

Wertheim, M. S. (1984b). Fluids with highly directional attractive forces. II. Thermodynamic perturbation theory and integral equations. *Journal of Statistical Physics*, *35*(1-2), 35–47. https://doi.org/10.1007/BF01017363

Wertheim, M. S. (1986a). Fluids with highly directional attractive forces. III. Multiple attraction sites. *Journal of Statistical Physics*, *42*(3-4), 459–476. https://doi.org/10.1007/BF01127721

Wertheim, M. S. (1986b). Fluids with highly directional attractive forces. IV. Equilibrium polymerization. *Journal of Statistical Physics*, *42*(3), 477–492. https://doi.org/10.1007/BF01127722

Wilson, G. M. (1964). Vapor-Liquid Equilibrium. XI. A New Expression for the Excess Free Energy of Mixing. *Journal of the American Chemical Society*, *86*(2), 127–130. https://doi.org/10.1021/ja01056a002

Wu, B., Dai, C., Chen, B., Yu, G., Liu, N., & Xu, R. (2019). Ionic Liquid versus Traditional Volatile Organic Solvent in the Natural Gas Dehydration Process: A Comparison from

a Life Cycle Perspective. *ACS Sustainable Chemistry & Engineering*, *7*(23), 19194–19201. https://doi.org/10.1021/acssuschemeng.9b05194

Wu, J., Lv, B., Wu, X., Zhou, Z., & Jing, G. (2019). Aprotic Heterocyclic Anion-Based Dual-Functionalized Ionic Liquid Solutions for Efficient CO2 Uptake: Quantum Chemistry Calculation and Experimental Research. *ACS Sustainable Chemistry & Engineering*, *7*(7), 7312–7323. https://doi.org/10.1021/acssuschemeng.9b00420

Wu, S.-H., Caparanga, A. R., Leron, R. B., & Li, M.-H. (2012). Vapor pressure of aqueous choline chloride-based deep eutectic solvents (ethaline, glyceline, maline and reline) at 30–70°C. *Thermochimica Acta*, *544*, 1–5. https://doi.org/10.1016/j.tca.2012.05.031

Xu, C., & Cheng, Z. (2021). Thermal Stability of Ionic Liquids: Current Status and Prospects for Future Development. https://doi.org/10.3390/pr9020337

Yang, H., Liu, Y., Ning, H., Lei, J., & Hu, G. (2017). Synthesis, structure and properties of imidazolium-based energetic ionic liquids. *RSC Advances*, *7*(53), 33231–33240. https://doi.org/10.1039/C7RA05601J

Yang, J., Sun, Z., Yu, B., & Chen, J. (2018a). Experimental comparison and optimization guidance of R1233zd(E) as a drop-in replacement to R245fa for organic Rankine cycle application. *Applied Thermal Engineering*, *141*, 10–19. https://doi.org/10.1016/j.applthermaleng.2018.05.105

Yang, J., Sun, Z., Yu, B., & Chen, J. (2018b). Modeling and optimization criteria of scroll expander integrated into organic Rankine cycle for comparison of R1233zd(E) as an alternative to R245fa. *Applied Thermal Engineering*, *141*, 386–393. https://doi.org/10.1016/j.applthermaleng.2018.06.001

Yang, J., Ye, Z., Yu, B., Ouyang, H., & Chen, J. (2019). Simultaneous experimental comparison of low-GWP refrigerants as drop-in replacements to R245fa for Organic Rankine cycle application: R1234ze(Z), R1233zd(E), and R1336mzz(E). *Energy*, *173*, 721–731. https://doi.org/10.1016/j.energy.2019.02.054

Yang, Z.-Z., He, L.-N., Zhao, Y.-N., Li, B., & Yu, B. (2011). CO2 capture and activation by superbase/polyethylene glycol and its subsequent conversion. *Energy & Environmental Science*, *4*(10), 3971. https://doi.org/10.1039/c1ee02156g

Yasumoto, M., Yamada, Y., Murata, J., Urata, S., & Otake, K. (2003). Critical Parameters and Vapor Pressure Measurements of Hydrofluoroethers at High Temperatures. *Journal of Chemical & Engineering Data*, *48*(6), 1368–1379. https://doi.org/10.1021/je0201976

Yokozeki, A. (2001). Solubility of Refrigerants in Various Lubricants. *International Journal of Thermophysics*, *22*(4), 1057–1071. https://doi.org/10.1023/A:1010695705260

Yokozeki, A., & Shiflett, M. B. (2007). Vapor-liquid equilibria of ammonia + ionic liquid mixtures. *Applied Energy*, *84*(12), 1258–1273. https://doi.org/10.1016/j.apenergy.2007.02.005

Yokozeki, A., & Shiflett, M. B. (2009). Separation of carbon dioxide and sulfur dioxide gases using room-temperature ionic liquid [hmim][Tf2N]. *Energy and Fuels*, *23*(9), 4701–4708. https://doi.org/10.1021/ef900649c

Yuan, W.-L., Yang, X., He, L., Xue, Y., Qin, S., & Tao, G.-H. (2018). Viscosity, Conductivity, and Electrochemical Property of Dicyanamide Ionic Liquids.

Yuichi, I., Ji, H.-S., & Cho, O.-J. (2002). *Method of producing difluoromethane* (US20040102659A1).

Yushu, C., Afef, A., Fabrice, M., Roland, S., & Jeday, M. R. (2012). Thermodynamic Modeling of Mixtures Containing Carboxylic Acids Using the PC-SAFT Equation of State. *Industrial & Engineering Chemistry Research*, *51*(42), 13846–13852. https://doi.org/10.1021/ie301930q

Zakhidov, A. A., Reineke, S., Lüssem, B., & Leo, K. (2012). Hydrofluoroethers as heat-transfer fluids for OLEDs: Operational range, stability, and efficiency improvement. *Organic Electronics*, *13*(3), 356–360. https://doi.org/10.1016/j.orgel.2011.12.004

Zéberg-Mikkelsen, C. K., Baylaucq, A., Barrouhou, M., & Boned, C. (2003). The effect of stereoisomerism on dynamic viscosity: A study of cis-decalin and trans-decalin versus pressure and temperature. *Physical Chemistry Chemical Physics*, *5*(8), 1547–1551. https://doi.org/10.1039/B301202F

Zeiger, B., Gschrey, B., & Kauffeld, M. (2016). Briefing Paper: Availability of alternatives to HFCs in commercial refrigeration in the EU. *Öko-Recherche*.

Zhang, Q., De Oliveira Vigier, K., Royer, S., & Jérôme, F. (2012). Deep eutectic solvents: syntheses, properties and applications. *Chemical Society Reviews*, *41*(21), 7108. https://doi.org/10.1039/c2cs35178a

Zhang, S., Chen, Y., Ren, R. X.-F., Zhang, Y., Zhang, J., & Zhang, X. (2005). Solubility of CO2 in Sulfonate Ionic Liquids at High Pressure. *Journal of Chemical & Engineering Data*, *50*(1), 230–233. https://doi.org/10.1021/je0497193

Zhang, Y., Otani, A., & Maginn, E. J. (2015). Reliable Viscosity Calculation from Equilibrium Molecular Dynamics Simulations: A Time Decomposition Method. *Journal of Chemical Theory and Computation*, *11*(8), 3537–3546. https://doi.org/10.1021/acs.jctc.5b00351 doi: 10.1021/acs.jctc.5b00351

Zhao, D., Liao, Y., & Zhang, Z. (2007). Toxicity of Ionic Liquids. *CLEAN – Soil, Air, Water*, *35*(1), 42–48. https://doi.org/10.1002/clen.200600015

Zhao, H., Xia, S., & Ma, P. (2005). Use of ionic liquids as 'green' solvents for extractions. https://doi.org/10.1002/jctb.1333

Zhao, Y., Gong, M., Dong, X., Zhang, H., Guo, H., & Wu, J. (2016). Prediction of ternary azeotropic refrigerants with a simple method. *Fluid Phase Equilibria*, *425*, 72–83. https://doi.org/10.1016/j.fluid.2016.05.010

Zhao, Y., Li, Z., Zhang, X., Wang, X., Dong, X., Gao, B., Gong, M., & Shen, J. (2019). Azeotropic refrigerants and its application in vapor compression refrigeration cycle. *International Journal of Refrigeration*, *108*, 1–13. https://doi.org/10.1016/j.ijrefrig.2019.08.024

Zhelezny, V., Sechenyh, V., Ivchenko, D., & Semenyuk, Y. (2014). Prediction of the surface tension for refrigerants and refrigerant-oil solutions (ROS). *International Journal of Refrigeration*, *40*, 241–245. https://doi.org/10.1016/j.ijrefrig.2013.12.003